Growth, Characterization and Assembly of Lead Chalcogenide Nanosemiconductors for Ionizing Radiation Sensors

by

Brandon J. Davis

A dissertation submitted in partial fulfillment
of the requirements for the degree of
Doctor of Philosophy
(Applied Physics)
in The University of Michigan
2022

Doctoral Committee:

Associate Research Scientist Mark Hammig, Co-Chair
Professor David Wehe, Co-Chair
Professor John Foster
Professor Cagliyan Kurdak

Brandon J. Davis

brandjov@umich.edu

ORCID iD: 0000-0003-2528-9472

TABLE OF CONTENTS

LIST OF FIGURES

Figures

LIST OF TABLES

Tables

LIST OF APPENDICES

Appendix

LIST OF ABBREVIATIONS

Acronym	*Definition*
AR	Auger Recombination
BF	Bright-Field
CB	Conduction Band
CM	Carrier Multiplication
CQD	Colloidal Quantum Dots
CSA	Charge Sensitive Amplifier
CTAB	Cetyltrimethylammonium Bromide (cationic surfactant)
CWB	Cold Water Basin
CZT	Cadmium Zinc Telluride
DF	Dark-Field
DIW	Deionized Water
DOS	Density of States
DPP	Diphenylphoshpine
E_B	Binding Energy
EG	Ethylene Glycol
EPD	Electrophoretic Deposition
FFT	Fast-Fourier Transform
FTIR	Fourier Transform Infrared Spectroscopy
HPGe	High Purity Geranium
HR	High-Resolution
II	Impact Ionization
IPA	Isopropanol
IR	Infrared

LED	Light Emitting Diode
LO	Longitudinal Optical
LOR	Lift-Off Resist
MCA	Multi-Channel Amplifier
MEG	Multiple Exciton Generation
NC	Nanocrystal; Nanocrystalline; Nanocrystallite
NIR	Near Infrared
NMR	Nuclear Magnetic Resonance
NP	Nanoparticle
OA	Oleic Acid
ODE	1-Octadecene
PE	Phenyl Ether
PL	Photoluminescence
PR	Photoresist
QD	Quantum Dot
QY	Quantum Yield
RTP	Rapid Thermal Processing
SAXS	Small-Angle X-ray Spectroscopy
SC	Single-Scattering
SCE	Silver Conductive Epoxy
SEM	Scanning Electron Microscopy
SNR	Signal-to-Noise Ratio
STEM	Scanning / Transmission Electron Microscopy
TAA	Thioacetamide
TDP	Trichloroethylene
TDPSe	Tris(diethylamino)phosphine – Selenide
TEM	Transmission Electron Microscopy
T_{Gr}	Growth Temperature
TGA	Thermogravimetric Analysis
TOP	Trioctylphosphine
TOPSe	Trioctylphosphine – Selenide
UV	Ultra-Violet

VB	Valence Band
XPS	X-ray Photoelectron Spectroscopy
XRD	X-ray Diffraction

ABSTRACT

The demand for precise and efficient nuclear radiation detection has increased dramatically, particularly in numerous scientific disciplines, as well as homeland security and medical imaging applications. Modern methods by which ionizing radiation was sensed has now heavily considered using nano-scale materials for the sake of effective counting. Nanocrystalline (NC), or quantum dot (QD), semiconductors themselves exhibit exploitable properties—such as tunable energy band gap and charge carrier multiplication (multi-exciton generation) which arise due to strong quantum confinement. With this, fabricating a quantum-dot-based semiconductor to operate as a high-performance detector, via a low-cost solution-based manufacturing method, can truly alter the capabilities of radiation detectors. Using this NC approach which primarily focuses on high atomic number and density materials, was investigated as a means to maximize charge creation while minimizing the uncertainty in that conversion, as the approach is based on favorable features of NC materials for their application to the detection of ionizing radiation. The intrinsically high charge mobility combined with high atomic number and density of the lead chalcogenides makes them attractive for sensing applications with highly penetrating quanta, such as x-rays and gamma-rays, as the lead chalcogenide materials possesses an extensive literature of synthetic routes with which one can explore the strong confinement regime in quantum dots.

By varying the reaction conditions, NCs of various sizes and shapes were synthesized, and their physical and opto-electric properties were investigated. Drop-, float-, or dip-coating NC dispersions on various metal contacts resulted in close-packed NC assemblies of lead

chalcogenides. However, in sensing architectures, the exploitation of various properties for each individual nanocrystallite (NC) is hampered by the need to transport the charge carriers throughout the active volume, a motion that can be retarded by energetic surface barriers typically in the form of insulating oxides. Various synthetic routes are investigated to fabricate lead chalcogenide QDs while the feasibility of utilizing NC materials as a basis for detecting ionizing radiation is also explored. QDs and their assembled structures were carefully investigated through characterization to determine their overall quality. Methods to improve NC interconnectivity were studied and mentioned. The prevention of surface oxidation through the fabrication of NCs was also explored, resulting in chemically and optically stable NCs for at least 1.6 years.

Overall, this study focuses on using solution-based methods to fabricate nano-semiconductor nuclear radiation detectors. Various recipes will be presented, as well as the electrical results of developed NC assembly samples, with the focus on improving the charge carrier transport properties of these NC assemblies.

CHAPTER I

Introduction

Nanoscience and nanotechnology have made significant developments in recent decades—impacting a variety of disciplines. As a result, the study of nanomaterials and nanostructures is a discipline that has a rich history. Nanomaterials and nanostructures are critical supporting elements for nanoscience and nanotechnology applications ranging from fields as diverse as manufacturing, energy environment, health, and medical treatments.

The development of the frontier fields of nanoscience and nanotechnology, nano-electronic technologies and devices, nano- or microfabrication techniques, nanobiotechnology, nanomedical diagnosis techniques, and nano-environmental monitoring and treatment techniques are all examples of how technology has impacted by the study of nanomaterials and nanostructures.

Furthermore, the in-depth study of nanomaterials and nanostructures at a fundamental chemical level is a valuable source for developing new concepts, methodologies, and approaches. At the same time, the nanomaterial market is a natural force for nanomaterial development.

There remains an active interest in the preparation and characterization of nanomaterials with the smallest dimensions for the development of NC-based semiconductors. When compared to their bulk equivalents and molecular materials, semiconductor nanomaterials offer intriguing physical and chemical properties as well as valuable functionalities. Some of the most appealing properties of these materials are their narrow and intense emission spectra, continuous absorption bands, strong chemical stability, processability, and surface functionality, just to name a few. A

tremendous number of articles on the synthesis of semiconductor NCs alone represents the evolution of "nanochemistry".[1] The spatial quantum confinement effect, for example, alters the optical properties of semiconductor nanoparticles significantly. The optical and surface properties of semiconductors are greatly influenced by their high dispersity (high surface-to-volume ratio), which is caused by both physical and chemical properties of the semiconductor. As a result, semiconductor nanomaterials have attracted significant interest in research and applications in a variety of disciplines, including solid-state physics, inorganic chemistry, physical chemistry, colloid chemistry, materials science, and, more recently, biological sciences, medical sciences, engineering, and interdisciplinary fields.

The energetic states of electrons and holes in semiconductor nanomaterials is principally regulated by the well-known quantum confinement effect, whereas phonon and photon transport properties are significantly influenced by the size and geometry of the materials.[2-4] As the size of the nanostructured material decreases, the specific surface area and surface-to-volume ratio increases dramatically.[3] Size, shape, and surface features may all be changed to alter the properties of the material for various purposes.[5] Nanoelectronics, nanophotonics, energy conversion, non-linear optics, nanoscale sensors and imaging devices, solar cells, catalysis, detectors, photography, biomedicine, and other emerging technologies have all benefited from these novel properties of semiconductor nanomaterials.

Sensing the non-equilibrium charge states produced in the interaction medium is at the basis of radiation detection and measuring technologies. Thus, charges in the form of electron-ion or electron-hole pairs can be detected by their effects on the electric field generated by the surrounding device design, or the light emitted by the radiative recombination of those charges can be monitored using scintillation photon detectors. Modern ionizing radiation detection

technologies, however, was primarily based on materials established decades ago, such as single-crystal scintillators (sodium iodide), semiconductors (silicon) HPGe and gas-filled counters. Despite the advancement of technology, the expectations for accurate and effective nuclear radiation detection arising from the increased concern over the threat posed by radiological and nuclear weapons are frequently not satisfied by these existing materials' merely sufficient performances. There are a variety of causes for this, including high underlying material prices, poor information-conversion efficiency with low-cost materials, or even engineering challenges due to efforts to implement the technology.

The participation of NC semiconducting materials can be utilized for their innovations in charge-creation mechanisms and charge-transport characteristics in solid devices to accomplish effective counting, optimal detector performance, and high-resolution imaging. Ultimately, NC semiconducting materials enable charge and phonon dynamics to be controlled by geometric control of the colloidal solid, making nanomaterials more appealing than current legacy materials. Semiconducting materials functioning as the interactive medium not only reduces costs on materials by employing a solution-based fabrication process, but it also has the capacity to convert ionizing radiation into information carriers with a greater multiplicity than a typical radiation detector.[6]

The tactic developed in this research involves employing NC (also known as “quantum dot”) assembly as a semiconductor compound. The following challenges must be overcome to realize the potential of quantum-dot-based semiconductor detectors, specifically: a) charge loss during the slowing-down of the charged-particle in the interactive media, b) charge trapping during subsequent electron and hole transport, and c) small detector volumes.[6-8] To construct a NC assembly, colloidal NC dispersions of lead chalcogenides were chemically synthesized and placed

onto silicon (Si) substrates which had an evaporated metal on top. The device assemblage was periodically evaporated with metal connections on top, followed by electrical property characterization. Finally, utilizing predominantly alpha and gamma sources, the reaction of the material to radiation impingement was investigated.

The most difficult aspect of this approach is achieving a high degree of NC uniformity within assemblies and minimizing the unavoidable colloidal flaws that can build up as more layers are cast upon a sample; consequently, effective charge carrier conductivity within the material is difficult to obtain. If a solution-processed device can arrange nanoparticles to the same degree as single-crystalline devices can order atoms, then the former technique has a significant cost advantage. I will explain several fabrication techniques and subsequent findings for the NC assembly samples that I have attempted to build as a nuclear radiation detector in this dissertation. The project was primarily focused on improving the self-assembly of NCs and charge carrier transport characteristics.

Narrow band gap lead chalcogenide QDs have a high photoluminescence (PL) quantum yield (QY).[9] PbX (X = S, Se) QDs have large Bohr radii for electrons and holes, allowing them to transport both electrons and holes at the same time (ambipolar).[10-11] However, charge transport in PbX QD thin-films is still relatively poor, restricting its commercial applicability. It's imperative to develop innovative techniques to enhance charge carrier transport and ways to do so within the NC fabrication and NC self-assembly processes in order to make QD materials appealing to industry. Both of these dilemmas are covered in the following thesis, which discusses Pb chalcogenide QDs and several approaches to increase interconnectivity.

In the theory section (Chapter II), I will provide background information that is required for a better understanding of the experimental work. QD synthesis and their properties are discussed,

followed by an introduction of carrier multiplication. This is followed by an overview about QD solids, then concluding with the focus of Pb chalcogenide QDs specifically. In the experimental section (Chapter III), I'll introduce several recipes and methods used for synthesizing NCs, sample and device fabrication to witness and/or embrace self-assembly, and material and device characterization methods for observing and fine-tuning the final product and/or self-assembly structures. Theoretical background on all characterization methods/devices used are shortly explained. I will provide outcomes from NC assembly detector samples based on the Pb chalcogenide materials used, constructed with a variety of fabrication techniques and NC layer configurations in the section which evaluates electrical responses (Chapter IV). Finally, in the conclusion (Chapter V), I'll provide an overall summary of the results, discuss the overall scientific impact this research has, offer ideas for future research paths on NC assembly detectors.

CHAPTER II

Background: Colloidal Semiconductor Quantum Dots

In the early 1980s, there was an initial spark that led to a surge of interest in the field of semiconductor nanoparticle research. Throughout the world, a few research groups, "Efros *et al*.[12-14], Brus *et al*.[15-17], and Henglein *et al*.[18]", all discovered color variations in the absorption spectra of semiconductor nanoparticles based on their size.[19] As Schornbaum *et al.*[19] and others believed, this finding led to the conclusion that optical and electrical characteristics of nanoparticles may be controlled by their form and physical dimensions, unlike bulk materials, where the optical and electrical properties are determined by the material's composition.

For a semiconductor, one of the most essential properties is the band gap. A band gap in a typical semiconductor is unique and depends on the atomic composition and structure. When photons with energies greater than the band gap interact with a semiconductor with "a direct band gap, electrons get excited and travel from the valence band (VB) to the conduction band (CB)".[19] When Coulombic interactions bind the electron and hole, they create a coupled electron-hole pair known as an exciton.

Semiconductor particles are usually referred to as quantum dots (QDs) when their size is less than its exciton Bohr radius α_B, which is defined as

$$a_B = \frac{\varepsilon_r m_e}{\mu} a_0 = \frac{\varepsilon_r m_e}{\mu}\left(\frac{\varepsilon_0 h^2}{\pi m_e e^2}\right) = \frac{\varepsilon_r}{\mu}\left(\frac{\varepsilon_0 h^2}{\pi e^2}\right), \tag{2.1}$$

$$\therefore\ a_0 = \frac{4\pi\varepsilon_0\hbar^2}{m_e e^2} = \frac{4\pi\varepsilon_0}{m_e e^2}\left(\frac{h^2}{4\pi^2}\right);\qquad \hbar\ (Planck's\ Const.) = \frac{h}{2\pi}$$

where a_0 is the Bohr radius for a hydrogen atom, ε_0 is the free vacuum permittivity, ε_r is the semiconductor's relative permittivity, μ represents the reduced mass of the electron and hole ($^{m_e m_h}/_{m_e + m_h}$), and e is the electron charge.[20]

Quantum confinement exists for the electrons and holes in all three dimensions because such small particle sizes exist. QDs are referred to as zero-dimensional materials because of their reduced dimensions. Figure 2.1 demonstrates how a band gap diagram transforms from a bulk material with continuous energy bands to a molecular size material with discrete energy levels, while QDs remain in the transitional state. As a result, the band gap of QDs grows while the QDs actually shrink.[1, 11, 21] The particle-in-a-sphere model[12, 22] explains this phenomenon. with the semiconducting QD depicted as a spherical mass with an insulating barrier surrounding it. All photoexcited electrons and holes are confined within a spherical QD possessing a constant potential (three-dimensional potential wall – Eq. 2.2). This scenario of a mass m particle constrained in a spherical symmetric potential wall, V, may be represented as:

$$V(r) = \begin{cases} 0, & if\ r < a \\ \infty, & if\ r \geq a \end{cases} \tag{2.2}$$

where the radius of a sphere is defined by *a*. Semiconducting QDs possess a crystal lattice that represents a periodic potential, which could leave the wave-functions of electrons and holes to be expressed as Bloch functions. As a result of solving the Schrödinger equation and accounting for the fact that the wave-function must decrease "to zero at the QD edge (considered by β in eq. 2.3), the particle has discrete energy levels".[19] Therefore, unlike in bulk semiconductors, the absorption and emission bands in QDs are discrete rather than continuous. The density of states (DOS) for the zero-, one-, two-dimensional and bulk semiconductors are shown in Figure 2.2. There "one can notice the number of states in a given energy level is also dependent upon the dimensionality of the semiconductors", resulting in sets of discrete delta functions for QDs.[19, 22]

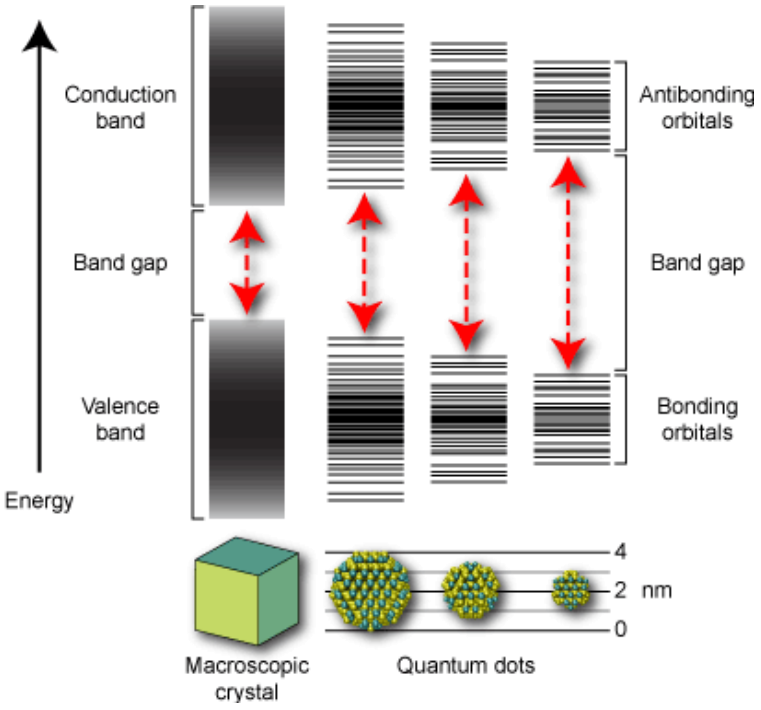

Fig. 2.1 | Energy band diagram for quantum dots of various sizes and bulk materials (evolution of atomic orbitals into crystal energy bands). The separation between the discrete energy levels reduces as the number of orbitals increases, eventually approaching a continuous band gap diagram for bulk materials. The energy band diagram for QDs may be found between continuous and fully discrete energy levels. Figure from reference.[20]

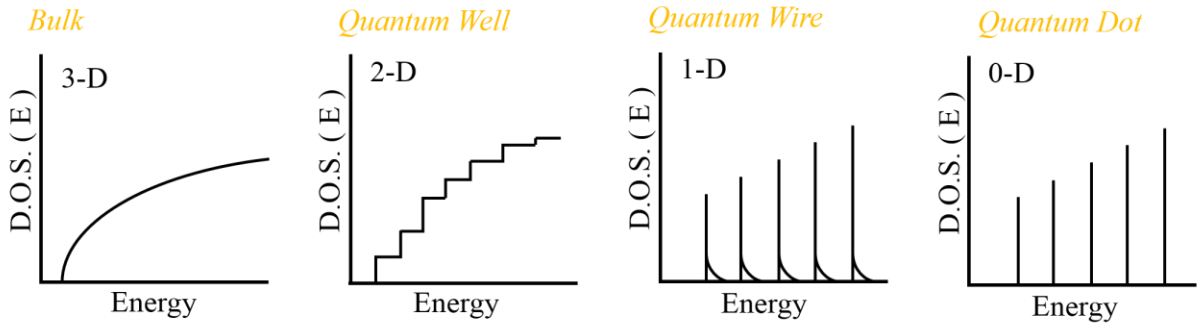

Fig. 2.2 | Schematic of density of states as system dimensionality is reduced. The density of states in different confinement configurations: (bulk – 3D) density of states is relative to one taking the square root of the energy; (well – 2D) DOS is independent of the energy; (wire – 1D) is relative to one taking the square root of the energy; (dot – 0D) are discrete. Figure adapted from reference.[22]

Furthermore, eq. 2.3 reveals QD band gap energy is inversely squared in relation to the radius, r_{QD}, which explains the blueshift in QD absorption as QD size decreases:[12, 22]

$$E_{bg} = \frac{h^2k^2}{8\pi^2m^*} = \frac{\hbar^2k^2}{2m^*} = \frac{\hbar^2\beta^2}{2m^*r_{QD}^2} \ , \tag{2.3}$$

where E_{bg} is the energy of the size-dependent band gap, h denotes Planck's constant, $\hbar$ denotes the reduced Planck's constant, and k denotes the wave vector $\left(\beta/r_{QD}\right)$.

Colloidal quantum dots (CQDs) are referred to QDs synthesized in solution. This way there is no confusion when distinguishing QDs from QDs produced by alternative deposition techniques, such as various vacuum-deposition processes. Since QDs were always synthesized in solution within the scope of this research, the word and acronym QDs will refer to CQDs for the sake of thesis. QDs synthesized in solution have an inorganic crystalline core that is stabilized by in-/organic surfactants (Fig. 2.3a). "QDs typically range in size from 2 to 50 nm, with the smallest

QDs containing "just under 100 atoms and the biggest QDs containing upwards of 100,000 atoms".[19] QDs also possess a rather large surface-to-volume ratio, providing reason as to why the surface has an unusually significant impact on QD properties, such as optical performance and charge transport for example.[19, 23]

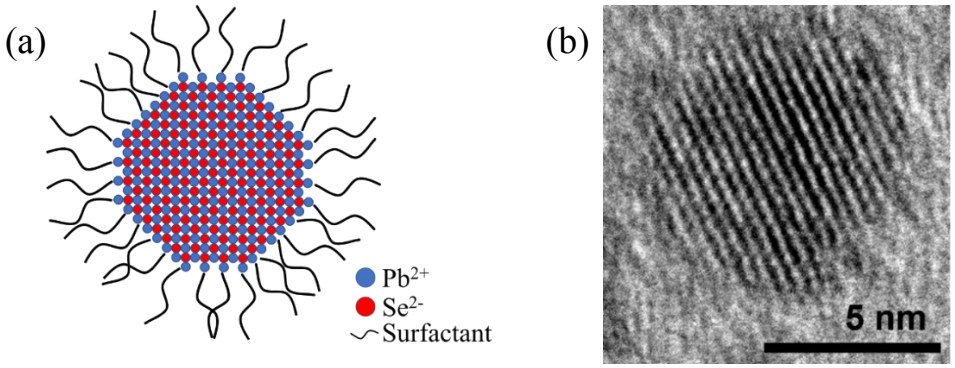

Fig. 2.3 | (a) A schematic of a PbSe QD incorporated with surfactants on the exterior while the outer shell is protected by Pb atoms. (b) High-resolution transmission electron microscopy (HRTEM) image showing visible PbSe QD, revealing lattice planes.

2.1 Synthesis via Hot-Injection

Initially, with starting QD research, it became exceedingly hard to manufacture monodisperse QDs inside such a regulated and repeatable manner exhibiting desired physical and chemical properties. Though Brus and Henglein's groundbreaking work detailed essential synthetic methods as well as a basic knowledge of electrical properties their initial syntheses resulted in polydisperse QD samples with a high defect content.[15-16, 24-27] To manufacture high-quality QDs with a limited size range and excellent crystallinity, an optimized synthesis was needed. Currently, we know that physical and chemical properties of QDs can be fine-tuned with precise control over their size, shape, and surface chemistry.[28]

Murray, Norris, and Bawendi reported an important hot-injection synthesis approach in 1993, creating a genuine turning point in QD research and triggering another surge in QD interest.[29] They discovered that by using a temporally discrete nucleation period, a hot-injection technique can produce monodisperse, highly luminous, well-passivated, and mostly unflawed QDs. Murray *et al*.[2, 29] used organometallic Cadnium (Cd) and/or chalcogenide (Se, S, Te) precursors, as well as a non-polar coordinating solvent with a high-boiling point to synthesize Cd chalcogenide QDs ranging from 1.0–12 nm in size.[19]

Typically, the synthesis fabricating QDs by way of hot-injection involves three parts: the precursors (defines the components of the inorganic core); the surfactant, (establishes colloidal stability, suppresses aggregation, passivates unsaturated surface dangling bonds, manages nucleation and growth); and the solvent (synthesis medium). Early on in this method, the coordinating solvent was also used as surfactant.[2, 29] Yu *et al*.[30] later developed a hot-injection synthesis employing octadecene as a non-coordinating solvent along with coordinating ligands. Syntheses the use using non-coordinating solvents and coordinating surfactants separately increase their flexibility and/or tunability due to the size and size distribution of the QDs produced, as they may be able to be regulated by the concentration of surfactant;[30] something that doesn't occur when only using a coordinating solvent.[19]

Many synthetic variables, such as surfactants and precursors (materials and concentrations), injection temperature, growth temperature, and growth time, can now influence size, size dispersion, shape, and composition of QDs produced via hot-injection synthesis.[31-32]

2.1.1 Nucleation and Growth in Solution Phase

The main notion of the LaMer theory, created in 1950, governs the nucleation and early growth of QDs, and is illustrated in Fig. 2.4. This framework states that in order to create monodisperse particles, nucleation and growth must be separated in time.[33] A burst of nucleation occurs after a rapid injection of a room-temperature precursor into a hot liquid, accompanied by the expansion of existing nuclei.[2] The LaMer nucleation theory, however, may not account for all events seen throughout QD growth. As a result, Rempel *et al*.[34-35] devised a step-by-step procedure: in the *first step*, monomers are generated from organometallic precursors, resulting in a rise in particle concentration and a growth of tiny clusters as a *second step*. Following the clusters, there is a size-focusing process in the *third step*, a pseudo state with an unchangeable average diameter and a *fourth step* of size distribution. Lastly, in the *fifth step*, Ostwald ripening occurs, which leads to defocusing. Defocusing occurs during the Ostwald ripening phase when small, high surface energy crystals dissolve at the cost of large crystals having low surface energy growing (Fig. 2.4).[19]

With existing theories combined, QD development may be portrayed as follows: the precursor breaks down at very high temperatures during nucleation, resulting in a supersaturation of monomers in solution. A rapid injection of the second precursor then separates nucleation and growth in time. The resulting nucleation burst decreases the monomer concentration under the nucleation threshold, resulting in a vast number of nuclei. Still, the monomers are in solution at this point, only contributing to remaining nuclei rather than forming new nuclei. The rapid injection of the second precursor (at room-temperature) into the heated first precursor solution then causes significant temperature decrease. However, the decrease in temperature guarantees that the growth temperature is lower than the injection temperature, preventing additional nucleation during the growth stage. Monomers are incorporated into existing nuclei to allow them to grow.[32]

The nuclei growth is diffusion-limited as long as the content of monomers within the solution is high, as this results in size-focusing. Due to small nuclei having a higher surface-to-volume ratio than large nuclei, the smaller nuclei will develop quicker than larger nuclei, causing all QD sizes to adjust.[31, 36] Slow Ostwald ripening happens when one or more precursors are completely consumed, resulting in a defocusing process. This reversal of size-focusing then results to a lack of monodispersity, thus a greater size distribution. The population of growing QDs remains unchanged during the focusing phase but drops during the defocusing phase, whereas the number of monomers reduces dramatically during the focusing phase but remains constant (or very low) during the defocusing phase.[2, 37]

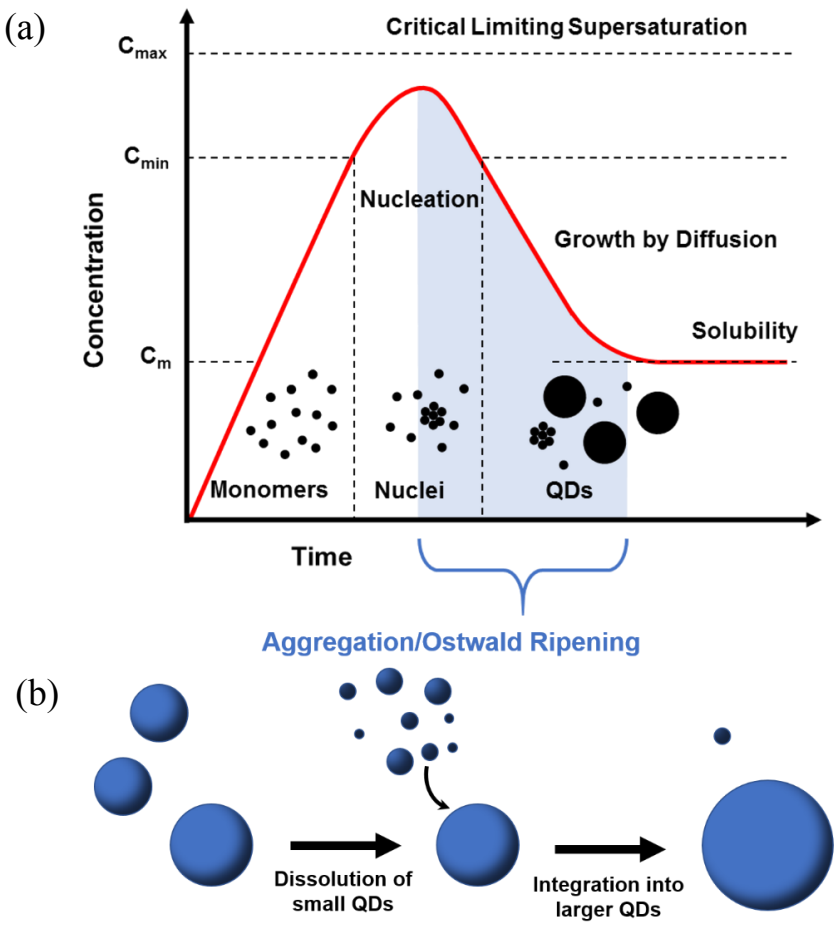

Fig. 2.4 | (a) LaMer diagram for the generation of monomers (atoms), nucleation, and subsequent growth of colloidal systems. (b) Illustration of Ostwald ripening process, where small crystals dissolve and integrate into large crystals. Figures adapted from references.[19, 33, 38]

2.1.2 Function and Influence of Surfactants

Surfactants utilized here in QD syntheses are often long-chain carboxylic acids, phosphonic acids, or amines. These surfactants, typically composed of an alkyl chain possessing carbon atoms (12 to 18 atoms), also possess an anchoring group (e.g., amino, carboxylic, phosphonato, etc.) that has a strong attraction for the QD surface.[39-40] The surfactants establish a steric barrier of reactants by dynamically coordinating with the surface of the developing QDs. As a result, at high

temperatures QD growth is rather sluggish, resulting in QD self-annealing. Internal grain boundaries and flaws are removed during the self-annealing process, resulting in very crystalline QDs that are and defect-free.[32]

2.1.3 Purification Process

Once a synthesis is completed, the QDs must be removed from the growth solution to remove unreacted precursors and/or excess surfactants. The post-synthesis process typically involves adding a polar solvent to the growth solution to destabilize the colloidal suspension, causing QDs to then experience aggregation and precipitation.[19] The QDs are then re-dispersed in a non-polar solvent to create a stable and defect-free colloidal suspension.[2, 32] However, the colloidal stability of the QDs is gradually reduced by adding polar solvent throughout these stages. Due to greater attraction forces along large QDs versus small ones, large QDs tend to aggregate and precipitate ahead of the smaller ones. This size-selective precipitation allows QDs with narrow size distributions to be separated. The after-effects that the post-synthesis processing can have on the final QD properties should not be overlooked, even if the purification procedure is vitally required.[41-42]

2.1.4 Controlled Growth of Nanocrystals

The properties of QDs are influenced primarily by their size and shape.[43-44] Presently, a wide range of well-defined shapes, counting as spheres, stars, rods, rings, etc. can be synthesized.[31, 45-49] Either oriented attachment,[49-50] kinetically induced anisotropic growth,[31, 51] or even seed-

mediated solution-to-solid growth[52] can be used to create these anisotropic forms.[19] Even so, additional components within the growth solution might also impact the QD form, resulting in shapes such as nanotubes.[53-54] The following is how anisotropic growth via oriented attachment was first explained:[50, 55-56] The nanocrystals (NCs) rotate continuously until they locate an identical crystal facet of a neighboring NC. They then merge spontaneously into two or more NCs to minimize surface energy by removing high-energy crystal facets (Fig. 3.63).[57-58] Short nanorods and long nanowires are common forms generated via oriented attachment,[59-60] but more complicated structures such as honeycomb superlattices have also been achieved.[61] Surfactants play a major role in kinetically induced anisotropic growth, although the heating regime and monomer concentration also contribute.[62-63] Although spherical QDs form within the thermodynamic growth regime, anisotropic QDs need the regime of kinetic growth, which is achievable with a high growth rate. At low growth rates, because high- and low-energy facets have only slight differences, all facets grow at the same pace. As a result, under the thermodynamic growth regime spherical QDs emerge. However, because the growth rate is proportional to the surface energy, high-energy facets would develop faster than low-energy facets at high growth rates. This causes fast-growing facets to be eliminated, leaving cubic QDs influenced by the slower-growing facets.[31] When an organic surfactant attaches to the facet of a crystal, the crystal's growth then becomes effected. Surfactants or surfactant combinations with various binding energies can be used to manipulate the growth kinetics of different facets, allowing for careful tuning of the final QD shape.[31] Even branching NCs can be produced if the QD seed has a polymorph crystal structure, which implies two or more crystal structures can coexist in just one NC.[51]

2.2 Optical & Electrical Properties of Nanocrystals

The quantum size effect is visible in QD absorption spectra, where the location of the absorption peak blueshifts as the QD diameter decreases (i.e., as the band gap increases) (Fig. 2.5). The initial transitions, as well as higher allowed transitions, are seen in the absorption spectra of monodisperse QDs. Furthermore, each sample of QDs has a size dispersion, causing the absorption peaks to expand. The smaller the size distribution of the QD sample, the noticeably higher the energy transition peaks are (the smaller the full-width half maximum (FWHM) of the first absorption peak is).[19] Deep and shallow trap states in QDs can be caused by a variety of factors. The abrupt termination of the crystal lattice, for example, causes numerous dangling bonds on the QD surface. Charge carriers can become highly restricted in these dangling bonds, which function as trap states.[22] Additional acceptor or donor levels created by crystal lattice imperfections can trap charge carriers as well. Surface oxidation can also cause flaws to form during and/or after QD growth.[64] Charge trapping by surface and/or mid-gap trap states can be detrimental (e.g., traps or non-radiative recombination locations, which reduce light-emitting diode (LED) efficiencies[65]) or beneficial (e.g., traps or non-radiative recombination sites, which increase LED efficiencies) depending on the QD application (e.g., trap states generate photoconductive gain in photodetectors[66]).

In summary, a QD sample of high-quality can be illustrated by its absorbance spectra, which are characterized by trap states, good exciton confinement, and a narrow size distribution. This is all because well-defined higher order absorption peaks, narrow absorption and the excitonic absorption peak characterize such high-quality QD samples.

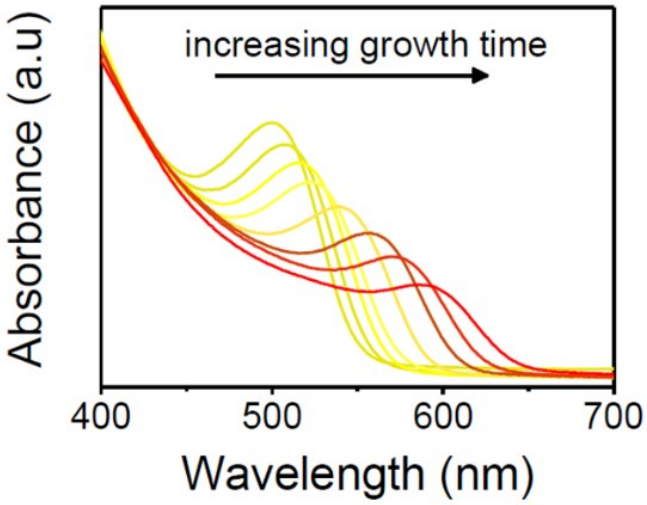

Fig. 2.5 | Absorption spectra of a sequence of QDs showing how, as growth time rises, the size of the QD increases, however, the band gap energy decreases causing redshifts in the absorption spectra. Figure from reference.[19]

The majority of QDs in solution are quantified by photoluminescence quantum yield (PL QY), which is the number of electron-hole pairs produced per absorbed photon.[67] The PL QY of average Cd chalcogenide QDs measured in solution right after synthesizing is 50%, but decreases to 5-10 % in thin-film form.[22] This strong difference in PL QY is due to the non-emitting QDs in thin films having a larger effect.[19] Due to QD films possessing QDs of various sizes, roughly only one non-emitting exciton state would be able to satisfy the emission of only some luminescent neighboring QDs.[22] Also, unlike QDs in solution, QD thin films possess surface traps which can't passivated with excess ligands.[22] Therefore, the PL QY is based on trap states, surfactants,[68] possible surfactant exchanges,[69] and solvents used during the purification process.[41] These components could either increase[68] or decrease[41] the intensity of PL. However, despite trap state and surfactant challenges and quenching effects, QDs still remain excellent candidates for light emitting and

identifying materials within optoelectronic applications due to their adjustable optical properties, spectrally narrow and efficient PL, and strong photostability.[19]

2.2.1 Non-/Linear Exciton Dynamics Optical Lattice & Electronic Properties

Consider first only linear exciton dynamics, in which only one exciton per photon is created on average when exciton energies are low and photons with energy equivalent to or higher than the band gap strike a QD.[19] An exciton is a Coulomb attraction-bound neutral electron-hole pair (Fig. 2.6a). Excitons can be relaxed in a variety of ways.[20] In the case of excitation energy being significantly greater than the band gap energy, E_{bg}, electrons and holes then possess excess kinetic energy ("hot" charge carriers) that could get lost until reaching the CB and VB edges via rapid intraband of an electron or hole thermalization. Intraband relaxation is a highly rapid process that takes several tens of femtoseconds to complete.[20] Electrons and/or holes from the VB and CB edges may be trapped and recombine after a set amount of time, or they may even recombine immediately without being trapped. Recombination can occur both radiatively (emitting a photon) and non-radiatively (releasing heat).[20] High-quality QDs with practically no trap states are associated with recombination that is primarily radiative with lifetimes ranging from a few nanoseconds to a few tens of nanoseconds. On the off chance charge carriers happen to be trapped, “trapping (many hundred femtoseconds to a some tens of picoseconds)” would be quicker than band edge radiative recombination; the reason being that once a charge carrier is trapped, the charge may recombine or experience more issues with becoming trapped in even deeper trap states, then changing to “lifetimes of hundreds of picoseconds to microseconds”.[19] However, in the event that excitation energies increase, exciton dynamics shift from linear to non-linear, where a photon can produce more than one exciton in the non-linear range, resulting in a biexciton (i.e. two

electron-hole pairs in neutral charge) production. More details of this phenomenon will be clarified within the next section.

2.3 Carrier Multiplication

Carrier Multiplication (CM), also known as multiple exciton generation (MEG), is a photogeneration method for multi-excitons in which a single photon produces two or more electron-hole pairs. During the CM process, a hot charge carrier with energy exceeding that of the band gap (either electron in conduction band or hole in valence band) experiences excitation with a valence band electron reaching the conduction band that then eventually relaxes (de-excites). Schaller *et al*.[70] published the first report of CM in QDs in 2004. In understanding the CM process, the photon energy being absorbed must be at a minimum of two times the band gap energy, E_{bg}, to produce CM.[71] This makes a small band gap material such as Pb chalcogenide QDs suitable for observing CM.[72-73]

Absorption of a photon with energy $h\nu \geq E_g$ in a typical semiconductor material produces a single electron-hole pair and excited charge carriers with a kinetic energy of at least kT above the CB and VB edges. As the carriers de-excite near the band edge, they would experience a variety of relaxation interactions, including carrier-carrier collisions, inter-valley scattering, and carrier-phonon interactions. The photon energy that exceeds the energy band gap is lost as heat in the phonon emission process until excited charge carriers achieve equilibrium by transferring excess kinetic energy to quantized lattice vibrations known as longitudinal optical (LO) phonons.

In the same instance, strong Coulombic interactions between carriers can activate a competitive carrier generation/relaxation medium between the CM and phonon emission (carrier

relaxing/cooling/de-excitation) processes.[71] Within this contest, the generating option is for a hot charge carriers' excess energy to be transferred to another carrier in the VB, causing that carrier to be excited across the energy band gap from a collision-like process known as Impact Ionization (*II*) (Fig. 2.6(b)). This is the inverse of a relaxation process, Auger Recombination (*AR*), where energy released by exciton recombination is exchanged to a third carrier (electron or hole), which is at that point energized to a higher energy level to later thermalize back to the first excited state (Fig. 2.6(a)).[19, 74-75]

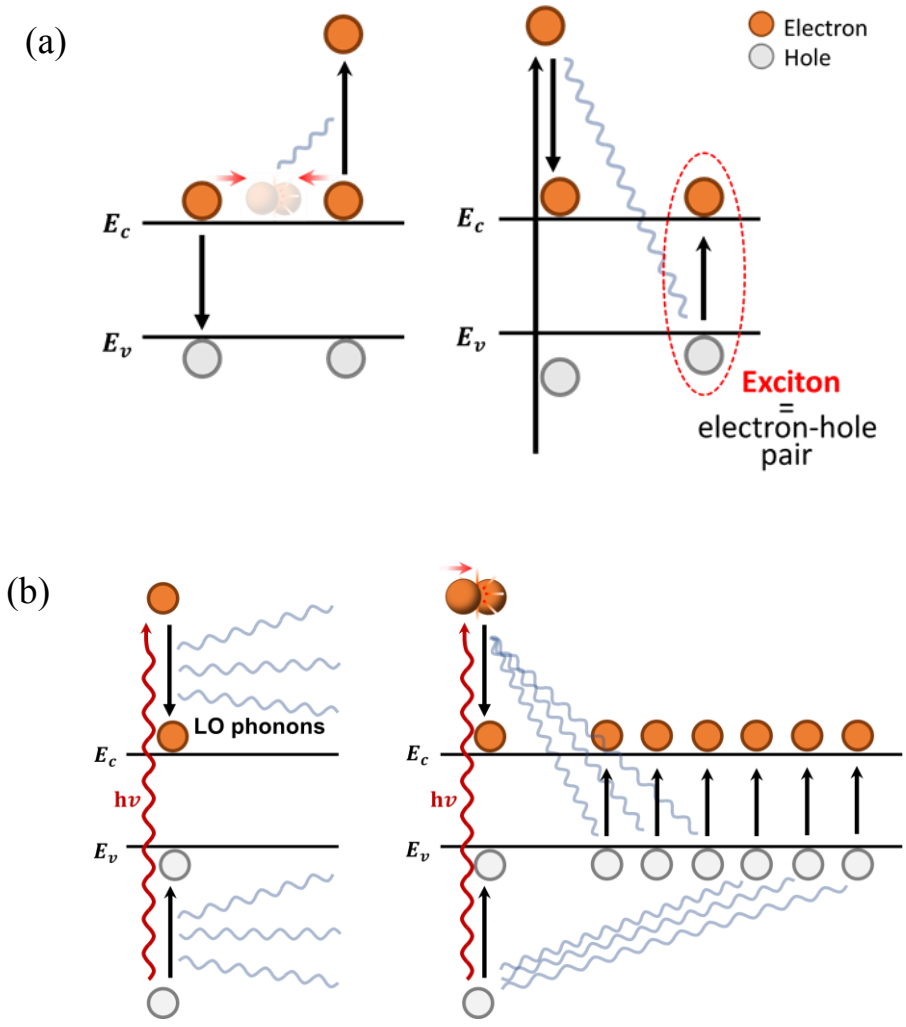

Fig. 2.6 | Schematic of the generation of multi-excitons via (a) Auger recombination (AR) and (b) Impact Ionization (II). Figures adapted from reference.[8]

Let us now look back at the general process of CM, where a hot electron and hole are produced and usually thermalize quickly to the band edge with excess energy being lost as heat via non-radiative recombination (*AR*).[76] This possesses a fundamental limitation to the efficiency of a solar cell.[71] In dealing with energy conservation, the smallest amount of photon energy required to initiate CM ($\hbar\omega_{CM}$) is $2E_g$.[77] However, CM thresholds for bulk materials are quite larger than this value since bulk semiconductors generally accept MEG as *II*.[77] Therefore, the CM threshold is decided by the conservation of energy and conservation of translational momentum which both help increase the CM threshold for bulk materials above $2E_g$. In applying energy and momentum conservation laws to a free-particle approximation,[77] a CM threshold of $4E_g$ can be achieved (parabolic bands with equal electron and hole effective masses; Fig. 2.7a). In the case for CM in QDs, translational momentum conservation is relaxed and energy conservation is used to primarily define the CM threshold to make a $2E_g$ limit.[77] However, experimentally there has been evidence of Pb chalcogenide QDs, with roughly equal effective masses of electrons and holes, showing the CM threshold is close to $3E_g$ (Fig. 2.7b).[77] There, the QY increases almost linearly while the steepness of the slope represents the various levels of CM efficiency. Considering solar applications, the CM QY is typically plotted versus the photon energy normalized to the band gap, which is symbolized as the band gap multiple, defined by $h\nu/E_g$ (Fig. 2.7c).[71, 77]

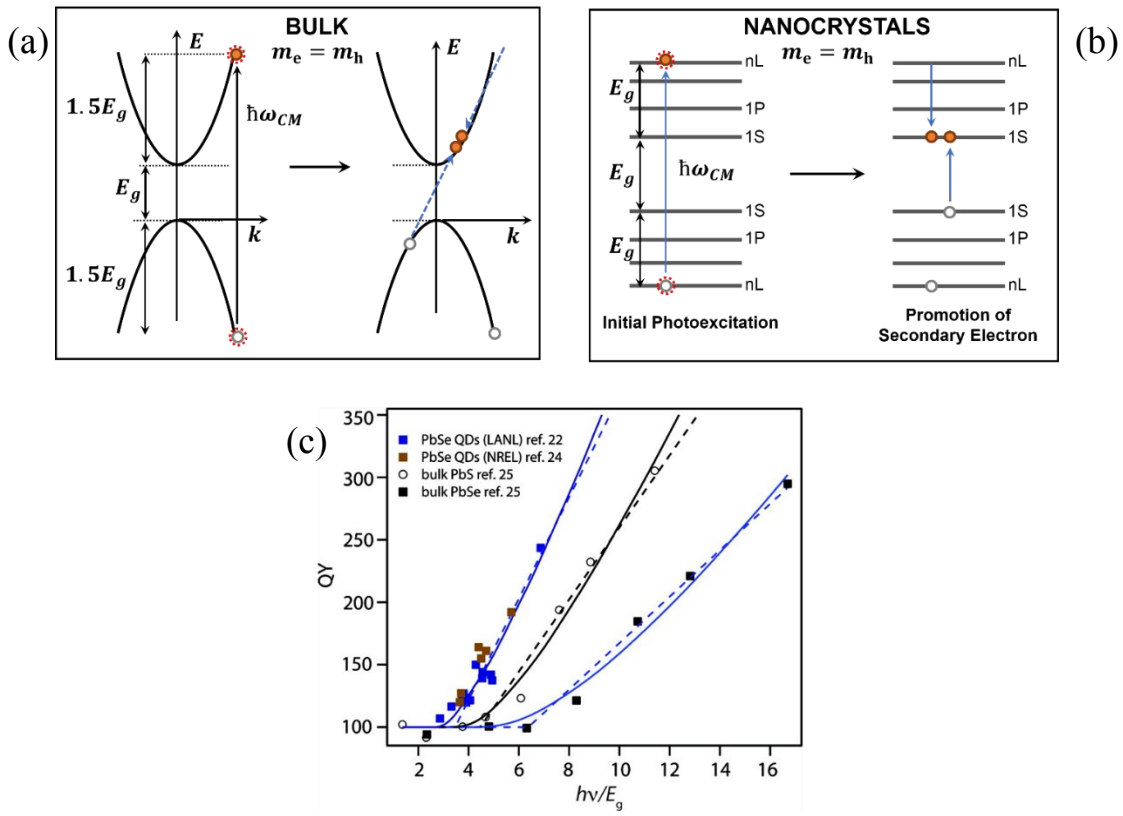

Fig. 2.7 | CM threshold in bulk semiconductors and QDs. (a) CM threshold experiencing restrictions imposed by energy and translational momentum conservation for both the photoexcitation (left) and impact ionization (right) steps. These restrictions provide a CM threshold for bulk to be greater than $2E_g$. In the scenario where $m_e = m_h$, the CM threshold rises to $4E_g$. (b) In the case of the QDs, the relaxation of momentum conservation rules can result in a much lower CM threshold. (c) CM QY versus band gap multiple (hv/E_g) for PbSe and PbS QDs and bulk. Figures adapted from references.[77-78]

The motivation for CM research comes from the potential it could have on applications in photovoltaics, where this phenomenon may possibly improve the power conversion efficiency of solar cells via higher photocurrent.[11, 40] As illustrated graphically in Fig. 2.8, conventional photovoltaic solar cells generate electricity by absorbing light or photons and producing a single electron hole pair.

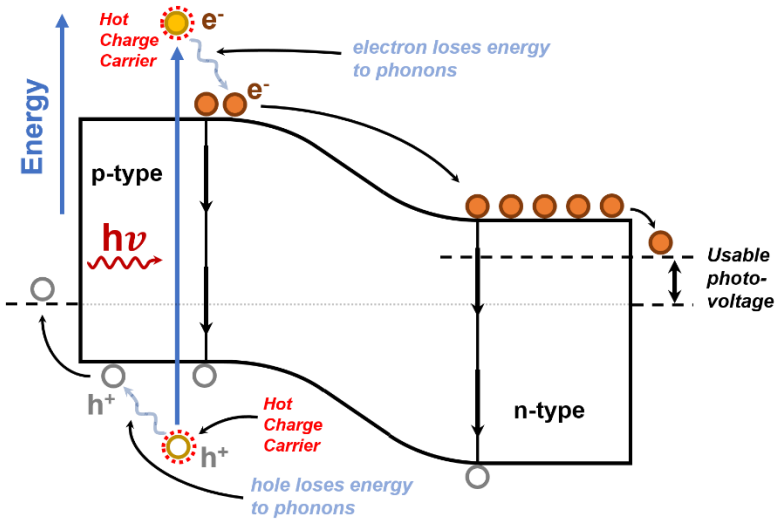

Fig. 2.8 | Schematic of a conventional p – n junction solar cell experiencing the energy conversion process. Absorbed light from photon energies greater than the band gap generates "hot" charge carriers (electrons and holes) with excess kinetic energy. The carriers lose energy by scattering with the lattice and/or emitting phonons. Figure adapted from reference.[79]

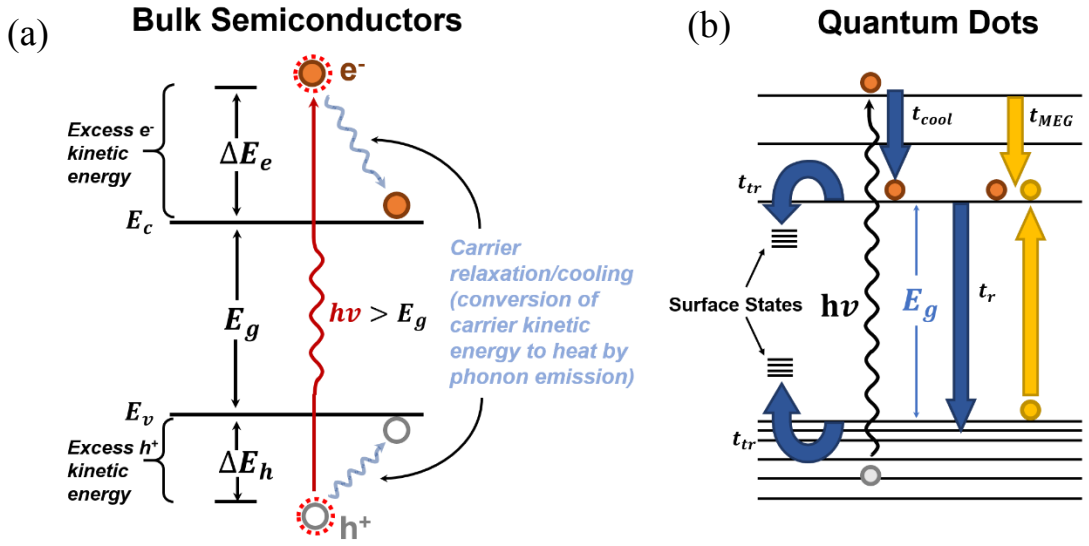

Fig. 2.9 | (a) Hot carrier relaxation/cooling dynamics within bulk semiconductors. (b) Charge carrier dynamics in QD semiconductors while under the quantum confinement effect. Excess energy from charge carriers is only produced at the allowable states of the QDs. The influence of surface states then becomes significant in QDs with their increased surface-to-volume ratio. Cooling by phonon emission then becomes less efficient while CM becomes more efficient. Figure adapted from references.[79-80]

Both processes are inefficient in the bulk state because of weak Coulomb interactions, translational momentum conservation restrictions, and rapid phonon emission competing with *II*. To enable the process, a lot of thermal energy is needed to produce momentum-conserving phonons.[79, 81]

Discretized electronic energy states of the carriers in the NCs reduce the availability of electronic states that satisfy energy conservation in the phonon emission process (Fig. 2.9(b)), resulting in unusually slow intraband relaxation processes, known as the "phonon bottleneck" effect. Phonon-emission-type carrier relaxation can only occur through multi-phonon relaxation, which is uncommon for highly confined carriers in NCs where energy level separation can surpass multiple LO phonon energies.[81-82] The energy loss exchanges can become dominated by *II*, which is the previously stated Auger-type process in which multiple excitons are generated from a single incident quanta, as illustrated schematically in Fig. 2.6(a).[72]

The enhancement of the Coulombic interactions, as represented by exciton and biexciton (a quasiparticle created from two free electrons) binding energies, is another important aspect of the quantum confinement effect in NC solids, with the latter providing a measure of the strength of the exciton-exciton interaction. As the NC size decreases, these energies rise, resulting in high-efficiency non-radiative decay of multi-excitons through *AR*, which counteracts *II* (see Fig. 2.6a). The symmetry of the matrix elements means that in quantum-confined NCs, both *II* and *AR* can be highly efficient.

The recombination dynamics of single and multi-excitons differ significantly in most techniques used to examine CM phenomena. In NCs, single- and multi-excitons degrade at different rates. This difference in decay time (nanoseconds for single excitons via slow radiative

recombination vs. picoseconds for multi-excitons) is due to the *AR* in multi-excitons becoming a single exciton, which may be observed as a fast decay component in the NC population dynamics.[79]

Many spectroscopic studies have discovered experimental evidence for efficient CM in quantum confined NCs using the two techniques. The initial study of highly effective CM in PbSe NCs was published in 2004,[70] and it was followed up by research on a variety of various NC compositions, including PbS, PbTe, CdSe, InAs, and Si.[77, 83-85] However, due to the observed quantum efficiencies (QEs) of photon-to-exciton conversion (a.k.a. CM yields) in early publications, recent studies have shown either significantly lower values,[86-87] or the CM effect not being detected at all.[88-89] This process has become a source of intense controversy. Several variables in the experiment are responsible for the considerable differences: (1) NC surface properties, (2) NC charging, (3) multiple photon absorption events, and (4) transient spectral shift.

Recent findings, however, have revealed the existence of more efficient CM in NCs than in bulk semiconductors. The CM is predicted to be more efficient in QDs, at least in theory, because of the restricted availability of electronic states, which limits the phonon emission process. Increased CM efficiencies have been linked to slow phonon-related carrier cooling in NCs.[90-91] This provides a compelling argument for using NC-based devices in the development of radiation detectors.

2.4 Quantum Dot Solids

QDs will never exist as individual particles in many applications; instead, they will exist as QD films. Thus, being able to produce homogenous films, as well as understand and control the

process behind QD coupling and charge transport, is critical.[92] In order to create effective devices, QD films have two significant disadvantages that must be solved. One being QDs exhibiting low charge carrier mobilities because of low electrical coupling within the QD solid. The other, being the issue, is QDs often having poor passivation and structural flaws, resulting in a high density of surface to "midgap-trap states" and "non-radiative losses".[19, 93] It is critical to enhance coupling, minimize trap states, and optimize "thin-film morphology" in order to apply QDs to commercial applications.[19, 92]

2.4.1 Formation of Thin Films - Solution-based Material Processing of QDs

Seeing that QDs could even be dispersed in volatile solvents, processing the material and forming QD thin-films on various substrates can be straightforward.[19] QD solids are another name for these thin films. QDs with a restricted size range along with a spherical form produce "hexagonal close-packed domains (10-100 nm)", allowing for strong interdot coupling.[19, 40, 73] QD films are formed using a variety of techniques, including spin coating,[94] dip coating,[95] drop-casting,[96] inkjet printing,[97] and spray coating.[98] While drop-casting may produce inhomogeneous films on occasion, spin- and dip-coating produce "homogeneous QD solids" with precise film thickness control.[19]

2.4.2 Improvements for Charge Carrier Transport

A uniform distribution of QD energy levels is a key prerequisite for interdot coupling and hence efficient charge carrier transport. In QD samples with a narrow size distribution, such a uniform energy level distribution is present.[99] However, QD films made of equally sized QDs are electrically insulating since they are coated with long-chain organic molecules that offer steric

stability to the QDs in solution. While doing so, they also prevent significant coupling and charge transfer between the QDs. The excitons produced will remain confined within a single QD due to the relatively low interdot coupling and will not be divided into free electrons and holes.[100] There are several approaches to enhance the coupling in QD solids to overcome this limitation.

The most common method for improving coupling is to execute a ligand exchange, which involves replacing long insulating ligands with short insulating ligands in order to minimize interparticle spacing.[101] Since it is crucial to preserve the QDs' distinct and size-dependent properties small organic molecules such as thiols,[102-105] amines,[92, 106-107] pyridine,[108] organic acids,[102, 109] or small inorganic capping molecules such as metal chalcogenide complexes[110-111] are just a few suitable short ligands. The inorganic molecules, which were initially utilized in 2009, enabled all-inorganic QD solids to be formed. They improved electronic transport by forming crack-free and entirely inorganic films, as well as a favorable highest occupied molecular orbital (HOMO) and lowest unoccupied molecular orbital (LUMO) engineering, resulting in extremely high charge carrier mobilities.[99, 110, 112] Ligands can be exchanged using one of two methods: solution phase ligand exchange (per-film-deposition)[107, 111] or solid state ligand exchange (post-film-deposition).[113] Crack-free and dense QD solids can be made using solution phase ligand-exchanged QDs in a single step process. Short ligands supplied by ligand exchange, however, typically reduce the colloidal stability of QDs, causing these dots to coalesce prior to even reaching film formation. A solid-state ligand exchange typically has two steps: first, the QD film is formed, and then the QD film is treated with a solution containing the exchange liquid. Trading long ligands for short ligands may cause volume loss, resulting in QD films with many breaks. When an electrode is evaporated on the film, these breaks can short-circuit the device, thus they must be avoided. Multiple layers created by a layer-by-layer procedure are required to cover the

cracks and produce a continuous film. The QD deposition and subsequent ligand exchange are repeated many times in this type of procedure.[92] The number of layers, the spin- or dip-coating speed, or the concentration of QDs in solution may all be used to control the film thickness.[19]

A ligand exchange can increase the amount of surface dangling bonds, responsible for trap states while also improving interdot coupling. As a result, ligand exchange reduces PL efficiency and may reduce charge carrier mobility due to charge entrapment.[73] Introducing halide anions is common method for minimizing trap states and effectively passivating the QD surface.[112, 114] For example, hydrazine on the other hand, "saturates surface dangling bonds" and reduces oxidation across the QD surface due to its lone pair of electrons.[19, 40]

Film annealing, chemical doping, QD shape optimization, and QD film optimization are also other ways to increase charge carrier transport in QD solids.[19] A loss of ligands occurs when a QD solid is annealed. Due to the fusing of neighboring QDs, ligand loss diminishes interparticle spacing and enhances the tunneling rate between QDs, however, it also broadens and redshifts the excitonic peak. Partial loss of quantum confinement happens to be the result of QD fusion.[115-116]

Furthermore, PbSe QDs, the main focus of this work, are not thermally stable enough to attain the high temperatures required for oleate pyrolysis, according to Law *et al*.[117]

Chemical doping improves charge transport by increasing the concentration of mobile carriers,[40] for instance by adding more charge carriers to the QD film.[99] The combination of ligand exchange with QD film doping, as described by Choi *et al*.,[99] leads to exceptionally high charge carrier transport. Controlled doping, on the other hand, is difficult to perform due to obstacles such as QD self-purification.[118] Shape optimization is the process of synthesizing cubes, wires, or sheets to maximize the amount of hopping incidents among QDs, therefore enhancing charge carrier

transport.[40] "Selective ligand displacement" causes to QD self-assembly by epitaxial necking between crystal facets, resulting in confined-but-connected superstructures.[19, 119-120]

2.4.3 Charge Carrier Transport Participation in QD Films

Charge carrier transport in QD films is a well-studied issue, and it is currently thought that in weakly coupled QD films (Fig. 2.10a),[105, 121-122] charge carrier transport shifts from hopping between localized states to continuous band-like transport in highly coupled QD films(Fig. 2.10b).[100, 123] The interparticle distance and the interparticle material affect the hopping probability of charges between QDs. The tunnel barrier width is represented by the interparticle distance, while the tunnel barrier height is represented by the interparticle material. As a result, decreasing the ligand length shrinks the tunneling barrier and enhances charge carrier mobility dramatically. Another method to enhance the hopping probability is to reduce the tunneling barrier height by substituting conjugated organic ligands or inorganic ligands for the initially saturated organic ligands.[95, 124] However, charge carrier hopping occurs not just between nearby QDs, but also across larger distances, which is referred to as variable range hopping.[125] Due to two distinct effects, charge carrier mobility rises with increase in QD diameter size when charge transfer occurs via hopping. The first effect being, fewer hopping incidents are required to transfer charge carriers across a particular distance covered by large QDs as compared to smaller QDs with that same distance in mind.[19] The second effect being, a decrease in band gap brings a decrease of trap state depth, while maintaining charge carriers that are less confined.[95]

Between QDs, charge carrier hopping happens with the release of heat, indicating that charge carrier hopping always requires a minimal activation energy. The activation energy will never dissipate for large excitation densities, even if it is lowered. A charge carrier transport in QD solids

with a negative temperature coefficient was recently discovered to strongly imply a band-like transport. Extended electronic states, which are no longer confined to single QDs, allow for band-like transmission. All of the high-mobility QD devices[126] within this discovery were fabricated using inorganically capped QDs,[99, 110, 126] demonstrating that enhancing QD surface chemistry is an important strategy for boosting charge transfer. While maintaining the distinctive quantum confined properties of QDs, band-like charge transport in highly coupled QD films approaches the mobilities of crystalline bulk semiconductors.[126] Because of electron delocalization, the "absorption bands of QDs are still present in the absorption spectra of QD solids", but they are to some degree redshifted and expanded.[19] In the end, the development of high mobility QD solids are capable of expanding commercial QD device applications.

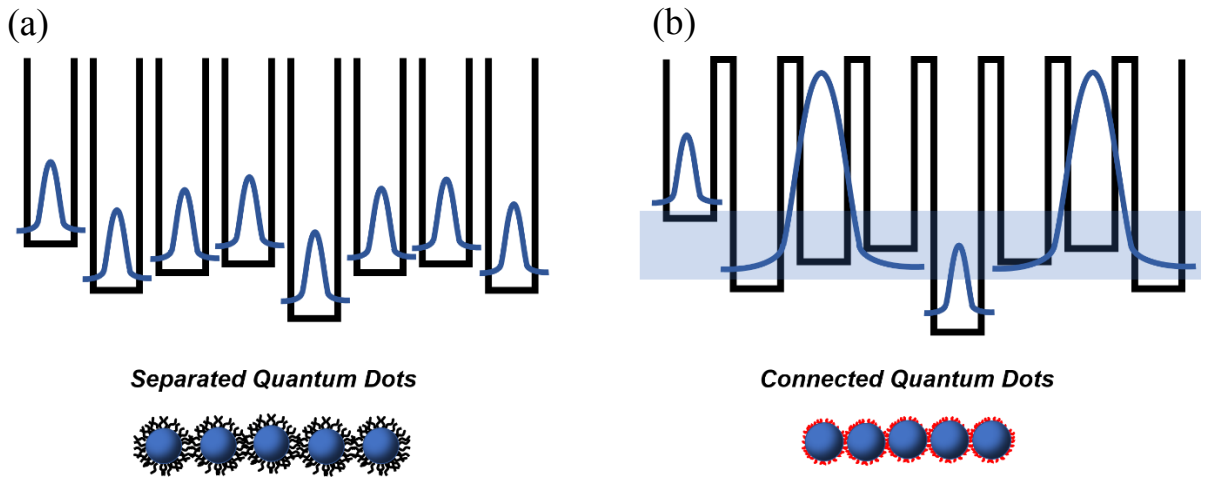

Fig. 2.10 | Schematic of charge carrier transport. (a) Charge transport in a weakly coupled QD film by hopping between localized states. (b) Coherent band-like transport of a highly coupled QD thin film. Figures adapted from reference.[126]

2.5 Lead Chalcogenide QDs

Lead chalcogenide QDs (PbX; X = S, Se, or Te) are VI-IV semiconductors made up of lead cations and chalcogenide anions. Murray *et al*.[127] was the first to achieve a hot-injection synthesis of colloidal lead chalcogenide QDs in 2001. The PbSe QDs were synthesized by injecting a room temperature combination of lead oleate and tri-n-octylphosphine selenide (TOPSe) into a rapidly stirred solution of hot diphenyl ether at 150 °C, producing QDs ranging in size from 3.5 - 15 nm. The size dispersion of the samples was narrowed after a size-selective precipitation.[127] Murrays' work even paved the way for Hines *et al*.[128] to develop the first hot-injection synthesis for PbS QDs in 2003. Using a synthesis based on lead(II) oxide (Pb precursor), bis(trimethylsilyl)sulfide (S precursor), oleic acid (surfactant), and octadecene (solvent), high quality PbS QDs with a size dispersion of 10-15% were achieved without post-synthesis size-selective precipitation.[128] Following these two syntheses, a slew of slightly modified syntheses yielded monodisperse PbS,[9] PbSe,[121, 129] and PbTe QDs.[130-132] Only PbS and PbSe QDs were utilized in this thesis, thus all of the following properties are only presented for those two materials.

Bulk PbS and PbSe have narrow band gaps of 0.41 eV[133-134] and 0.28 eV,[129, 135] respectively, and absorb and emit light within the near-infrared (NIR) range. They possess substantial excitonic Bohr radii (PbS 18 nm,[134] PbSe 46 nm[135]), allowing them to easily access strong quantum confinement regime, even for large QDs, easy.[11] PbS and PbSe QDs may simultaneously transport both electrons and holes because to their nearly identical and large Bohr radii for electrons and holes (23 nm (PbSe)[11]; 10 nm (PbS)[10]), therefore PbX QDs are ambipolar materials because of this characteristic.

Lead chalcogenide QDs can be synthesized in a broad size range of 2 -10 nm,[136] with a adjustable absorbance range of 750 - 2400 nm.[137] PbX QDs have a centrosymmetric rock salt

crystal structure, with six non-polar {100} facets and eight polar {111} facets on the surface of the PbX crystals. Either Pb cations or chalcogenide anions terminate each of the {100} facets. Statistically, 89 % of lead chalcogenide QDs exhibit a dipole moment, most commonly in the ⟨001⟩ direction (Fig. 2.11), which is dependent upon the distribution of chalcogenide or Pb rich facets.[49, 138-139] Moreels *et al*.[134, 140] discovered that PbX QDs have a non-stoichiometric Pb/X ratio due to an overabundance of Pb atoms on the QDs' surface, while the core is quasi-stoichiometric.[135, 141-142] The stoichiometry of PbX QDs must be carefully tailored since it has a significant impact on their electrical properties.[143]

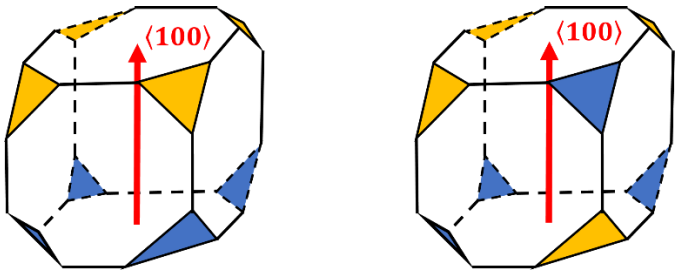

Fig. 2.11 | Schematic of the dipole moment within Pb chalcogenide (X) QDs. The PbX QDs possess eight {111} facets which are terminated by either Pb cations (blue) or chalcogenide anions (maize). Based on the distribution of the eight polar {111} facets, mathematically 89% of Pb chalcogenide QDs contain a dipole moment which would be most commonly in the ⟨001⟩ direction (red). Figure adapted from reference.[49]

PbX QDs are air and humidity sensitive, as they can oxidize rapidly. The adsorption of O_2 and H_2O can occur after a PbX QD thin-film experiences only a brief exposure to air. However, with an extensive time of oxygen exposure, an oxide shell can form, and the oxidation of the PbX QDs then becomes permanent. At that point, the QD film's conductivity is substantially reduced by the passivating oxide shell. Because small QDs have a greater lead concentration at the surface than

larger QDs, they have a more packed ligand shell along with improved surface passivation. PbX QDs should be processed and studied within an inert environment to avoid oxidation and loss of ambipolar behavior.

The quality, size, and shape of PbX QDs are all influenced by the synthetic procedures. When opposed to a low injection temperature, a high injection temperature produces bigger QDs.[137] Furthermore, certain ligands (such as oleic acid) encourage spherical growth, whereas others (such as oleylamine) favor cubic QD formation by having a greater growth rate in the ⟨111⟩ direction than in the ⟨100⟩ direction. Anisotropic PbX QDs may also be synthesized by directed attachment, which is fueled by dipole-dipole interactions and a decrease in surface energy.[19, 49, 138]

CHAPTER III

Experiments: Syntheses, Characterization, and Fabrication

3.1 Nanocrystal Fabrication

The following subsections detail the highly refined synthesis recipes required to achieve PbS and PbSe NPs of various size, shape, and dispersity. Note that these procedures are an important output of the research because achieving reproducibly monodispersed PbX, colloidal NCs via organic synthesis procedures are an experimental challenge that requires detailed adherence to experimental steps. These steps were typically optimized via feedback from TEM micrographs that detailed the size, shape, and most importantly, the interconnection morphologies of the NCs. The characterization of the resulting solids is discussed after the recipes are detailed.

3.1.1 Chemicals and Materials

Acetonitrile (≥99.5%), Isopropanol (IPA, ≥99.5%), lead(II) oxide (PbO, 99.99%), methanol (≥99.8%), oleic acid (OA, tech. grade 90% and 99%), trifluoroacetic acid (99%), trifluoroacetic anhydride (99%), tris(diethylamino)phosphine (TDP, 99%), ethanol (200 proof), selenium pellets (Se, ≥99.99%, trace metal), trioctylphosphine (TOP, tech grade 90%), 1-octadecene (ODE, tech. grade 90%), acetone (reagent, ≥99.5%), chloroform (≥99%) and diphenylphosphine (DPP, 98%), diphenyl ether (PE, $(C_6H_5)_2O$; 99.99%), methanol (anhydrous, 98%), *n*-hexane (anhydrous, 95%), lead(II) acetate trihydrate, 99%, (lead source; $Pb(Ac)_2$, $(CH_3COO)_2Pb \cdot H_2O$)),

cetyltrimethylammonium bromide, (cationic surfactant; (CTAB, $CH_3(CH_2)_{15}N(Br)(CH_3)_3$)) thioacetamide, (sulfide source; (TAA, CH_3CSNH_2)), and trichloroethylene (TCE, 99.5%) were all purchased from Sigma-Aldrich with logical analytical-grade purity and were utilized with no further purification. E-pure deionized water (DIW, 18.2 $M\Omega \cdot cm^{-1}$) was obtained from Thermo Scientific Barnstead Water Purification System.

General Methods. All glassware was cleaned with aqua regia (3:1 HCI/HNO_3) and soaked at least overnight in a base bath (125.0 g of Potassium hydroxide (KOH), 2.0 L of 2-Propanol, 500.0 mL of DIW). All chemical procedures were performed using standard air-free techniques on a Schlenk line under nitrogen or in a nitrogen-filled glovebox unless indicated otherwise.

3.1.2 NC Syntheses

All colloidal syntheses were performed through high-temperature solution-phase routes based on the principles of a few standard QD hot-injection syntheses reported by C. B. Murray *et al*.[29, 127] The reported methodologies have been adapted and further modified to yield Pb chalcogenide compounds. A schematic illustration of the experimental setup can be seen in Fig. 3.1.

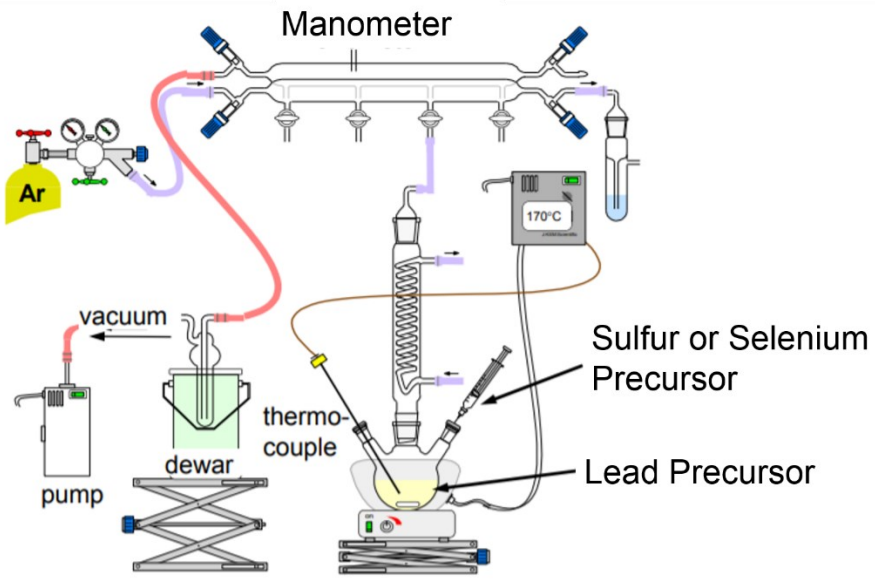

Fig. 3.1 | Schematic of a typical synthesis setup to perform a hot-injection QD synthesis under inert atmosphere. Figure adapted from reference.[19]

3.1.2.1 TOP-PbSe NC Synthesis

The TOP-PbSe QD synthesis was performed in the following manner: PbO and Se dissolved in TOP and used as organo-metallic precursors while ODE serving as high-temperature organic solvent.

Preparation of Se precursor. TOP-Se (1M) was prepared by adding 3.95 g of Se and 50.0 mL of TOP to a one or three-necked flask capable of maintaining at least 75 mL, equipped with a stir bar, on a hot plate with magnetic stirring at ~50°C until solution becomes completely clear. The solution could stir overnight if deemed necessary.

Preparation of lead (Pb) oleate. The Pb oleate precursor is prepared by combining 4.0 g of PbO, 13.0 mL OA (tech. grade 90%) and 20.0 mL of ODE to a three-necked flask, equipped with stir bar, connected to vigurex column and a vacuum adapter on the center neck. Two outside

exposed necks were sealed with rubber septa. Resultant dissolution was first degassed until bubbles ceased, then heated to ~165°C while stirring until solution became transparently yellow. The temperature was then dropped to ~110°C and once stable, degassed for ~1 hr. The mixture was then cooled to room temperature.

TOP PbSe QD Fabrication (TOP PbSe-F1). The temperature for Pb oleate batch increased to ~170°C (injection temperature). Once the batch reaches the desired temperature, the heat was turned off and 3.0 mL of TOP-Se was injected while vigorously stirring. After a growing time ranging from 2 to 7 min., the solution in the glassware was placed into a cold-water basin (CWB) to quickly cease nanoparticle growth. Once temperature of solution dropped below ~40°C the glassware containing solution is removed from CWB and ready for transfer into vials.

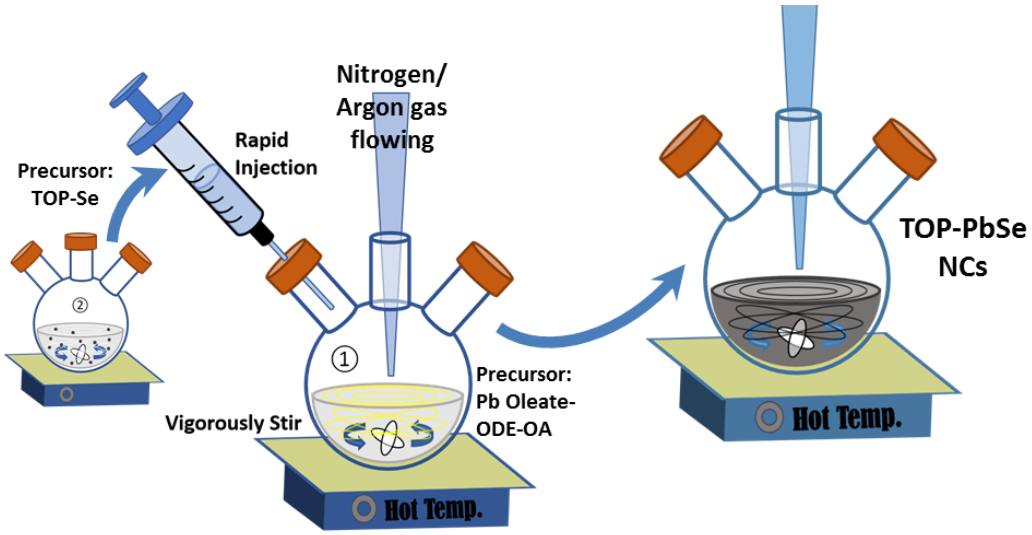

Fig. 3.2 | Schematic of a modified solvo-thermal synthesis carried out for the fabrication of only PbSe NCs, using lead(II) oxide (PbO), a pre-prepared trioctylphosphine-selenium (TOP-Se) solution and 1-octadecence (ODE) as the solvent.

PbSe Clean-Up procedure. The dark residue within the glassware is transferred into 50 mL vials, each holding an equal amount of PbSe solution (~17 mL). The vials each receive enough acetone to fill to the 50 mL line marked on surface of vials. Vials are then shaken and placed in beakers to settle and witness separation of NCs from liquid. Vials are then lightly shaken again and placed in centrifugation chamber for 5 min. at 4.4 krpm. A dark cone of NCs should be seen at bottom of vials while supernatant is seen above and removed while the nanoparticle cone maintains its position. 5-7 mL of chloroform was then introduced into the vials for the NC filled cones to be dispersed. Sonication and vortex spinning help in the breakdown process. Once evenly dispersed, acetone was once again brought into the vials filling them up to ~50 mL line. Vials are shaken and centrifuged again. The process of chloroform and acetone (polar and anti-polar solvents) was repeated 1-3 more times. Afterwards, the vials possessing these NC filled cones are placed inside a desiccator under vacuum overnight.

3.1.2.2 TOP-PbSe NC Synthesis with Phenyl Ether (PE)

Pre-preparation of Se precursor. TOP-Se (1M) was prepared by adding 3.95 g of Se and 50.0 mL of TOP to a one or three-necked flask with at least a 75 mL capacity, equipped with a stir bar, on a hot plate with magnetic stirring at ~50°C until solution becomes completely clear. The solution could stir overnight if deemed necessary.

TOP-PbSe QD Fabrication (TOP-PbSe-F2). Typically, 1.081 g of $Pb(Ac)_2$ is added into 1.5 mL of PE and 3.6 mL of OA (tech. grade 90%) in a 3-neck flask connected to a vigurex column with constant stirring by a magnetic stirrer at ~1100 rpm. Pb mixture heats to 150°C under flowing argon for 30 min, then cools to room temperature. Under argon atmosphere, the room temperature

solution then subsequently mixes with 8 mL of 1M of TOP-Se solution. PE (15 mL) also heats in glassware to 150°C under argon in another glassware while being vigorously stirred. Once PE reaches the 150°C temperature, 8.0 mL of the $Pb(Ac)_2$–TOP-Se combination, once cooled down to room temperature, rapidly injects into the heated PE while still vigorously stirring. After injection, the temperature drops and settles to ~121°C (growing temperature), at which the reaction could continue to grow for 6 – 25 minutes (growing time). The heating mantle then turns off and gets removed to introduce a CWB. Modifications of this PbSe synthesis, such as changes in the temperature of PE to 180°C prior to the $Pb(Ac)_2$–TOPSe combination injection and allowed time for NC growth were both attempted.

Clean-Up Procedure. Once the final solution cools to room temperature, the glassware holding the fabricated PbSe solution is removed from submersion within the CWB to prevent the solution from freezing over. TOP–PbSe–PE solution was poured into a 50 mL conical tube followed by a light acetone (~5 mL) and heavy ethanol (~20 mL) additions to induce the NCs over the course of several hours. Following the visual precipitation, the solution was put through centrifugation at 4400 rpm for ≥ 10 min. Visual inspection are performed after centrifugation, and the supernatant is poured out while PbSe NCs remained still at the bottom of the centrifugation tube afterwards. The PbSe NCs are dispersed with small amounts of toluene (≤ 5 mL), making this a complete round of the clean-up procedure. Typically, 2 – 3 rounds of the clean-up process take place with the 2^{nd} and 3^{rd} rounds each using 20 mL of ethanol. If during any visual inspection the solution appears to be cloudy or without a supernatant to decant, the allowed time for centrifugation is increased. Occasionally, PbSe solutions have needed to be centrifuged for additional minutes to hours. Prior to the final redispersion of PbSe NCs with toluene, the NCs dried in the glove box under vacuum for a small amount of time so that a proper weight of the NCs

could be acquired. The amount of toluene solvent is dependent upon the desired concentration for the final PbSe NC colloidal solution. The PbSe colloidal solution are then stored at room temperature, and occasionally monitored for stability.

Modification 1. Still synthesizing through the high-temperature solution-phase route, instead of applying the heated solvent , PE, to TOP–Pb–Se combination which is under room temperature, the TOP–Pb–Se combination is injected into the hot PE. In doing so, this creates an opportunity for extended growth periods since PE is typically at 180 °C prior to TOP–Pb–Se injection. The synthesis is also performed in this manner because the necessary materials used for retracting hot (180 °C) PE were not always at our disposal.

3.1.2.3 TOP-PbSe NC Synthesis with DPP

3.1.2.3.1 TOP-PbSe NC Syn.: Single Precursor Injection with DPP

Pre-preparation of Se precursor. For preparation of the Se precursor, TOP-Se (1M) is first prepared by adding 3.95 g of Se and 50.0 mL of TOP (technical grade 90%) to a one or three-necked flask with at least 75 mL capacity, equipped with a stir bar, on a hot plate with magnetic stirring at ~50°C until solution becomes completely clear. The solution could stir overnight if deemed necessary.

Preparation of Pb oleate (Pb precursor). For preparation of Pb oleate, 5.0 g of PbO, 18.05 mL OA (tech. grade 90%) and 20 mL of ODE (tech. grade 90%) are all combined in a three-necked flask, equipped with stir bar, connected to a vigurex column and a vacuum adapter on the center neck. The other necks are sealed with rubber septa. The resultant dissolution is first degassed until bubbles ceased, then heated to ~165°C while stirring until the solution becomes transparently

yellow. The temperature is then dropped to ~110°C and once stable, degassed for ~1 hr. The mixture is then cooled to room temperature.

TOP-PbSe QD Fabrication (TOP-PbSe-F3). For the creation of PbSe NCs, a pre-prepared batch Pb oleate already in glassware would reach a temperature of ~170°C (injection temperature). Once the batch reaches this desired temperature, heat is turned off and 5.0 mL of TOP–Se is injected while vigorously stirring. The colloidal solution is then given time ranging from minutes to hours while at a specified growing temperature (typically ~80 °C) to allow the NCs to grow uniformly. The freshly created NCs in glassware are then placed into a CWB to quickly cease NC growth. Once the temperature of solution drops below ~20°C, the glassware containing the solution is removed from the CWB and NCs are ready for transfer into vials.

Clean-Up Procedure. After the synthesis is completed, a clean-up procedure is used to remove excess capping ligand. The dark residue within the glassware is transferred into 50 mL vials, each holding an equal amount of PbSe solution (~17 mL). The vials each receive enough acetone to fill to the 50 mL line marked on surface of vials. Vials are then shaken and placed in beakers to settle and witness the solution become turbid and separate/precipitate the NC particles from the chemically altered solution. Vials are then lightly shaken again and placed in centrifugation chamber for 5 min. at 4.4 krpm. A dark cone filled with NCs should be seen at bottom of vials while supernatant is seen above and removed while the cone maintains its position. 5-7 mL of chloroform is then introduced into the vials for the NC filled cones to be dispersed. Sonication and vortex spinning help in the breakdown process. Once evenly dispersed, acetone is once again brought into the vials filling them up to ~50 mL line. Vials are shaken and centrifuged again. The process of chloroform and acetone (polar and anti-polar solvents) was repeated 1-3

more times. Afterwards, the vials possessing these NC filled cones are placed inside a desiccator under vacuum overnight.

Modification. Modifications of this PbSe synthesis have been attempted, introducing either less OA or the addition of a reducing agent such as DPP. For OA adjustments, 13 mL of OA, instead of 18.05 mL, was introduced into the synthesis. For DPP, 345 μL was added to every 5 mL of pre-prepared TOP-Se solution (1 M of Se) while in a glove box. A reduction of the TOP-Se solution 5 mL to 3 mL was also occasionally made, while still adding 345 μL of DPP when needed. With the inclusion of DPP, this PbSe synthesis was carried out with the intention of possessing a feed molar ratio of [0.6 DPP : 8 Pb : 1 Se] and without DPP a feed molar ratio of [8 Pb : 1 Se].

3.1.2.3.2 TOP-PbSe NC Syn.: Multiple Precursor Injection with DPP

Pre-preparation of Se precursor. TOP-Se (1M) is prepared by adding 3.95 g of Se and 50.0 mL of TOP (tech grade 90%) to a one or three-necked flask with at least 75 mL capacity, equipped with a stir bar, on a hot plate with magnetic stirring at ~50 °C until solution becomes completely clear. The solution could stir overnight if deemed necessary. Additional molarities of 0.5 – 2.0 M Se were made as well by adding the following amounts of Se to 50.0 ml of TOP: 0.5 M, 1.97 g Se; 0.6 M, 2.37 g Se; 0.7 M, 2.76 g Se; 0.8 M, 3.16 g Se; 0.9 M, 3.55 g Se; 1.0 M, 3.95 g Se.

Pre-preparation of TOP-Se-DPP. With premade TOP-Se, based on the amount of injections going into a synthesis, the total volume of DPP is ~350 µl for each injection. Therefore, a single injection synthesis requires at least 3.0 ml of TOP-Se with ~350 µl of DPP.

Preparation of Pb oleate (Pb precursor). The Pb-Oleate precursor is prepared by combining 5.0 g of PbO, 13 mL oleic acid OA (tech. grade 90%) and 20 mL of ODE (tech. grade 90%) to a three-necked flask with at least 75 mL capacity, equipped with stir bar, connected to vigurex column and a vacuum adapter on the center neck. The other remaining exposed necks are sealed with rubber septa. Resultant dissolution is first degassed until bubbles ceased, then heated to ~165 °C while stirring until solution becomes transparently yellow. The temperature is then dropped to ~110°C and once stable, degassed for ~1 hr. The mixture is then cooled to room temperature.

TOP-PbSe-DPP QD Fabrication. Two separate batches of Pb oleate were prepared in glassware just mentioned above. After room temperature is reached, the temperature for batch one increases to ~170 °C (injection temperature) while batch two increases 140 °C (growing temperature). Once the batch one reaches the desired temperature, heat is turned off and TOP-Se-DPP is injected while vigorously stirring. For a second injection, after a desired growing time passes in batch one, 10 mL of batch two was pulled from the glassware and injected into batch one while more TOP-Se-DPP was also injected simultaneously all while still vigorously stirring. For a third injection, again after a desired growing time passes, 10 mL of batch two was pulled from glassware and injected into batch one while simultaneously injecting TOP-Se-DPP and vigorously stirring. After the desired amount of injections are completed the solution, while still in glassware, was placed into a CWB to quickly cease NC growth. Once the temperature of solution drops below ~20°C the glassware containing solution is removed from CWB and ready for transfer into vials.

PbSe Clean-Up procedure. The dark residue within the glassware is transferred into 50 mL vials, each holding an equal amount of PbSe solution (~17 mL). The vials each receive enough acetone (reagent, ≥ 99.5%) to fill to the 50 mL line marked on surface of vials. Vials are then shaken and placed in beakers to settle and witness separation of nanoparticles from liquid. Vials

are then lightly shaken again and placed in centrifugation chamber for 5 min. at 4.4 krpm. A dark cone filled of NCs should be seen at bottom of vials while supernatant is seen above and removed while the nanoparticle cone maintains its position. 5-7 mL of chloroform is then introduced into the vials for the NC filled cones to be dispersed. Sonication and vortex spinning helped in the breakdown process. Once evenly dispersed, acetone was once again brought into the vials filling them up to ~50 mL line. Vials are then shaken and centrifuged again. The process of chloroform and acetone (polar and anti-polar solvents) is repeated 1-3 more times. Afterwards, the vials possessing these NC filled cones are placed inside a desiccator under vacuum overnight.

3.1.2.4 TDP-PbSe NC Synthesis

Synthesis of Pb(oleate)$_2$ from lead trifluoroacetate. The Pb-Oleate precursors were synthesized using the general method developed by Hendricks *et al.*[144] with some modifications. PbO (5.0 g, 22.4 mmol) and acetonitrile (10 mL, 191.5 mmol) are added to a ≥ 250 mL round-bottom three-neck flask. While the suspension stirs, at least the bottom half of the flask is submerged into an ice bath for ~10 minutes. Trifluoroacetic acid (0.35 mL, 4.48 mmol) and trifluoroacetic anhydride (3.1 mL, 22.4 mmol) were added (t ~ 2-4 sec). After ~15 minutes the yellow lead oxide dissolves, producing a clear and colorless solution that is then allowed to warm to room temperature. In parallel, OA (14.2 mL, 45.03 mmol), IPA (90 mL, 1.18 mol) and triethylamine (7.0 mL, 50.63 mmol) were added to a 500 mL filtering (side-arm) flask and stirred vigorously for ≥ 5 minutes. The lead trifluoroacetic solution is then added to the oleic acid solution while still stirring, producing a white powdery precipitate. Next, the mixture is heated to reflux (~85°C or until bubbling occurs) to dissolve the precipitate at which a clear and colorless solution

results ($t \sim 30$ min.). The heat is then removed, and the flask is allowed to cool to room temperature for > 2 hours, followed by further cooling in a cylindrical dewar flask holding liquid nitrogen (LN_2) reaching –20°C for > 2hours. The resulting white powder was then isolated by suction filtration using a Buchner funnel and filter adapter. This was done to thoroughly filtrate and wash the slurry white solution with methanol (≥ 900 mL), while breaking up any large pieces by either carefully stirring or using a spatula to fracture and disassemble any aggregation. Once all were washed and de-clustered, the white powder upon the filter paper was then dried under vacuum for > 6 hours in a decanter. Afterwards, the white powder was further granulated by breaking down any large clumps to become free-flowing for ready experimental use. The free-flowing white powder was then stored in a nitrogen-filled glovebox. Typical yields are 15.5 g – 16.4 g (90 - 95%).

TDP-PbSe NCs were synthesized and purified using the general method developed by Koh *et al*.[145] with slight modifications.

Pre-preparation (Se precursor). TDP (27.68 mL; 101.0 mol) and Se pellets (2.16 g; 27.4 mmol) are added to ≤ 50 mL three-neck flask and vigorously stirred until all selenium was dissolved, resulting in the TDP-Se precursor with 1 M Se. The precursor was stored in a nitrogen-filled glovebox for later use.

TDP-PbSe QD Fabrication. Dried Pb-Oleate (0.77 g), OA (0.4 mL; 1.2 mmol) and ODE (5.0 mL; 15.6 mmol) are mixed in three-neck flask under N_2 and heated to 150°C with vigorous stirring. Next, 3 mL of TDP-Se is rapidly injected into the Pb-oleate mixture, and the reaction continued with no interruptions for a growing time ranging from 1 – 5 min depending on the NP particle size targeted. After the growth period, the reaction was cooled to room temperature using

a liquid nitrogen bath. A purification procedure proceeded by adding the NP solution to the centrifugation vial along with ~0.5 mL hexane and ≥ 5 mL of ethanol and centrifuging at 4.4 krpm for 5 min. The product typically forms a fractured black solid mass at the bottom of a vial which was isolated by decanting the supernatant. This procedure was carried out once more and placed under vacuum in a desiccator overnight.

3.1.2.5 PbS Nano-/Microcrystal Synthesis

The combination of lead sulfide, PbS, was completed by thermal decay of TAA in a fluid arrangement with $Pb(Ac)_2$ at a suitable initial reaction temperatures and times of reflux within the presence of the surfactant, CTAB. In a typical experiment, 3.0 mmol (0.38 g) of $Pb(Ac)_2$ and 13.7 mmol (0.5 g) of CTAB were broken down into 13.3 mL of DIW, in a three-neck flask furnished with a condenser column. The blends were then heated to 80°C under constant mixing. The TAA solution (1.6 mmol (0.12 g) of TAA and 10 mL of DIW) was added drop-wise, with a pressure-equalizing dropping funnel, to the above $Pb(Ac)_2$–CTAB solution while at 80°C (initial reaction temperature), eventually getting up to the final concentrations of 0.013 mol/L $Pb(Ac)_2$ and 0.07 mol/L TAA, for a molar proportion of the $Pb(AC)_2$/TAA to be 2/3. The shade of the reaction mixture changed to black gradually in the dropwise strategy. The point at which the expansion of TAA was finished, the reaction blend was heated to 100°C and refluxed for ≥ 30 min. The resulting dark samples were washed several times with water and ethanol, and afterward dried overnight at room temperature in a glove box. This synthesis has additionally been adjusted for molar ratios ranging from 1/3 – 2/1, surfactant amounts ranging from 0.5 – 3.0 g, and time frames for dissolving chemicals for PbS NC fabrication all to observe changes in morphologies or potential nanostructures. Utilizing the drop coating method, we arranged a several examples for different

3D and 2D gatherings of PbS dull-tipped and truncated octahedral, small/large multipods, and star-shaped dendrites. After one 25 μL droplet was put on silicon, Si, substrates the solutions were dried in air. PbS particles, at that point, unexpectedly embraced arranged structures of all shapes and sizes clusters with moderate solvent evaporation times.

3.2 NC Sample Preparation

If properly coupled with organic ligands, synthesized NCs can naturally self-assemble. The evaporation of the solvent is accompanied by the solution-based formation of the colloidal assembly. The dynamics of the assembly formation vary depending on the nature of the solvents' viscosity, volatility, and compatibility. The most essential yet significant challenge in the NC technique is how to maximize colloidal ordering once the solvent evaporates.

Drop-casting, dip-coating, slide-casting, and spin-casting are the four major deposition techniques for depositing NCs dispersed in a solvent on to a substrate. However, we shall only address two of them in this thesis: drop-casting and dip-coating. Drop-casting is the technique of placing a droplet of NC solution on a substrate and repeating the process while permitting the solvent to evaporate between applications. Dip-coating makes use of the adsorbing characteristics of the NCs since they possess a very high surface energy due to the high surface-to-volume ratio. Utilizing a liquid substrate to weaken the capping ligands around the NCs, a process called oriented attachment, is an alternative to the two major deposition techniques employed in this study. While

the solvent evaporates, this technique permits nearby NCs to move closer together through facet attraction.

The strategies outlined above can be coupled with ways to improve the assembly's charge transport properties. Layer-by-layer deposition, for example, can be used in all three of the abovementioned procedures to produce a uniform NC assembly.

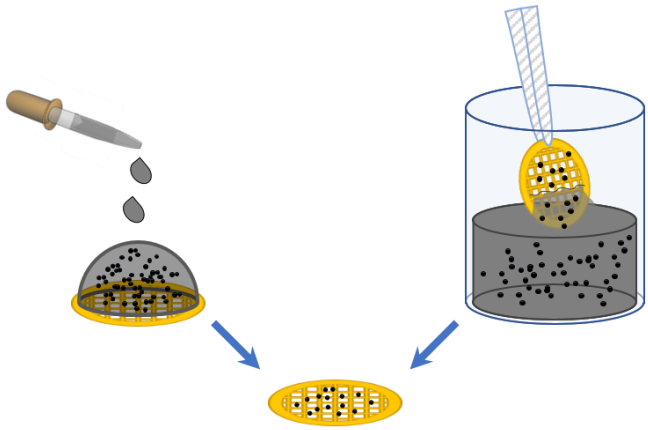

Fig. 3.3 | Schematic illustration of drop-casting (left) and dip-coating (right) onto a copper-mesh grid. Both techniques require solvent evaporation (bottom) over time prior to TEM observation.

3.2.1 Plain NC Assemblies

Both drop-casting and dip-coating are used to create NC assemblies from the colloidal dispersed solutions as they were synthesized. This can be seen in Fig. 3.3.

3.2.2 Drop-Cast NC Self-Assembly Fabrication

To visually analyze fabricated PbS and PbSe NCs, colloidal solutions possessing these NCs are drop-cast onto a copper mesh grid, which is later observed on a transmission electron

microscope (TEM). This can be seen in Fig. 3.3 (*left*), where a copper meshed grid is horizontally positioned, and one to two drops of diluted colloidal solution are gently drop cast onto the grid surface. Over time, the solvent evaporates, leaving behind the fabricated NCs and the natural self-assembly which took place from drop-casting.

Due to the large size of the PbS NCs, the PbS colloidal solutions are often directly deposited onto a SEM holder to optically characterize the NCs. Fig. 3.4 displays an SEM holder completely coated with PbS NCs. Seeing that PbSe NCs are on the scale of single digit nanometers, this same method was not carried out as frequently since TEM would be the better option.

Fig. 3.4 | The top surface of an SEM holder completely coated with PbS NCs for SEM analysis.

3.2.3 Dip-coat NC Self-Assembly Fabrication

To visually analyze fabricated PbS and PbSe, diluted colloidal solutions possessing these NCs were placed in a vial. With the edge of a copper-mesh grid held by tweezers, the grid is dipped into the diluted colloidal solution 1 to 2 times. Once the solvent fully evaporates, the sample can

be observed on a transmission electron microscope (TEM). This can also be seen in Fig. 3.3 (*right*). Just as for drop-casting, over time, the solvent evaporates, leaving behind the fabricated NCs and the natural self-assembly which took place from dip-coating.

3.2.4 Oriented Attachment

Oriented attachment, a process which when carried out correctly, can bring about self-organization and interatomic bonding for adjacent NCs, as there are two options which exist as seen in Fig. 3.5. The successful collision of NCs of shared orientation, which must occur in the colloidal dispersion state, can be seen if choice 1 is selected. Option 2 joins NCs from particle rotation. Despite NPs having rotational freedom, this alternative requires particle rotation to be dominant in a weakly flocculated colloidal state with significant particle interaction. If a superlattice is present, an alternative would be a decrease in interparticle spacing and increase in interconnectivity. Going the route of option 1 shows effective particle collisions with mutual orientation, which occurs in the colloidal dispersion state. At that moment, the number of collisions among particles can be high within the dispersed colloidal solution. However, with option 2 NCs are joined via particle rotation. With this option, particle rotation must be dominant in a weakly flocculated colloidal state in which there is major interaction between particles, despite NCs still possessing properties of rotational freedom. Either option will reduce interparticle spacing and increase interconnectivity throughout a superlattice.

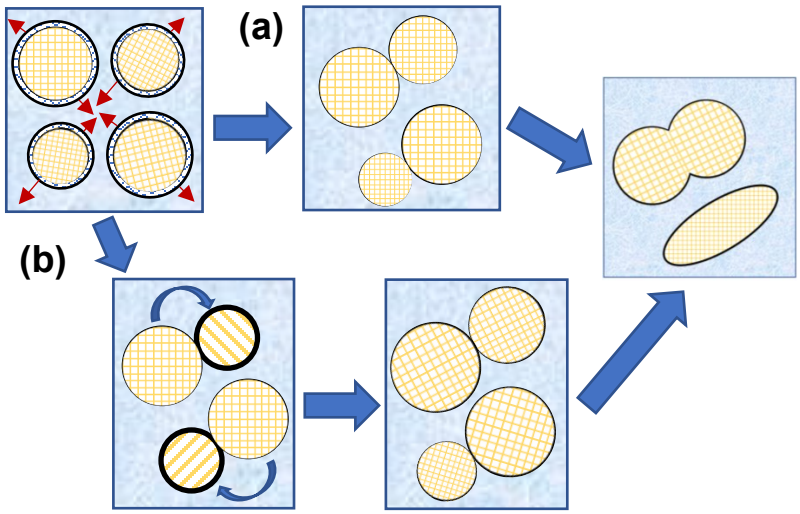

Fig. 3.5 | Schematic of oriented attachment by way of (a) collision of particles or (b) particle rotation.

3.3 Material Characterization

3.3.1 Absorption Spectroscopy

An analytical instrument of absorption spectroscopy is used to obtain information about the electronic states of lead chalcogenide QDs. When light with a photon energy higher than the band gap of the QD contacts with electron/s in the ground state, it is absorbed, causing electron/s to be excited from the VB to the CB, transforming the QD from the electrical ground state to the excited state. Light absorption causes a band rather than a single sharp peak in the absorption spectrum due to a particular energy distribution of the electronic states arising from the QD size dispersion. This band's shape, position, and intensity represent the basic properties of the Pb chalcogenide QD batch. However, spectrometry is a technique for determining how much electromagnetic radiation (light) a chemical substance absorbs (or emits or reflects) by measuring the intensity of light passing through a sample solution. Each chemical absorbs or transmits light over a specific

wavelength range, according to the basic principle. A spectrophotometer is a device that measures the amount of photons (intensity of light) absorbed as they pass through a sample solution. The amount of a known chemical compound (concentrations) may also be measured using the spectrophotometer by measuring the intensity of light detected. In a variety of disciplines spectrometry is one of the most effective methods of quantitative analysis.

Absorption spectra were measured with a Cary 5000 UV-Vis-NIR spectrophotometer at room temperature A background spectrum of the solvent used is obtained and concentrations were measured for the solution samples to be analyzed. All optical experiments are usually carried out in the solvent TCE; however, a few measurements were performed in hexane and/or toluene. Pb chalcogenide QD solution samples were measured using quartz cuvettes with optical path lengths of 1 cm.

The property of each solution sample was left for interpretation given the absorption bands' presentation within collected spectra.

The wavelength of a QD solution sample's first excitonic absorption peak may be calculated from its absorption spectra. The band gap energy, E_{bg}, of the corresponding QD solution sample may be determined using the following equation:

$$E_{bg} = \frac{hc}{\lambda}, \tag{3.1}$$

where λ is the wavelength, h is Planck's constant, and c is the speed of light. Following that, the sizes of the PbSe QDs were determined with the following equation:[140]

$$E_{bg} = -0.25 + \frac{1}{(2.576\mathrm{e}^{-5})d^2+(0.13)d+0.5}, \tag{3.2}$$

where *d* represents the diameter (in nm) of the PbSe QD. The sizes of the PbS QDs were not determined seeing that they've taken several different forms and are larger than the Bohr radius for PbS.

3.3.2 Scanning Electron Microscopy

Scanning electron microscopy (SEM) is a type of electron microscopy that is used to examine a sample's surface topography and composition. An SEM microscope generates a variety of signals at the surface of solid samples using a concentrated beam of high-energy electrons. The signals generated by electron-sample interactions disclose information on the sample's exterior morphology (texture), chemical composition, and crystalline structure and orientation of the sample that make up that very sample, among other things.[146]

Depending on the accelerating voltage and the density of the sample, the electron beam penetrates the sample to a depth of a few microns when it strikes the surface. Secondary electrons, backscattered electrons, and characteristic X-rays are produced as the electrons interact with the sample. One or more detectors gather these signals to create images, which are eventually shown on a computer screen.

The highest resolution attained in a SEM is determined by several factors, including the size of the electron beam and the electron beam's interaction volume with the sample. Some SEM devices can attain resolutions of less than 1.0 nm; however, they cannot give atomic resolution.

SEM images are measured on a FEI Helios 650 Nanolab scanning electron microscope at 20 kV (with electrons and ions of 0.1 pA – 65 pA) as well as an FEI Nova 200 Nanolab, operated from 0.1V - 30 kV, respectively.

3.3.3 Transmission Electron Microscopy

In transmission electron microscopy (TEM) electrons are generated from an electron gun and commonly accelerate at 80-400 kV, depending on material properties and resolution needs. To eliminate electron scattering by particles in the air, the electron beam is transmitted in vacuum. A vertically aligned condenser lens system focuses the beam, allowing for a changeable illumination aperture, hence a changeable illumination area. Following that, the beam strikes the sample, causing a strong interaction between the beam and the material, resulting in elastic and inelastic electron scattering. To be transparent to most electrons, the sample must be very thin (often a few tens to hundreds of nanometers). The transmitted and forward scattered electrons will be guided through another lens system before being projected onto a fluorescent screen, which is generally connected to a charge-coupled device (CCD) camera. The magnified images will then be projected in the image plane while the diffraction planes are projected in the back focal plane. The three most common imaging styles in TEM are the bright field (BF) TEM imaging, dark-field (DF) TEM or STEM imaging, and high-resolution (HR) TEM imaging. Images are created exclusively with the direct beam in BF-TEM imaging utilizing an objective aperture that is inserted into the back focal plane and voids any electrons dispersed to higher angles. A diffracted beam is used to produce images in DF-TEM imaging. HRTEM imaging uses all, largely coherent electron waves to create an interference image based on phase contrast with resolutions as low as 0.1 nm. The

electron beam is in focus with a condenser lens system to a diameter of about 0.1 nm in scanning transmission electron microscopy (STEM), and then swept in a scan over the sample. Furthermore, using energy-dispersive X-ray spectroscopy (EDX), a TEM may be also used as an analytical electron microscope to determine the elemental composition of small areas of a sample.[147]

STEM and high-resolution STEM (HRSTEM) were carried out by using a JEOL 2100 at 200 kV, respectively. Samples for TEM/STEM images were prepared by dropping an aliquot of solution on a 300-mesh carbon-coated copper grid and allowing the solvent to evaporate at room temperature

3.3.4 X-ray Photoelectron Spectroscopy

X-ray photoelectron spectroscopy (XPS) is a surface sensitive method for non-destructively analyzing the elemental composition, including the oxidation state, of a material's surface. XPS spectra are produced by irradiating a solid surface with an X-ray beam while measuring the kinetic energy of electrons released from the top 1-10 nm of the material under investigation. X-rays with a certain energy, *hv*, are focused onto the substance to conduct XPS examination. These X-rays penetrate the sample's surface and emit electrons from the core levels of the surface components of the material being studied. The kinetic energy of the ejected electrons is then measured and analyzed with a spectrometer (i.e., an electron multiplier), therefore, a photoelectron spectrum is recorded by counting ejected electrons over a range of electron kinetic energies. The attenuation length of the electrons determines the depth of investigation in XPS, which ranges from 1 to 10 nm. The elemental binding energy, E_B, of an electron is defined as $E_B = hv - E_K - W_{SP}$, where hv is the X-ray photon energy, W_{SP} is the spectrometer's work function, and E_K is the kinetic energy

of the emitted electron. Lastly, the X-ray intensity is plotted against the binding energy, allowing for an identification of elements as well as their oxidation states.[148] Peaks in the spectrum are caused by atoms emitting electrons with a certain energy. The energy and intensity of the photoelectron peaks allow for the identification and measurement of all surface elements.

XPS data were obtained using Kratos AXIS Ultra XPS with aluminum anode (Al Kα = 1.486 KeV).

3.3.5 Fourier-Transform Infrared Spectroscopy

Infrared (IR) spectroscopy is a vibrational spectroscopy technique that uses an IR spectrum to identify chemical bonds in a molecule. A sample's IR spectra profile is a unique chemical fingerprint that may be used to screen and scan samples for a variety of compounds. A sample is subjected to IR light that is repeated at several frequency ranges. Some light wavelengths are absorbed in the sample, which causes some molecules to move (vibrate). The IR light that is converted into molecular motion is partially absorbed, while the remainder passes through or beyond the sample. When IR light is focused onto a sample, it is attenuated when it passes through the sample material. The IR spectrum is created in transmission mode by detecting the IR radiation that remains after transmission. Data is captured using an interferometer and retranslated to a spectrum with the assistance of a Fourier transformation in Fourier-transform (FT) IR spectroscopy. The IR peaks' duration, shape, and height are all direct reactions to chemical bonds within the sample. The usefulness of IR spectroscopy arises because different chemical structures (molecules) produce different spectral fingerprints.

FTIR spectra were recorded using a Nicolet iS50 FTIR Spectrometer (Thermo Scientific).

3.3.6 Nuclear Magnetic Resonance

Nuclear Magnetic Resonance (NMR) spectroscopy is an analytical chemistry technique used in quality control and research for determining the content and purity of a sample, as well as its molecular structure. NMR, for example, may be used to analyze mixtures containing known chemicals quantitatively. NMR may be used to compare unknown compounds to spectral libraries or to deduce the basic structure directly. NMR may be used to determine molecule conformation in solution as well as analyze physical properties at the molecular level once the basic structure is understood.

Many nuclei have spin, and all nuclei are electrically charged, according to the NMR principle. An energy transfer from the base energy to a higher energy level is feasible when an external magnetic field is introduced (generally a single energy gap). Energy is transferred at a wavelength that corresponds to radio frequencies, and energy is emitted at the same frequency when the spin returns to its base level. The signal that corresponds to this transfer is measured and processed in a variety of ways to produce an NMR spectrum for the nucleus in question.

For NMR analysis, both samples were uniformly dispersed in benzene-d_6. ~1.0 mL of each NC solution was transferred into an NMR tube with a lid/stopper prior to measurement. NMR spectra was recorded with a Varian MR400 of 400 MHz.

3.3.7 X-ray Diffraction

X-ray powder diffraction (XRD) is a rapid analytical technique that can provide information on unit cell dimensions, but most commonly it is used for phase identification of crystalline materials. In addition to phase identification, XRD also provides information on how the actual structure differs from the ideal one due to internal stresses and defects. The analyzed material is typically a homogenized finely grounded powder.

XRD is a technique that involves irradiating a material with incident X-rays and then measuring the intensities and scattering angles of the X-rays that leave the material. When a monochromatic X-ray beam interacts with a target material, the scattering of those X-rays from atoms within the target material is the primary effect. The dispersed X-rays interact constructively and destructively in materials having regular structure (i.e. crystalline). X-rays may be thought of as waves of electromagnetic radiation, while crystals are regular arrays of atoms. The interaction of incident X-rays with the electrons of crystal atoms scatters the incident X-rays. Elastic scattering is the name given to this process, and the electron is the scatterer. The scatterers in a regular array produce a regular array of spherical waves. These waves cancel each other out in most directions due to destructive interference, but they contribute constructively in a few select directions, as specified by Bragg's law:

$$2d \sin \theta = n\lambda \,, \tag{3.3}$$

where d is the distance between diffracting planes, θ is the incidence angle, n is an integer, and λ is the wavelength of the beam. The specific directions appear as reflections (spots on the diffraction pattern). As a result, in a crystalline sample, this equation links the wavelength of electromagnetic radiation to the diffraction angle and lattice spacing (X-ray diffraction patterns

result from electromagnetic waves impinging on a regular array of scatterers). These diffracted X-rays are then detected, analyzed, and counted. The size and shape of the material's unit cell determine the possible diffraction directions. The type and arrangement of atoms in the crystal structure determine the intensity of the diffracted waves. However, most material are polycrystalline aggregates (powders) which are composed of numerous small crystallites in all possible orientations, unlike single crystals. Therefore, when an X-ray beam is focused on a powder with randomly oriented crystallites, the beam will view all potential interatomic planes.

Due to the random orientation of the powdered material, all potential diffraction directions of the lattice should be achieved by systematically adjusting the experimental angle and scanning the sample across a range of 2θ angles. Conversion of the diffraction peaks to d-spacings allows identification of the mineral because each mineral has a set of unique d-spacings. This is usually accomplished by comparing d-spacings to established reference patterns.

X-ray diffraction (XRD) of the TDP-PbSe NCs (in powder form) was carried using a Rigaku Miniflex 600 XRD with CuKα radiation.

3.3.8 Small-Angle X-ray Scattering

Small-angle X-ray scattering (SAXS) is an analytical technique that measures the intensities of X-rays scattered by a sample as a function of the scattering angle. SAXS is a small-angle scattering (SAS) method that provides information on the internal structure of disordered and partially ordered systems as well as particle sizes and shapes. This technique is one of the most versatile at determining the structural properties of nanomaterials. Measurements are taken at very

small angles, usually between 0.1 and 10 degrees. Solid objects, powders, gels, and liquid dispersions are all possibilities, as are amorphous, crystalline, and semi-crystalline samples.

According to Bragg's law, as the scattering angle decreases, the structural features being investigated get larger. Therefore, when a material contains structural features on the nanometer scale, generally in the range of 1-100 nm, a SAXS signal is seen.

SAXS measurements typically use a transmission geometry. The use of X-ray optics results in an extremely narrow yet strong incident X-ray beam. This is because the sample's comparably weak scattering radiation signal must be detected in close proximity to the direct beam ("small angles"). It's also critical to have a detector with good linearity, a large dynamic range, and low intrinsic noise.

For characterization of the NC solids using SAXS, the dried samples were exposed to a synchrotron using a diffractometer (Ultima IV Automated Multipurpose X-ray Diffractometer) with an x-ray energy of 40 kV (44 mA), powered by 2.2 kW of Cu Kα radiation.

3.4 NC Fabrication Results

3.4.1 PbS Nanocrystals

Introduction

Structural control of nano/micro-crystals with well-defined morphology is a fundamental target for today’s material chemistry, as size, form, and composition are vital to their physical and chemical properties.[149-150] The ability to adjust these parameters offers an opportunity to further

understand the relationship between structures formed and their properties in detail. Additionally, architectural control over the building blocks for well-defined morphologies is just as essential for the success of devices composed of crystals fabricated from their initial atomic scale. Specifically, preparation of metal sulfide semiconductor crystals with various morphologies has been observed by others and reported, which included multi-armed rods and spiral-configured CdS crystals,[151-153] as well as belt-/comb-/cross-shaped and sheet-like structures.[154-155] Novel examples of radially aligned AgS rods[156] and a variety of CuS particle assemblies[157] have also been reported by others as well. In spite of the fact that different forms of assemblies have been published, it still remains a great challenge to develop an efficient methodology for making novel stratified structures based on semiconductor crystals.

Amongst numerous metal sulfides, lead selenide (PbS) remains valuable and happens to be part of a classic group of IV-VI semiconductors with a low band gap energy, E_{bg}, (0.41 eV) and large excitation Bohr radius (18 nm).[133] Its large absorption cross-section, strong quantum confinement of both electrons and holes,[11] and tunable band gap from near-infrared to visible spectral region[158] are all reasons why it's gained such considerable interest. As a result in several areas, equivalent to photovoltaics, photo-detectors, electroluminescence, solar absorbers, thermal and biological photos, and laser mode locks, PbS has a wide range of applications in numerous fields.[72, 159-165] Even nonlinear optical third-order properties of PbS NPs were reported, which may have potential applications for light-emitting diodes and high-speed optical switches.[166] In this way, syntheses of novel PbS crystals with numerous morphologies and dimensions are going to be engaging for purposeful and potential applications of the future.

To this point, PbS crystals produced have been set up with various morphologies, such as wires,[167-168] rods,[169-170] tubes,[171] flowers,[172-173] hollow spheres,[174] stars with six symmetry horns,[175]

ellipse to parallelogram,[176] dendrites composed of arms,[177] hierarchic stars with symmetrical arms, rod clusters,[178] orthogonal wire arrays and networks.[179] Syntheses of these successful crystals use one of the many created strategies, including solvothermal and hydrothermal methods, ultrasonic irradiation, microwave-assisted heating, electrodeposition, thermolysis, template, self-assembly, and chemical vapor deposition. In any case, establishing a straightforward, naturally inviting, and comprehensive building strategy for large-scale synthesis of ordered PbS crystals with complex arrangements is still challenging. A technique that may possess all the necessary qualities would be a wet chemical course, also known as a "bottom-up" self-assembly approach, with its additional large-scale production and cost efficiency benefits.

There are a few reports using surfactant inclusion complex to induce the assembly and surface functionalization of nanocrystals (NCs) with semiconductors.[180-182] Thus, the supramolecular surfactant complex can be used as a structure-directing agent in the manufacture of semiconductor nanomaterials, as it has the potential to interact with solid surfaces and selectively absorb to manage the direction of crystal growth on particular aspects of crystals. In this work, we report the development of PbS octahedra, multipods, hyperbranched particles, and dendritic structures within aqueous solutions containing CTAB complexes. Meanwhile, CTAB is a cationic surfactant that has a positively charged head group and a long aliphatic hydrophobic hydrocarbon chain,[183-184] allowing CTAB-assisted growths to be simple, highly reproducible syntheses of octahedral PbS NCs with self-assembled branching / dendritic structures.

Even a simple method for selective control over hierarchical PbS microstars with hexa-symmetrical dendritic arms and PbS nano-/microstructures was developed using CTAB. More emphasis was put into understanding the microstars' creation process and growth mechanism with

hexa-symmetric arms, as well as several pivotal factors influencing the development of the hierarchical PbS structures.

3.4.1.1 Change in Morphology

After observing several syntheses which discuss different stages of PbS NP assembly (the shape evolution of PbS NPs or things within those realms), here we display results from a PbS synthesis to express how a large variety of NPs can be fabricated. The explored reactions allow one to produce a variety of forms that can enable new optoelectronic devices. The produced morphologies and nano-/microstructures have been investigated with SEM and TEM observations for visual evidence of the nanostructures. For SEM, typically the PbS colloidal solution is drop-casted onto a SEM holder resulting in what can be seen in Fig. 3.4. Dividing the various PbS particle shapes in terms of morphology, we developed 4 different products: normal/truncated nano-octahedra, star-shaped multipods, six-arm nano-/microscale star-shaped dendrites, dendritic mono-arms.

3.4.1.1.1 Nano-octahedral & Fused NCs

The following sections detail the results of the various PbS-based aqueous synthesis procedures. The motivation for making multipod and dendritic structures is that one can achieve strong-confinement along the various arms of the NP in a NP that is on the micrometer scale rather than the nanometer scale. If the dendritic PbS NC is crystalline, then the challenge associated with electrically interconnecting a multitude of NP building blocks get commensurately reduced. The drawback of using PbS is that since the Bohr radius is smaller than that of PbSe, the strong-confinement-induced diminishment in the thermal noise is less pronounced. Nevertheless, the

following series of narratives explains the evolution of the approaches that allowed us to make PbS NCs with microscopic extents and nanoscopic charge-confinement.

One of the first particle morphologies that we observed using this hydrothermal-based synthesis, were relatively poly-dispersed truncated octahedral NCs with an average diameter of 44.6 ± 4.9 nm after at least a day of reaction time, at 90 °C. Fig. 3.6a displays evidence of jointed NCs, composed of imperfectly fused NPs (2-4), to create a larger NC. This sample contains PbS building blocks, suggesting that high yield can be readily achieved by this synthesis consistently. At first glance, the type of PbS NCs produced possesses a cube-like shape (Fig. 3.6a), but through more careful observation they are more of an octahedral form. This can be proven by the SEM image below in Fig. 3.6b as well. The vertices of the joined NCs are assumed to be along the six <100> directions. With a plethora of nano-octahedra NCs, well-defined or not, we see the NCs have tendencies to group together.

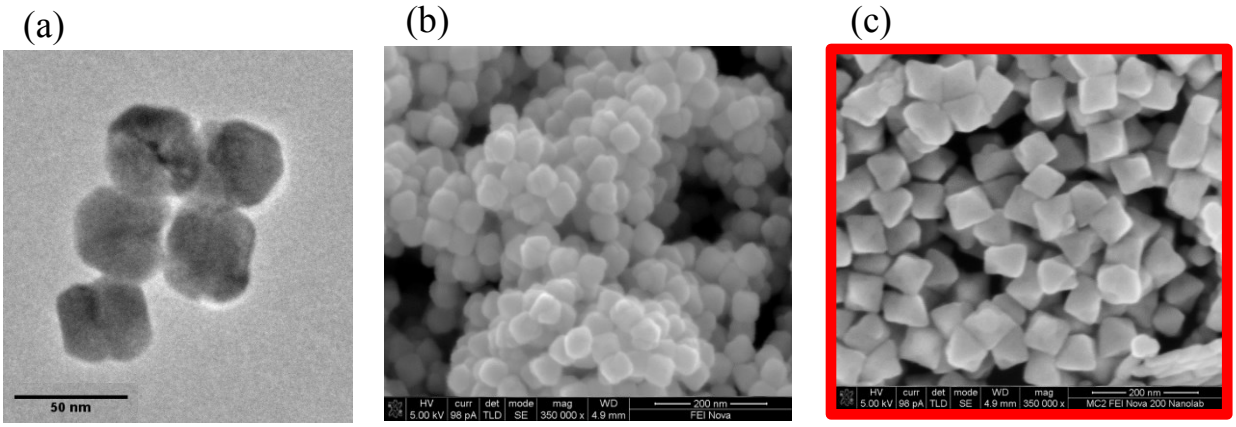

Fig. 3.6 | TEM and SEM images of octahedral-shaped PbS NC samples prepared under standard conditions to form octahedral-shaped PbS NPs. (a & b) Some cases show NCs, varied in size, fuse into larger NCs, in the form of dull-tipped octahedrons while in other case we see (c) octahedra with more shape definition to recognize their vertices are along the ‹100› directions.

3.4.1.1.2 Six-arm Star-Shaped Multipods

These joined NCs are considered to be the building blocks for the architecture of the nano-/microstructures seen later in this section. The NCs are transformed into multipods, or nano-stars, after extending their time of growth. This additional time pushes NCs closer to mono-dispersity and enhance shape definition to be considered more octahedra-like NCs. We observed multipods with a tip-to-tip (opposite ends) average length to be 132.8 ± 6.8 nm for small nano-stars while the larger NCs stand at 178.5 ± 7.9 nm. Both sizes are confirmed by SEM images (Figure 3.7 – 3.9), where well-defined nano-stars with horns are clearly observed. The low-magnification image seen in Fig. 3.7 also displays the formation of uniform star-like NCs while a TEM image of a singular multipod can be seen in Fig. 3.9. In both images of the PbS NC multipods, a single PbS NC can be seen, deposited with three lower vertices on the surface (lower level; red) while the other three vertices stick out in the upper level (blue).

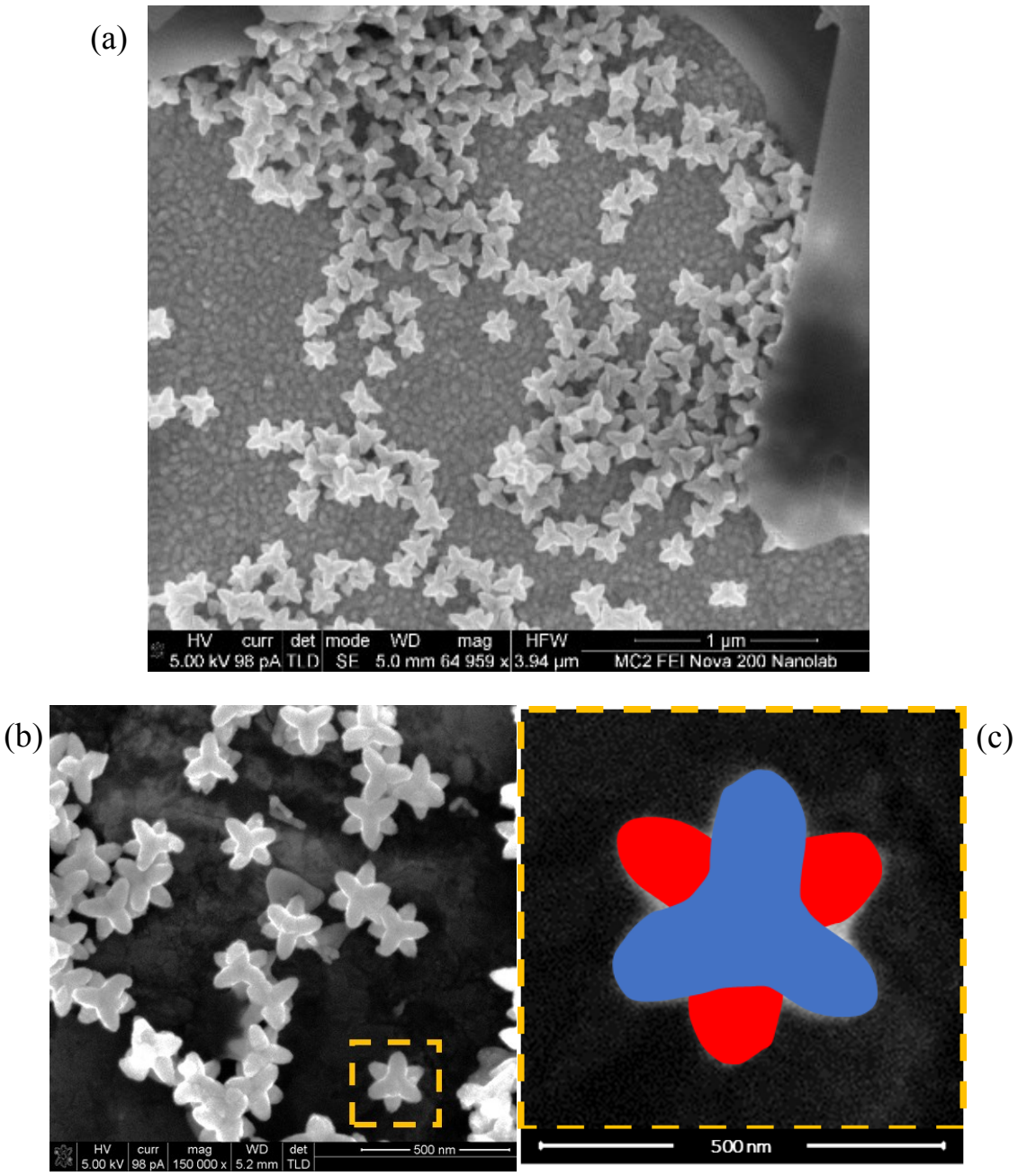

Fig. 3.7 | SEM images observing PbS NCs with arms of minor elongation from the vertices (six) of the octahedron building blocks to form nanoscale star-shaped NCs. (a & b) Several multipod-shaped NCs, piled and standing-alone, on Au plated surface. (c) Singular PbS multipod displaying six vertices; 2B vertices allowing the multipod to stand along the floor (red) and the remaining vertices pointing up and out away from the floor (blue).

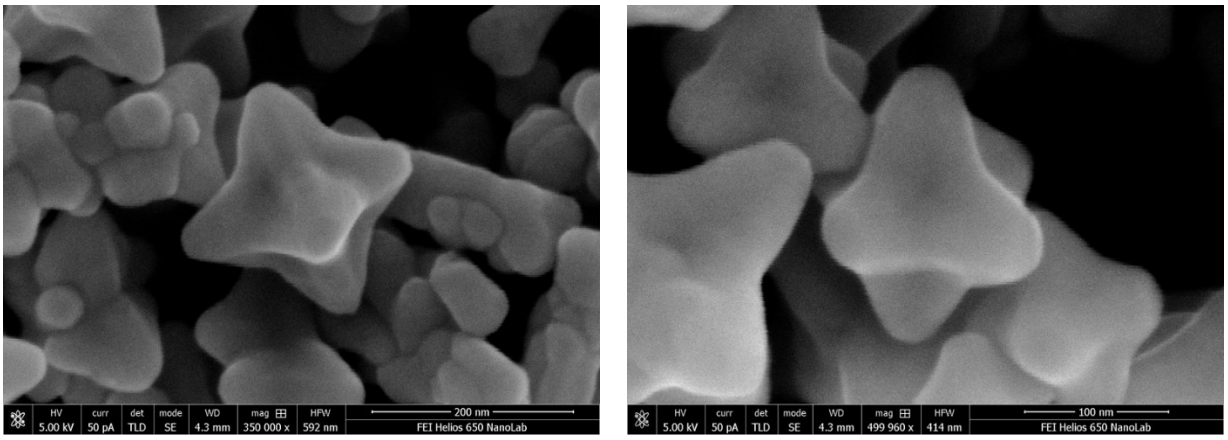

Fig. 3.8 | Additional SEM images observing PbS NCs with arms of minor elongation from the vertices (six) of the octahedron building blocks to form nanoscale star-shaped NCs.

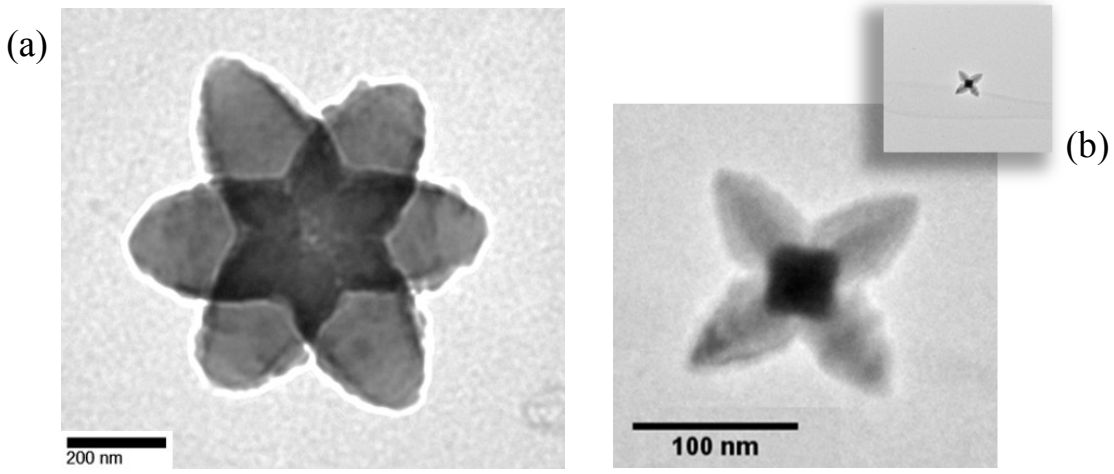

Fig. 3.9 | High-and low-resolution TEM images of PbS multipods from various angles along a copper-mesh grid. Each displays a vertex where (a) shows all vertices can be seen along with its thicker nucleus or (b) a top view into a vertex which allows for the only 4 vertices to be shown.

3.4.1.1.3 Microscale Star-Shaped Dendrites (Snowflakes)

Our fabricated NCs can also be transformed into hyperbranched stars or dendrites, complex superstructures with simultaneous elongation of the six vertices of the octahedra shape from the initial stage. Faceted rods come together to contribute to this new formation, resulting into six-arm

star-shaped particles with lengths of ~700 - 2000 nm. Images below (Fig. 3.10, 3.11) show the main six-arms growing along the <100> direction of the octahedrons with secondary nanorods (NRs) (or branches) oriented perpendicularly to the four remaining <100> directions. Over time, the thickness of the branches increases as well, eventually forming into six-arm branched star-shaped snowflakes where the microrods dominate. Fig. 3.10 shows typical dendrites, each having dendritic arms (6) made of long central spines and secondary branches. These hexa-symmetric arms extend from the NC center base to tip of the dendritic arm with a length of ~0.8 ± 0.1 μm. Observing Figs. 3.10 – 3.12, we notice each dendritic arm (long axes) displays 4 branches (shorter axes). The branches (or nanorods) are parallel to each other in the same plane while also perpendicular to the arm upon which they reside.

(a) (b) (c)

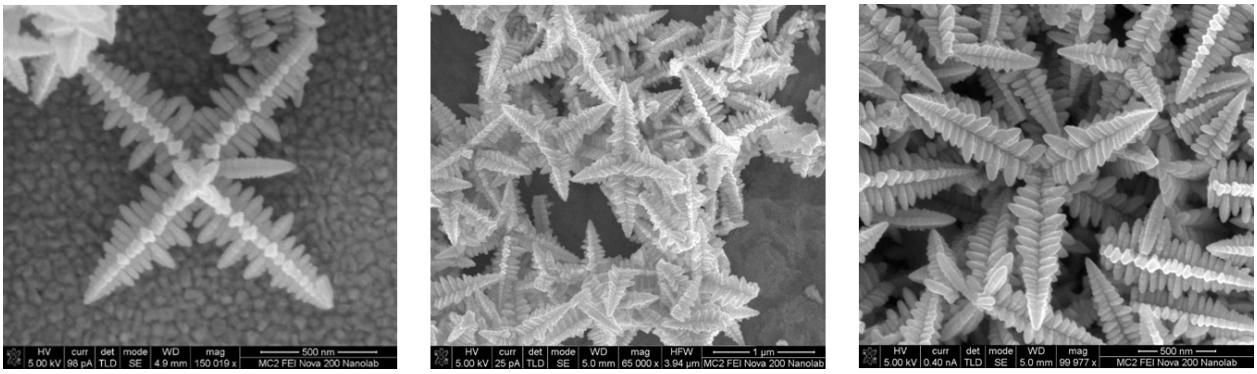

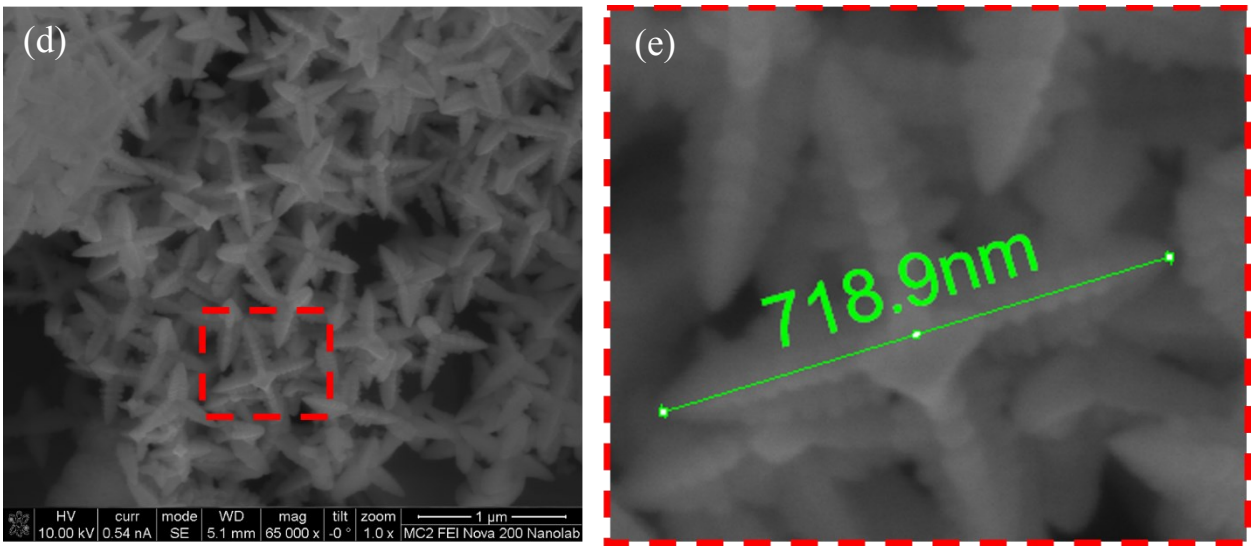

Fig. 3.10 | SEM images observing stars made of six elongated branches (hyperbranches) from the vertices of the octahedron building blocks. (a) PbS hyperbranched star with bottom arm removed from star. (b) Cluster of multiple PbS hyperbranched stars intertwined after drop-casting colloidal solution. (c) SEM image centered at base of PbS hyperbranched star with viewpoint of only three hyperbranched arms. (d) Low- and (e) high-resolution imaging, displaying full length of snowflake-shaped NCs.

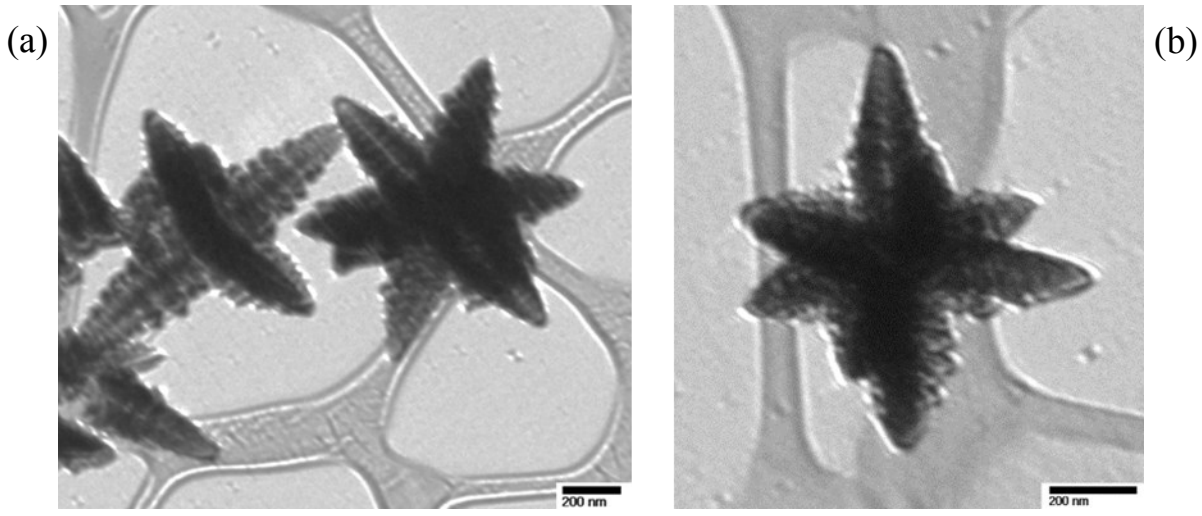

Fig. 3.11 | TEM images observing stars made of six elongated branches (hyperbranches) from the vertices of the octahedron building blocks. (a & b) TEM images of hyperbranched star/s.

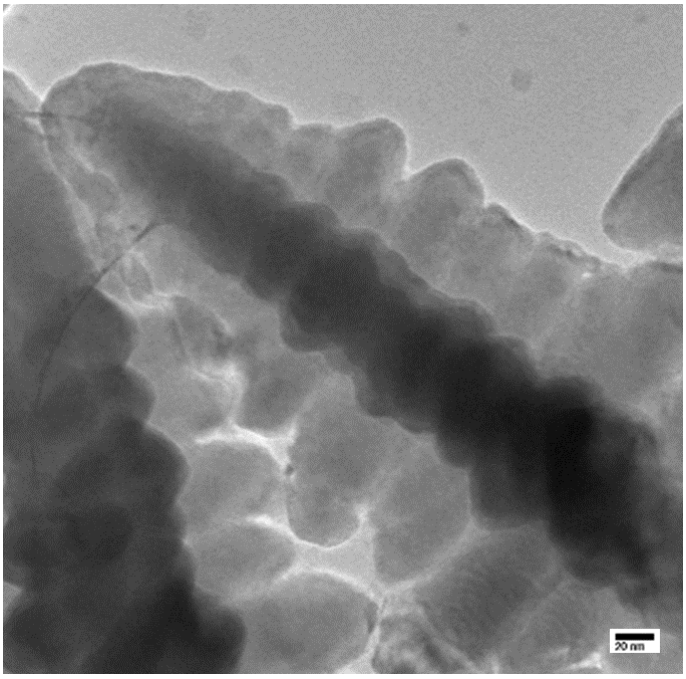

Fig. 3.12 | High-resolution SEM images observing branches attached to dendritic arms of stars made of six elongated branches (hyperbranches) from the vertices of the octahedron building blocks.

3.4.1.1.4 Dendritic Mono-Arms

At times, the junction of the six-arm star-shaped microcrystals experience deconstruction due to forces that lead to the disbanding of arm/s, as seen in Figs. 3.13, where several broken arms, roughly ~500 - 900 nm (~860 ± 12 nm) in length, appear throughout the samples. It would seem the cause of this breakage is due to collisions of star-shaped NCs, however, there is a phenomenon that the six-arm star-shaped microcrystals break by ultrasonic waves of radiation or even due to cavities being within the arms themselves.[185-186] Further experimentation will need to be conducted to determine such a hypothesis.

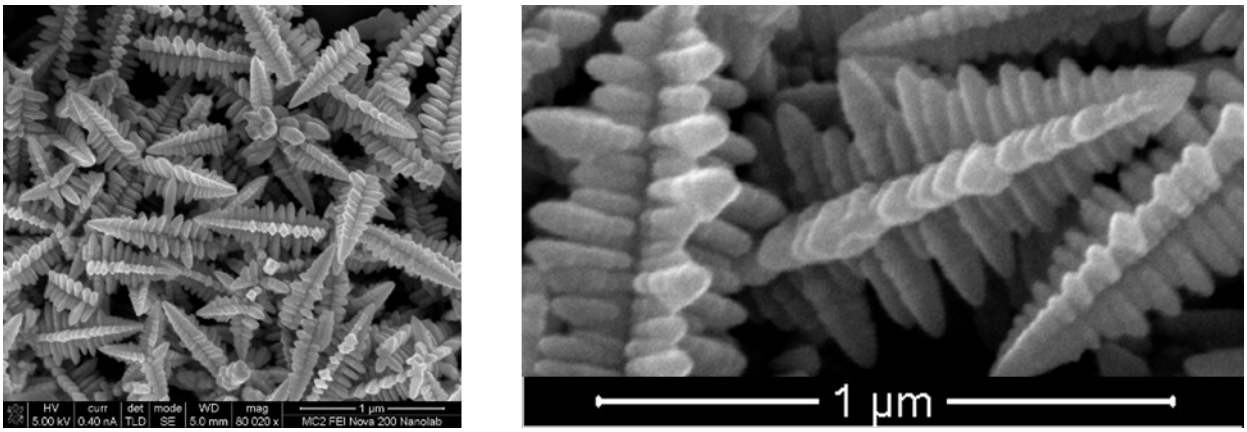

Fig. 3.13 | SEM images of dendritic mono-arms. The "nanorods" along each arm are perpendicular to the trunk while the branches themselves possess complex structures. Every portion of the mono-arms are composed of elongated octahedral and small branches (4) throughout the length of the arm just as in the full-body dendrites.

3.4.1.2 Discussion

As discussed in Chapter 1, it is generally agreed that NC formation within solution involves two steps: (1) a sudden increase in monomer concentration to a supersaturated level, triggering nucleation and (2) subsequent growth from seeds with progressive consumption of monomers in solution.[187-188] However, the product's morphology and structure are determined by both the nuclei's crystalline phase and growth rate of the different crystal surfaces.[189] It is also well-known that surface energies of different crystallographic planes are generally different, as a general sequence can be revealed as $\gamma\{111\} < \gamma\{100\} < \gamma\{110\}$.[189]

The disparity in relative growth rates between the six {100} and eight {111} facets of a seed, possessing either a normal or dull-tipped octahedron shape, would be responsible for its nano-/microscale geometry. The growth rate along the <100> direction of a seed can be often favored, with help of the surfactant used, subsequently causing the {111} facets to disappear and fully expose {100} facets only. In this case, six-branched star-shaped crystalline NCs are formed due to

the growth rate along the six <100> directions or vertices of the "used to be" octahedra.[186] Since the {111} facets of our PbS NCs are charged facets containing only Pb or S atoms while the {100} facets are uncharged containing both Pb and S atoms, the molecules of our cationic surfactant, CTAB, selectively stabilizes the negatively charged {111} facets containing only S atoms due to the positively charged ionic headgroups of CTAB ($–N(CH_3)_3^+$).[169]

For the case of an adequate amount of CTAB (1.0 mmol), the surface energy of the {111} facets would decrease significantly due to the absorption of CTAB, which results in a relatively decelerated growth of the {111} facets, thus forming nano-octahedra with the promotion of truncated octahedra generation from both {111} and {100} facets.[188] However, with a low CTAB concentration to attend the S^{2-} sights (whether in solution or along the NC surface), either uniform growth occurs along the entire exterior of our dull-tipped octahedra NCs or they experience growth alterations which could bring about octa-symmetric structures with a true excess of dissociated S^{2-}—both possibilities preventing <100> directional favoritism. This continuation results in a transformation from octahedra (initial longest tip-to-tip dist. ≈ 59.9 ± 5.0 nm) into truncated octahedra and/or a cube-like shape, either of which being larger than the original octahedra (final longest tip-to-tip dist. ≈ 96.5 ± 5.5 nm).

Figs. 3.14 – 3.24 displays images depicting both scenarios, as we have taken the liberty to experiment with less and more than the required amount of CTAB while synthesizing PbS NCs as follows: CTAB : $Pb(Ac_2)$: TAA molar ratios of 1.3/1/3 and 2.7/1/1. Results of the 1.3/1/3 CTAB : $Pb(Ac_2)$: TAA molar ratio reveal NCs altered from dull-tipped octahedra to truncated cubes of rough surfaces. Adding to this scene, the low Pb^{2+} concentration within the solution leaves PbS

nuclei to no longer continue consuming more ions for growth into larger NCs, therefore, the NCs remain small. This further encourages S^{2-} to flow freely throughout the system (regardless of pace at which TAA solution is being dropped into system), leaving NC roughness attributed to either dissociated S^{2-}, the CTAB concentration at a low level only covering groups of NCs (instead of individual NCs) or headgroups within CTAB attending to the overflow and/or dissociated S^{2-} sites instead of filling across the {111} facets of the PbS NCs. With either the three options, over the course of a low heating period, minor growth along the {100} facets occurs, leading to only minor shrinkage of {111} facets as evidenced by Figs. 3.14, as it shows the stage of the PbS NCs after t ≈ 1.5 hrs, revealing much smoother NC surfaces with transitions into truncated cube sphere-like structures.

Adjusting the CTAB : $Pb(Ac_2)$: TAA molar ratio to 2.7/1/1, the PbS NCs become much smoother with transitions into truncated cube sphere-like structure. Figs. 3.15 bears witness to the benefit of higher Pb and CTAB content within the system, showcasing occasional facet-to-facet interconnectivity appeal.

Going through the initial stages of the PbS NC morphology, when NCs are under 100 nm in diameter, we turn to Figs. 3.16 – 3.21, where we observe NC growth over the course of an hr. As previously mentioned, the initial form of our NCs is octahedron with the six <100> vertices extending away from the NC base throughout (Fig. 3.16). At t ≈ 10 min. (Fig. 3.17), the {100} and {111} facets experience growth, creating a dull octahedron structure with slightly rough surfaces. At this point, an adequate amount of time for the NCs to grow has not occurred for NCs to encounter enough CTAB along the {111} facets for facet growth prevention. At t ≈ 20 min. (Fig. 3.18), the NCs take more of a cube-like form, still experiencing roughness. At t ≈ 30 min., it

becomes noticeable that if the {111} facets appear to grow, the {100} facets grow at a faster rate. This is proven by NCs having a slight nanocube-like structure seen across Fig. 3.19. At t ≈ 45 min. (Fig. 3.20), more NCs continue to make the transition into a nanocube-like form with more definition and slight fusing of neighboring NCs at the {100} facet. At t ≈ 1 hr, the level of roughness that once existed has ceased. Nearly all NCs possess the nanocube form and have connected and/or fused with neighboring NCs, as seen in Fig. 3.21. This process was experimentally repeated and shown in Figs. 3.22 – 3.24.

With the addition of a highly concentrated TAA solution, more S^{2-} can be released slowly during the heating process, resulting in more PbS crystal nuclei in solution—hence the reason for slowly dropping the solution into the system. However, if the amount of the Pb source happens to be insufficient, there would not be enough Pb^{2+} to consume the growth of PbS nuclei, and thus much smaller PbS NCs eventually form under this condition. It should be noted that the proper amount of CTAB molecules could still suffice for the stabilization of the {111} facets of the PbS nuclei in this scenario.

(a)

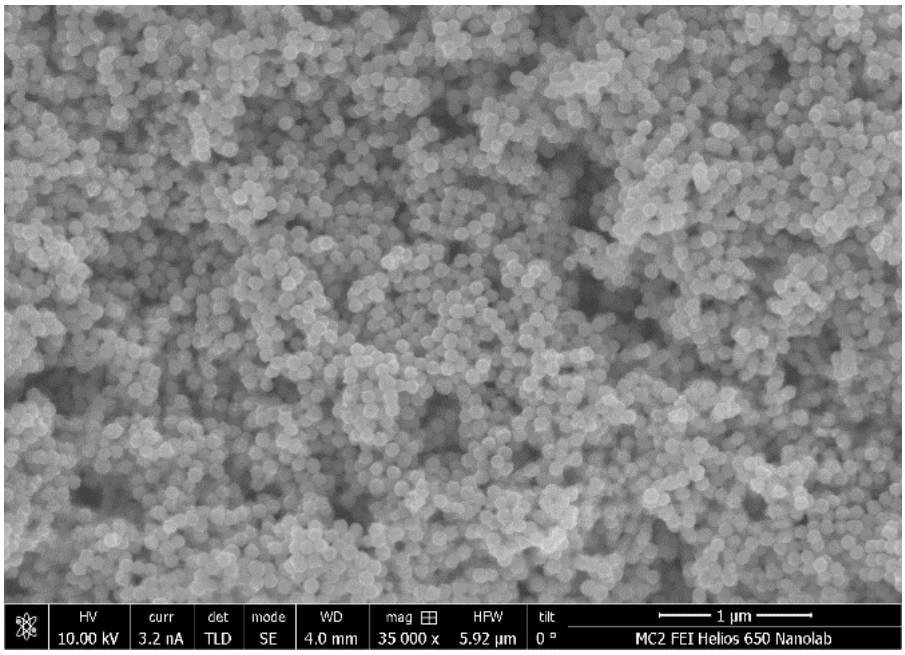

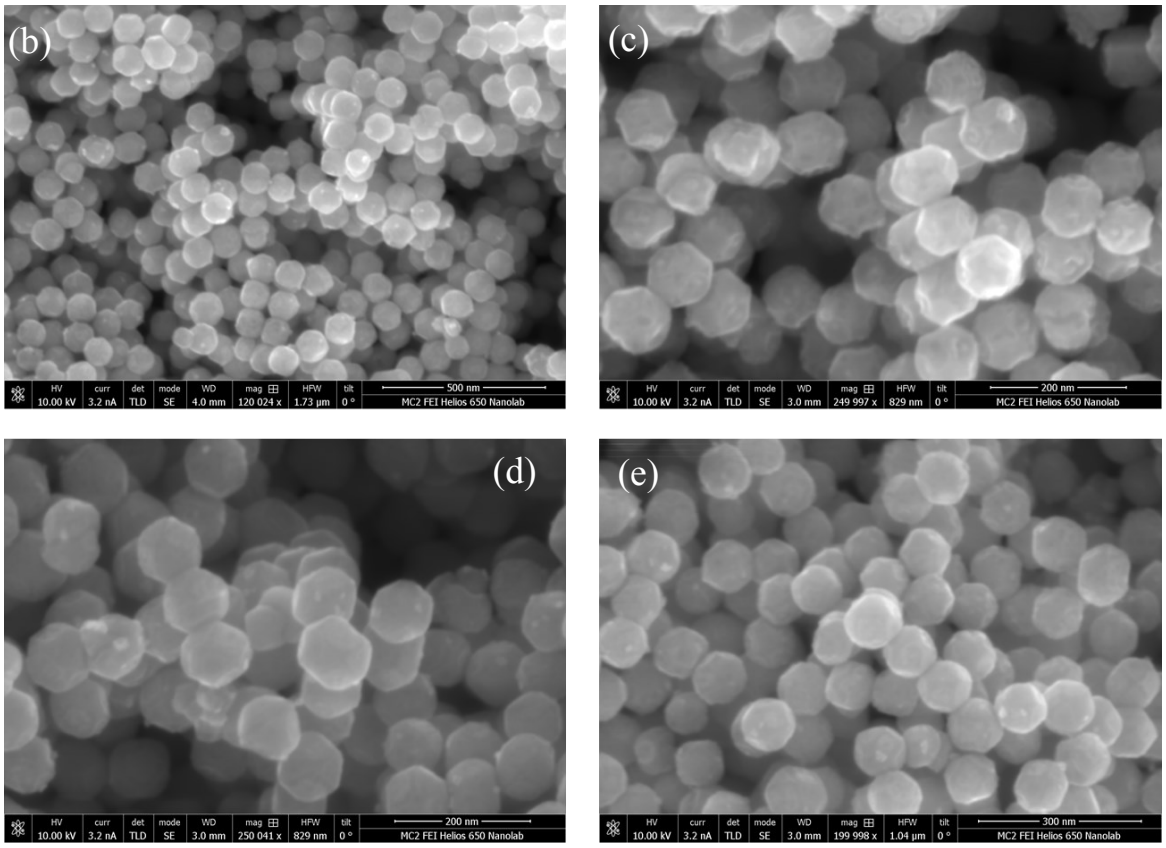

Fig. 3.14 | SEM images of truncated PbS octahedra synthesized at an initial reaction temperature of ~40 °C, with refluxing for 1.5 hrs. at 98 °C. Molar ratio of $Pb(Ac_2)$ / TAA = 1/3. (a) High-resolution SEM image of truncated PbS NCs stacked atop each other. (b) High-resolution SEM image of truncated PbS NCs almost all sitting along a flat surface within valley of NCs. (c) High-resolution SEM image of truncated PbS NCs self-assembled into facet-to-facet connectivity due to facet attraction.

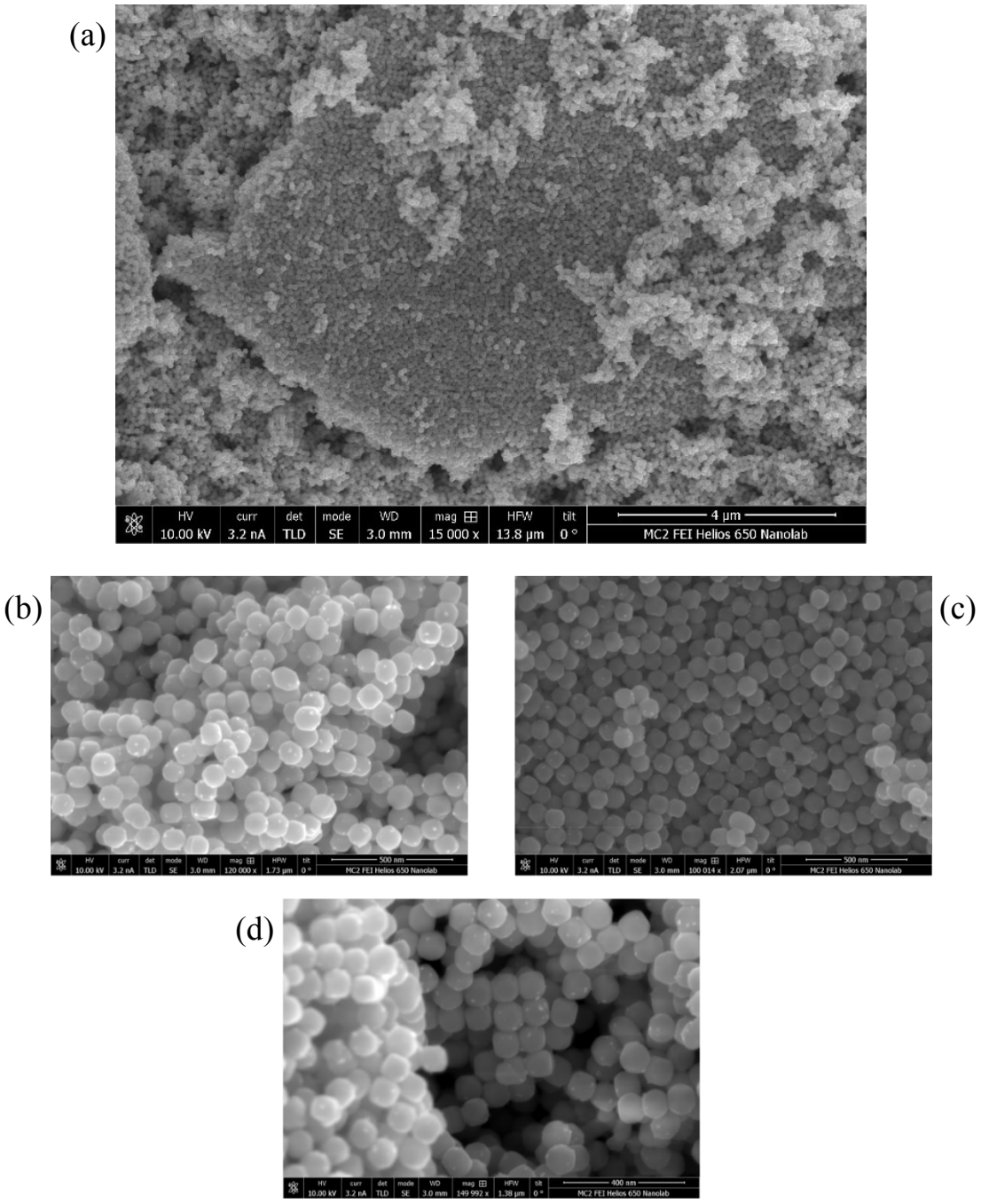

Fig. 3.15 | SEM images of truncated PbS nanocubes synthesized at an initial reaction temperature of 43 °C, with refluxing for 26 hrs. at 98 °C. Molar ratio of Pb(Ac_2) / TAA = 2/3. (a) Low- and (b) high-resolution SEM images showing truncated PbS NCs stacked atop each other. (b) High-resolution SEM image of truncated PbS NCs almost all sitting along a flat surface within valley of NCs. (d) High-resolution SEM image of truncated PbS NCs self-assembled into facet-to-facet connectivity due to facet attraction.

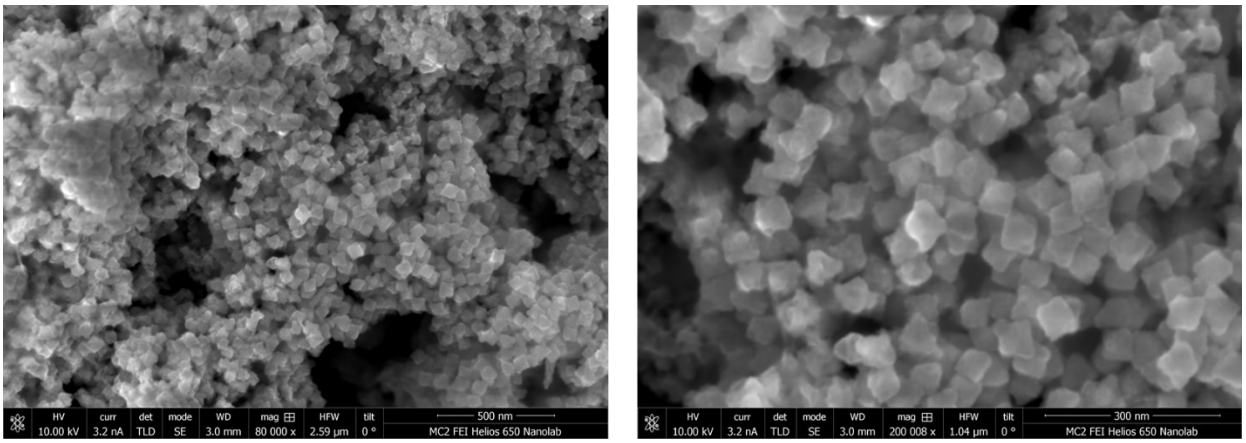

Fig. 3.16 | Morphological evolution process of PbS NCs: SEM images of a sample synthesized at an initial temperature of 98 °C, prior to any $Pb(Ac_2)$ / TAA drops entering the glassware and any amount of refluxing time, t = 0 min.

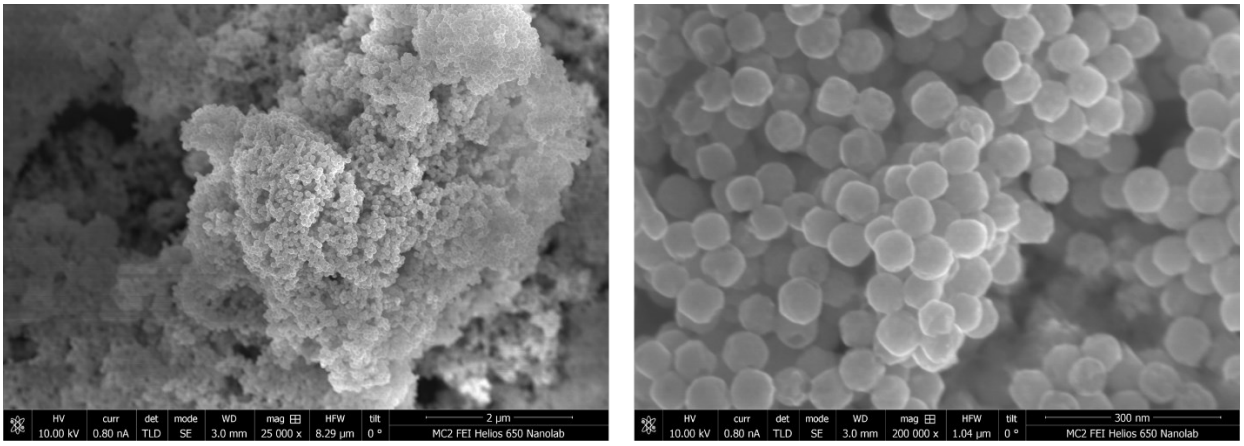

Fig. 3.17 | Morphological evolution process of PbS NCs: SEM images of a synthesized sample where $Pb(Ac_2)$ / TAA (molar ratio = 1/1) drops entered glassware at 65 °C and growing temperature of 98 °C, after a refluxing time, t = 10 min.

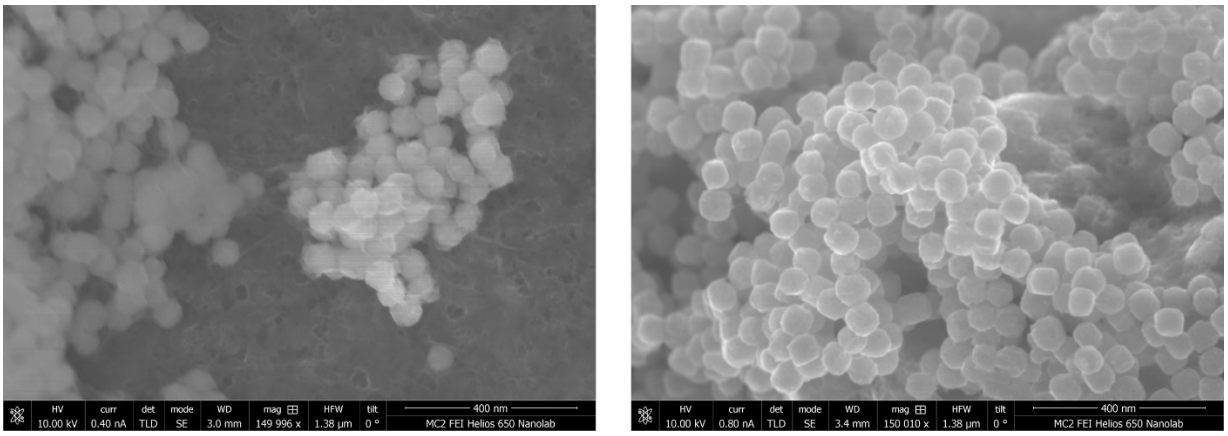

Fig. 3.18 | Morphological evolution process of PbS NCs: SEM images of a synthesized sample where $Pb(Ac_2)$ / TAA (molar ratio = 1/1) drops entered glassware at 65 °C and growing temperature of 98 °C, after a refluxing time, *t* = 20 min.

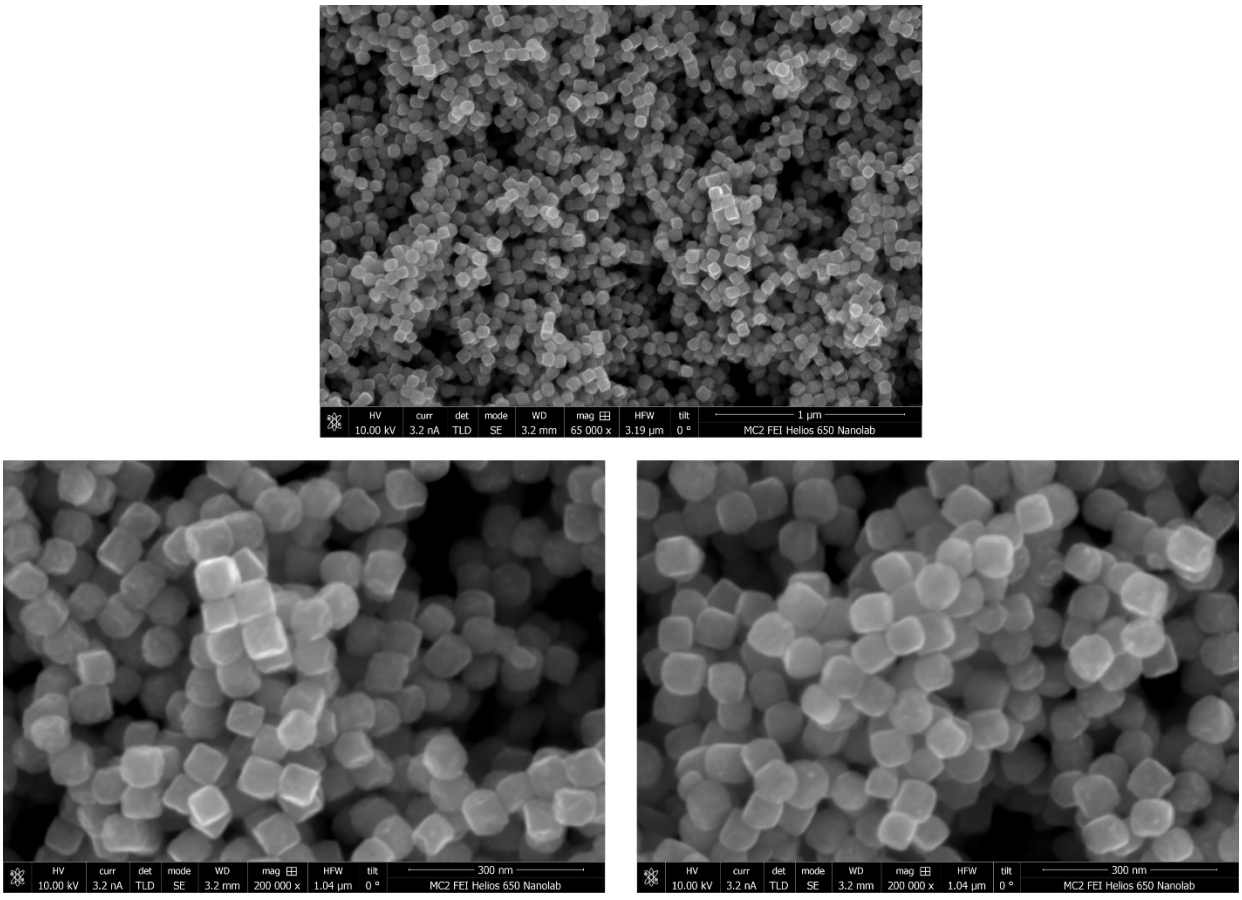

Fig. 3.19 | Morphological evolution process of PbS NCs: SEM images of a synthesized sample where $Pb(Ac_2)$ / TAA (molar ratio = 1/1) drops entered glassware at 65 °C and growing temperature of 98 °C, after a refluxing time, *t* = 30 min.

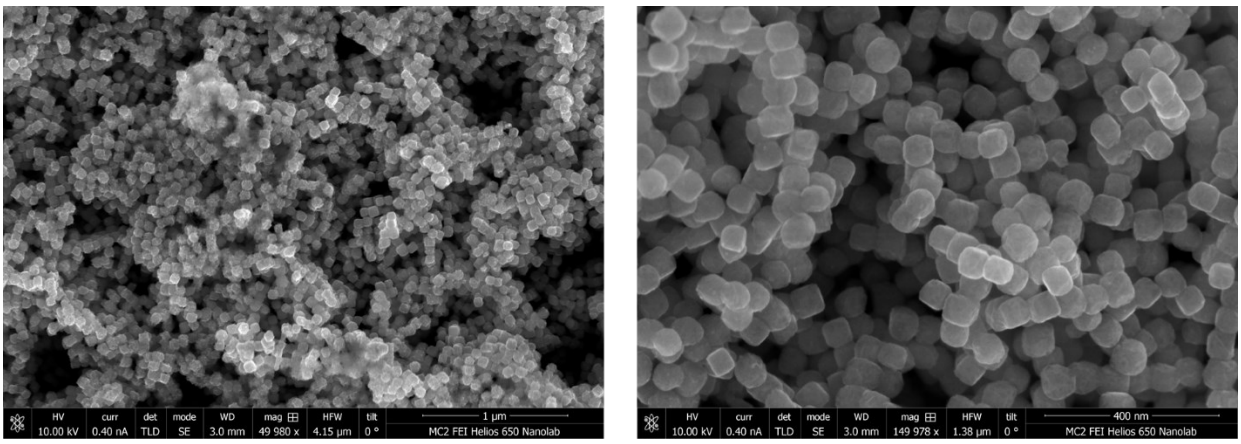

Fig. 3.20 | Morphological evolution process of PbS NCs: SEM images of a synthesized sample where $Pb(Ac_2)$ / TAA (molar ratio = 1/1) drops entered glassware at 65 °C and growing temperature of 98 °C, after a refluxing time, *t* = 45 min.

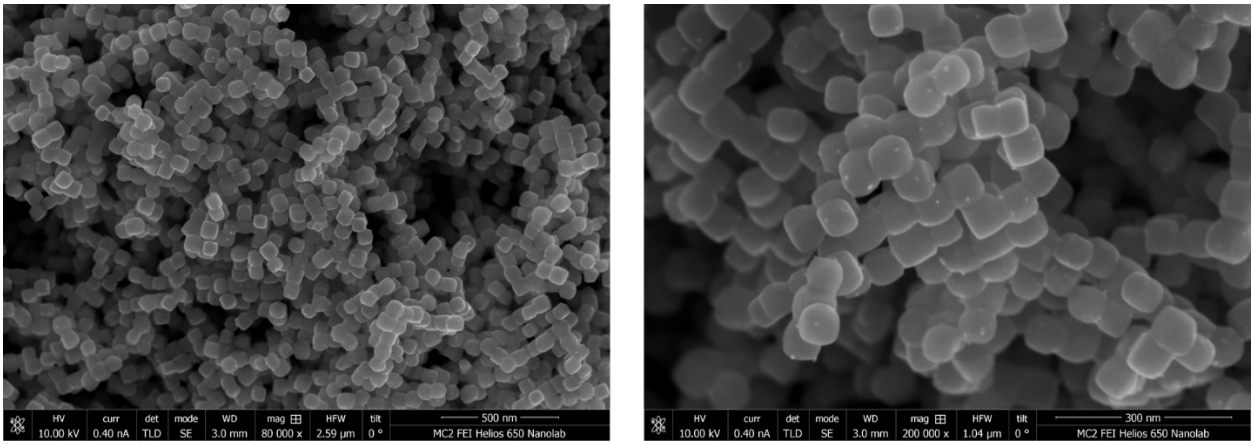

Fig. 3.21 | Morphological evolution process of PbS NCs: SEM images of a synthesized sample where $Pb(Ac_2)$ / TAA (molar ratio = 1/1) drops entered glassware at 65 °C and growing temperature of 98 °C, after a refluxing time, *t* = 1 hr.

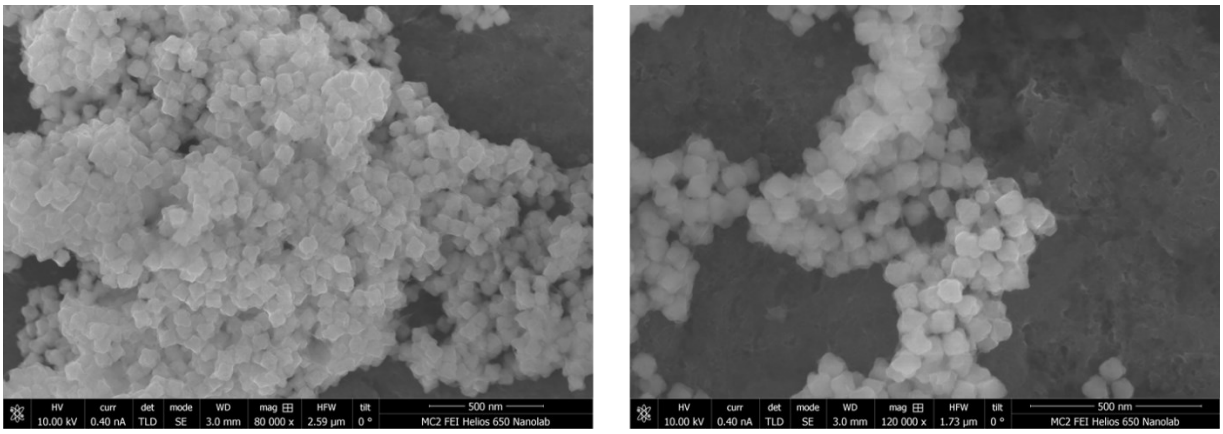

Fig. 3.22 | Morphological evolution process of PbS NCs: SEM images of a 2nd synthesized sample where $Pb(Ac_2)$ / TAA (molar ratio = 1/1) drops entered glassware at 45 °C and growing temperature of 98 °C, after a refluxing time, *t* = 5 min.

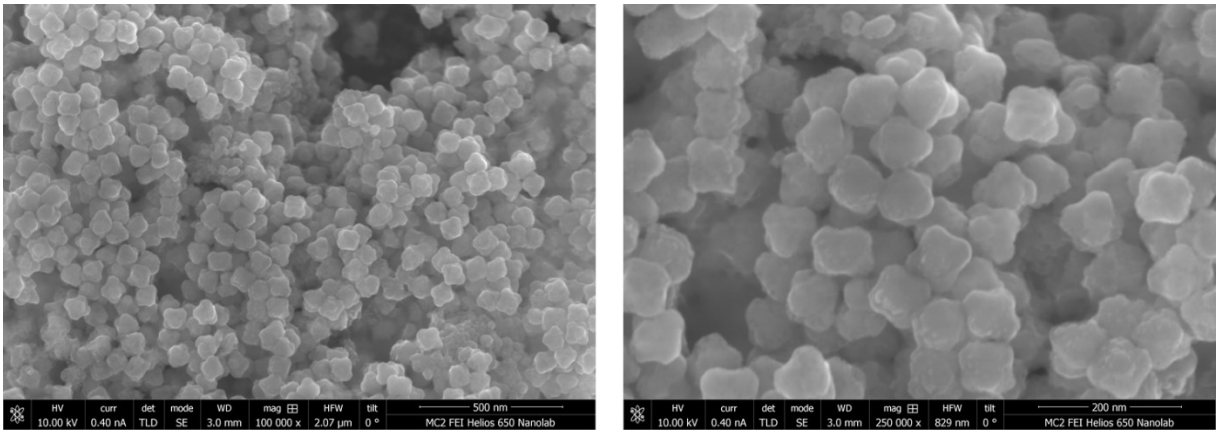

Fig. 3.23 | Morphological evolution process of PbS NCs: SEM images of a 2nd synthesized sample where $Pb(Ac_2)$ / TAA (molar ratio = 1/1) drops entered glassware at 45 °C and growing temperature of 98 °C, after a refluxing time, *t* = 10 min.

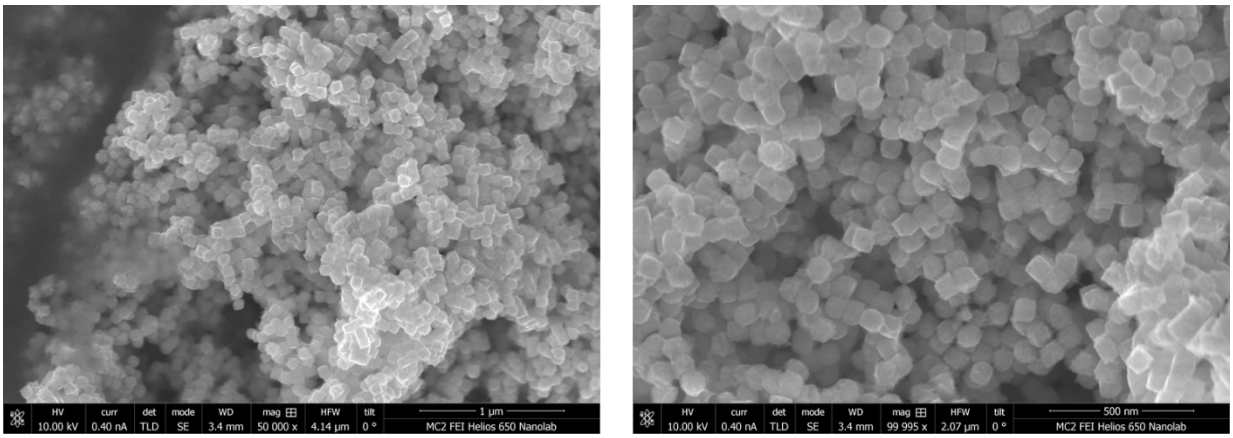

Fig. 3.24 | Morphological evolution process of PbS NCs : SEM images of a 2nd synthesized sample where Pb(Ac_2) / TAA (molar ratio = 1/1) drops entered glassware at 45 °C and growing temperature of 98 °C, after a refluxing time, *t* = 1 hr.

By increasing the concentration of the TAA solution, though it does not influence the nuclei formation process, it does however create more dissociated S^{2-} in the solution to consume some of the CTAB molecules through static interactions. This means a reduced number of CTAB molecules as capping agent to stabilize {111} facets of octahedral-shaped PbS nuclei, which ultimately leads to the formation of small PbS NCs. Further increasing the concentration of TAA leads to the gradual disappearance of the outer {111} facets coupled with the emergence and gradual increase of the outer {100} facets.

The next stage includes the nucleation reaction leading to PbS stars. Early NPs are still present in copious amounts at this stage and thus they assume the job of building blocks in the transition from octahedron to multipod shaped NCs. One can observe, at this point, attachments of NPs, or branches, growing into superstructures, as seen in Figure 3.6 – 3.9.

The creation of dendritic facetted crystals and/or multi-armed structures relies heavily on the role of branching growth functions. Taking the growth of a crystal for example, as it grows, ions

and/or molecules absorb along the crystals surface, creating a concentrated cloud of diffusion field/s around the crystal itself. This results in crystal apexes growing at a faster rate than its central sections, seeing that the apexes protrude into the highly concentrated regions within the diffusion layer. However, the consequence would be that the highly concentrated monomer regions close to the crystal surface eventually diminishes, then suppressing the crystals growth rate. Still, branches would at least begin their initial crystal form through the advancement of the facets. This method, better known as diffusion-induced branching growth, is capable of being self-sustaining with the help of faster growing branches that advance beyond and into territories of even higher monomer concentrations, contributing to further developments.[186] During this period of crystal growth, growth conditions such as concentration and temperature (to amplify or minimize the effect of diffusion) can still be adjusted to control formation and/or branching growth preferences.

Branching growth typically plays a significant role in the creation of facetted crystals of dendrites or multi-armed structures.[190] As a crystal grows, near the surface, ions or molecules are absorbed and a concentrated diffusion field forms around that crystal. This makes the apexes of a polyhedral crystal, which protrudes further into regions of higher concentration within the diffusion layer present around each NC, grow faster than the central sections of facets, and thus further depletes the concentration of monomers close to those regions, therefore further suppressing their growth rate.[186, 191] As a result, branches may start their initial form of crystals through the development of new facets. During the crystal growth, preference for habit formation and branching growth can be altered by modifying growth conditions such as concentration and temperature which amplify or minimize the effect of diffusion. Over time, the correspondence in the decrease of amounts of NCs in the medium and the joint enlargement of the multipods is

consistent with the conclusion that branch growth has begun (Figs. 3.7, 3.9). The NCs with sizes of 132.8 ± 6.7 nm, which are identical within the experimental error to the average size of the NCs at 148.1 nm, are a representation of this stage.

In addition to the second stage of the PbS NC morphology variation, the formation of large clusters also occurs. However, their appearance cannot be clarified by means of the same growth process as in the initial stage. The clusters are formed by association of individual NCs in the same initial stage and SEM images can provide solid evidence for this, as seen in Fig. 3.25.[186] Naturally, the formation of clusters occurs when the concentration of NCs generated in the first stage are well above the supersaturation threshold in respect to their agglomeration (a mass or collection of things) into a large cluster.[186]

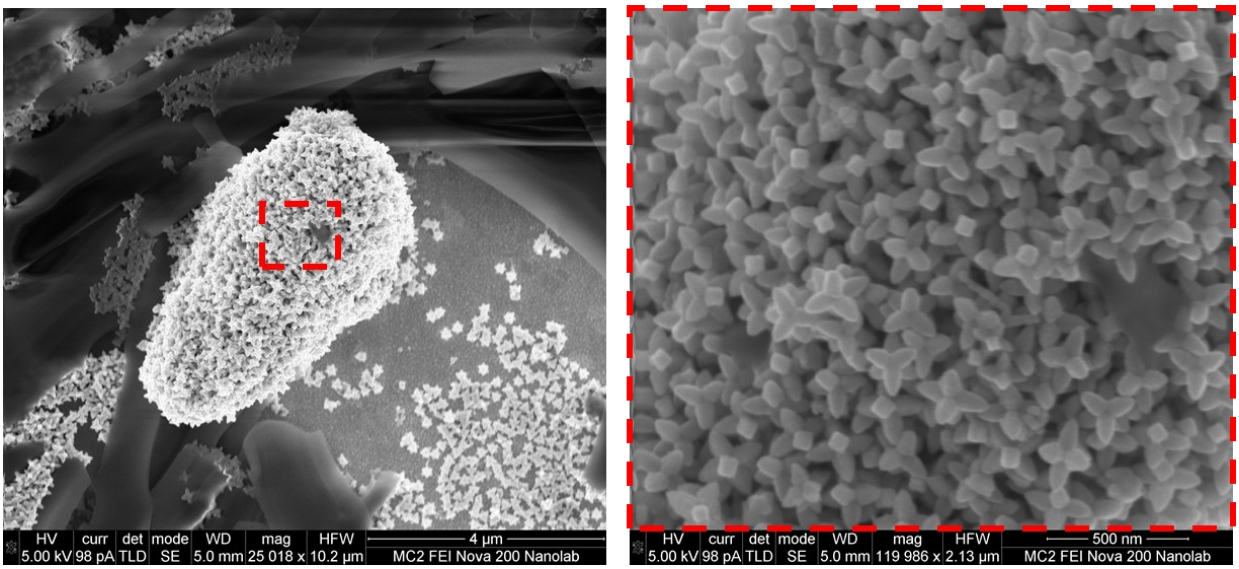

Fig. 3.25 | SEM images of star-shaped PbS NCs. (a) Low-resolution image of star-shaped NCs coming together, forming a large cluster. (b) High-resolution image of the cluster surface, displaying star-shaped PbS NCs which have come together randomly.

Provided the similarities between multipods and self-limited supraparticles, the switch of the assembly from multipods to hyperbranched stars can be understandable. This shift of the self-assembly patterns occurs in light of the fact that the forces of van der Waals attraction can no longer overcome charge-charge electrostatic repulsion between mesocrystals and singular NCs.

At this level, weaker forces in addition to the attractive and repulsive forces, such as the dipole-dipole attraction for example, becomes a pattern-determining feature for the interactions. Then pure geometry of the hyperbranched stars indicates the assembly has chosen linear patterns. Numerous nanoscale materials possess essential axial anisotropic properties due to the presence of electrical dipoles in NCs. The involvement of the dipole moment in PbS and other NCs with cubic rock-salt formations has been established in previous papers and their attraction to NC dipoles has already been involved in several self-assembly processes. [49, 175, 189, 192-193] Comparing the $<100>_{NP}$ axis of PbS and other semiconductor NCs with rock-salt structures, such as CdTe, CdS, PbSe and ZnSe, they are all related with the most prominent dipoles. Therefore, the creation of the branches along $<100>_{multipod}$, that is associated with $<100>_{NP}$, is to be expected within the hyperbranched systems.

The formation of large dendrites is speculated to be related to hyperbranched star stabilization.[186] By balancing and canceling the vectors of accumulated dipoles in opposite directions, the support for the increase in polarization of polar 1D structures could be obtained. In the simplest case for PbS hyperbranched stars, such directions can be captured as six vectors all pointing away from the central point of origin following the 3D Cartesian Coordinate System. On the off chance that such a dipole cancellation does occur, the build-up of the polarization energy would not preclude further assembly since one may also create a parallel with six ligands/ions

positioned midway around a focal molecule as an alternative, separately the most well-known theme in metal—organic complexes and ionic crystals. Knowing that long-chain components makes it simpler for electrons to dislodge, the more swiftly dislodged electrons arise, the more likely the NCs are polarized. It should not be surprising to see the same motif in nanoscale objects from this perspective.

Macroscopic cancelation of dipolar vectors indicating to inverse bearing is vital yet doesn't eliminate a significant part of the real polarization energy. This is often so since, major parts of polarizing energy such as, loss of configurational entropy of polarized molecules of the medium function over distances of molecular size, for example. Gathering of dipolar NPs inside a microbranch may imply that a rearrangement of charges happens all throughout the developing assembly. However, a rearrangement of charges is not practical for insulating materials and broad bandgap semiconductors, thus, dipolar chains are small, as it the case for ZnO.[194] However, PbS has a much higher conductivity, which greatly encourages the dispersion charges until NPs are joined to one another. SEM images in Fig. 3.15 and 3.26, which show practical interfaces between the gathered NPs, further help the capacity to bear charges across an assembled superstructure (HRTEM of snowflakes).

3.4.1.2.1 Closely Packed Arrays of PbS Star-Shaped Multipods

To build optoelectronic devices from manufactured PbS NCs, there is a desire to accomplish fabricated PbS-based NCs possessing capabilities to attain tightly packed systems with standardized structural assemblies. All samples seen up to now, within this publication, have been derived from the same typical synthesis which has achieved hexa-symmetric multipods and star-shaped NC fabrication—forms which may fit the bill. These nano-stars were developed for their

in-situ source of sulfide ions, of TAA, while in the presence of the cationic surfactant, CTAB. The PbS NCs show a well-defined star-shape with six symmetrical arms, arranged along the <100> direction with separations between opposite tips being ~210 nm. With an increased yield of nano-stars along with additional analysis, small areas of clustered multipods became interdigitated by spreading their arms into the joints of their neighboring multipods to form minor assemblies with active close-packing. Below, small zones of naturally occurring self-assembled 2D arrays are visible in Fig. 3.26, inspiring further theoretical work to be achieved for PbS nanoscale star-shaped multipods from a monolayer 2D array.

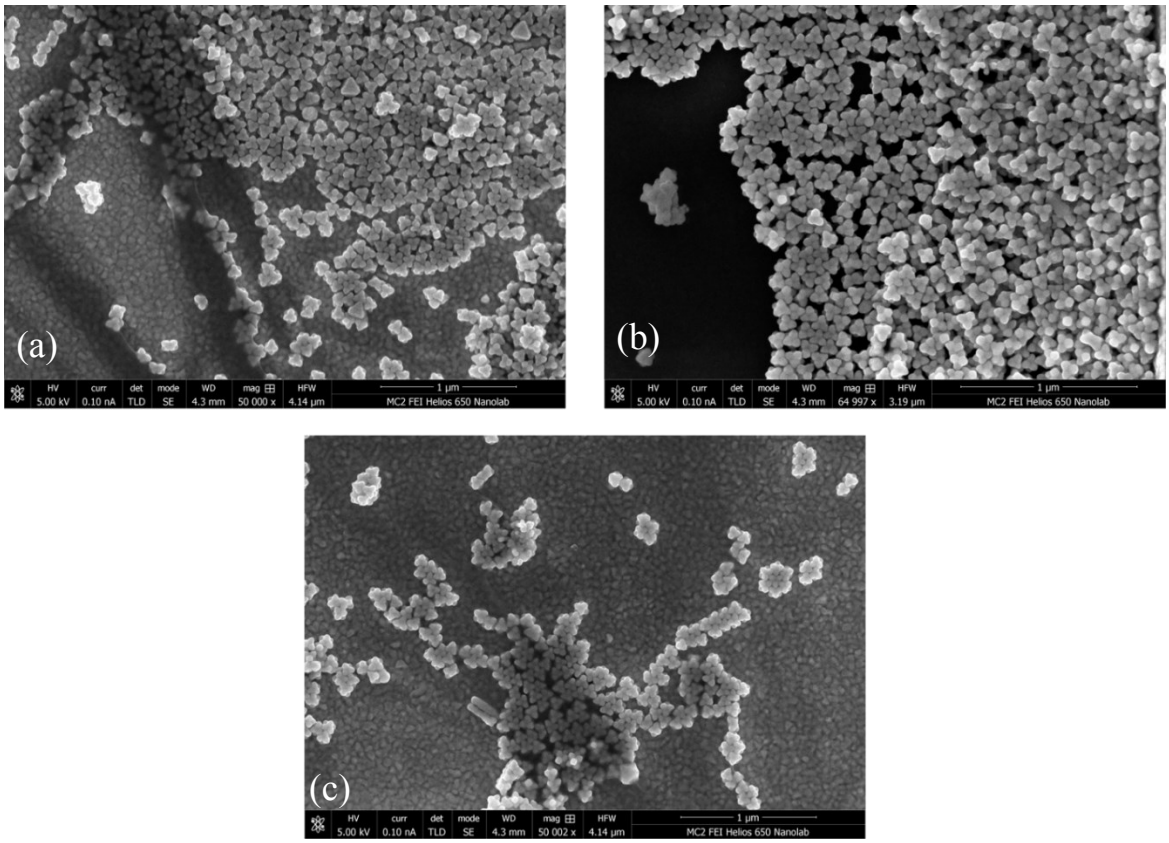

Fig. 3.26 | SEM images of PbS octahedra in a loosely interdigitated structure throughout the sample. (a) Primarily one layer of PbS octahedra self-assembled across an SEM sample holder. (b) 2-3 layers of PbS octahedra self-assembling atop a Si wafer with evaporated Au. (c) Few PbS octahedra self-assembled into occasional tightly interdigitated structures with neighboring NCs.

3.4.1.2.2 Closely Packed Arrays of PbS NCs

The method for preparing the nano-stars to assemble into several 2D or 3D arrays of *fcc* (or *hcp*) superlattices includes drop-casting a small volume of solution atop a silicon wafer and/or SEM sample holder, and then allowing the solution to dry in open air. While the aqueous solution evaporates, the NCs naturally adapt to ordered structures at a rate which can vary across different areas of the sample if the local concentration and temperature profile differs. In quantifying the packing information of these areas, the packing data should obey the following equation[185]:

$$d = \left(\sqrt{3}/_{2}\right) l - a \tag{3.4}$$

The distance a nano-star overlaps a neighboring nano-star, here, is defined as *a*, the distance between neighboring vertices in a single nano-star, *l*, and the center to center distance between neighboring nano-stars is *d*. When observing the PbS nano-stars we've fabricated, as in Fig. 3.27, SEM observations give values of ~86 nm for *d*, ~95 nm for *l*, and ~1 nm for *a*, making all distances consistent with what has been seen. As hoped, the image also shows the acquired 2D and 3D assemblies of nano-stars self-assembled into *fcc* (or *hcp*) arrays.

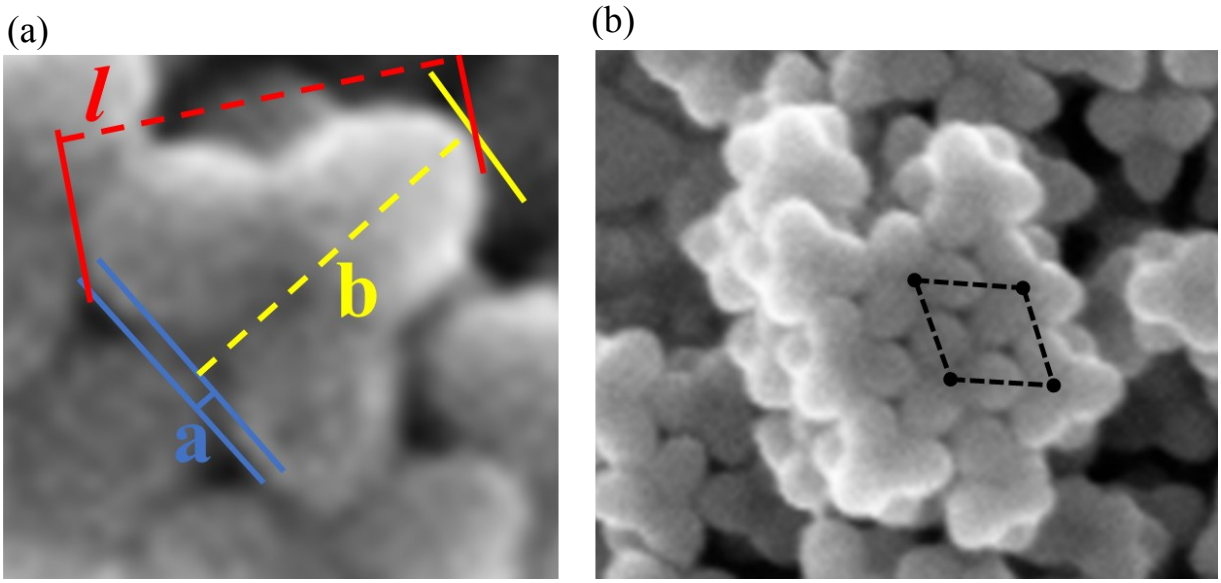

Fig. 3.27 | (a) SEM image displaying how PbS octahedra were measured with $d = \left(\sqrt{3/2}\right) \cdot l - a$. (b) SEM image showing several PbS octahedra interdigitated and closely packed in small structure.

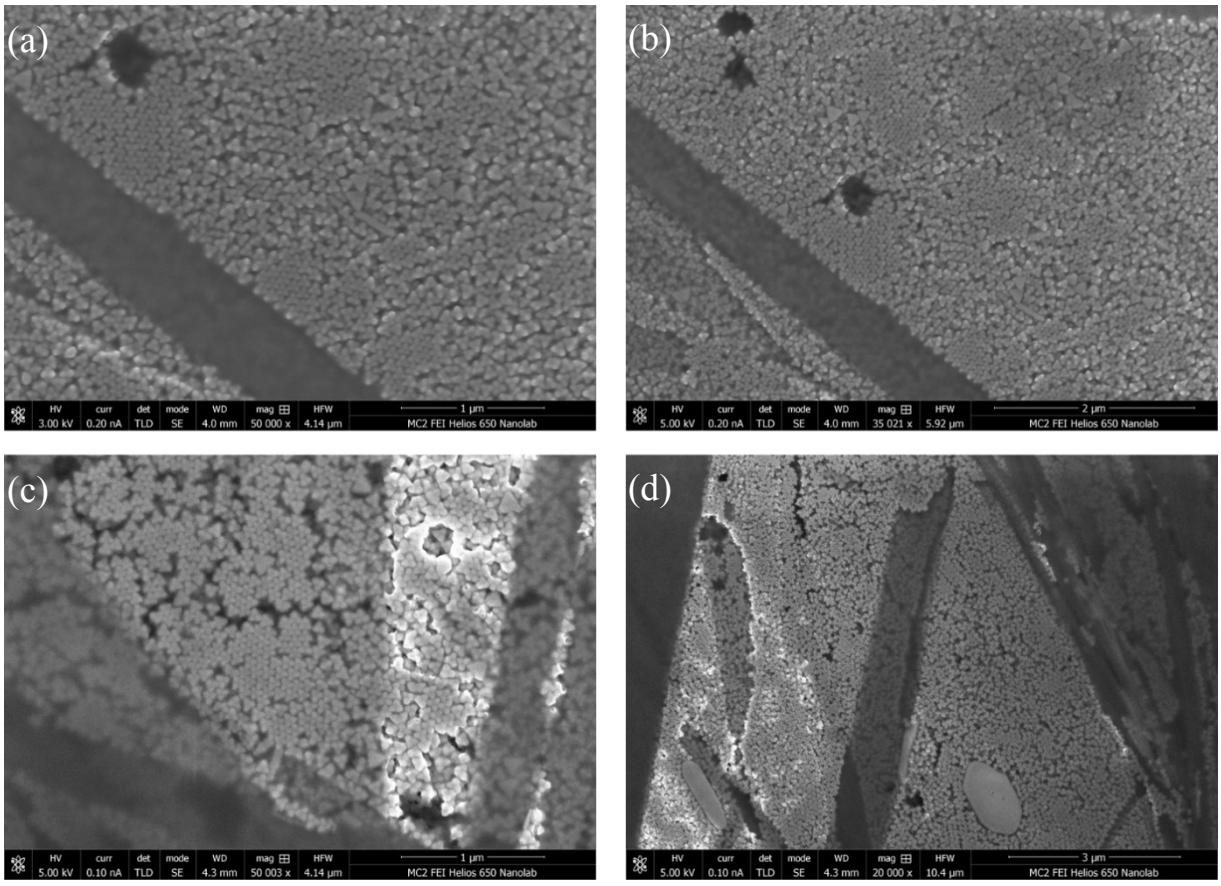

Fig. 3.28 | Low-resolution SEM images of PbS octahedra heated to (a & b) 75 °C and (c & d) 80 °C during the self-assembly process.

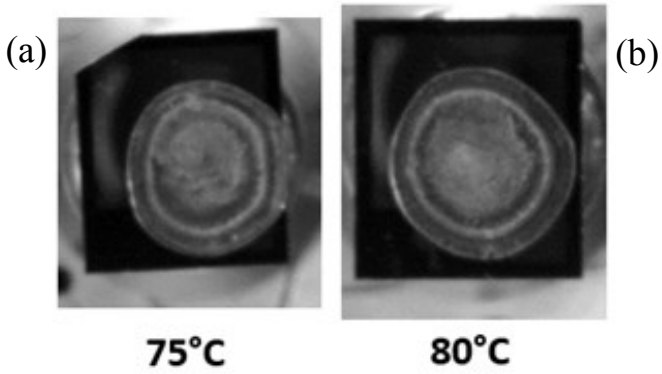

Fig. 3.29 | Optical images of Si wafers heated to (a) 75 and (b) 80 °C with colloidal solution of PbS octahedra on top during the self-assembly process.

Since the NCs were passivated by a surfactant, repulsive electrostatic/steric interactions that supported close-packed structures can dictate the PbS assembly. In this environment, surfactants at the interface between the aqueous solution and the outside surfaces of the NCs retard the efficiency with which NC stream openly into the aqueous solution to form stable NC regions. The resulting self-assembly has then begun by dissipation of the solution through heating. This dissipation enhances the coverage of the NCs, which initiates the noncovalent interactions and self-assembly to create superlattices. In this cycle, self-assembly is based on a subtle balance between entropy claims and van der Waals attractions between NCs and their ligands' hydrocarbon chains placed on the NC surface. By way of aggregation, the surfactants' hydrocarbon chains naturally interdigitate with the hydrocarbon chains of the primary ligands located along the outer surface of the NC assemblies through hydrophobic-hydrophobic and van der Waals interactions. The resulting colloidal NC superlattices can then be well distributed in an aqueous solution to then be collected and purified by centrifugation and filtration. In our experimental case, the concentration of the surfactants in the PbS dispersions was strong enough to make particles positively charged and stable in water, which is important for the creation of 2D and 3D assemblies, as stated earlier. However, within the process of eliminating excess precursors and washing NCs with deionized water several times, a standard practice in our NC clean-up process, the PbS nano-stars may ultimately have less than an adequate amount of surfactant coating. This may lead to disarranged collections of NCs due to the more prominent van der Waals attraction and absence of oppositely charged ions which were initially absorbed along the NC surface.

In addition to an adequate surfactant concentration, heating is also required to remove organic solvents, thereby increasing the NC concentration, inducing the process of self-assembly via

increased NC interaction rate. Typically, the temperature should be greater than the solvents' boiling point and lower than that of water. In order to prepare ordered superlattices, higher temperatures (> 70 °C) are ordinarily utilized because the thermal energy enables the adjustment of the NCs spatial positions and counteracts the loss of configurational entropy. Otherwise, once the temperature decreases to ~40°C, random superlattices are acquired due to the thermal energy not being sufficient enough to defeat the deficiency of configurational entropy.

Experimentally pinpointing an optimal temperature for evaporating the aqueous solution, heating the Si wafers at ~70 °C was sufficient for self-assembly from preliminary results. Using a study across a range of temperatures (60, 65, 70, 75, 80 °C), the most long-ranged self-assembly was encountered at 75 and 80 °C. As hoped, maintaining a temperature of ~70 °C for the PbS aqueous solution to be evaporated while on Si wafers affected the self-assembly of the final products. Figure 3.28 shows the SEM image of a sample holding a high yield of nanoscale star-shaped multipods. Several locations appear to experience interdigitation with neighboring NPs, notably with a consistent grey color, while the surrounding areas encounter multipods randomly aligned in various directions visually seen with white hints along the grey areas throughout. These images show the potential within forming nanopatterns through nanoscale star-shaped multipods. Though there seems to not be enough surfactant in coating the multipods, further modifications can present larger superlattices of interdigitated NPs. This discovery brings us further to creating optoelectronic devices using these star-shaped multipod PbS NCs.

3.4.2 TOP-PbSe Nanocrystals

TEM micrographs of the PbSe NCs for the single injection method display spherical, octahedra and star-like shapes as seen in Figs. 3.32 and 3.34. Figure 3.30 shows the absorbance spectra of PbSe NCs synthesized with a spherical shape from the steps and described procedure in Section 3.1.2.2. The PbSe NCs absorbed at wavelengths of ~1064 and ~1186 nm for PbSe NC samples 120414 and 12815, respectively. Considering the band gap energy, E_{bg}, can be determined very precisely from absorbance measurements, the common equation for calculating the energy of a photon results in bandgap energies of 1.16 ± 0.08 and 1.05 ± 0.08 eV for PbSe 120414 and 12815, quite far from that of bulk PbSe ($E_{bg} \approx 0.28$ eV).

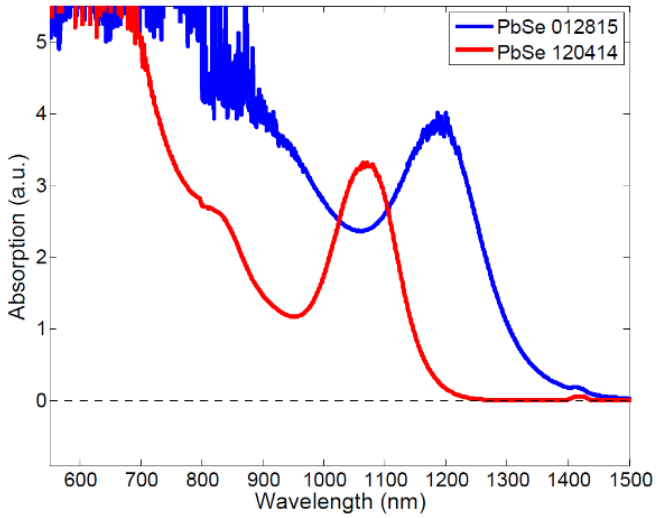

Fig. 3.30 | Absorption spectra of successful solvothermal syntheses for TOP-PbSe NC fabrication. Absorbance peaks reside at 1186 nm (blue) and 1070 nm (red).

With the help of the ImageJ program (https://imagej.nih.gov/ij/), NC sizes and size-dispersions can be measured. This sharpness of the first exciton peak in Fig. 3.30 indicates that the size uncertainty is small. This is confirmed in the TEM micrographs that yield a low size dispersion

due to average diameter sizes of 3.5 ± 0.4 and 3.9 ± 0.6 nm, respectively, for the spherical PbSe NC samples 120414 and 12815. The corresponding FFT pattern confirms the d-spacing of the spherical PbSe NCs to be 2.95 ± 0.02 nm. Noting that the TEM micrographs in Fig. 3.31 each show the self-assembly of many hundreds of spherical PbS NCs, the images show that the NCs exhibit short- to mid-range directional ordering at various angles, as seen in Fig. 3.31 (a, b), with the samples only being fabricated from drop- and dip-casting toluene-based colloidal solutions onto TEM copper-mesh grids. Here, we witness PbSe NC distributions in cluster format along specific areas of a TEM grid, displaying NC orientations to be in random directions.

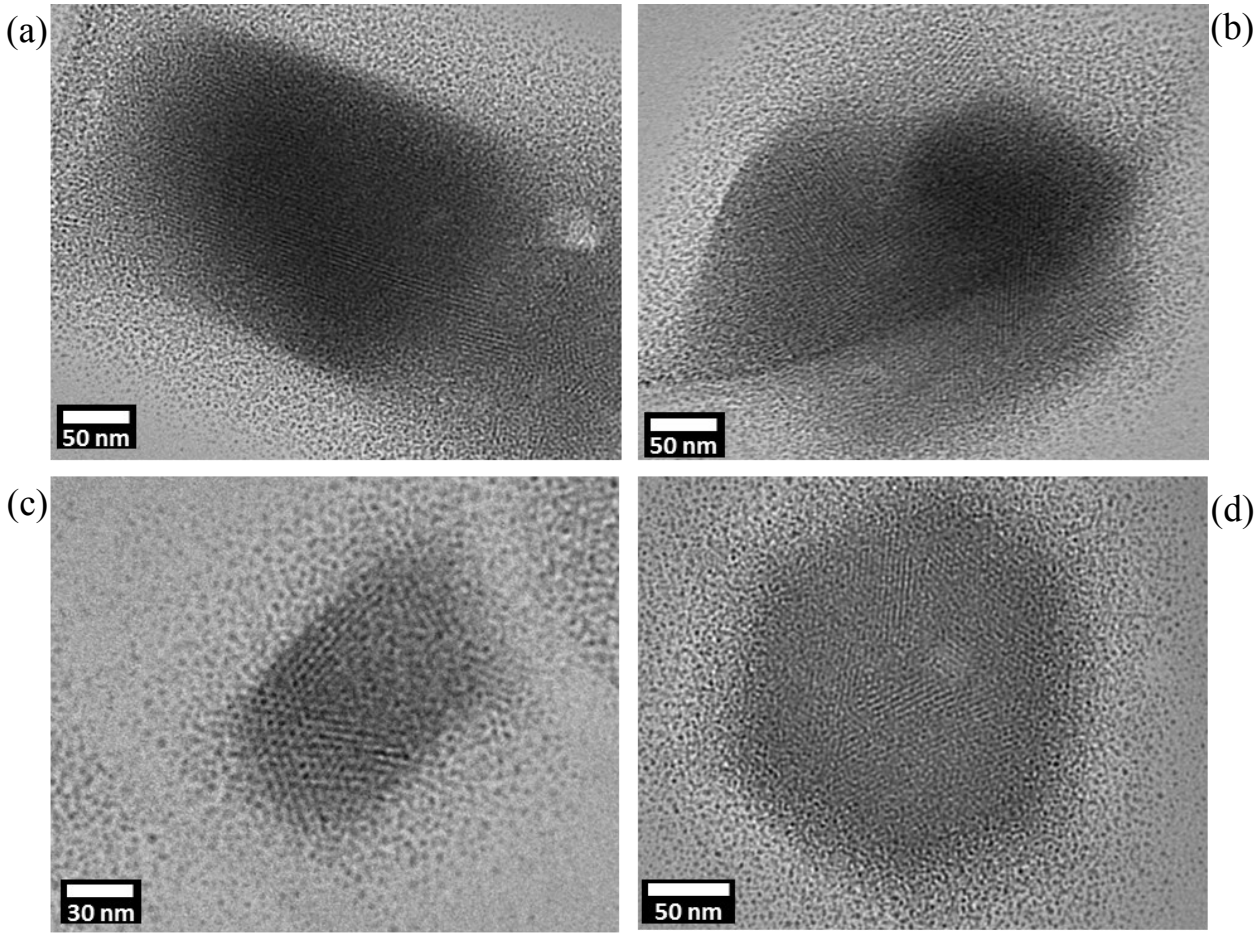

Fig. 3.31 | TEM images of spherical PbSe NC samples. (a) Primarily one-directional ordering with the NCs forming interconnection with several visible lines throughout the darkened areas of the micrograph after dip-casting. (b) Multi-directional NC ordering along the darker regions of the micrograph after dip-casting. (c) Small NC clusters still holding multi-directional ordering after dip-casting. (d) Multi-directional ordering while the superlattice still conforms to the shape of a hexagon after drop-casting.

Several sections within the imaging of PbSe NC sample 120414 were investigated and shown in the STEM images of Fig. 3.32. The overall size of several NCs and the occasional directional NC ordering is clear to see throughout the micrographs. This was the first sample to show minimal interparticle spacing, along with excellent average size distribution. An almost closely packed superlattice exists in some locations, while in others interconnectivity exists as NCs form clusters with the occasional fuzziness in the micrographs due to beam focusing with TEM.

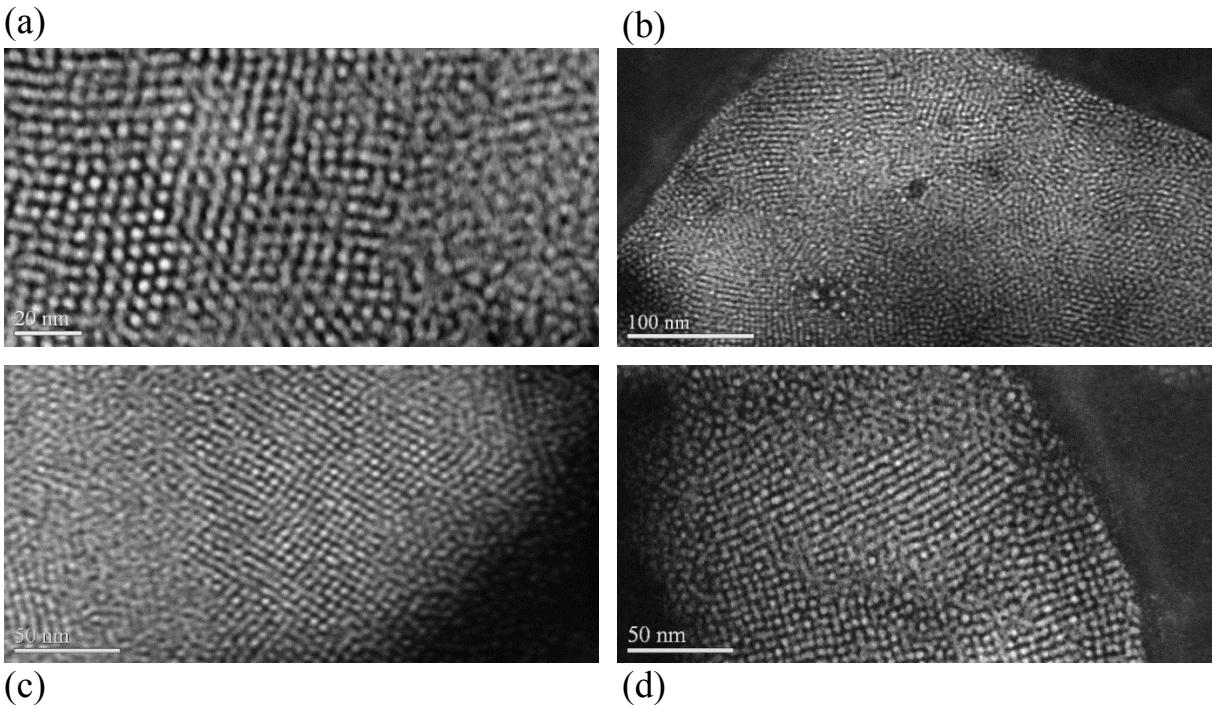

Fig. 3.32 | STEM images of spherical PbSe sample 120414. (a) High-resolution image displaying well-defined NCs in occasional short-range multi-directional ordering NCs along with

areas of NC clusters. (b, c) Micrograph showing PbSe NC superlattice along copper border of TEM grid. (d) Displaying streaks of NC; overlapping NCs forming straight/curved lines throughout.

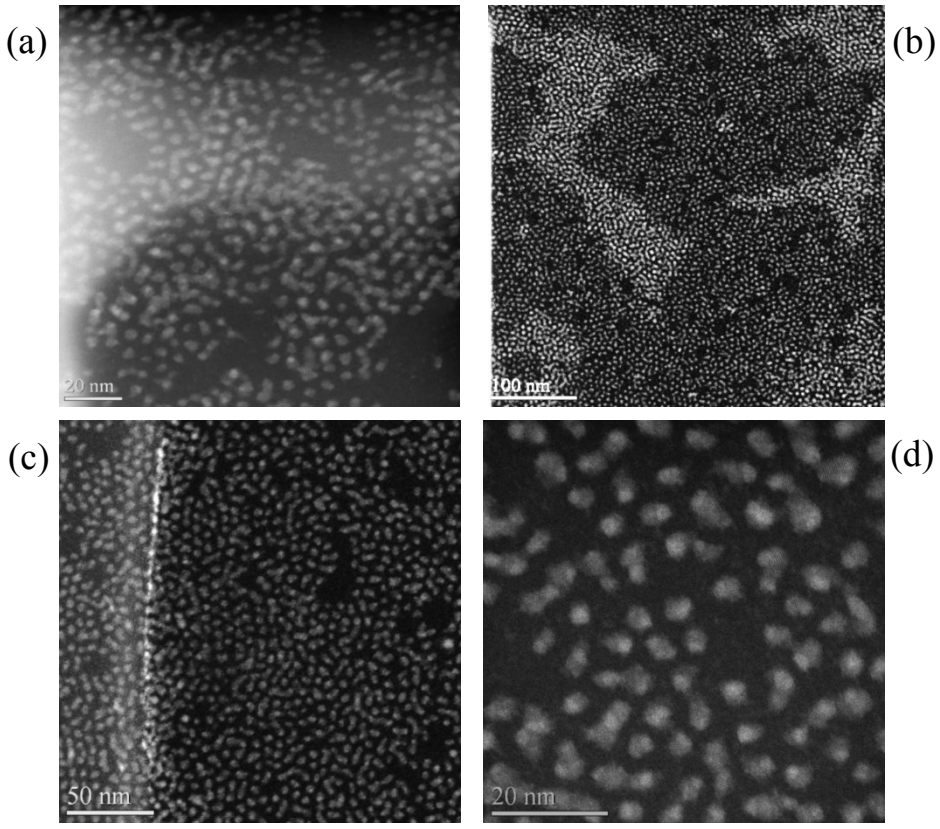

Fig. 3.33 | STEM images of non-spherical PbSe NC sample 12815. (a) After drop-casting, the micrograph shows a strong case of non-uniformity. (b) Low-resolution image of mono- and multi-layers of selected area, after drop-casting. (c) Dip-casting copper-mesh grid into colloidal solution. (d) High-resolution image of the non-spherical NCs within the PbSe colloidal solution, after dip-casting.

Though absorbance spectra from both PbSe samples show good results, TEM images of PbSe NC sample 12815 help validate the relative broadness of its absorbance peak. Despite the irregular shape of the NCs within this sample, the d-spacing of the NCs was still collected through TEM imaging with FFT patterns, confirming the d-spacing of the non-spherical PbSe NCs to be 3.72 ± 0.04 nm. Table 3.1 lists the overall shape and conditions for several experiments involving this

synthetic approach. Both the spherical and non-spherical PbSe batches are representations of the synthesis carried out at the lowest and highest temperatures. The rest of the PbSe samples, however, failed at the task of either fabricating spherical NCs or forming a somewhat sharp absorbance peak. The absorption peak of sample 12815 provides an understanding of what is to be expected with star-like samples, seen in Fig. 3.34. The PbSe NC samples holding star-like structures are seen in the red squares of Fig. 3.34 (a, b), where lone NCs come across as having the octahedron shape, while Fig. 3.34c holds what looks to be a six-point star, as the darkened circle in the middle of the four perpendicular arms seems to be the arms pointing out of the frame.

Table 3.1 | Synthesis of PbSe NCs at various reaction conditions – growth temperature (T_{Gr}) and growth time (G_T); downsized synthesis for samples 30615 and 21716-2.

PbSe Sample #	$Pb(Ac)_2$ (g)	PE (mL)	OA (mL)	TOP-Se (mL)	G_T (min.)	T_{Gr} (°C)	NC Shape
120414	1	15	3.6	8	6	~134	nearly spherical
12215	1	15	3.6	8	24	~145	star-like
12815	1	15	3.6	8	12	180	non-spherical
30215	1	15	3.6	8	6	~143	star-like
30415-2	1	15	3.6	8	6	~148	star-like
30615	0.19	5	0.64	1.45	8	~148	star-like
21716-2	0.19	5	0.64	1.45	?	~147	nearly spherical

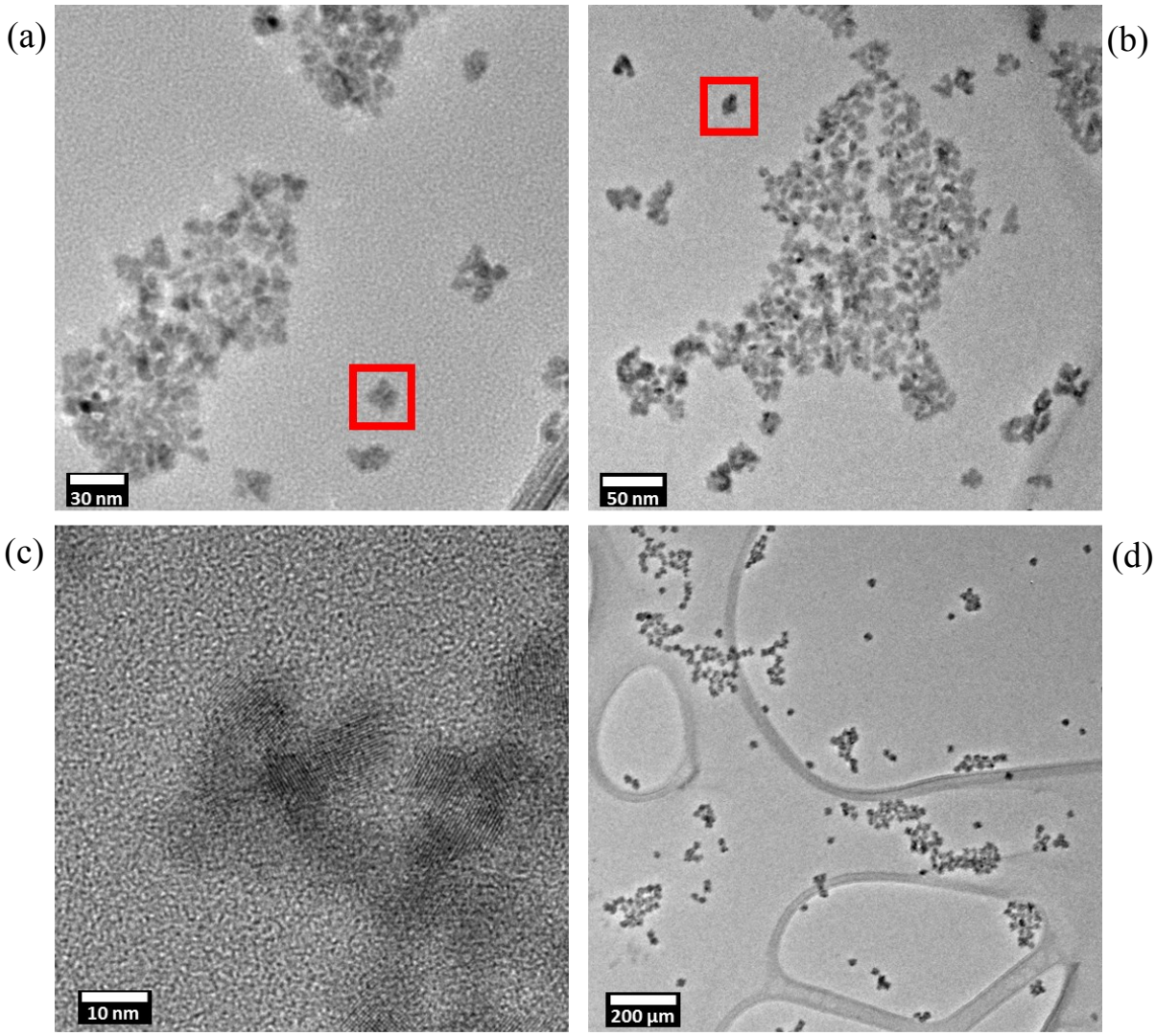

Fig. 3.34 | TEM images of non-spherical PbSe samples. (a & b) Samples PbSe 30415-2 displaying occasional stand-alone star-shaped NCs along various areas of the grid. (c) HRTEM micrograph showing a star-shaped NC along the edge of a cluster from sample PbSe 30615. (d) Low-resolution image still displaying small star-shaped NCs throughout.

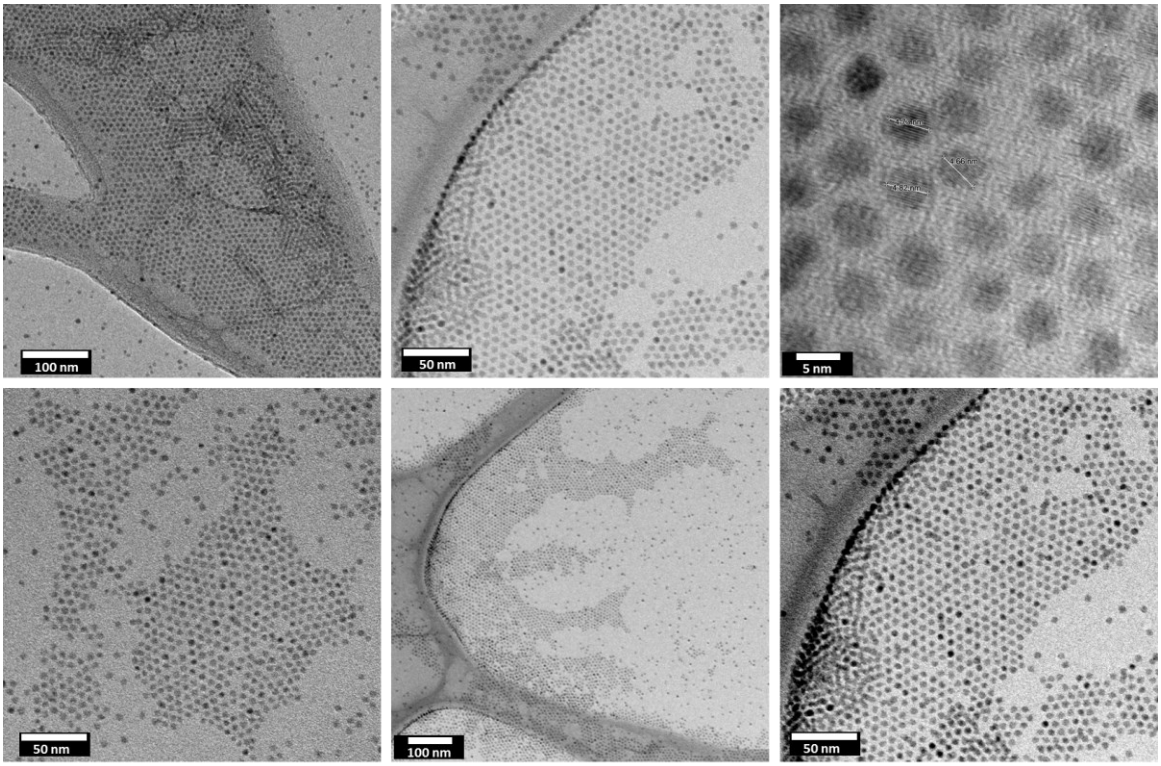

Fig. 3.35 | TEM images of spherical-shaped TOP-PbSe NCs. All images reveal a randomized ordering while NCs experience interparticle spacing after the self-assembly process ends and solvent is evaporated.

Aside from interconnections with the NC self-assembled structures, there were also structures of interparticle spacing ranging from 0.5 – 2.3 nm. The NCs are typically drop-casted atop a copper mesh TEM grid and allowed time for solvent evaporation for self-assembly to take place. This drop-casting results in the same type or randomization throughout the images seen above. Interparticle spacing may exist here with oleic acid playing a major role while other chemicals/ligands were removed from during the clean-up procedure. Ideally, one would want to reduce the interparticle spacing while maintaining the nearest neighbors associated with a close-packed structure. However, preserving structural order after doing something such as ligand

exchange in a thin film is challenging due to the large reduction in (colloidal) lattice constant associated with the removal of bulky ligands in an NC thin film.[195]

The results of the PbSe synthesis pertaining to this section was carried out with the NCs not forming into a spherical shape consistently; however, naturally self-assembled superlattices show that spherically-shaped NCs can also result in long-range order. Nevertheless, the following synthetic and experimental designs to further reduce the interparticle spacing resulted in a lack of reproducibility to the degree to which the interconnected NCs had minimal gaps across large volumes.

3.4.3 TOP-PbSe NC Syntheses with DPP

3.4.3.1 TOP-PbSe NC Synthesis: Single Precursor Injection with DPP

3.4.3.1.1 Results & Discussion

The TOP-PbSe synthesis involving a single injection including DPP (Section 3.1.2.3) yielded the following results.

The TOP PbSe synthesis pertaining to single injection DPP was studied by varying NC growth periods, growth temperature as well as through optical characterization. In addition, the role of OA was partially studied with a variation in the amount going into the synthesis during the last few experiments, as when induced by OA, it has been documented to show slow kinetics of a less

discrete, more prolonged nucleation event.[196] More detail of the fabricated PbSe NC batches can be seen in Table 3.2 and 3.3.

Table 3.2 | Synthesis of PbSe NC with the inclusion of DPP (diphenylphosphine). Synthesis runs primarily varying in growth temperature and overall growth time.

PbSe Sample #	T_{Gr} (°C)	PbO (g)	OA (mL)	ODE (mL)	TOP-Se (mL)	DPP (µL)	G_T (hh:mm)
41015-DPP	80	5.89	18	20	5	345	2:18
41715-1-2-DPP	156	5.89	18	20	5	345	2:00
50715-DPP	80	5.89	18	20	5	345	1:00
53115	80	5.89	18	20	5	345	1:00
60415	no heat	5.89	18	20	5	345	2:10
60515	~155	5.89	18	20	5	345	0:30
110315-DPP	165	5.89	13.5	20	5	345	0:20
22316	120	1.4725	4.5	5	1.25	86.25	1:00
92816		5.89	13	20	5	none	

Table 3.3 | Comparison of results from synthesis of PbSe NCs involving DPP (diphenylphosphine).

PbSe Sample #	1st Exciton Peak (nm)	Bandgap En. (eV)	NC Diameter + Std. Dev. (nm)	D. Spacing (nm)
41015-DPP	1557	0.796	4.8 ± 0.8	3.06
41715-1-2-DPP	1609	0.771	5.9 ± 1.2	
50715-DPP	1659	0.747	5.4 ± 0.9	3.01
53115	1604	0.773	4.7 ± 0.9	
60415	1404	0.883	5.1 ± 0.5	
60515	1542	0.804	4.9 ± 0.4	3.03
110315-DPP	1498	0.828		
22316			5.6 ± 0.7	
92816	1401	0.885	6.1 ± 0.7	3.08

In comparing the two PbSe NC sets, one being all syntheses carried out prior to PbSe 60415, there are noticeable changes in the shape of the absorption maxima when transitioning from broad to sharp indicating a decreased size distribution within the NC solution as well for all PbSe NC batches done on and after PbSe 60415 (batches possessing fresh PbO).

An establishment of how E_{bg} decreases as NCs increase in size is made as the fabricated PbSe NCs increase in size such that the band-gap approaches that in bulk with 0.27 eV.[196-197] With execution of this single injection synthesis including DPP, all PbSe colloidal batches experience no significant difference in the absorbance spectra. The peaks observed in Fig. 3.36 illustrate discrete energy levels found in sufficiently small NCs.[198] The noticeable discontinuity around ~1700 nm in each spectrum is due to a diffraction grating change in the spectrophotometer. All syntheses before PbSe 60415 display peaks centered around ~1606.6 nm, on average, revealing broader size distributions as the peaks possess dull maxima with wide ranges.

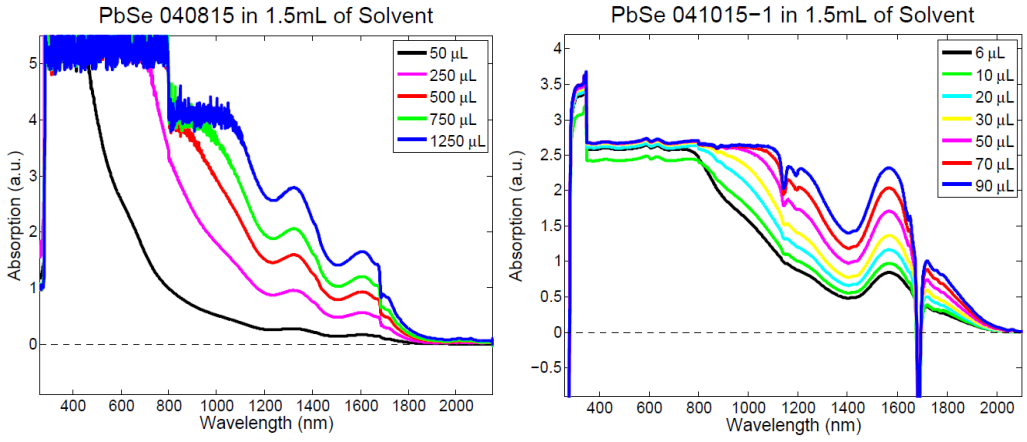

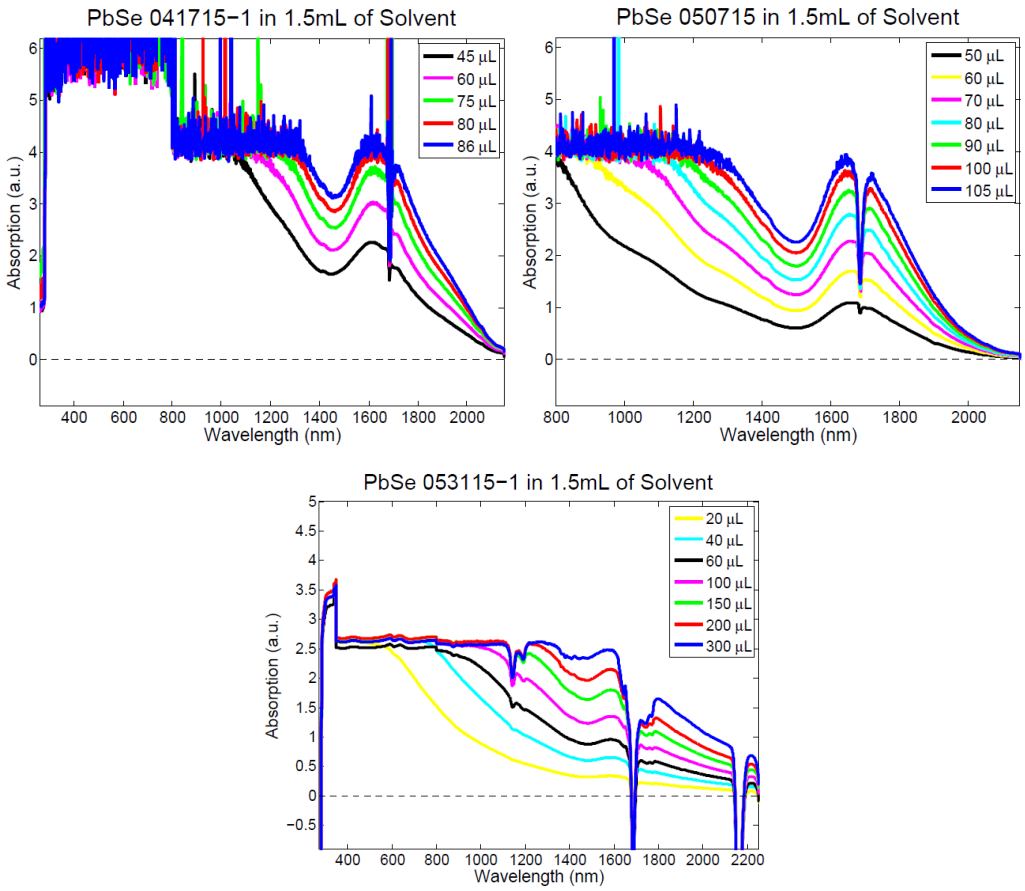

Fig. 3.36 | Absorption spectra from PbSe NCs syntheses involving DPP (diphenylphosphine) (carried out on and/or before 60415), all showing broad absorption peaks.

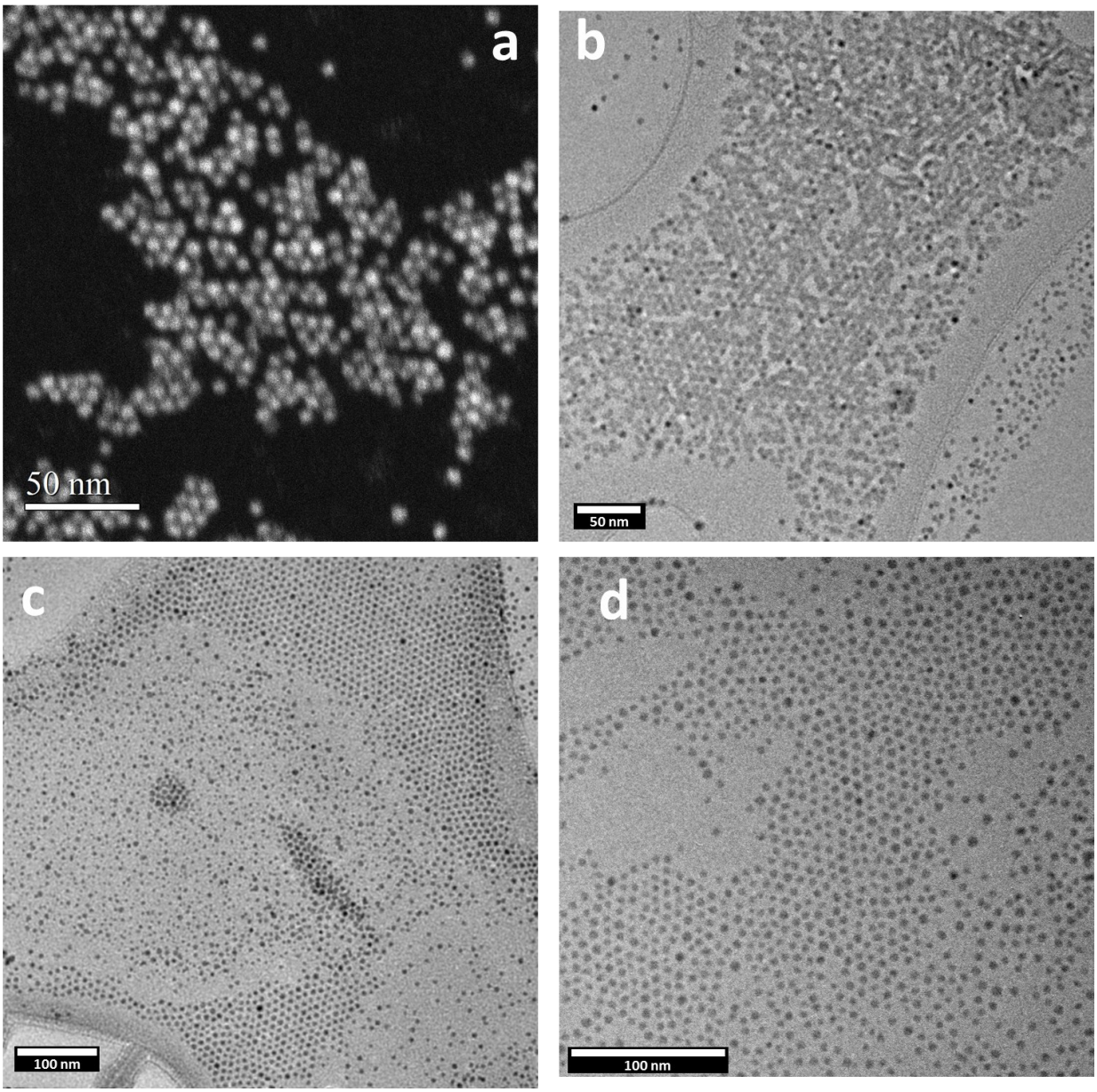

Fig. 3.37 | TEM micrographs of PbSe colloidal solutions with broad size distributions. (a) Scanning TEM (STEM) of PbSe 40815, displaying small clusters along the wide stream of NCs. (b) Highly concentrated area of PbSe 41015 NCs along the thick copper border of the copper-mesh grid, showing interconnectivity potential. (c) A very large super-lattice within PbSe 41715 as the NCs lay atop the copper borders within the copper-mesh grid. (d) NCs of PbSe 50715 in a large group, as they even go beyond the current visual frame in a monolayer throughout.

The absorbance spectra of PbSe 41015 did not lead one to believe, optically, the NCs would align and interconnect on the thicker regions or the copper-mesh grid, as seen in Fig. 3.37b. In efforts to repeat the phenomenon, the synthesis was duplicated and then modified by temperature and growth time for chances of improvement with uniformity in PbSe samples 41715-2 and 50715. However, interconnectivity by way of bridging/necking never repeated itself through this synthesis.

As expected, the TEM images of Figs. 3.37 validates the spectra's broadness at the maxima and width for all samples fabricated prior to PbSe 60415, as their E_{bg} range from 0.74 to 0.88 eV for PbSe NCs ranging from 4.7 to 6.8 nm in diameter. Comparing samples fabricated on and after PbSe 60415, the absorbance spectra looks quite sharp throughout all samples, having E_{bg} ranging from 0.8 to 0.88 eV for PbSe NCs with diameters 4.9 to 6.6 nm. This can be seen in Figs. 3.37 and 3.39. Notice how all single injection syntheses ran on and after PbSe 60415 involve a new batch of PbO, which allows secondary exciton transitions to be visible (secondary humps in Fig. 3.38 for instance) with each synthesis when reaching growth times of $\geq$ 20 min in total, while the peaks are sited around ~1461.3 nm on average.

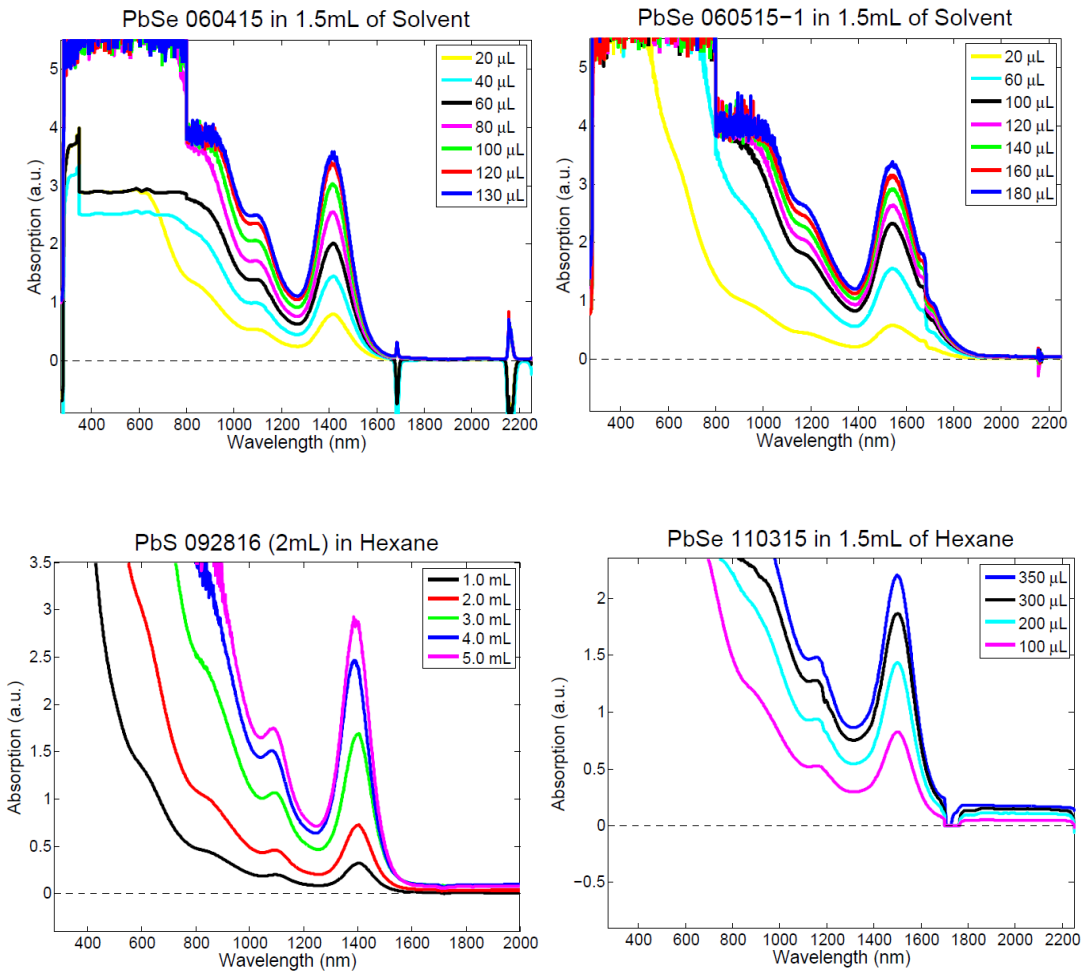

Fig. 3.38 | Absorption spectra from PbSe NCs syntheses involving DPP (diphenylphosphine) (carried out after 60415), all showing sharp/narrow absorption peaks.

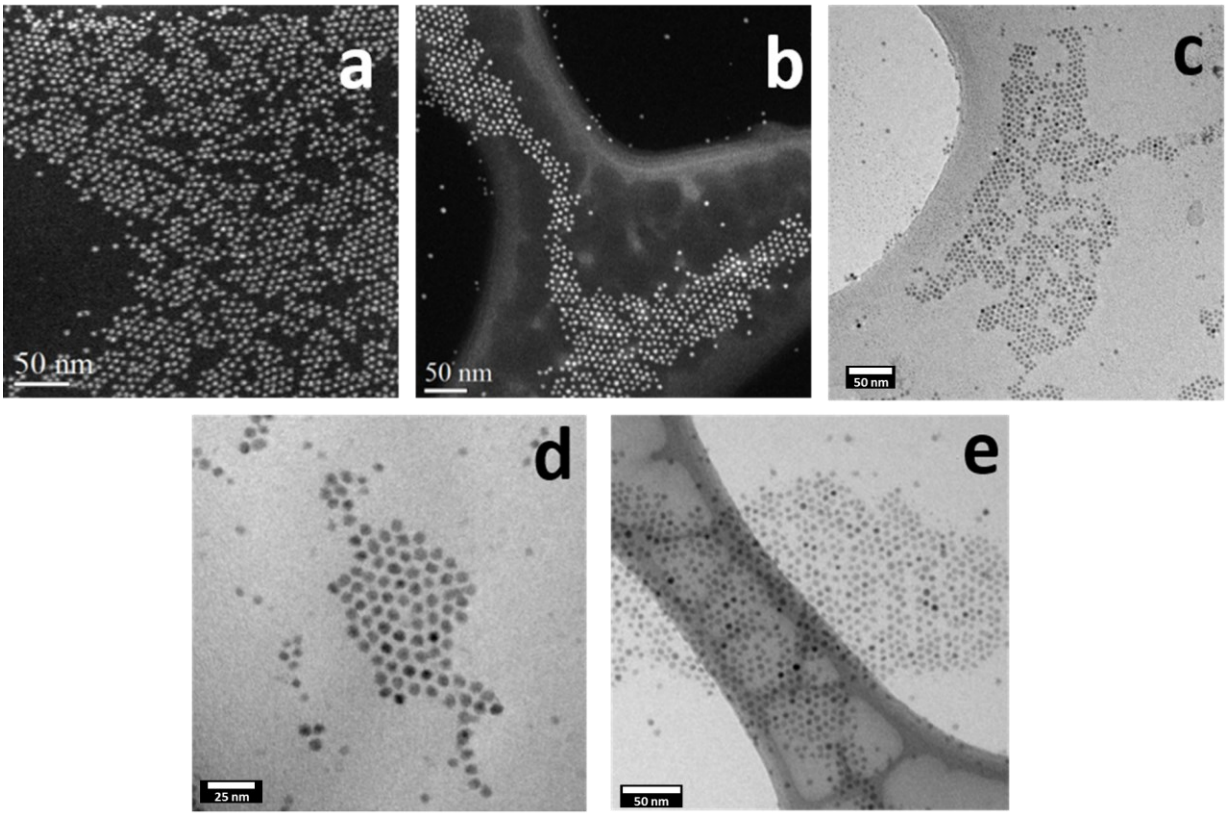

Fig. 3.39 | TEM micrographs of PbSe colloidal solutions with narrow size distributions. (a) Scanning TEM (STEM) of PbSe 60415, displaying a wide stream of disordered NCs. (b) A stream of NCs (PbSe 60515) primarily over the thick copper border of the copper-mesh grid. (c) A small area displaying PbSe 22315 NCs as the NCs lay atop the copper borders within the copper-mesh grid. (d) NCs of PbSe 92816 in a large group, as they even go beyond the current visual frame in a monolayer throughout. (e) NCs of PbSe 110315 crossing over thick and thin copper of the copper-mesh grid.

Though the NCs seen in Fig. 3.39 possess a smaller window of diameter size, there remains inconsistency in the overall NC size when fabricating PbSe NCs with this synthetic route as the NCs have a higher occurrence of disorder. More importantly from a device perspective, there exists gaps between the NCs because of the organic capping ligands, which can prevent effective transport. A consistent flow of NCs along thick and thin regions of the copper-mesh grid is apparent. Here, again lies the potential for interconnectivity within the NC clusters. Knowing there

is a need to connect NCs for the sake of nanostructural ordering within radiation detection devices, efforts to reduce the interparticle spacing was the next step, along with increased level of uniformity. Considering the amount/concentration of chemicals going into this single injection method, OA was suspected as possible culprit for this issue of interparticle spacing. As a way to reduce the size of the spacing, we incorporated more Se precursor. In doing so, we hoped to create a thinner OA capping ligand layer which surrounds each NC, results of which are discussed next.

3.4.3.2 TOP-PbSe NC Synthesis: Multiple Precursor Injection with DPP

The TOP-PbSe synthesis involving multiple injections including DPP (Section 3.1.2.3.2) yielded the following results. An evaluation of the relationship between band gap and size is validated.[196-197] With the execution of a multiple injection synthesis, the majority of the PbSe colloidal batches experience a slight blue shift in their absorbance spectra. The peaks observed here in Fig. 3.40 illustrate discrete energy levels found in sufficiently small NCs.[198] Again, the noticeable discontinuity around ~1700 nm in each spectrum is due to a diffraction grating change in the spectrophotometer. Secondary and tertiary transitions are visible with each synthesis reaching growth times of 10 min between injections rounds. Of all runs, two syntheses (yellow and purple lines), however, display broad peaks at ~1680 nm, revealing broad size distributions for both batches, however still larger NCs than the rest of the PbSe batches. The latest synthesis (green line) displays a double absorbance peak, with ~1518 nm in the middle, indicating a bi-modal size distribution, with two major NC sizes within the colloidal solution.

As expected from quantum confinement, the TEM images of Fig. 3.41 – 3.47 validates the slight blue shift within the absorbance spectra, which is away from the bulk of PbSe with E_{bg} ranging from of 0.73 to 0.86 eV for PbSe NCs ranging from 4.3 to 6.5 nm in diameter. More detail of the multiple injection PbSe batches can be seen in Tables 3.4 and 3.5.

Table 3.4 | Comparison of results from synthesis of PbSe NCs involving DPP (diphenylphosphine) and multiple injections of TOPSe-DPP.

PbSe Sample #	1st Exciton Peak (nm)	Bandgap En. (eV)	NC Dia. + Std. Dev. (nm)	D-Spacing (nm)
30617	1494	0.83	5.32 ± 0.53	3.05
32017	1641	0.756	5.65 ± 0.53	2.991
61717	1701	0.729	5.71 ± 0.68	3.013
62017	1677	0.739	4.92 ± 0.49	3.024
71017	1454	0.853	5.34 ± 0.41	2.925
81017	1565	0.792	4.29 ± 0.53	2.291

Table 3.5 | Synthesis of PbSe NC with the inclusion of diphenylphosphine and multiple injections of TOPSe-DPP.

PbSe Sample #	Total DPP Amt (μL)	TOPSe-DPP Inj. Amts (Each of 3 Rounds) (mL)	Time b/w Injs. (min)
30617	350	3, 2, 1.5	11, 10, 5
32017	350	3, 3, 3	17, 5, 5
61717	483	3, 2, 1.5	9, 7, 5
62017	350	3, 2, 2	11, 6, 9
71017	350 or 483	3, 2, 2	9, 10, 10
81017	350 or 483	3, 2, 2	9, 16, 24

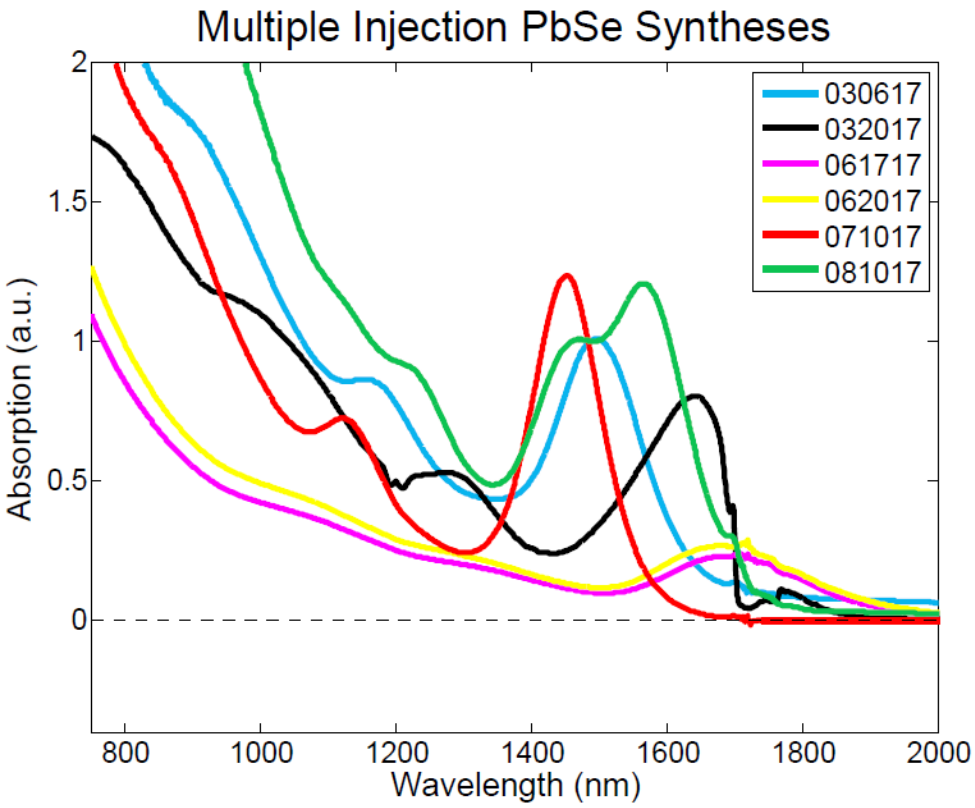

Fig. 3.40 | Collection of Absorption spectra from PbSe NCs syntheses usually involving DPP (diphenylphosphine) and multiple injections of TOPSe-DPP. Samples PbSe 30617, 71017 and 81017 all stand out with sharper absorption peaks than the rest.

Consequently, when inspecting both the single and multiple injection versions of this synthesis, it's reasonable to conclude the more Pb and Se precursors coming into the synthesis contributes to not only a higher yield, but it also may increase the chances for square ordering.

PbSe sample 32017 still shows interparticle spacing similar to single injection runs, however, in thinner areas of copper-mesh grid lines and/or chains of PbSe NCs form along with multilayers of NC thickness spread throughout the regions. High resolution TEM images of this sample show lattice fringes in various directions throughout the NC chain, showing NCs are laying across neighboring NCs to form this structure. PbSe samples 61617 and 71017 both also show multilayer

NC thicknesses, however, sample 71017 shows NCs along the thick copper regions of the TEM grid with occasional NC chains appearing in various places (Fig. 3.44 (a, f)).

Considering how the multiple injection synthesis is carried out in far less time than the single injection process, the additional injections must be playing a crucial role in increasing the number of NCs throughout the colloidal solution.

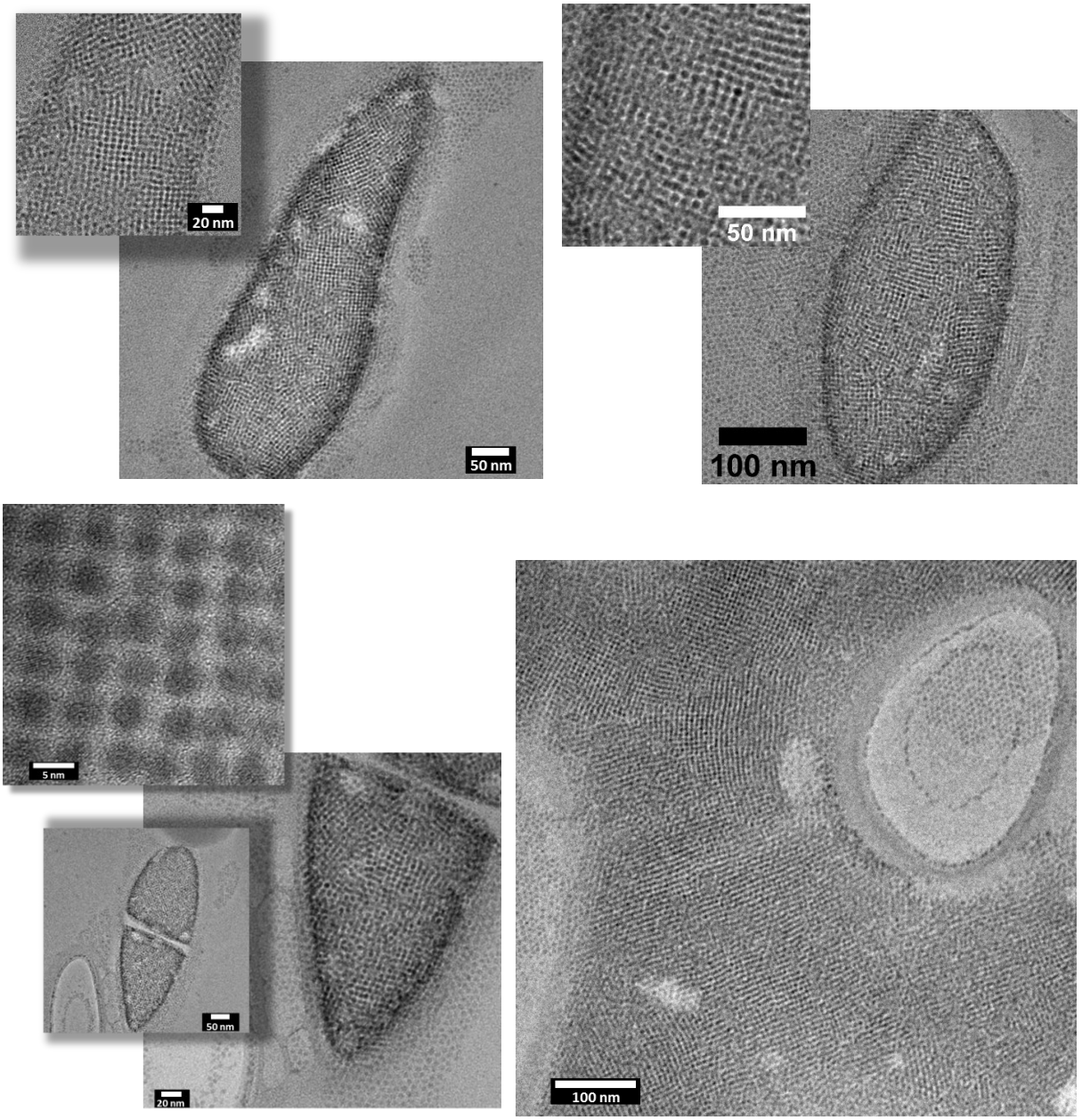

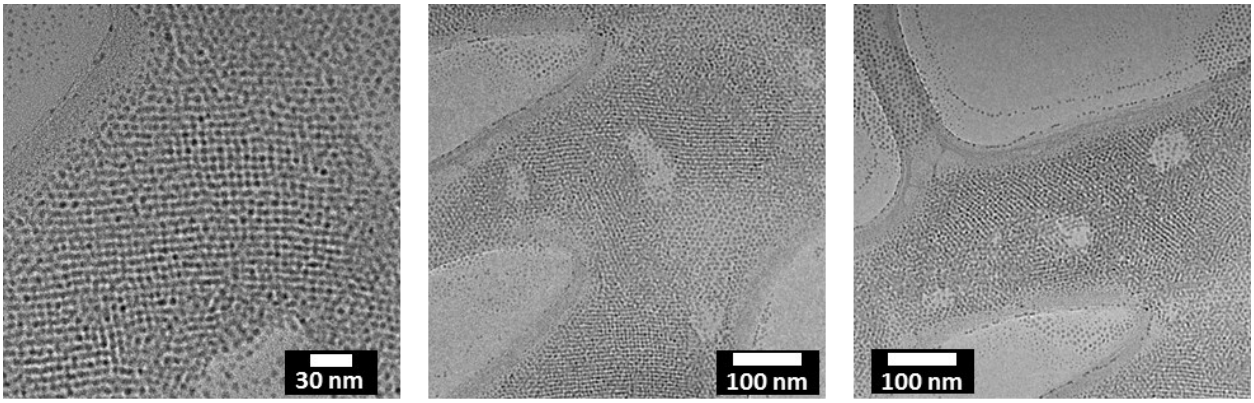

Fig. 3.41 | TEM micrographs from multiple injection synthesis sample PbSe 30617. All sample images are the result of dip-casting the copper-mesh TEM grid into so diluted colloidal solution.

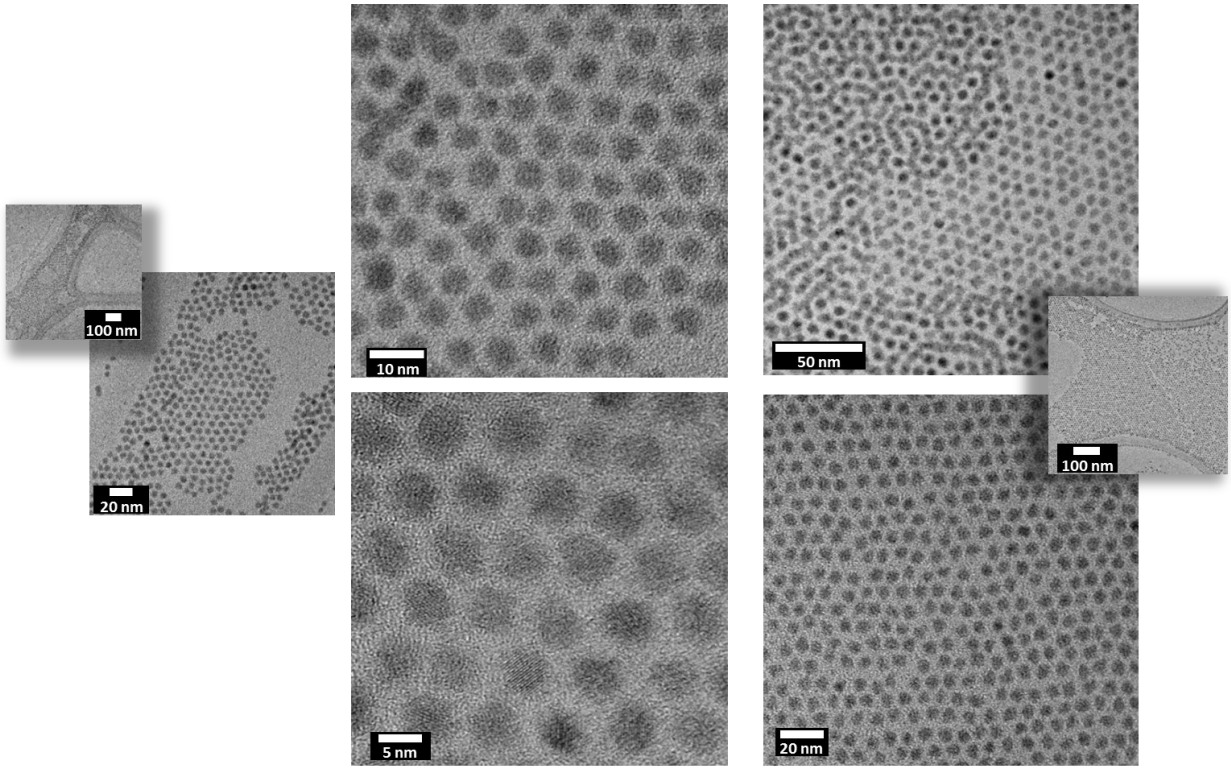

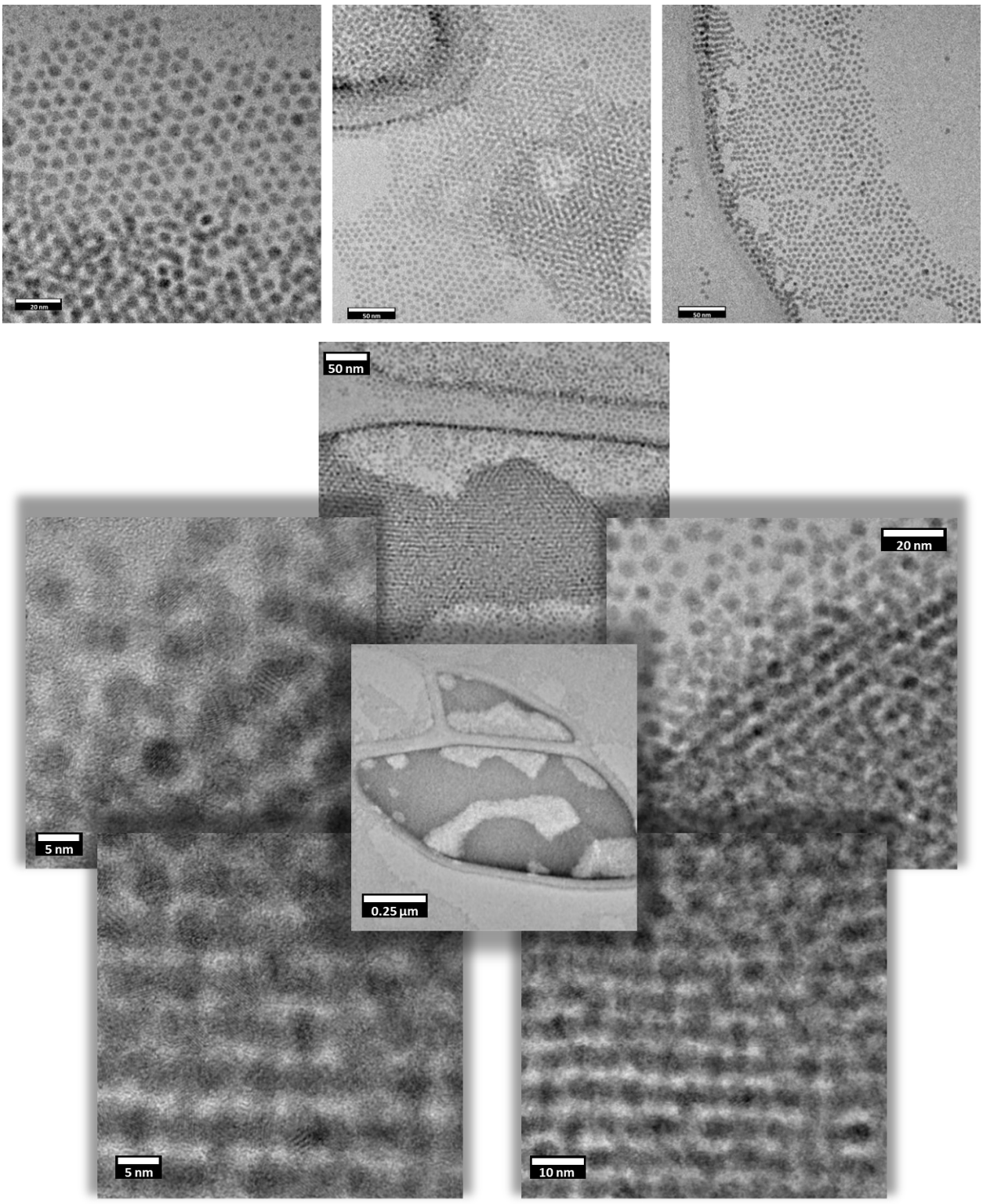
20 nm
50 nm
50 nm
50 nm
20 nm
5 nm
0.25 µm
5 nm
10 nm

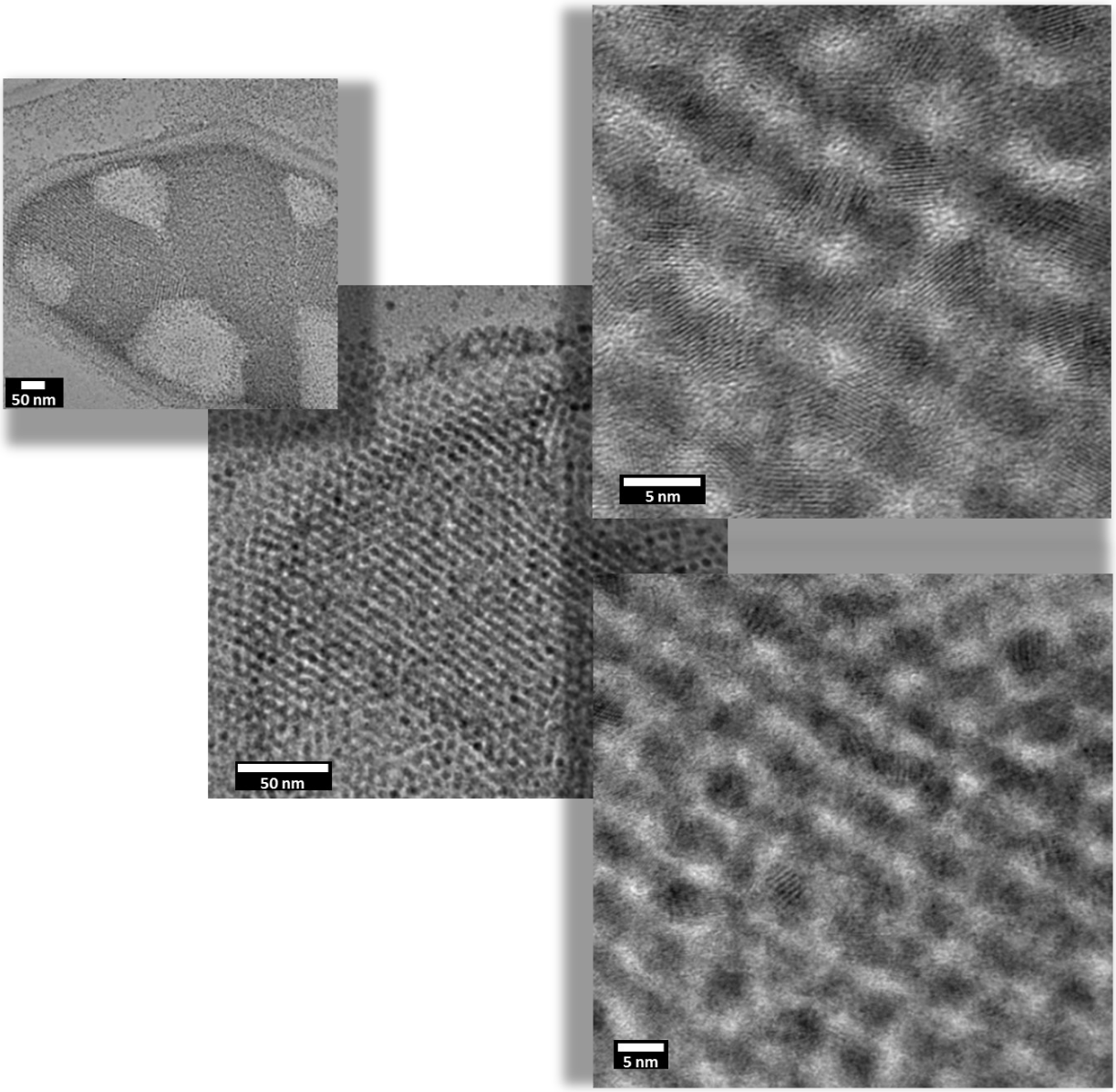

Fig. 3.42 | TEM micrographs from multiple injection synthesis sample PbSe 32017. All sample images are the result of dip-casting the copper-mesh TEM grid into so diluted colloidal solution.

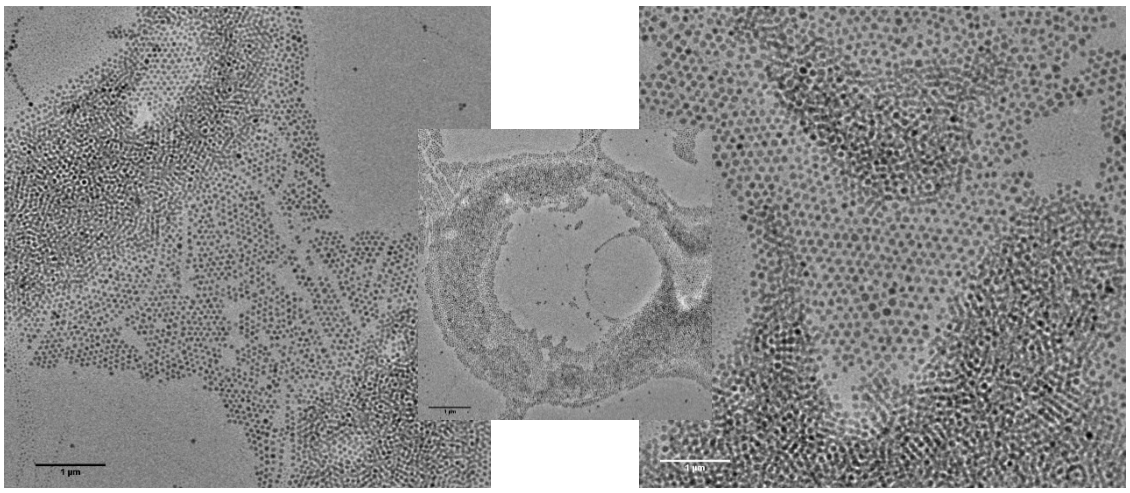

Fig. 3.43 | TEM micrographs from multiple injection synthesis sample PbSe 61617. All sample images are the result of dip-casting the copper-mesh TEM grid into so diluted colloidal solution.

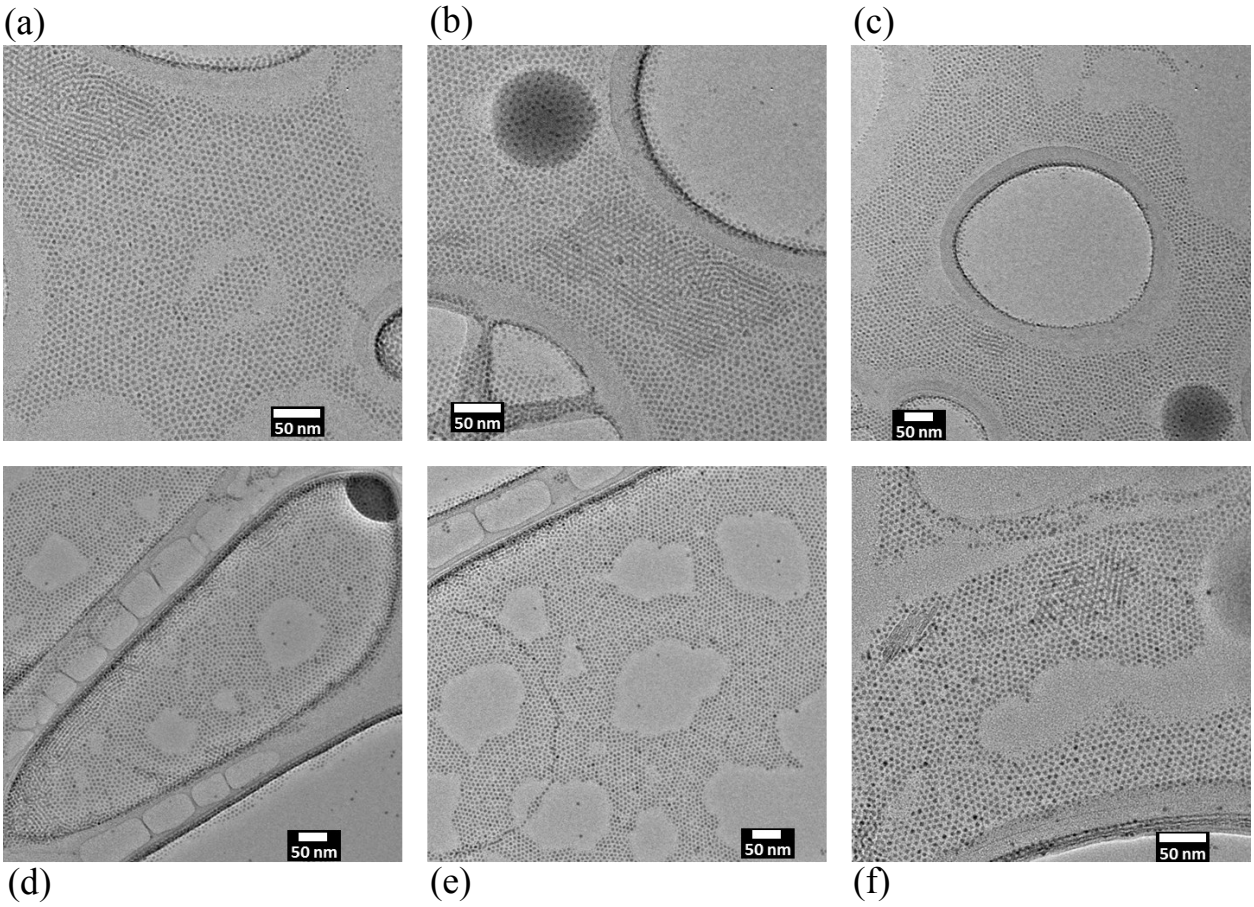

Fig. 3.44 | TEM micrographs from multiple injection synthesis sample PbSe 71017. All sample images are the result of dip-casting the copper-mesh TEM grid into so diluted colloidal solution.

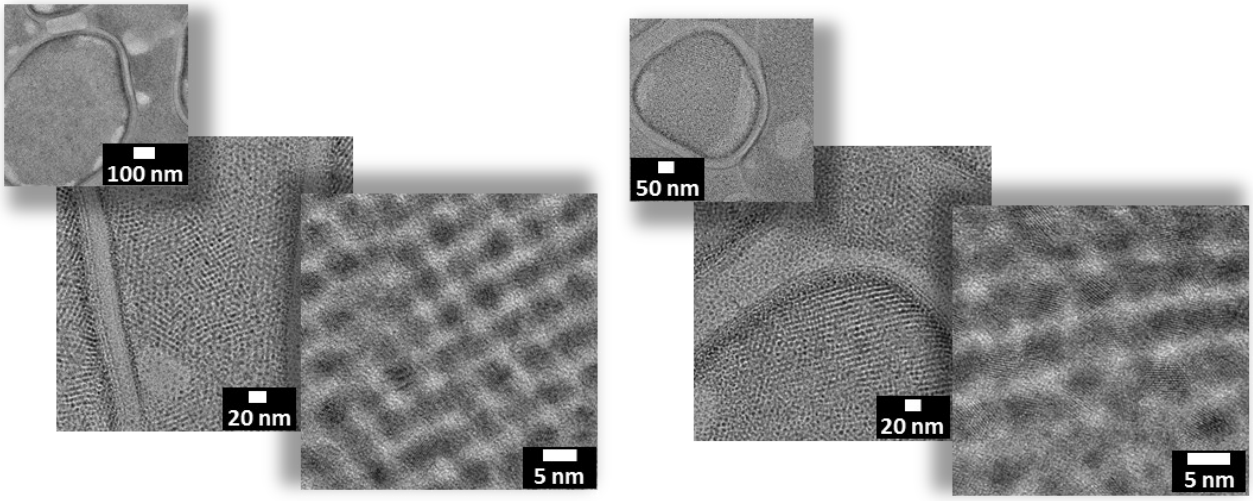

Fig. 3.45 | TEM micrographs from multiple injection synthesis sample PbSe 71017. Sample images here are the result of drop-casting diluted colloidal solution atop copper-mesh TEM grid.

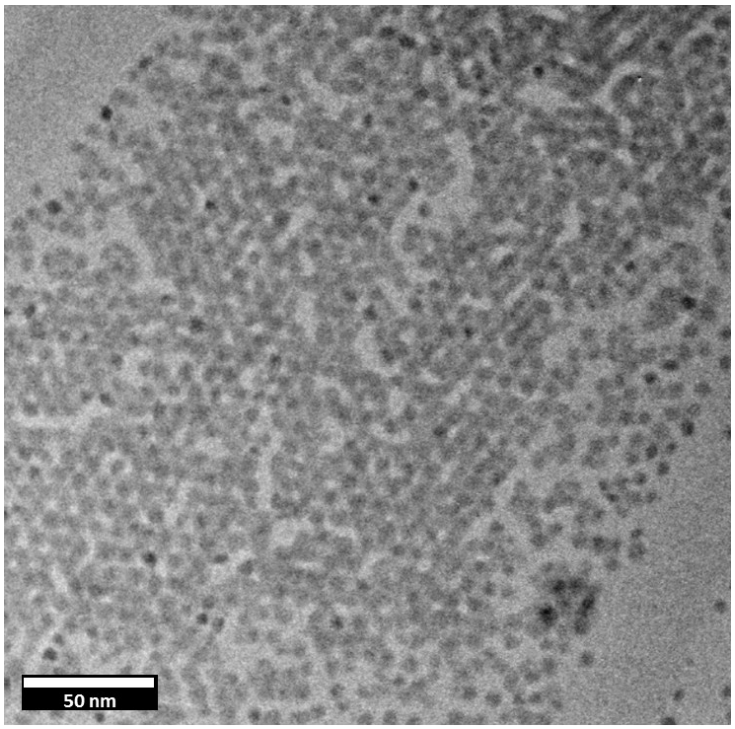

Fig. 3.46 | TEM micrographs from multiple injection synthesis sample PbSe 30617. Sample images here are the result of drop-casting diluted colloidal solution atop copper-mesh TEM grid.

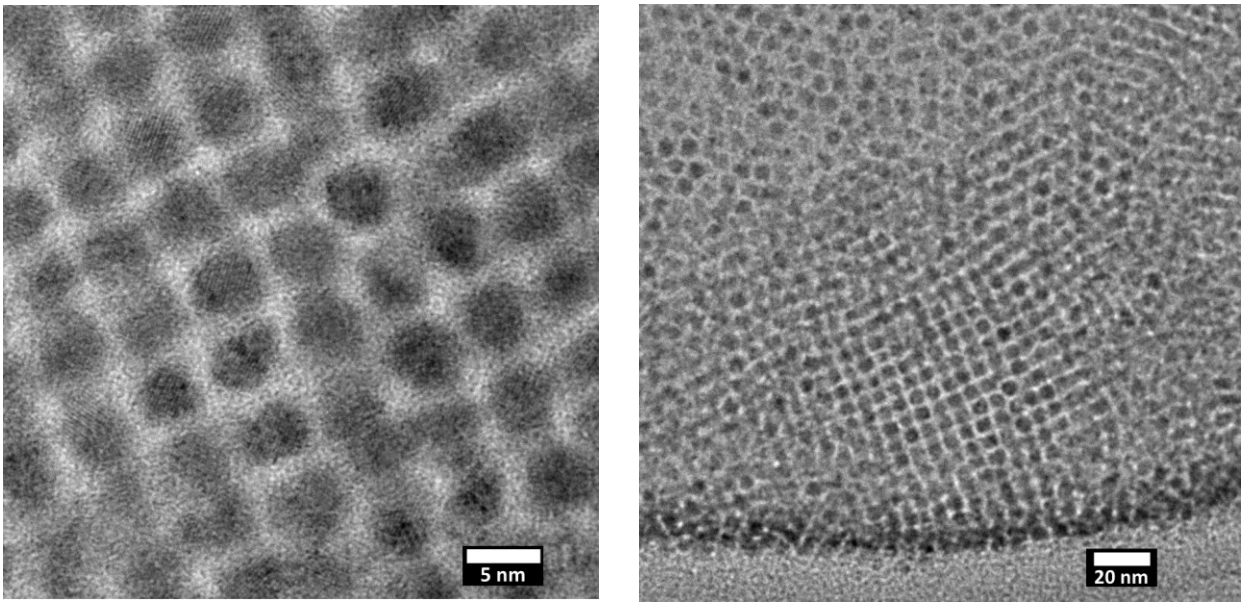

Fig. 3.47 | TEM micrographs from multiple injection synthesis sample PbSe 81017. Sample images here are the result of drop-casting diluted colloidal solution atop copper-mesh TEM grid.

With the increase in both Pb and Se precursors in this multiple injection synthesis, a noticeable difference is apparent when compared to only single injections. Figs. 3.45 – 3.47 (samples 30617, 71017, 81017) show cases of primarily square-ordering across various areas of the copper-mesh grids with sample 30617 showing self-assembly in various morphologies before full-on square ordering as in sample 32017. Since the nanostructural difference can vary across the TEM grid, this reflects the importance of NC colloidal concentration because different sections of the irregular copper-mesh grid are exposed to different NC concentrations during drying. Sample 32017 is still at a phase of hexagonal orientation, while 30617 experiencing square ordering. This is due to the rate at which the solvent being used to uniformly disperse the PbSe NCs, hexane, evaporates when drying the sample onto copper-mesh grid once drop-/dip-coating has been applied. The boiling point of hexane sits at a low value of ~156.2 °F, which can allow the solvent to evaporate rapidly on the grid. Consequently, this results in NCs finding their final position much

more rapidly (a few seconds) than for slower drying solvents. onset of greater nanostructural order depends on the NCs having a high degree of freedom to rotate into attractive facet/s of neighboring NCs and time to find that orientation. In general, hexagonal ordering can be easily repeated, as seen in 61617 and portions of 71017. Experimentally, hexagonal ordering is acceptable, but for the sake of fabricating a long-range interconnected NC-semiconductor, interparticle spacing will need to be reduced to induce particle-to-particle electrical coupling.

In observing Figs. 3.42, 3.43, and 3.46 (samples 30617, 32017, 71017), we notice NCs self-assembled in lines/streaks across the TEM frame in areas of high nanocrystalline concentration. HRTEM images show an overlap of NCs throughout these streaks by way of their darkened features. Visible NCs lattices and fringes can also be seen, pointing in randomized directions throughout. Here, interconnectivity is apparent.

TEM images of samples 30617 and 81017 both display PbSe NCs which have experienced extensive time going through physical transitional phases, adjusted into positions which favor facet attraction and/or Van der Waals interaction throughout certain areas. This process begins with the continuous degree of freedom with the help of the solvent, as Geuchies, J. J. *et al*.[199] and Whitham, K. & Hanrath, T. *et al*.[200] have studied the formation mechanism of two-dimensional (2D) square PbSe NC superlattices in situ and have showed NCs undergoing this remarkable sequence of phase transitions. During solvent evaporation, the NCs adsorb at the liquid-air interface without long-range order. As the NC concentration at the liquid-air interface increases, the adsorbed PbSe NCs align their atomic lattices and fuse into a hexagonally coherent region with a thickness of almost one NC,[201-203] like in Fig. 3.42. The NCs align to one of their {100} directions, opposite to the liquid-air surface. In favor of electrostatic and van der Waals interactions between opposite {100} facets, rotational freedom for the NCs is slowly diminished, resulting in a reduced NC-NC

distance. Due to the directionality of these in-plane {100} facet attractions, the superlattice changes its symmetry from hexagonal to square. Different superlattice geometries may also be obtained by adjusting the synthesis conditions, such as an immediate square superlattice geometry, where the NCs have a {100} facet pointing upwards, as in Fig. 3.41 (a, b, c) rather than the {111} facet for a hexagonal superlattice geometry,[203-204] in Fig. 3.47.

It is also of note that dip-coating revealed better results, versus drop-casting the colloidal solution to the copper-mesh grid. When comparing the two method for NC deposition, dip-coating gives NCs the chance to cover more area with a complete submerge. Once lifted out of the diluted colloidal solution a very thin solvent layer stays on the surface for the liquid/air interfacial interactions to occur. With drop-casting, the NCs still experience the liquid/air interface, however, an aliquot hemisphere chooses to have its solvent evaporate from the outside in. Meaning, the concentration of NCs increases as the solvent evaporates from outside then evaporation transitions to the center over time. In theory, the dip-coating process was fairly simple by angling the container of colloidal solution and allowing the copper-mesh grid to stay submerged for a small amount of time. However, this method came across as a more suitable approach for self-assembly of multiple thin film layers when the packing density isn't critical. With that said, the sample fabrication process for characterization was carefully carried out since errors could possibly cause thicker samples to appear throughout optical TEM imaging. This deposition method was heavily considered and carried out for the device fabrication process rather than for all TEM samples. The drop-casting deposition PbSe samples did manage to get NCs to self-assemble into square-ordering with much less inter-particle spacing versus the dip-coating PbSe samples. However, the dip-coated samples reveal NC chains, as seen in Fig. 3.42, something not witnessed in drop-coated samples.

The discussion above focused on a particular ligand (TOP) that coordinates the PbSe NCs. As shown above, if that ligand is removed via the synthesis and cleaning procedures described above, then ordering on the micrometer-scale can be achieved. However, when attempting to extend that ordering to the millimeter-scale, which is necessary to stop highly penetrating radiation, we desired a more dynamic ligand that facilitated the growth of square-ordered sections as shown above. The following describes the results of that transition, which resulted in a high yield of colloidal solids that operated as effective sensors.

3.4.4 TDP-PbSe NCs

Introduction

Lead chalcogenide NC-based optoelectronic devices derived from solution-based synthesis procedures offer the promise of facile manufacturing, simple device architectures, and enhanced control over the solid's thermal and optical properties via size and shape control of the nanocrystalline constituents. Known for its strong quantum confinement effects over a wide range of sizes due to its relatively large exciton Bohr radius (46 nm), PbSe has been heavily studied.[11, 129] For instance, the promise of high carrier multiplication efficiency in PbSe has inspired the use of PbSe-based optoelectronic devices ranging from photodiodes to photovoltaic cells.[72, 205-210]

If one can discourage thermal loss processes and preferentially de-excite above-bandgap carriers via carrier multiplication, which is typically termed multi-exciton generation (MEG) when quantum-confined materials are employed, then the conversion efficiencies of optoelectronic devices can be enhanced. A *phonon bottleneck effect* was predicted and observed to be particularly

prominent in semiconductor quantum dots (i.e. semiconductor NCs confined in three-dimensions).[80, 130, 211-213] Time-resolved spectroscopic observations of PbSe and PbTe carrier relaxation dynamics in Geiregat *et al.*[212] and Böhm *et al.*,[214] respectively, showed that carrier populations beyond the discretized energy states and into the condensed density-of-states energy manifold contained regions of transient stability, where the electron-phonon energy exchange rate could be restricted so that cooling rate of hot carriers could be diminished. The degree of which MEG can play a prominent role in a sensor's operation depends on the energy of the impinging quantum relative to the material's E_{bg} as well as the charge-transport characteristics after their creation.

For solar optical photons, the power conversion efficiencies of photovoltaic devices can potentially be enhanced by exploiting MEG in nanostructured media without having to resort to multiple junction designs.[215] Unfortunately, the relatively high energy-threshold beyond which MEG is present ($h\nu > 2.9\ E_g$ for PbTe[214] or > 3.4 for PbSe[211-212]) as well as the gradual increase in the MEG efficiency beyond that threshold[215] have prevented photovoltaic device efficiencies from achieving technologically impactful values, as of yet, despite substantial efforts to exploit the phenomenon.[72, 80, 130, 211-217] However, if the impinging quanta possesses an energy that is well above the band-gap, such as in the case of x-rays or nuclear radiation (gamma-rays, alpha particles, neutrons), then the delta ray that results from such an interaction can possess a large carrier population with energies that can be orders of magnitude greater than the band-gap energy.

One might, therefore, be able to exploit MEG to produce high-energy sensors within which a greater portion of the initial particle energy is converted into those information carriers (photons in scintillators and electron-hole pairs in semiconductors) that can contribute to the signal formation. Indirect scintillating radiation detectors- in which the impinging quanta is first

converted into optical photons that are subsequently transformed into the measured current- can efficiently detect gamma-rays and neutrons but at the typical cost of poorer energy-resolution relative to direct detectors. Solution-processed nanostructured materials can be of particular utility when characterizing broadly distributed sources, such as those imaging instruments coupled to neutron or x-ray sources.[216-217] For instance, a colloid composed of nanosheets of cesium lead bromide ($CsPbBr_3$) was shown to have a good light yield (~21,000 ph/MeV) and facile process compatibility with x-ray imaging configurations.[216] Other inorganic halide perovskites and organic-inorganic halide perovskite nanocrystallites have been demonstrated as effective conversion media for fast neutron imaging.[217] However, for pulse-mode radiation spectroscopy- in which the energy of each impinging quanta is measured- scintillators in general and nanostructured scintillation media in particular typically deliver an energy resolution that is at least an order-of-magnitude worse than state-of-the-art semiconductor detectors. Ideally, one would couple the low-cost and large-area form-factors typical of solution-processed scintillators with the high-resolution performance delivered by semiconductor-sensors derived from silicon, cadmium telluride (CdTe), cadmium zinc telluride (CZT), or high-purity germanium (HPGe).

We previously showed energy resolutions comparable to that produced by HPGe detectors cooled to cryogenic temperatures in drop-cast PbSe solids bounded by gold electrodes.[6] However, extending the depth of the drop- or spun-cast self-assembled solids to the millimeter and centimeter scales relevant to high-efficiency x-ray and gamma-ray detection can be challenging because of crack formation that may accompany the drying of solids. One can utilize a polymeric template upon which NCs are bonded to extend the active volume of the sensor,[218-219] but an alternative approach is presented in this paper where macroscopic colloidal crystals are fully grown in a stability-enhanced PbSe solution.

A sizable detecting volume is of little use if barriers preventing effective change transport are distributed throughout the colloidal solid. A second aspect of this paper concerns the prevention of oxidation on the PbSe NC surface, which can act as a barrier over which carriers must surmount or tunnel through in order to facilitate charge transport and collection. In fact, oxidation upon air exposure can result in chemical instability for PbSe NCs, thereby hindering the development of PbSe NC-based optoelectronic devices.[114, 220-221]

As an example, PbSe NCs fabricated with trioctylphosphine selenide (TOPSe) experience degradation when exposed to oxygen.[222-223] Specifically, the selenium (Se) within the chalcogenide surface is readily oxidized when interacting with oxygen, thereby creating charge trap states. This can cause PbSe NCs to experience oxidation quite rapidly and uncontrollably based on particular conditions pertaining to the synthesis. Thus, it is particularly important to prepare air-stable PbSe NCs for an effective integration of NCs into a variety of devices.

Various reports characterizing the surface atoms of PbSe NCs that undergo oxidation (PbO, SeO_2, $PbSeO_3$) have helped put strategies in place for alleviating these instabilities.[224] Passivating the surface of PbSe NCs with an inorganic shell is an option; for instance, Pietryga *et al*.[213] reported on the growth of a CdSe shell on PbSe NCs (via cation exchange) that was significantly more stable against oxidation. However, the CdSe shell tends to serve as a barrier for charge transfer between NCs. This makes the use of PbSe/CdSe core/shell NCs in devices limited. Bae *et al.*[114] reported improvements in the optical properties and enhanced stability toward oxidation of PbSe NCs. However, the approach was based on the Cl_2-facilitiated removal of surface Se atoms, forming a passivation sub-monolayer of $PbCl_x$ which could effectively prevent oxidation during long-term air exposure at the possible expense of PbSe NC uniformity.

Here, we report a solution-process method to synthesize PbSe NCs. The introduction of tris(diethylamino)phosphine (TDP) as the Se precursor generates chemical stability for the PbSe NCs via improved surface passivation. TDPSe, which was produced by the reaction of TDP with elemental Se, was used as a selenium precursor instead of TOPSe. The alteration of ligand structure drastically enhanced the air stability of PbSe QDs through the formation of P–O moieties on QDs surface that passivated the reactive PbSe surface.[225-229]

3.4.4.1 Results & Discussion

3.4.4.1.1 Long–Term Stability of TDP-PbSe NCs

The effective electronic coupling of the NCs throughout the solid is required to facilitate lossless charge transport and collection, a property required to make a faithful measurement of the energy deposited by the incident quanta. The transformation of the nanoparticle solution into a sensing colloidal solid must therefore avoid loss mechanisms which could enhance the surface interfaces. One mechanism through which thermal losses and trapping can be decreased is through the growth of Pb and Se oxides at the PbSe NC surface. One can passivate the NC surface via core-shell NCs[213, 230] or via lead-halides,[6, 219, 231] but both can modify the band-structure and minority carrier population and thereby affect the overall device design. Instead, we passivated the NC surface via phosphorous-oxygen (P–O) moieties, as derived from TDPSe as the Se precursor,[232] and showed that at least 1.6 years of stability against oxidation was successfully realized, as detailed next.

As detailed in the Synthesis for TDP-PbSe NCs, we utilized a solution-process to synthesize a colloidal solution of monodisperse PbSe NCs. Highly air-stable PbSe NCs can be produced by: (1) introducing the TDP as a Se source within the Se precursor, in the form of TDPSe (denoted as TDP-PbSe NCs) instead of TOPSe (denoted as TOP-PbSe NCs), and (2) fabricating lead oleate of high purity, achieved by adjusting the conditions of the Pb precursor. In order to facilitate high reactivity, pure hydroxide-free lead oleate was prepared by dissolving lead oxide in trifluoroacetate anhydride solution followed by the neutralization of the lead trifluoroacetate product with oleic acid and triethylamine (more detail in Section 3.1.2.4).

In the TDP-PbSe synthesis, the Pb precursor used here was similar to that described by Hendricks *et al.*,[144] who reported a variety of substituted patterns for finely controlled PbSe NCs with conversion kinetics of trisubstituted selenoureas. The approaches taken to produce the final product of TDP-PbSe NCs can be complicated because key reagents and intermediates are unstable and must be prepared in multiple steps.

Despite the shape and size control that can be derived from the synthesis of TOP-PbSe NCs, they can be unstable in ambient conditions due to their high susceptibility to oxidation, resulting in undesired alterations in the properties of the NCs.[93, 225, 233] The surface atoms of PbSe NCs can form oxides, such as PbO, $PbSeO_3$, SeO_2.[220] In order to investigate the stability of the TDP-PbSe NCs, we stored the NCs under ambient conditions (see Section 3.1.2.4), and their optical absorbance spectra was recorded over time. As shown in Fig. 3.48b, the optical response of the TOP-PbSe NCs blue shifts and diminishes in luminescent intensity rapidly (on the order of a few days), an oxidation and destabilization of the NC electro-optical properties that continues beyond the 4 days shown. In contrast, the shape and peak position of the absorbance distribution for the TDP-PbSe NCs remain stale for at least 585 days of air exposure (Fig. 3.48a).

The optical characterization measurements thus indicate that the TDP-PbSe NCs are air-stable for years. To isolate the physical cause of the stability, we first characterized the microstructure of the NCs themselves as follows. When TDP interacts with the surface of PbSe NCs, the ligand-NC interaction can cause both the rearrangement of surface atoms as well as an effective passivation of the surface dangling bonds by TDP or its derivatives. [221, 225, 234-235]

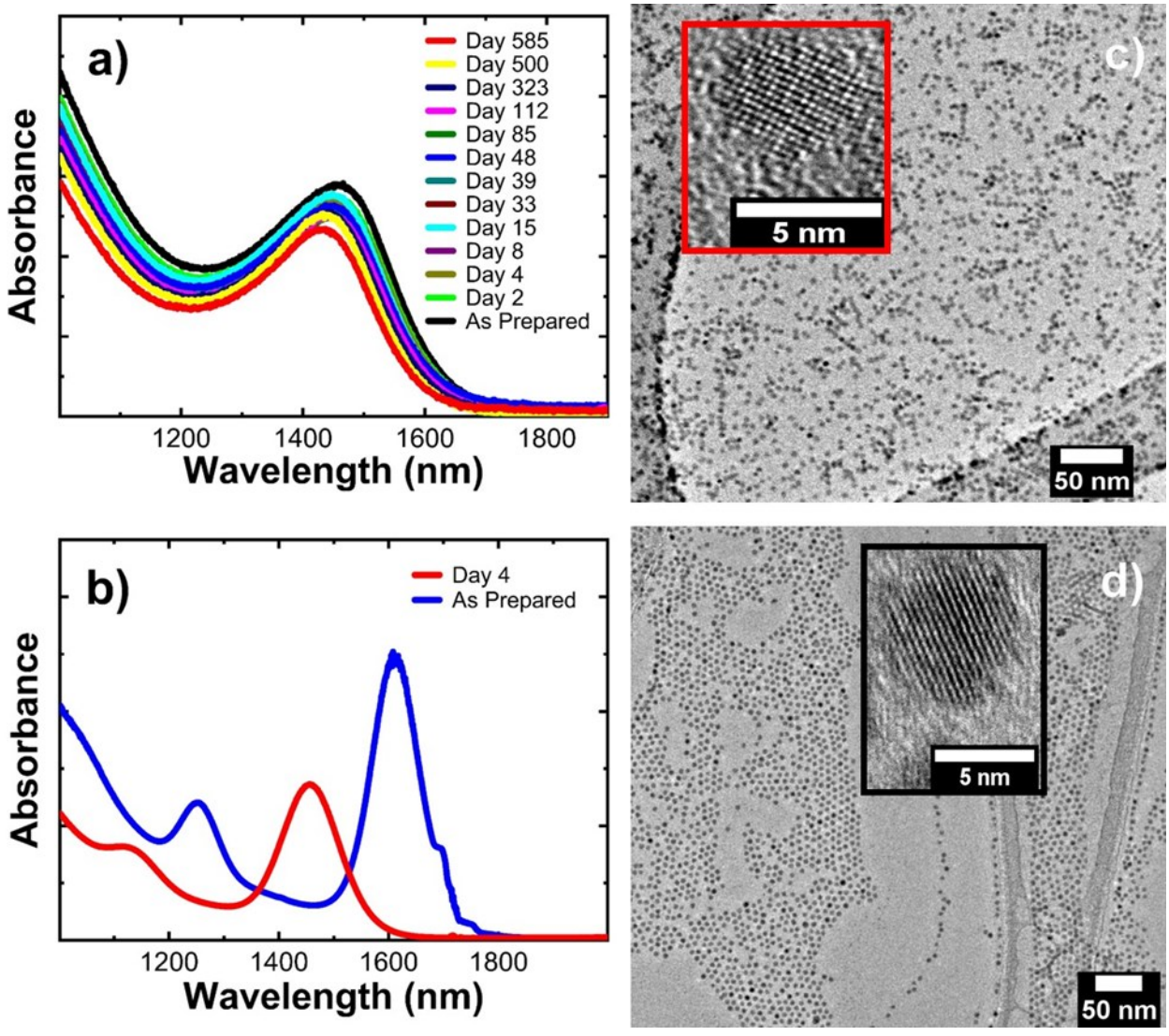

Fig. 3.48 | Property Comparison of TOP- and TDP-PbSe NCs. Absorbance spectra of (a) TDP-PbSe NCs and (b) TOP-PbSe NCs dispersed in tetrachloroethylene (TCE). Absorbance spectra were recorded with the NCs as prepared and then following air-exposure for days (shown in

legend) following the synthesis. The colloidal solutions experienced air exposure in ambient conditions. (c) Transmission electron microscopy (TEM) images of (c) spherical PbSe NCs with 1 M TDPSe possessing a diameter of 5.3 ± 0.4 nm and (d) rhombicuboctahedron PbSe NCs with 1 M TOPSe having a diameter of 5.5 ± 0.6 nm. Scale bars are 50 nm. The insets show HRTEM images of a TDP-PbSe NC outlined in red in c, and a TOP-PbSe NC outlined in black in bd Both nanocrystals possess a lattice spacing of 3.1 Å, which corresponds to the expected PbSe (200) plane separation.

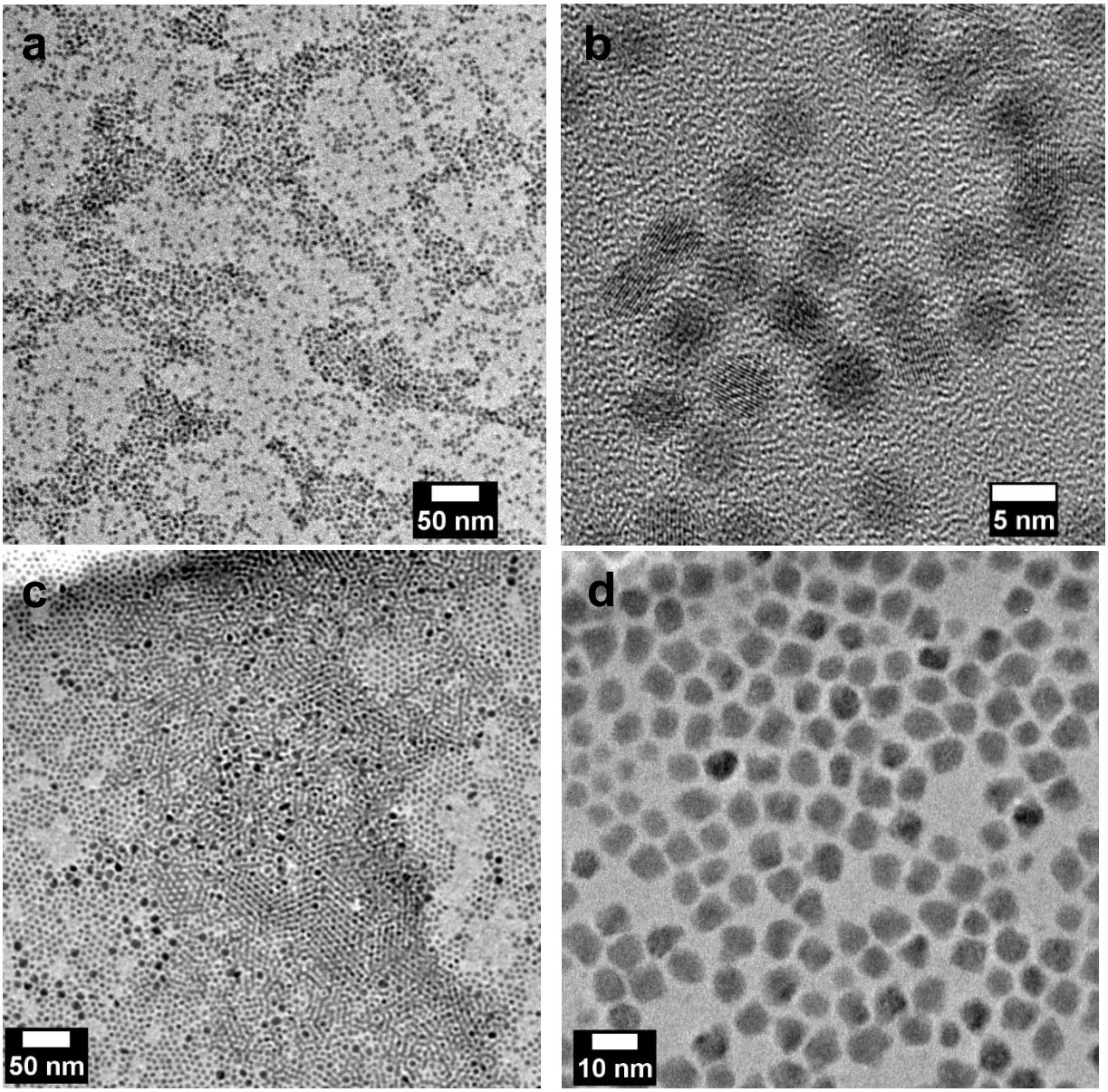

Fig. 3.49 | TEM micrographs of spherical TDP-PbSe NCs sample fraction at (a) low, and (a) high magnification after precipitation with TCE. Comparing TDP-PbSe NCs to TOP-PbSe NCs, sample fractions of TOP-PbSe NCs at (c) low, and (d) high magnification after precipitation can be seen here as well. The oddly shaped NCs have a diameter of 3.4 ± 0.5 nm.

Transmission electron microscopy (TEM) images of monodisperse TDP-PbSe NCs are compared to those of TOP-PbSe NCs in Figs. 3.48 (c, d) at both low and high magnifications. Note that although the PbSe NC assemblies on the TEM grids were formed by drop-casting, the colloidal solids used to form the photosensing structures were interconnected slowly in solution at lower NC concentrations. The TEM micrographs indicate the NCs coordinated with TDP have a greater shape uniformity than those derived from TOPSe (Fig. 3.48 (c, d)). Furthermore, the PbSe NCs derived from TDPSe are more spherical, while the TOPSe-based PbSe NCs tend to have a rhombicuboctahedron shape (Fig. 3.49).

High-resolution (HR)TEM images of TOP- and TDP-PbSe NCs are shown in the insets of Fig. 3.48 (c, d), respectively. Fast Fourier Transform (FFT) analysis of the fringes reveals a rock salt PbSe crystal structure with a 3.0 Å lattice space, which corresponds to the {200} lattice vector matching that of crystalline bulk PbSe.[225] Thus, with the equivalent PbSe (200) lattice spacing and comparable quasi-spherical shape observed for both TOP- and TDP-PbSe NCs, XRD and TEM analyses suggest TOP- and TDP-PbSe NCs have nearly indistinguishable structures and therefore do not result in disparate structure-induced enhanced stability of the TDP-PbSe NCs.

In quantifying the effects of TDP-PbSe bonding, we conducted crystallographic analyses of TOP- and TDP-PbSe NCs. X-ray diffraction (XRD) patterns of TOP- and TDP-PbSe NCs, such as those shown in Figure 3.50a, demonstrate that the expected rock salt PbSe structure is preserved

regardless of the ligand, although the NC shape can be slightly modified as revealed in the integrated peak ratios ((111)/(200): 0.34 and 0.29 for TOP- and TDP-PbSe NCs, respectively).

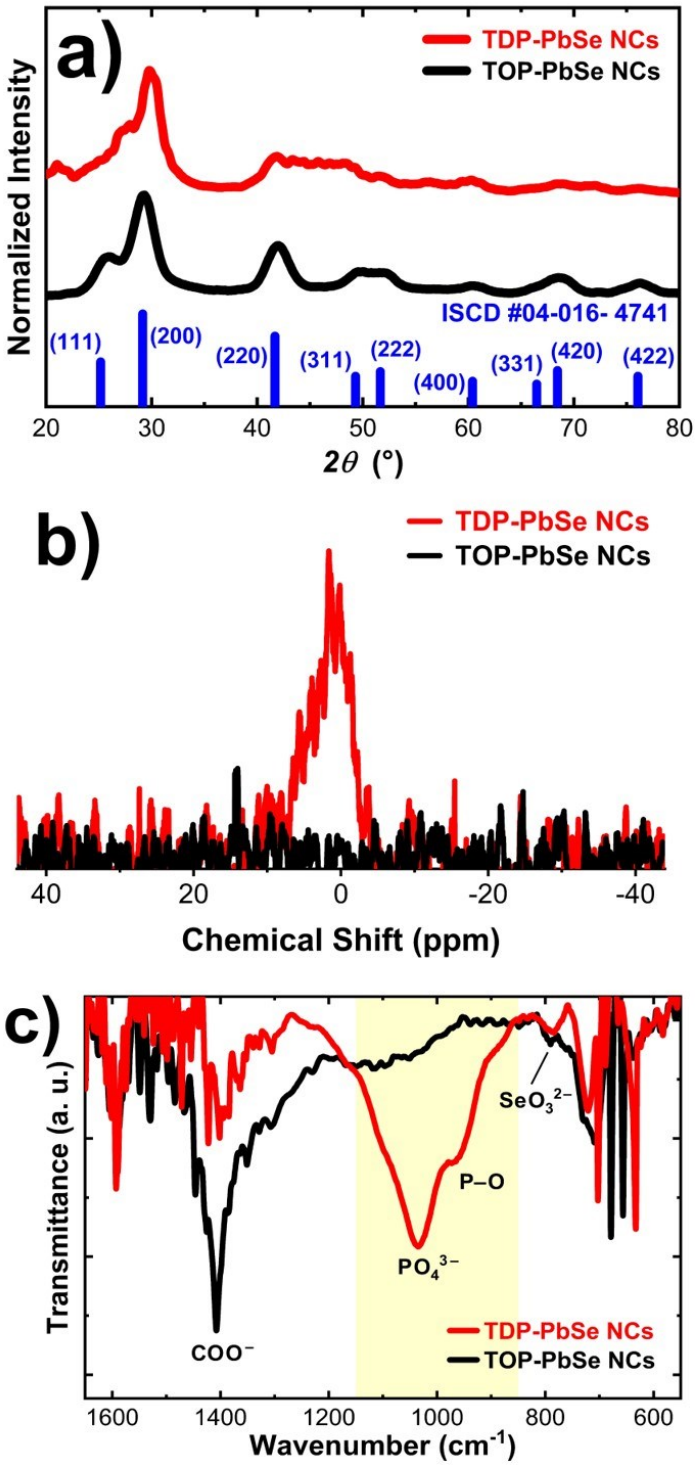

Fig. 3.50 | Structural and Surface Property Comparison of TOP-PbSe and TDP-PbSe NCs. (a) XRD patterns of TDP- (red) and TOP-PbSe (black) NCs. The patterns match the bulk rock salt PbSe pattern taken from ICSD #01-085-7901 (blue). (b) $^{31}P\{^{1}H\}$ NMR spectra of TOP-PbSe NCs and TDP-PbSe NCs dispersed in benzene-d_6. (c) FTIR spectra of TDP- and TOP-PbSe NCs along the stretching vibrational region of P–O at the range of 850 – 1150 cm^{-1} (yellow shade).

In order to elucidate the surface bonding differences between the two ligand approaches, Fig. 3.50b displays $^{31}P\{^{1}H\}$ NMR spectra of TOP- and TDP-PbSe NCs. The presence of a surface bound phosphorus species is demonstrated by the large resonance in the TDP-PbSe spectrum at ~2 ppm (Fig. 3.50b) in contrast to the absence of the peak in the TOP-PbSe NC distribution.[236] The existence of phosphorus is additionally apparent and verified by FTIR spectra shown in Fig. 3.50c, in which P–O– stretching bond lies between 850 – 1150 cm^{-1}. Previous cleavage studies on phosphonic acid (PA) capped CdSe NCs using bis(trimethylsilyl)sulfide ($(TMS)_2S$) or bis(trimethylsilyl)selenide ($(TMS)_2Se$),[237-238] suggest the surface of the TDP-PbSe NCs possess P–O moieties, such as those shown schematically in Scheme 3.1. In those studies along with that by Woo *et al.*,[225] TDP derivatives were bound to the NC surface and cleaved by adding $(TMS)_2S$ (or $(TMS)_2Se$). When in the presence of TMS-chalcogenide, only TDP derivatives on the NC surface possessing P–O moieties tend to move to bind with TMS because it is thermodynamically preferred.

In our case, though diethylamine is already included in the TDPSe precursor, an excess amount can introduce a ligand exchange within the colloid.[239] The diethylamine can adsorb onto the PbSe NCs via strong coordination bonds with surface metal atoms—a driving force for ligand exchange.[239-240] The involvement of diethylamine in our Se precursor is capable of removing our natural capping ligand, that being OA, and in doing so, provide the PbSe NCs with a diethylamine monolayer.[239] Keeping in mind diethylamine is also a small molecule,[239] this monolayer can then be removed/released from the NC surface and colloid during the heating process of this metal chalcogenide synthesis when reaching temperatures ≥ 150 °C. Following the thermal conditioning, a derivative of TDP, or phosphorus-containing elements of TDP, are left behind along the NC

surface with either a combination of OA residue or minor surface oxidation, together forming P–O moieties and/or some form of it along the PbSe NC surface.[225, 241] As a result, the NMR and FTIR analyses indicate that during the synthesis of TDP-PbSe NCs, TDP transforms into its derivatives forming P–O moieties which passivate the surface of the PbSe NCs.

Scheme 3.1. Synthesis of TDP-PbSe NCs. (a) Synthesis of lead oleate (from lead oxide). (b) Synthesis of PbSe nanocrystals from lead oleate and TDP. Et_3N, triethylamine; $R_a = C_{17}H_{33}$; $R_b = C_4H_{10;}$ Pb(oleate) = $Pb(R_aCOO)_2$. (c) Hypothesized schematic showing that the recently fabricated PbSe NCs initially possess OA and TDP along its surface as well as within the colloid. During heating of the PbSe synthesis and the clean-up procedure, components of TDP assist in the formation of P–O bonds and/or some derivative of TDP, as defined by:

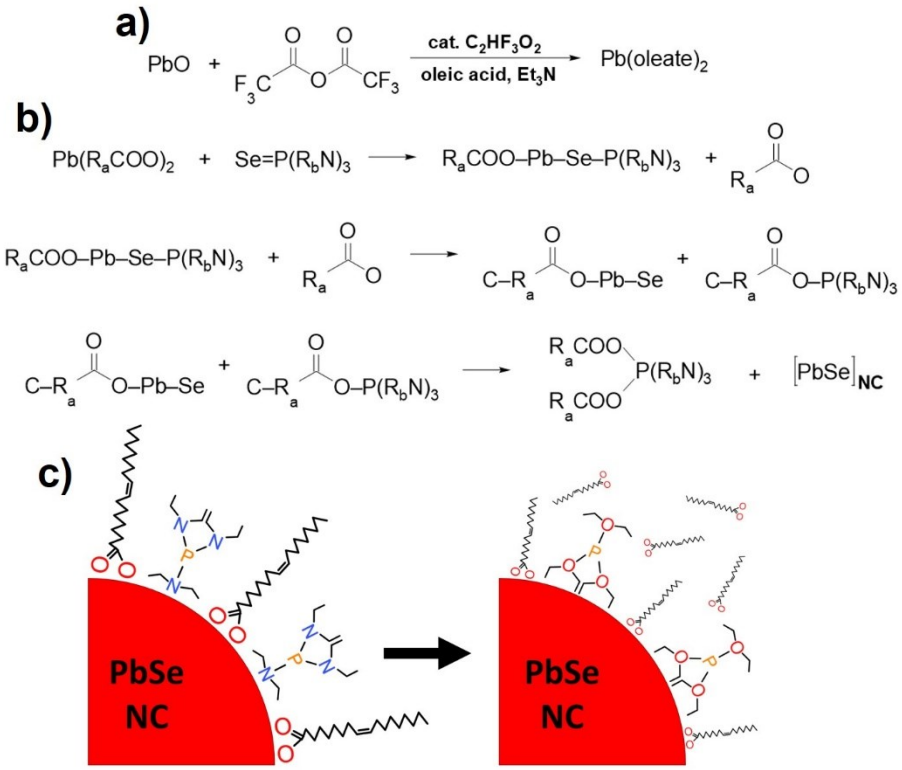

The optically-revealed long-term air stability of TDP-PbSe NCs and the FTIR and NMR surface bonding measurements corroborate the hypothesis that the surface bound P–O moieties

account for the enhanced stability of the PbSe NCs by preventing the environment-induced alteration of the PbSe NC surface. In order to detail the nature of surface passivation, we conducted x-ray photoelectron spectroscopy (XPS) studies. For Pb, two peaked features at ~137.9 and ~142.9 eV derived from the Pb $4f_{7/2}$ and Pb $4f_{5/2}$ spin-orbit coupled doublet dominate the XPS spectra in the range of 135 to 147 eV (Fig. 3.51 (a, c, e)). Three contributions lie within each peak, which were fitted and analyzed. First, elemental Pb (Pb^0; Pb_m) at ~136.9 and ~141.8 eV correlated to Pb–Se bond within PbSe is present. Second, the prominent natural oxide (Pb^{2+}; Pb_1) at ~138.8 and ~143.7 eV attributed contributions from Pb oleate, $Pb(CROO)_2$; lead oxide, PbO; lead hydroxide, $Pb(OH)_2$; or their combination due to the higher binding energy of Pb–O versus Pb–Se.[220, 242] Finally, oxidized and carbonated Pb (Pb^{2+}; Pb_2) are evident at ~138.8 and ~143.7 eV representing lead carbonate, $PbCO_3$. The Pb spin-orbit splitting separation values of Pb $4f_{7/2 - 5/2}$ are ~4.89 eV for all PbSe samples, which is consistent with the standard spin-splitting value of 4.9 eV (Pb $4f_{7/2–5/2}$).[218, 243]

Note that the 117-day old TDP-PbSe sample (Fig. 3.51a) exhibits a relatively higher contribution from the Pb^0 valence state compared with the elevated Pb^{2+} features from the TOP-PbSe samples (Fig. 3.51 (c, e)) which are far less aged, at 5- and 55-days-old respectively, showing the lack of oxidation in the TDP-PbSe NCs compared with the TOP-PbSe NCs. Although we exposed both TOP- and TDP-coordinated NCs to air in our study, others reported supporting XPS results when comparing air-free and air-exposed PbSe samples due to disparate formation intensities of PbO and/or $Pb(OH)_2$.[244-247]

For the Se XPS scans in the 50 – 63 eV range (Figs. 3.51 (b, d, f)), $3d_{5/2}$ and $3d_{3/2}$ spin-orbit split peaks indicate the presence of Se^{2-}, Se^0 and Se^{4+} (~53.8, ~55.4, ~58.5 eV). Specifically, the 117-day old air-exposed TDP-PbSe sample only possesses a single ~53.58 eV peak attributed to

the most reduced state of Se existing as selenide (Se^{2-}). The deconvolution of this state (Fig. 3.51b) showed two contributions from Se $3d_{5/2}$ and Se $3d_{3/2}$, at ~53.6 and ~54.4 eV, respectively. However, the presence of oxidation is marked for both the 5- and 55-day-old TOP-PbSe samples. Specifically, Fig. 3.51 (d, f) reveal additional features, one being elemental Se (Se^0) at ~55.4 eV, attributed to a Se excess detected along the surface of the NCs, and the other feature being oxidized Se (Se^{4+}) at ~58.5 eV, which is most likely due to SeO_3^{2-} or SeO_2. The spin-orbit splitting separation values of Se $3d_{5/2}$ and Se $3d_{3/2}$ are of 0.86 eV for all PbSe samples, which is also in sync with a literature value of 0.86 eV (Se $3d_{5/2-3/2}$).[243]

Finally, the XPS data also indicated the presence of phosphorus (P) because its inclusion in the fits of the TDP-PbSe spectra improved their quality. Elemental P is usually observed at ~130.0 eV, a contribution that partially overlaps the Pb $4f_{7/2}$ component in the right-most shoulder of Fig. 3.51a. The additional underlined presence of P–O signals along the range 130 – 137 eV could be attributed to a phosphate (PO_4^{3-}) at the lower energies and phosphorus oxides (P_2O_5, P_4O_{10}, or their combination) at higher energies. Specifically, elemental $P2p_{3/2}$ and $P2p_{1/2}$ peaks were included in the fits and the peak at 131.4 eV was attributed to the P^+ ion since it has been mentioned the donor ion P^+ should be ~1 eV higher than that of P^0.[248] The P2p peak at 133.5 eV represents a second $P2p_{3/2}$ component and lastly, the peak at 134.3 eV, attributed specifically to phosphate, was assigned to the second $P2p_{1/2}$ component. Both P2p sets possess a fixed spin-splitting of 0.8 eV, in comparison with literature value of 0.85 ± 0.5 eV.[249]

With NMR and FTIR spectra revealing the presence of phosphorus-bound moieties, XPS spectral curve fitting showing the mitigation of Pb and Se oxidation, and optical data indicating long-term stability for TDP-coordinated PbSe NCs, the material characterization shows that TDP-ligands provide a more effective means through which robust and stable device behavior can be

elicited. Furthermore, as shown next, their relatively weak and dynamic bonding to the NC allows PbSe NC-to-NC atomic bonding and therefore bridges through which charges can transport from dot-to-dot.

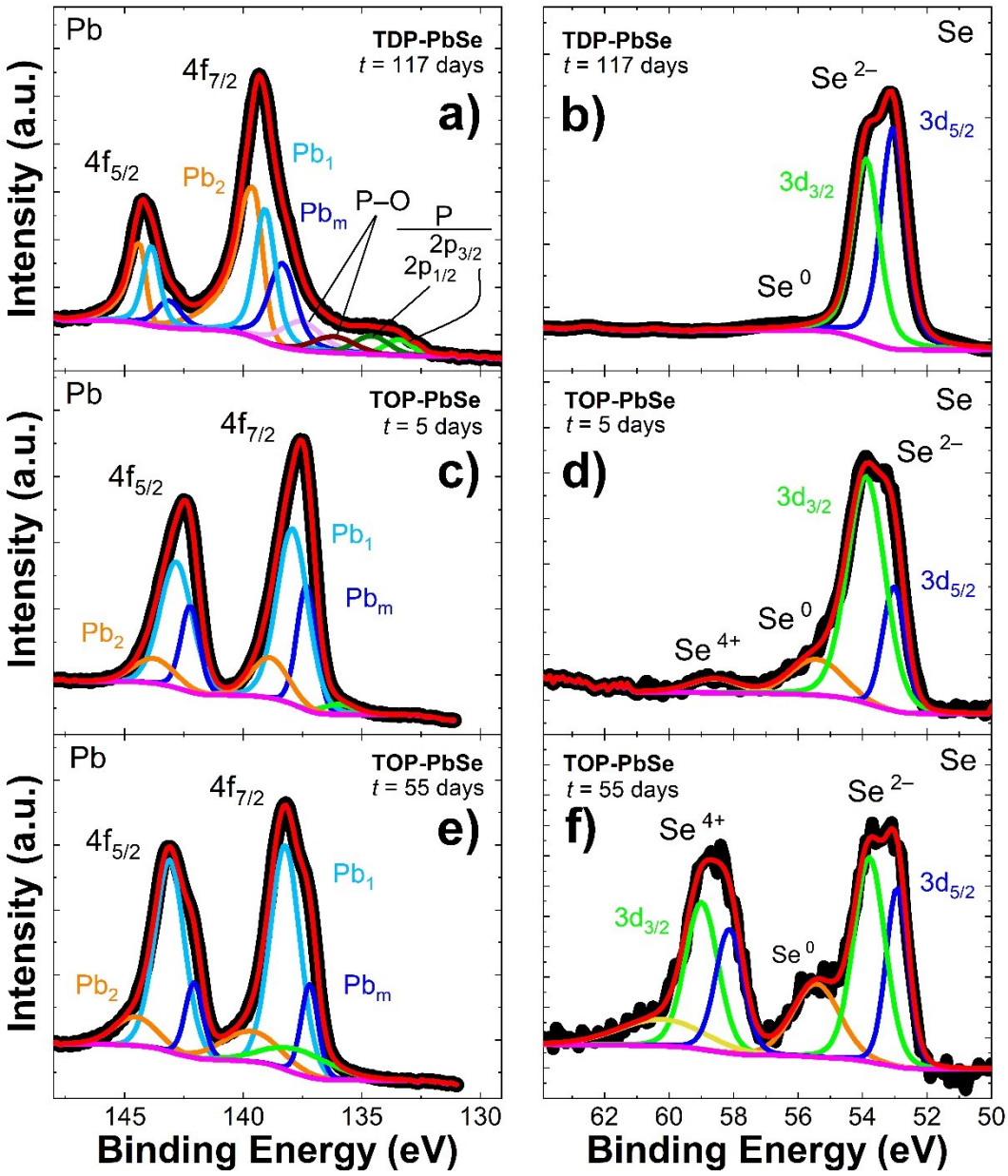

Fig. 3.51 | Valence State Variation of TOP-PbSe and TDP-PbSe NC Surface Atoms. Pb 4f (left) and Se 3d (right) XPS spectra collected from (a, b) TDP-PbSe NCs along with (c, d) relatively fresh and (e, f) old TOP-PbSe NCs. The shift in binding energy from Pb 4f XPS spectra displays

passivation of Pb by P–O moieties in the 117-day old TDP-PbSe case when contrasted with spectra from 5- and 55-day-old TOP-PbSe NCs. In Se 3d XPS spectra, there is no shift in binding energy, however, increased Se oxidation is observed in the TOP-PbSe samples as they age.

3.4.4.1.2 Solution-Growth PbSe Colloidal Crystals with NP Necking

For the efficient stopping of x- and gamma-rays, the solids must be millimeters or centimeters thick. The greatest challenge of implementing ~5 nm diameter NCs in a thick sensing solid is that the charge carriers may have to transport over millions of NCs and therefore millions of interfaces. Fortunately, as we showed in Lyu *et al.*,[218-219] in the context of gold and silver nanostructured conductors, if one can remove or tunnel through the ligand and create a high-enough density of NCs so that percolation paths are created through the solid, then charge-transport to the collecting electrodes can be realized.

The self-assembly of semiconductor NCs can be facilitated by confining the formation of NC superlattices at a liquid–air interface.[250] Specifically, upon drop-casting a colloidal solution of NCs, the NCs adsorb at the liquid–air interface and self-organize into large-area superlattices upon solvent evaporation. The exact structure of the superlattice which forms depends on interactions between the NCs[251-252] and the interaction of the particles with the interface. This method has been expanded to form molecularly connected NC solids through a process called oriented attachment: a vital process in geology,[199] which has recently gained much interest as a preparation tool in semiconductor nanoscience. Oriented attachment is a process which results in the self-organization and interatomic bonding of adjacent NCs, the latter characteristic important for rapid inter-particle charge-transport. Oriented attachment can be achieved via the mutual crystallographic orientation

of neighboring NCs during with direct collisions or via bridging and necking of the NCs, creating closely packed nanostructures and/or superlattices.

We have not yet characterized the exact nature of the colloidal-solid growth in the PbSe solution, whether it be a classical crystal growth method in which NCs epitaxially bond to a nucleate or an alternative pathway. However, TEM micrographs of PbSe show that if the solution is highly concentrated, which can occur along the indentions of a TEM grid, then square-ordering and colloidal crystal growth is facilitated (Fig. 3.52). A mechanism through which NCs can be concentrated is the alternative crystallization pathway described in Gebauer *et. al.*[253-254], in which prenucleation clusters can be formed within the solution where the NC freedom-of-motion is restricted and NC-to-NC attachment becomes more favorable. For instance, we observe the formation of cubic colloidal crystals within clusters of PbTe NCs that may consist of ~4000 NCs originally in a prenucleation dynamic spheroid, in which the inner cube is more tightly bonded than the NC jacket.[255] When the PbSe colloidal solids are agitated in the solution, on can observe a flux of NCs from the solid's surface, suggesting that a similar mechanism, in which cluster formation is followed by NC interparticle bonding, may be occurring.

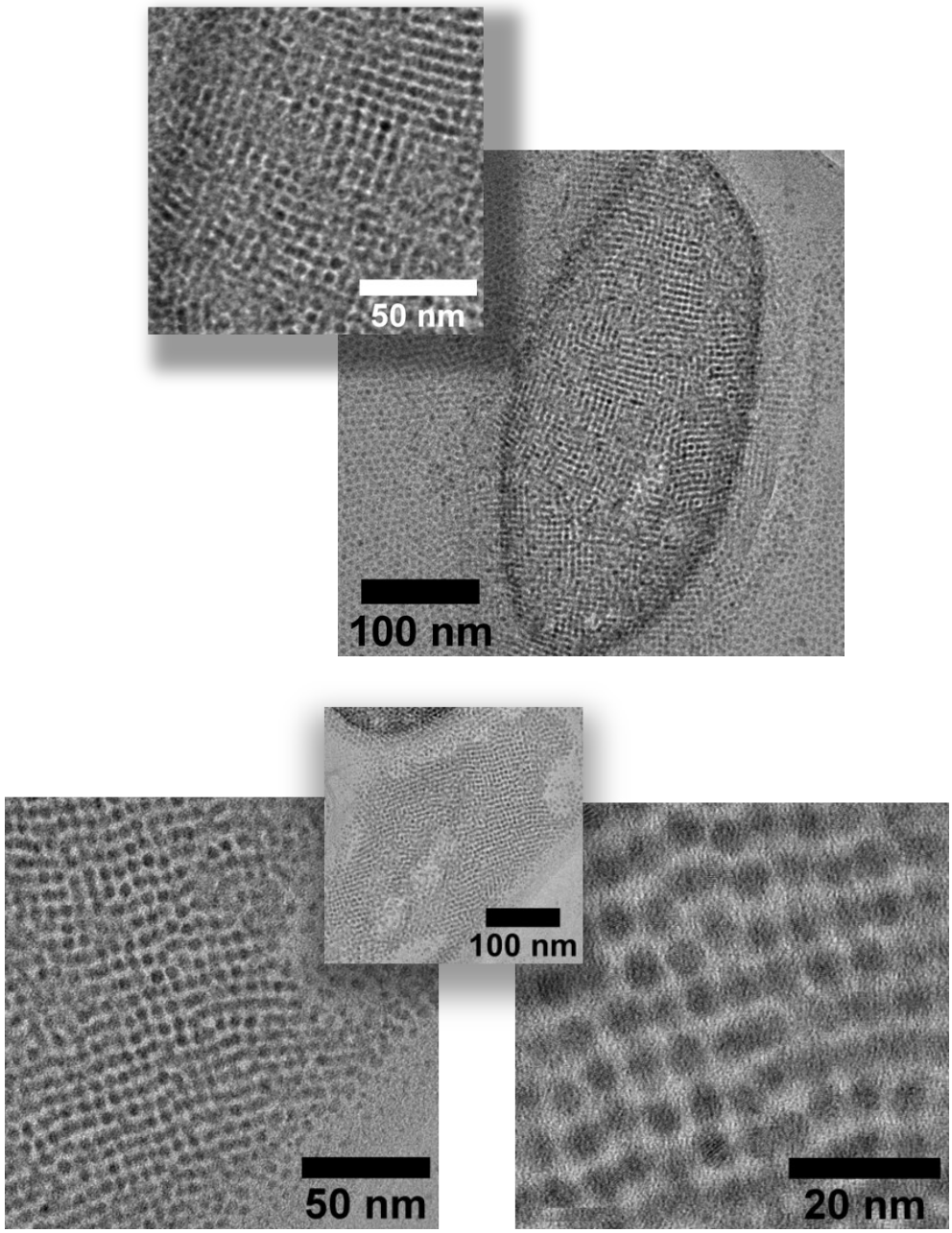

Fig. 3.52 | TEM micrographs of PbSe-TDP NCs forming into square lattices in those regions of the TEM grid where the PbSe solution becomes most concentrated during solvent drying.

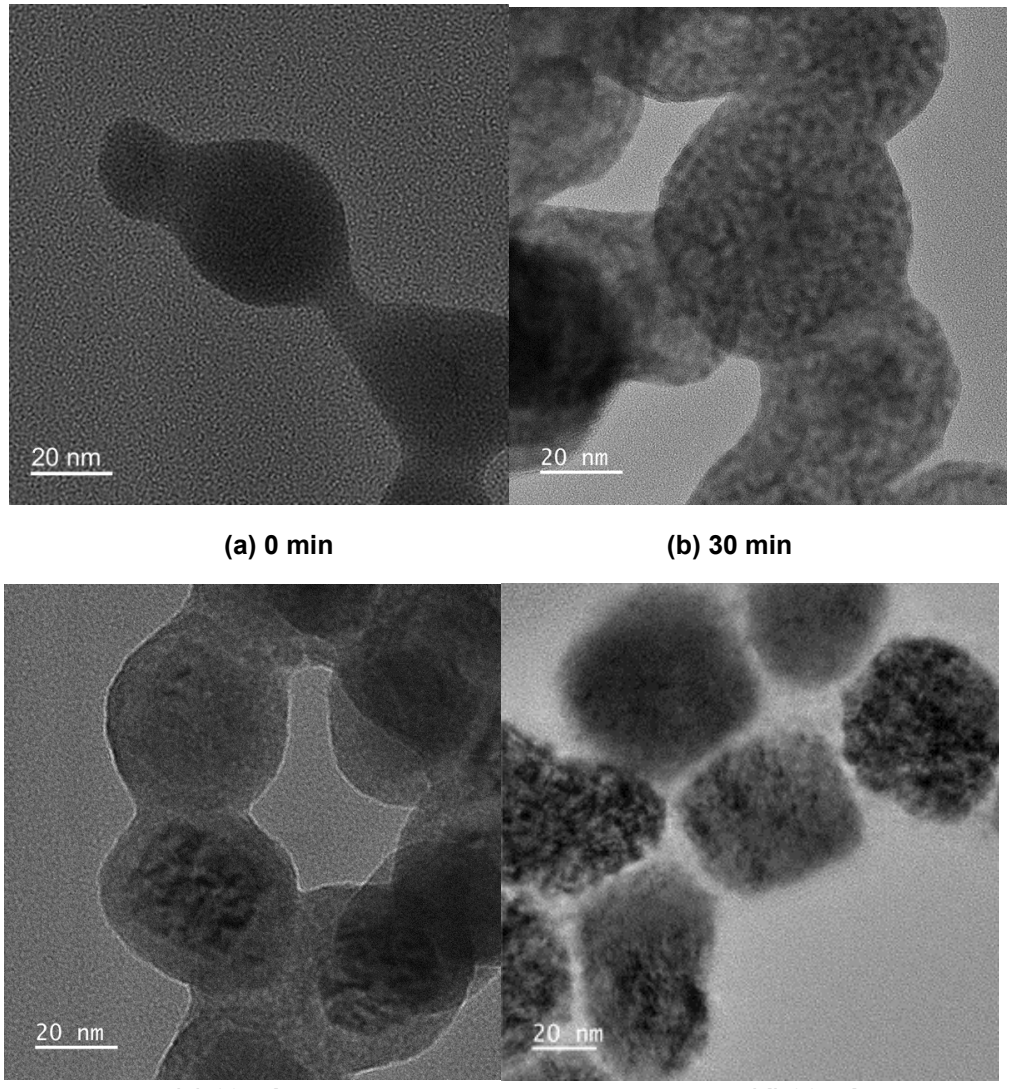

Fig. 3.53 | Alternative crystallization mechanism in which pre-critical clusters of NPs are formed within which colloidal crystals are formed. The time shows the reflux time (at 100 ^{0}C) of the PbTe colloidal solution.[61] The PbTe example shows: (a) the formation of prenucleation cluster at 0 min followed by (b) post-critical nucleation in which a dark shadowed cubic structure begins to grow within the cluster. (c) The cubic PbTe colloidal solid grows as the PbTe NCs in the jacket are consumed until (d) cubic PbTe clusters result.

Whether the NCs are formed at an interface or within a concentrated colloidal solution, the TDP-PbSe NCs can form into close-packed superlattices, as shown in the TEM micrographs of Figs. 3.54a. When colloidal solutions of sufficient density are created, the TDP-PbSe NCs form

into large-scale loosely bonded clusters, as shown in Fig. 3.54b, in which some PbSe solids are accompanied by PbSe sedimentation. One can also fully incorporate the PbSe NCs into the solid (Fig. 3.53) depending on the growth recipe. If the organic solvent (trichloroethylene (TCE)) is allowed to evaporate, then the mm-scale clusters solidify into mechanically colloidal solids, such as that shown in Fig. 3.54c. Although they are mechanically robust enough to be readily handled with tweezers, surface damage can result from excess force (Fig. 3.55c). As shown in the 2D small-angle x-ray scattering (SAXS) pattern derived from solidified PbSe (black curve of Fig. 3.54d), there is enough structural ordering that peaks in the scattering pattern can be observed. The particle and pore-size analysis derived from the (blue) modeled curve of Fig. 3.54d indicates a NC diameter of 6.3 nm ± 0.8 % and a particle separation of 0.9 nm. The solids exhibited a density of 3.84 g/cm^3 (compared to a single-crystal PbSe density of 8.77 g/cm^3) as measured via direct measurements of the solid's mass and volume which is roughly consistent with the SAXS-derived volume fraction of 46.9 %. Among the various solids formed through the different chemical procedures described in this Chapter, this solution-grown TDP-PbSe approach produced the best sensing solids, in that that possessed both high energy-resolution and high manufacturing yield, as detailed in Chapter 4. First, we will describe additional studies regarding the role of oleic acid in the different ligand systems.

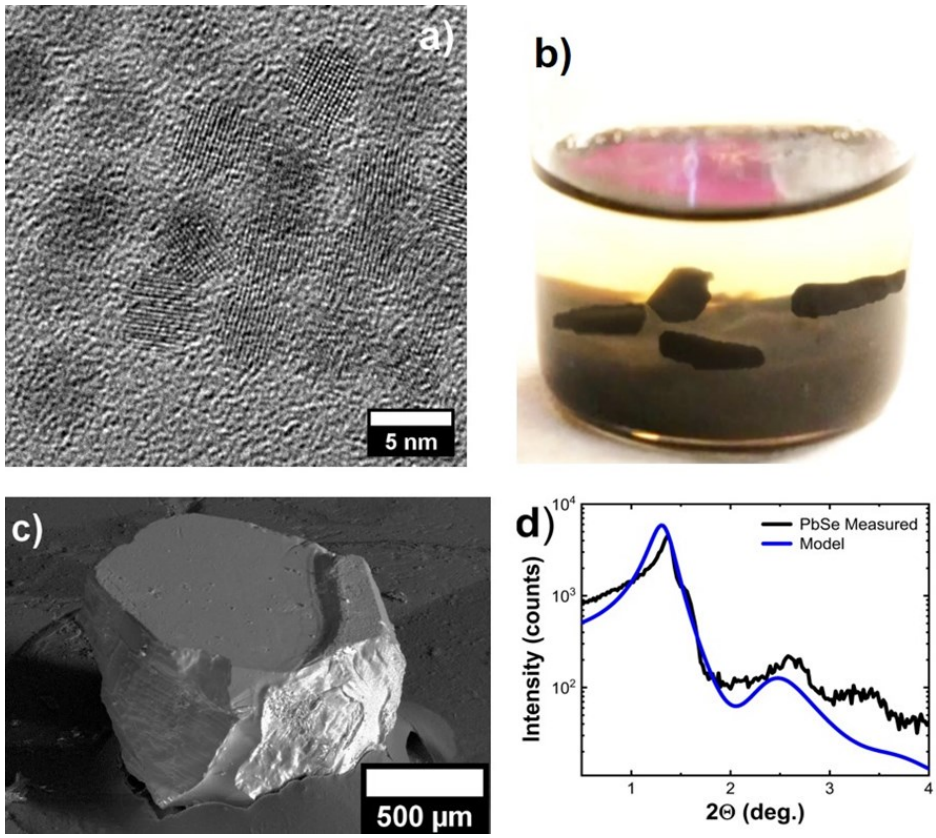

Fig. 3.54 | High-resolution TEM (HRTEM) micrographs of solution of TDP-PbSe NCs in TCE exhibiting oriented attachment. (a) Shows an example of square ordering within the TDP-PbSe sample and the formation of NCs into an atomically interconnected chain. (b) The formation of colloidal TDP-PbSe solids in TCE solution. (c) A colloidal solid after solvent evaporation. (d) Small-angle x-ray scattering, as a function of the 2θ scattering angle, from a solution-grown solid of PbSe nanocrystals after full drying of the solid, showing the measured data (black) and the modeled distribution (blue).

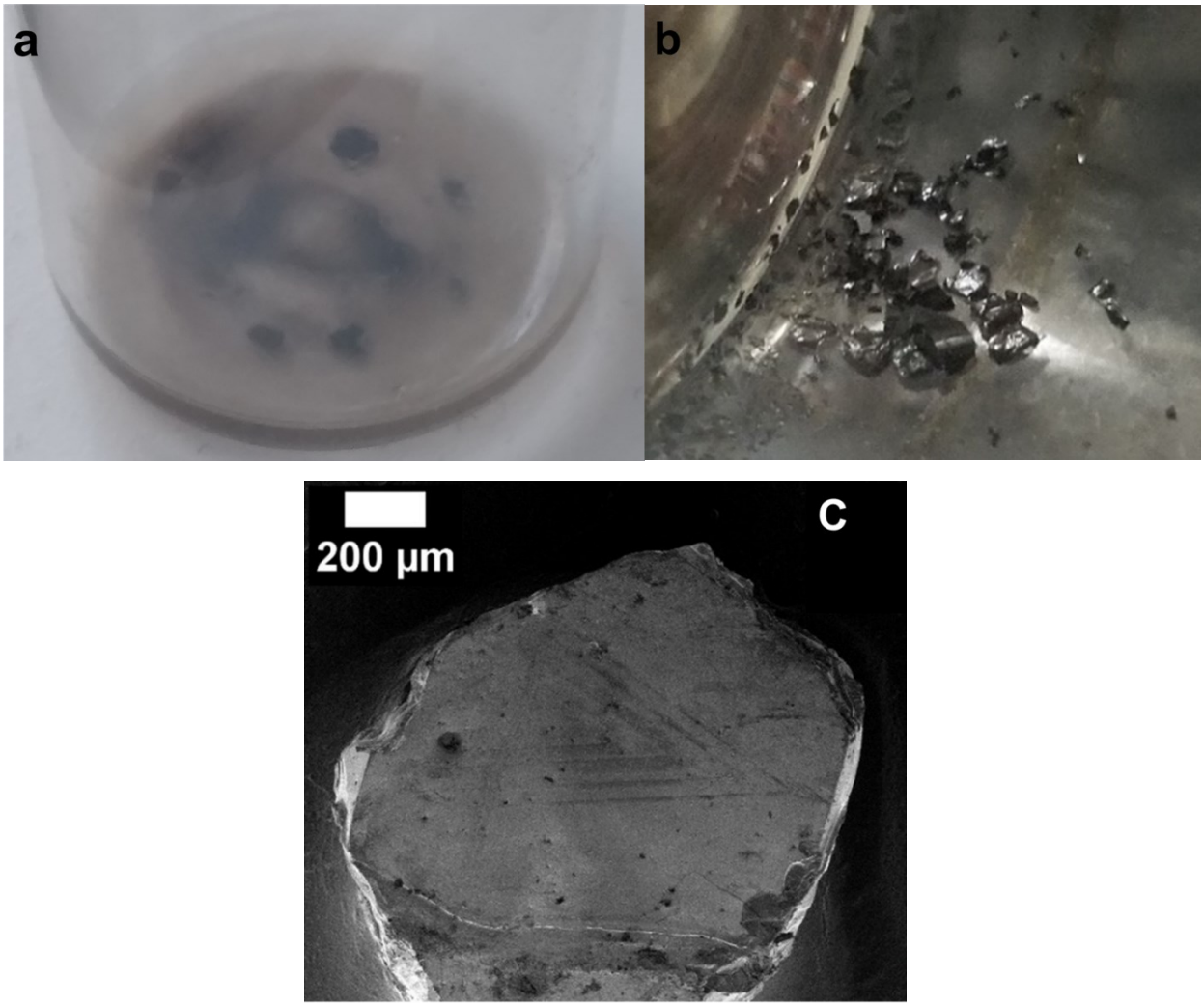

Fig. 3.55 | (a) The formation of colloidal TDP-PbSe solids in (transparent) TCE solution in which the NPs are largely incorporated in the solid, as indicated by the clear solution and bottom of the vial. (b) Photograph of remaining pieces after a solid sample composed of TDP-PbSe NCs broke apart during handling. (c) Chevron shape on surface of TDP-PbSe crystal caused by tweezers.

3.5 TOP vs. TDP: Oleic Acid & Oxidation

3.5.1 TOP-PbSe-DPP NCs: Variation in Molar Concentration

To understand the role oleic acid has on our fabricated PbSe NCs and make positive adjustments experimentally, we carried out a variety of PbSe syntheses with modifications in Se precursor concentration. Nuclear Magnetic Resonance (NMR) was used to assess the samples purity level with the presence of un/reacted precursor/s. Knowing which element exists in excess within the colloidal solution gave vital information on improving experiments for future reference. While retrieving this data, a small catalog was developed in which one can vary Se molarity (0.5 - 1.0 M) and observe the impact on the surface. The same preparations made here are the same as for our TOP-PbSe-DPP synthesis previously discussed in Section 3.1.2.3. TEM images for the following Se molarities are seen in Fig. 3.56.

In the 0.5 M sample, in the first row of Fig. 3.56 (b, c), we see nanowires have been fabricated, however, a closer look into Fig. 3.56c reveals those nanowires created from NC building blocks. The 0.6 M sample, shown in second row of Fig. 3.56 (e, f, g), shows square ordering NCs and facet interconnectivity while showing their atomic lattice throughout. A stronger case of this can be seen in Fig. 3.56 (i, j, k), as the 0.7. M sample is the first to display an assembly within thinner regions of the copper-mesh grid. In Fig. 3.56 (m, n) we observe how the single and multiple layers the PbSe NCs can assemble, as the 0.8 M sample is the first to display this feature. In observing samples 0.9 and 1.0 M, (Fig. 3.56 (q, r, s) and Fig. 3.56 (u, v, w)) weak and strong *bcc* nanostructures can be seen, informing us of a higher level of NC uniformity along with these stronger concentrations.

In observing absorbance for the 0.5 – 1.0 M samples, we see broad peaks for 0.5 – 0.8 M samples as the standard deviation values of their PbSe NC size ranges from ± 0.3 – 0.5 nm.

With the absorbance spectra of the 0.5 M sample offsetting from the baseline, it is possible the catalysts, or excess Pb within the solution, diminishes the chance for PbSe NCs to be fabricated. The lack of Se precursor within this sample may cause this to occur, contributing to a low yield, seen visually through the TEM images. This then allows for an excess amount of Pb to exist within the solution in the end, which can prevent the catalysts from being removed with the standard polar/anti-polar solvent clean up procedure.

The absorption spectra from the 0.6 M sample shows a broad peak, however, the solution possessed enough Se to satisfy the minimum requirement to maintain stability, unlike the 0.5 M sample. The TEM images show the potential with the 0.6 M solutions as they have semi-square ordering nanostructures, however, the NC size has slightly increased. NC uniformity then plays a major role in not developing full fledge symmetries since NCs of similar size typically come together.

In the sample of 0.7 M, we encounter, again, larger PbSe NCs than the previous concentration. Heavy concentrations of NCs within the thin regions of the copper-mesh grid speaks to a certain level of uniformity being reached. TEM images here also feature NCs making contact to neighboring NCs, almost as if to form hexagonal symmetries throughout.

For the 0.8 M sample, the NC yield and concentration within the colloidal solution allows one to witness multilayer NCs. The NC size for this batch is larger than the previously mentioned concentrations, which allows for this high NC yield to occur, though the absorbance peak is still broad.

As the absorbance spectra for sample 0.9 M shows as narrow and sharper peak than the previous concentrations, the high yield contributes to an overflow of NCs now along the thin copper-mesh

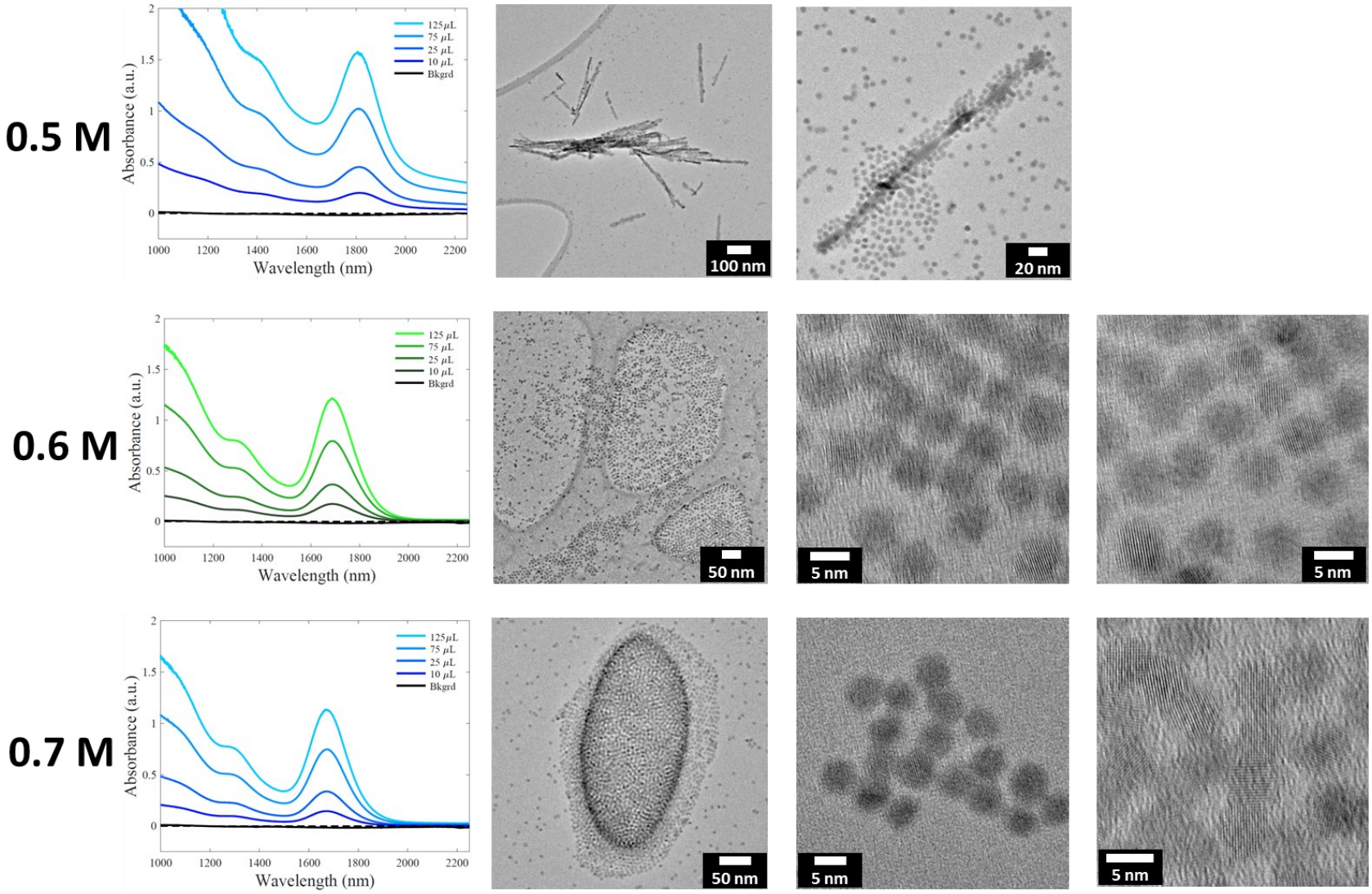

Fig. 3.56 | Absorption spectra (*left column*) & TEM images (*three right columns*) of PbSe NCs varying in Se molarity. Row 1: (a), (b), (c) - 0.5 M Se; Row 2: (d), (e), (f), (g) – 0.6 M Se; Row 3: (h), (i), (j), (k) – 0.7 M Se

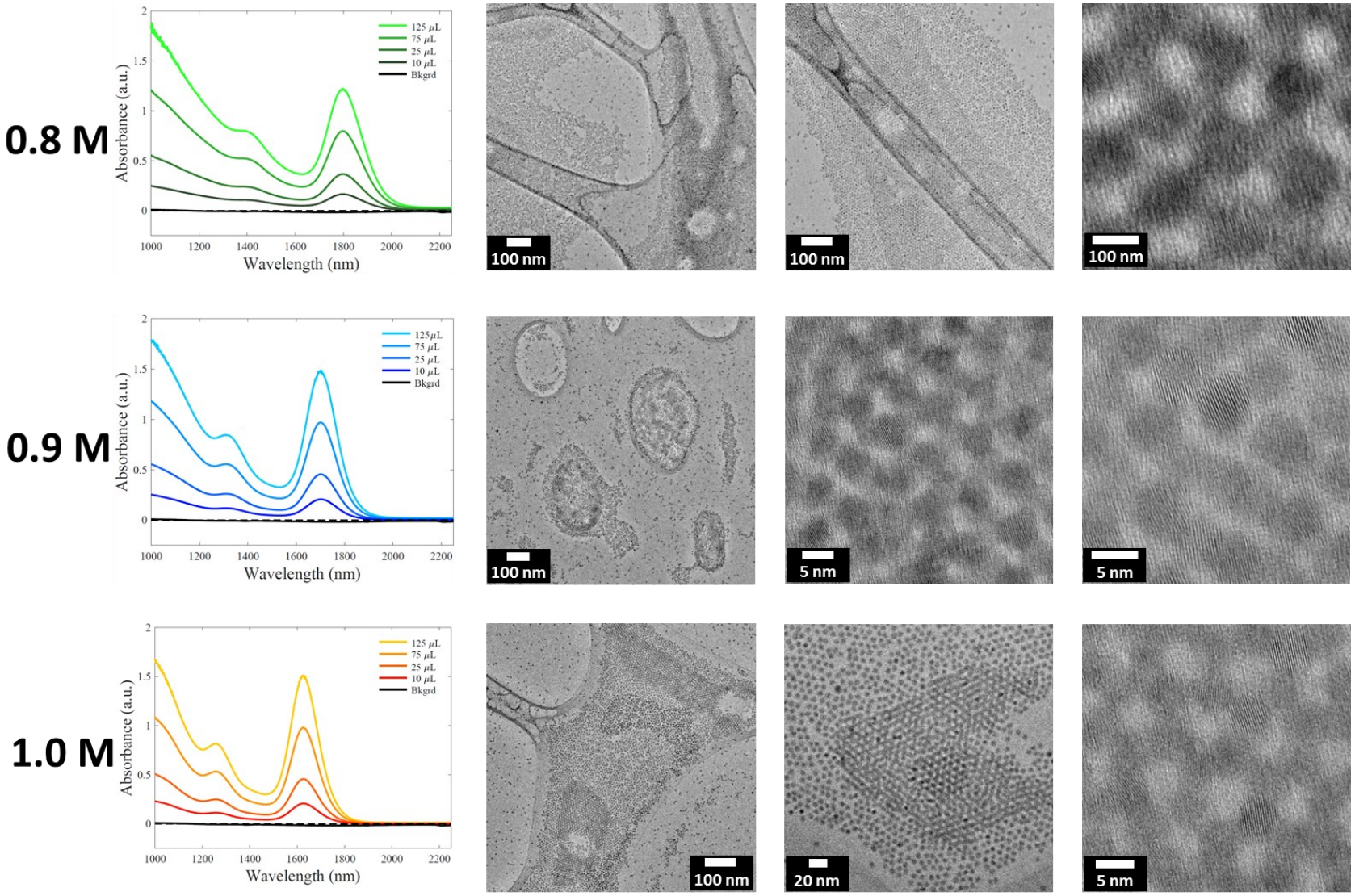

Fig. 3.57 (*Fig. 3.56 cont.*) | Absorption spectra (*left column*) & TEM images (*three right columns*) of PbSe NCs varying in Se molarity. Row 4: (l), (m), (n), (o) – 0.8 M Se; Row 5: (p), (q), (r), (s) – 0.9 M Se; Row 6: (t), (u), (v), (w) – 1.0 M Se

Table 3.6 | Average diameter size on nanometer scale from each PbSe synthesis that varied in Se concentration from 0.5 – 1.0 M.

Molarity of Se in PbSe NCs (M)	Avg. NC Diameter Size (nm)
0.5	2.79 ± 0.49
0.6	2.84 ± 0.29
0.7	2.92 ± 0.27
0.8	3.25 ± 0.26
0.9	2.93 ± 0.2
1.0	2.67 ± 0.18

grid as well as visible multilayers throughout. Possessing one of the lowest standard deviations, this sample seems to hold more uniformity than most of the others. TEM images of the 0.9 M sample show NCs making facet contact, reflecting the high uniformity within the sample.

The sample with a Se concentration of 1.0 M exhibited the sharpest absorbance peak and hence, the lowest standard deviation. This quality, along with the high NC yield, is due to the high Se concentration going into the synthesis. The NCs assemble into *bcc* symmetry, but without the high Se concentration, the other solutions could not fabricate enough NCs to even attribute to such symmetry.

One can see an obvious change in morphology as we increase Se concentration, through Figs. 3.56 and 3.57. As a result of low Se concentrations, PbSe NCs experience transformations into rod/nanowire-like features. This confirms staying at a 1:1 molar ratio is still the best option for fabricating PbSe NCs, as it also produces the best case for overall NC uniformity.

Those above (samples 0.5 - 1.0 M) lacked interconnectivity over large volumes. We therefor conducted an investigation into how much of the OA capping ligand was removed through the clean-up procedure as revealed vis NMMR, with the results shown in Fig. 3.58.

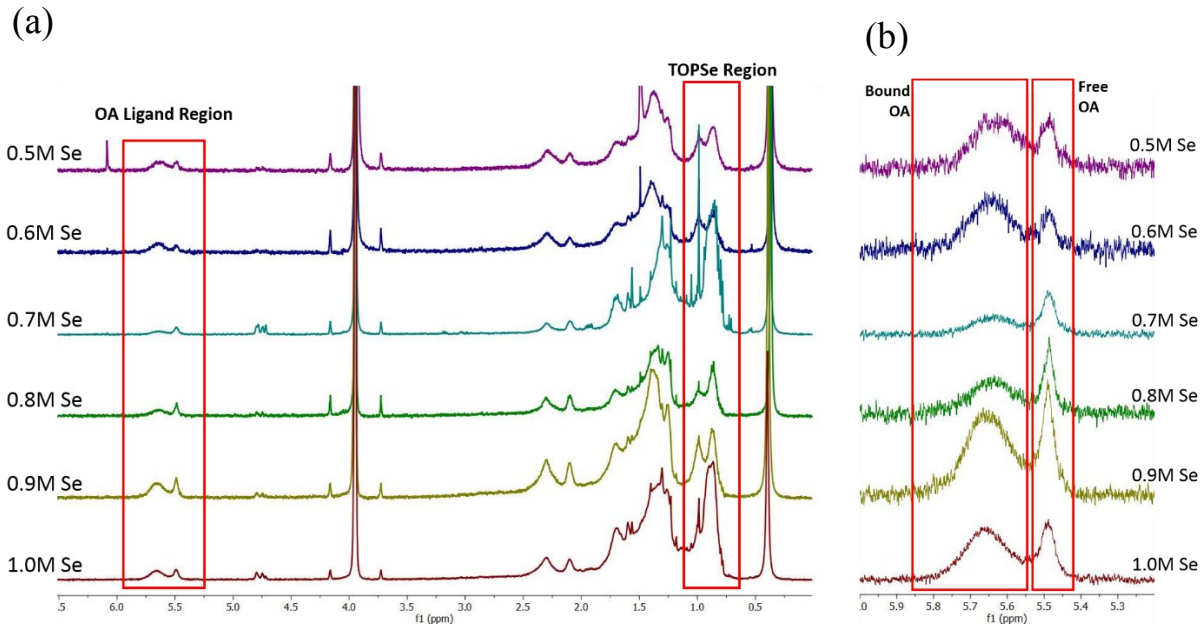

Fig. 3.58 | ^{1}H NMR spectra of isolated TOP-PbSe NCs. (a) Right red box: TOP-PbSe region; Left red box: Signals of free and bound oleic acid. (b) More detail on free and bound oleic acid throughout samples varying in Se molarity (0.5 – 1.0 M).

Ignoring the TOPSe region of the spectra and only observing the OA capping ligands highlighted in Fig. 3.58b, one can see free and bound oleic acid within the colloidal solutions prepared. Samples 0.5 and 0.6 M show quite large bound OA peaks, while samples 0.7, 0.8 and partially 0.9 M have quite sharp peaks of free or unbound oleic acid capping ligands.

3.5.2 Oxidation in TOP-PbSe-DPP NCs

Fabricated PbSe NCs experience oxidation soon after the above-mentioned synthesis has been carried out. This was initially realized by way of absorbance spectra, which can be seen in Fig. 3.59.

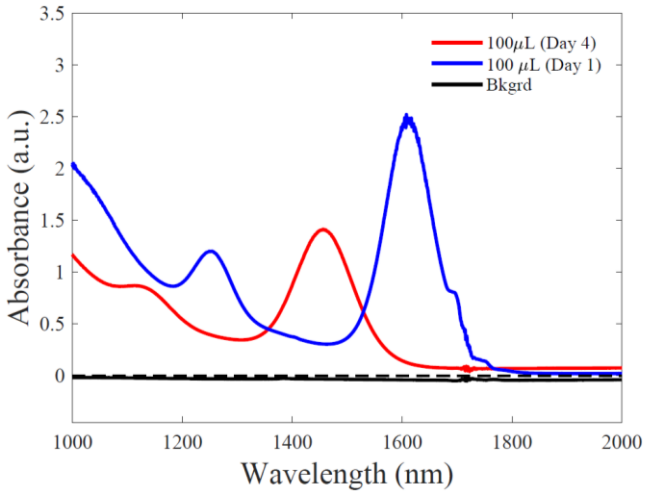

Fig. 3.59 | Absorption spectra of a successful solvothermal synthesis for TOP-PbSe NC fabrication (blue). After only 4 days of the colloidal solution of PbSe NCs absorption spectra (red) blue-shifted with the 1st absorption peak changing from 1608 to 1459 nm.

In general, we aren't concerned with oxidation in solution because the NCs are intended to be integrated into a colloidal solid soon after their creation. Nevertheless, for long-term sensor stability, we wished to find a chemical solution that makes the NCs insensitive to oxidation in the air and in solution. Looking deeper into reasons for the oxidation, we conducted decomposition measurements from NMR spectra seen in Fig. 3.60.

Experimentally, we observed the decomposition rate of the combined reaction of Pb oleate and Se precursor at 120 °C by way of $^{31}P\{^{1}H\}$ spectra. The reaction, 1M TDP-PbSe colloidal solution, decomposed by 47% in just 3 min. However, the decomposition rate of the reaction

producing 1M TOP-PbSe decomposed by 2% by 10 min. then 12% by 30 min., suggesting TDP accelerated the precursor decomposition. Thus, the very presence of TDP plays a critical role in the higher precursor and decomposition and morphology control in our TDP-PbSe syntheses.

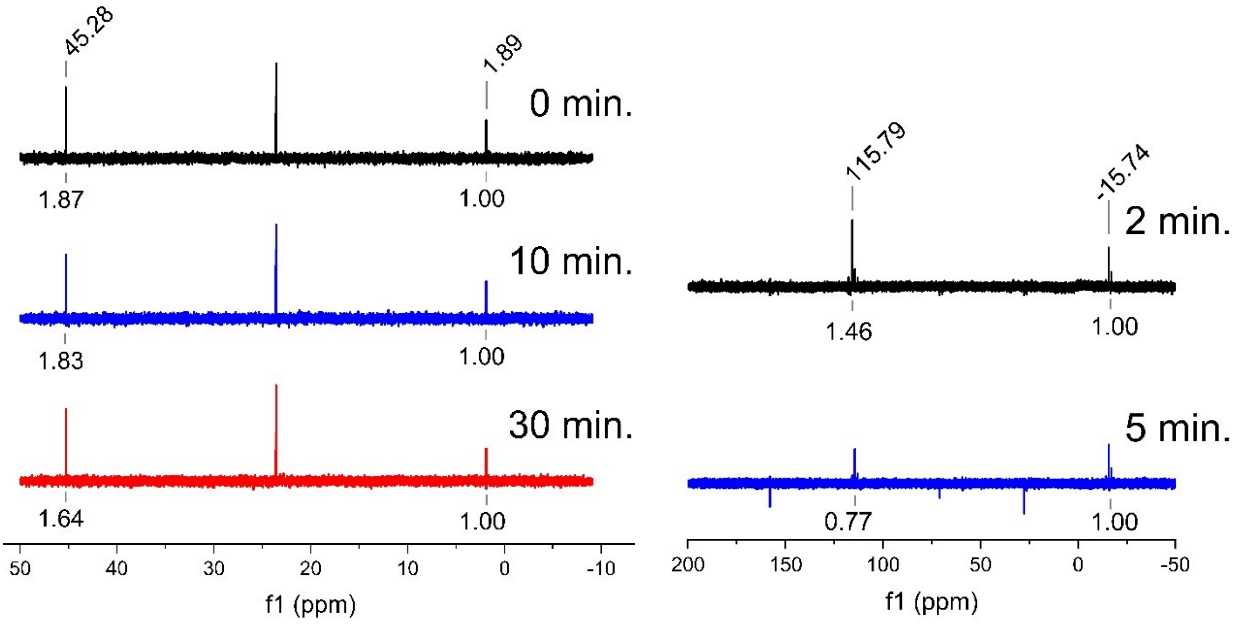

Fig. 3.60 | The decomposition of (*left*) 1M TOP-PbSe and (*right*) 1M TDP-PbSe monitored by $^{31}P\{^{1}H\}$ NMR spectra a 150 °C. (*left*) Colloidal solution decomposed by 2% in 10 min. then 12% by 30 min. (*right*) Colloidal solution decomposed by 47% in only 3 min.

It is well-known that the amine group is weakly binding on the surface of our TDP-PbSe NCs, specifically on the {111} facets.[49] It is also possible that released amine species from TDP could accelerate the attachment process removing {111} facets of PbSe. Whatever the case may be, it may be crucial to have TDPSe as a Se precursor to produce PbSe NCs.

3.6 Oriented Attachment with Liquid Substrate

3.6.1 Liquid Substrate: Ethylene Glycol

Oriented attachment was performed at room temperature. A 20 mL beaker was filled with ~10 mL of ethylene glycol (EG) to serve as an immiscible liquid substrate for the NC solution. For preparing the NC solution, 1.2 µL of a PbSe colloidal solution with an initial concentration of ~0.09 mol/L (25 g/L) was diluted by adding 50 mL of solvent for the final concentration of 3.0×10^{-6} mol/L. Once fully dispersed, a volume that would completely cover the top surface of EG inside the beaker was gently drop-casted, as seen on the left of Fig. 3.61. As the solvent dries, one can witness the NCs drawing closer together to form various nanostructures, as seen in Fig. 3.62. After solvent is fully dried, a sample was mechanically scooped by way of a TEM grid and dried in vacuum to remove any residual EG, as seen in Fig. 3.63. For assurance of the solvent being removed, the beaker was heated at 30 °C for 24 hrs. prior to sample collection.

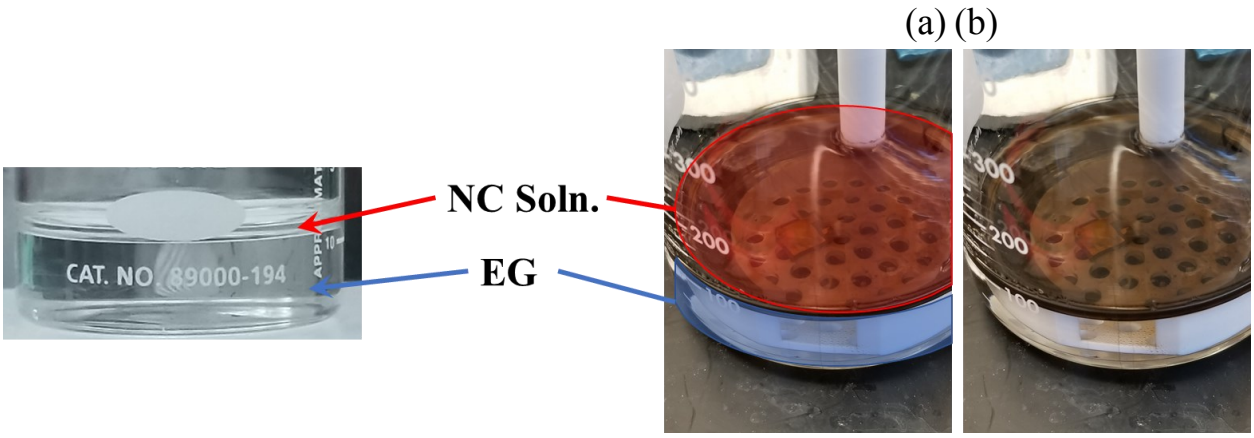

Fig. 3.61 | (a) Small open beaker possessing a thin layer of diluted PbSe colloidal solution atop ethylene glycol (EG) to oriented attachment to eventually take effect to create interconnected superlattice/s. (b) A less diluted PbSe NC solution atop EG in a 1 L beaker. A polyethylene strainer and substrate are placed within the EG as a method to apply a smooth layer of PbSe Ns across the substrate surface.

Fig. 3.62 | Topical view of PbSe colloidal solution atop EG while inside a plastic dish. These images are collected after toluene solvent has completely dried and the PbSe NCs have transitioned and/or rotated into their final spots.

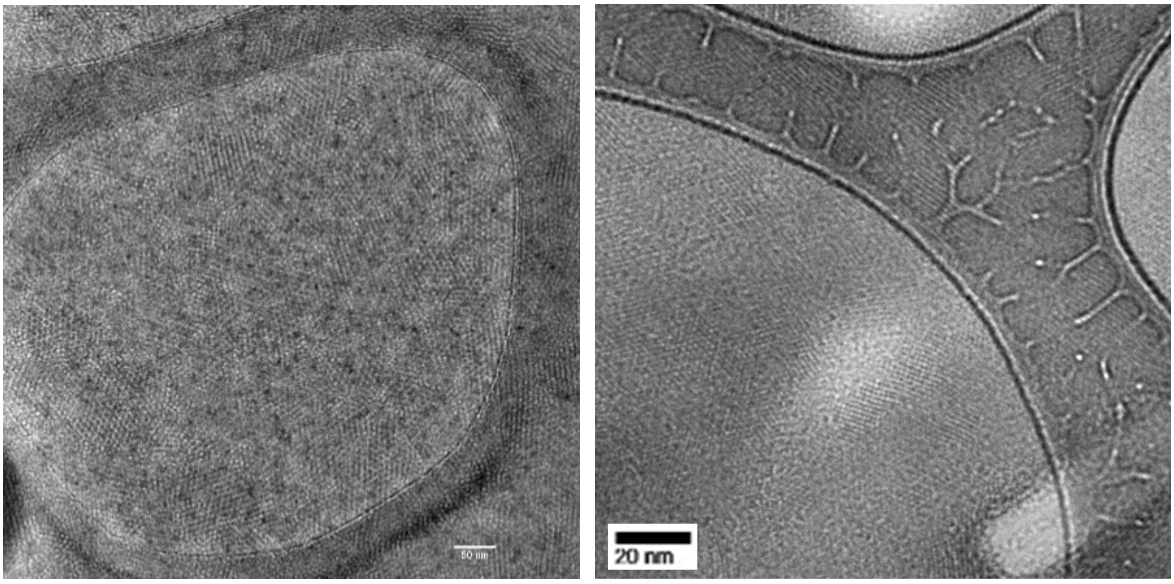

Fig. 3.63 | Fabricated superlattice after a dense PbSe NC layer experienced oriented attachment for an extended period. Copper-mesh grid still collects samples possessing multiple layers of PbSe NCs which formed into superlattices.

Results

Refer to Section 3.2.4 for a phenomenological discussion of the nature of oriented attachment, as in Fig. 3.64.

Experimentally, the NCs start with complete dispersion in the solvent of choice. One could think they may experience many collisions once casted onto EG, however, with hydrocarbon chains still surrounding each NC at this point, an entanglement of the extensive hydrocarbon chains would occur, truly preventing NCs from getting close enough to join in any capacity (option 1, in Fig. 3.65). NCs then adsorb at the solvent/air interface until the solvent fully evaporates since, at that point, it is the only interface in existence for the NCs to be associated with. Once the solvent does fully evaporate, the lower half of the NCs become half-immersed in the EG while the upper is half-immersed into the air, representing NCs getting adsorbed at the EG/air interface. This results in the NCs forming into monolayers and/or a superlattice with hexagonally packed ordering, as seen in Fig. 3.65a. Over time, the nanostructure of hexagonal order gradually converts to a square geometry, as seen in Fig. 3.65 (c, d). During this transition, residual solvents evaporate and NCs can align one of their <100> directions perpendicular to the surface of EG. Attractions along the {100} or {111} NC facets, perpendicular to the interface, rotate towared each other involving themselves in oriented attachments. As a result, the NC–NC distance gets increasingly reduced. If a superlattice is present it could then change from hexagonal to square ordering as Fig. 3.65c shows the slow superlattice transitioning from one to the other. This then forms a tightly packed nanostructure which can be seen through an SEM of Fig. 3.65e. Success was achieved in this PbSe synthesis somewhat truncated nanocubes possessing uniformity in size and shape after many experimental repetitions (Fig. 3.65d).

The close-packed square-ordered colloidal assemblies composed of square-shaped PbSe NCs, in Figs. 3.65 (d, e), are particularly intriguing from the perspective of one wishing to detect highly penetrating ionizing radiation. In particular, one of the potential drawbacks of a nanostructured solid is the lower density than the equivalent single crystalline or homogeneous solid. Ideally, one

would prefer to grow the NCs into square-shaped solids that align along their axes, similar to that shown in the figures, rather than to utilize spherical-shaped NCs that have both a small contact area overlap and substantial open volume. The challenge in using square NCs in large-scale assemblies is the reduction in the symmetry of the NC which restricts the degrees of freedom with which the NCs can self-assemble.

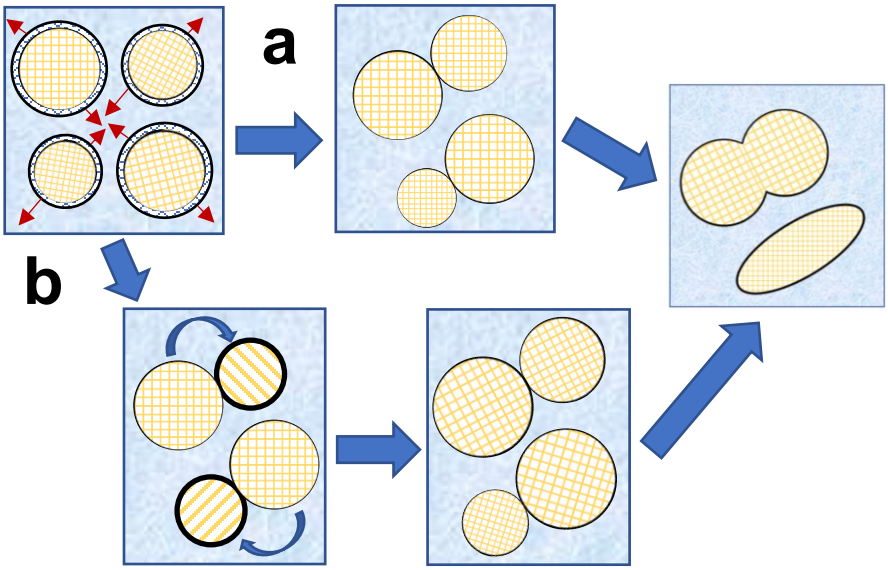

Fig. 3.64 | Schematic of oriented attachment by way of (a) collision of particles or (b) particle rotation.

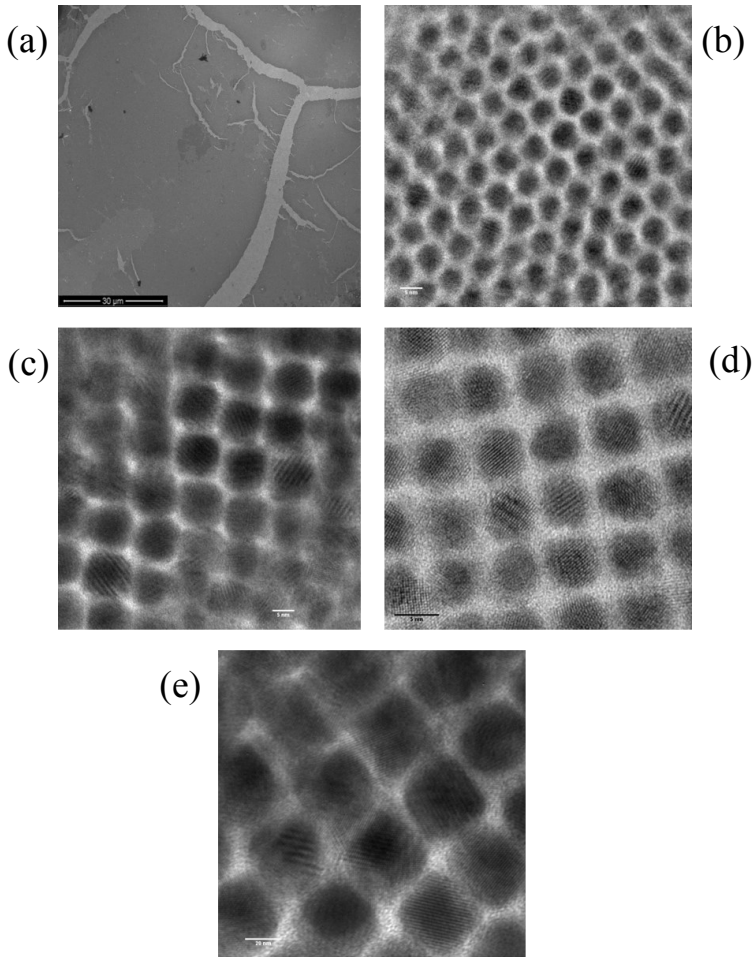

Fig. 3.65 | TEM micrographs of PbSe NCs in (b) hexagonal symmetry and (c) square symmetry. (d) PbSe NCs experiencing square ordering after oriented attachment has occurred, however, with the extension of {111} facets applied. (e) The PbSe NCs transitioning and/or rotating from hexagonal ordering into new positions of square ordering by way of the process of oriented attachment. (a) SEM micrograph of PbSe NC superlattice and/or NC films look in low-resolution.

Six {100} and eight {111} facets comprise the PbSe NCs, where the Pb and Se atoms are combined to form the {100} facets while the {111} facets are comprised of only Pb or Se. Due to the variation in electronegativities between Pb and Se, {111} facets come to be polar, leaving their structure to determine how electric charge is distributed within the PbSe NC. The most straightforward way to maintain PbSe stoichiometry is to terminate four (of the eight) {111} facets

with Pb and the other four with Se. An entire NC normally lacks central symmetry and has a dipole moment along the <100>, <110>, or <111> axes, depending on how the {111} facets are arranged, respectively.[49] This may explain why PbSe NCs are oriented along different crystallographic axes, with the majority of PbSe NCs in a distribution having a dipole moment greater than zero.[49]

NCs of uniform scale and morphology have been commonly manufactured using EG.[199, 225, 256-257] When using EG for oriented attachment, the capping ligands, which are hydrocarbon chains, penetrate into the EG once the NCs meet the EG/air interface. This may result in the acyl chain organization to detach the weakly attached capping ligands of the {100} facets and possibly the capping ligands as well. The detached ligands are then adsorbed by EG, allowing NCs to then rotate freely into other attractive facets. The NC lattice cannot be seen in the structure until the capping ligands are removed. The NCs come closer together as more capping ligands are removed over time. The superlattice then takes on a hexagonal symmetry due to the directionality of the in-plane {100} attractions. It may even apply a bcc nanostructure due a to multilayered assembly as seen in Fig. 3.66 (a, b).

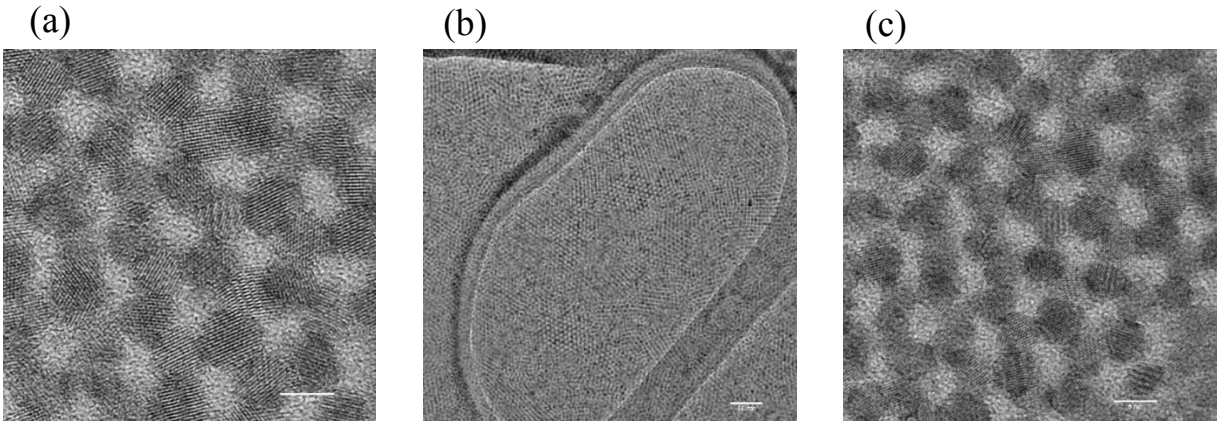

Fig. 3.66 | TEM micrographs of PbSe NCs after experiencing oriented attachment and thorough drying period. Both (a) and (b) show *bbc* ordering once the degree of freedom has allowed the NCs to reach then attach to {111} facets of neighboring PbSe NCs.

The longer the NCs sit atop the EG, the more likely the superlattice will eventually shift to square symmetry. The reason for the delay may be due to leftover solvent from ligand corona or pockets between capping ligands.[256] Since the limited volume of solvent is not the bulk solvent, evaporation of the solvent in these areas may take a longer time to complete. The NCs are eventually able to coordinate their <100> directions perpendicular to the EG/air interface after the solvent remains have been fully removed. However, electrostatic and van der Waals interactions between opposed {100} facets increasingly limit rotational independence. Overall, the directed connection mechanism observed here may be called a statistical process governed by collision frequency.[258] Because of this, isotropic and anisotropic NCs of different directions can be observed during the growth phase of superlattices.[259-260] This is one of the reasons why we are seeing interconnectivity between neighboring NCs at the moment, presumably at the {111} facets.

All of the TEM micrographs above show that depositing TOP-PbSe NCs upon an EG interface successfully creates interconnected superlattices through which charge can flow. However, the challenge of growing millimeter-thick samples from a liquid-interfacial approach remains unsolved. Specifically, we repeatedly dipped a substrate upon the interface as a way to build-up the thickness, however, the growth was non-uniform. Furthermore, this proved to be a far less facile manufacturing approach than the TDP-PbSe solution-growth approaches. Nevertheless, this interface-induced ligand removal remains an attractive option to making nanostructured sensing structures.

3.6.1.1 Nanowire-Like Structures

While tightly packed nanostructural geometries were created, minor and major irregularities were also made. Instead of an overall connection, we saw long stretches of intertwined PbSe NCs within thin sections of the copper-mesh grid. Though our chemical reaction was carried out at a low temperature to prevent the formation of nanowires (e.g., interaction at 180 °C and growth at 150 °C),[49] our drying process was usually carried out at room temperature. Naturally, nanowires have low crystallinity and various stack faults at room temperature, which tells us the state of nanowire-like assemblies can be even worse since the temperature is a step below that of room termperature.[49]

The growth of nanowire-like assemblies is likely to be governed by an avalanche-like mechanism, led by a combination of increasing polarizability and scaling of the dipole moment of the growing PbSe nanowire-like pieces as the number of attached NCs increases, just like actual nanowire expansion. NCs are pushed to bind to the ends of nanowire-like assemblies when their dipole moment is greatest along the <100> axis, according to this theory.[49]

PbSe nanowire-like pieces expand radially after being formed by adsorbing Pb and Se precursors from surrounding solutions. Smooth nanowire/nanowire-like fragments would have resulted if the growth of the (111) planes had been steady. In our case, however, the {111} facets do not terminate with development, resulting in such smoothness. It is likely that the molecules' strong binding on the nanowire-like pieces surface slows growth on both the (100) and (111) planes, providing more time for atom diffusion on nanowire-like piece surfaces. Another explanation is that there isn't enough Pb and Se precursor within the solvent.[49]

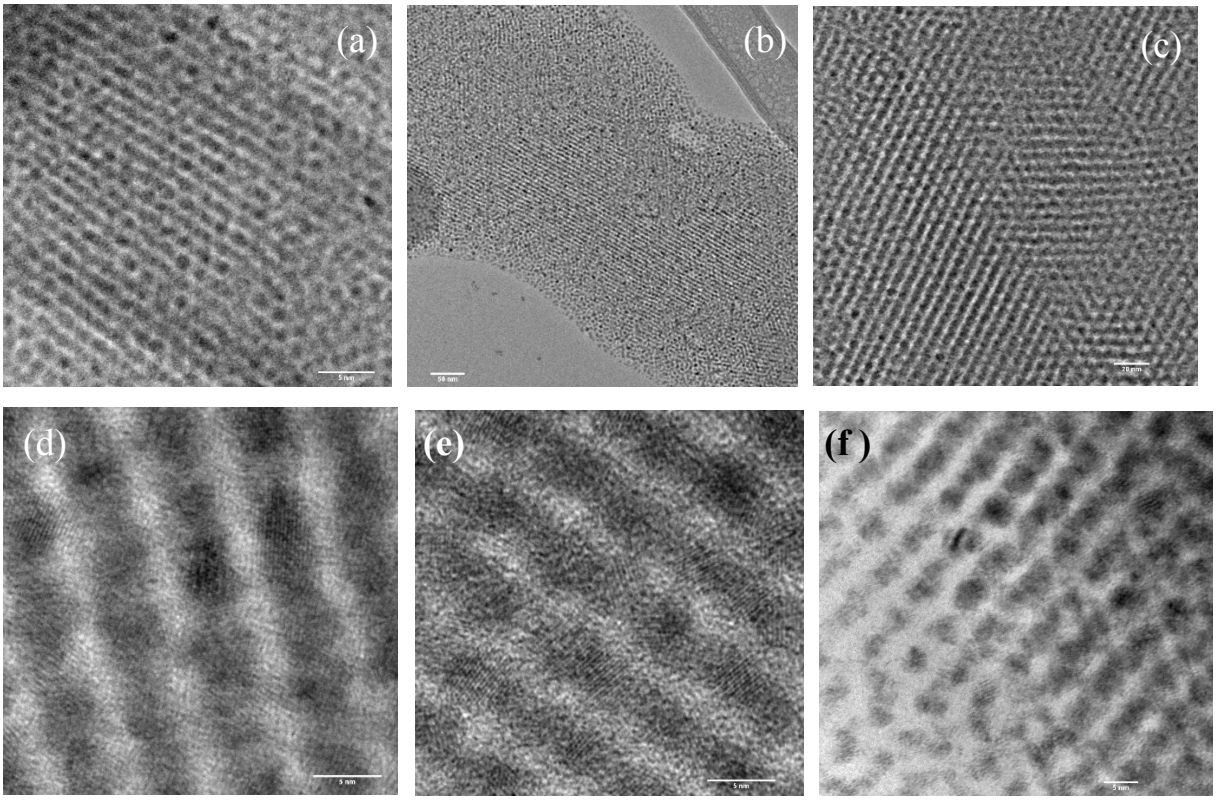

Fig. 3.67 | TEM images of nanowire-like assemblies throughout. Both (a), (b) and (c) show low-resolution imaging as a way to observe the lengths they cover. Images (d), (e) and (f) being high-resoluion imaging providing detail of their structure with PbSe NC building blocks.

3.6.1.2 Excess Fluid

It was very evident in the SEM imaging when either the EG or solvent had not completely evaporated. Fig. 3.68 demonsrates this, with unexpected aliquots and breakage in what was meant to be a closely-packed network of PbSe NCs. Though large potions of NC superlattices can be seen in, the interference of the solvent/EG can truly reduce the chances of collecting a promising sample for further examination. Applying the PbSe colloidal solution atop the EG softly is key just as much as allowing a more than reasonable time for drying samples for further characterization.

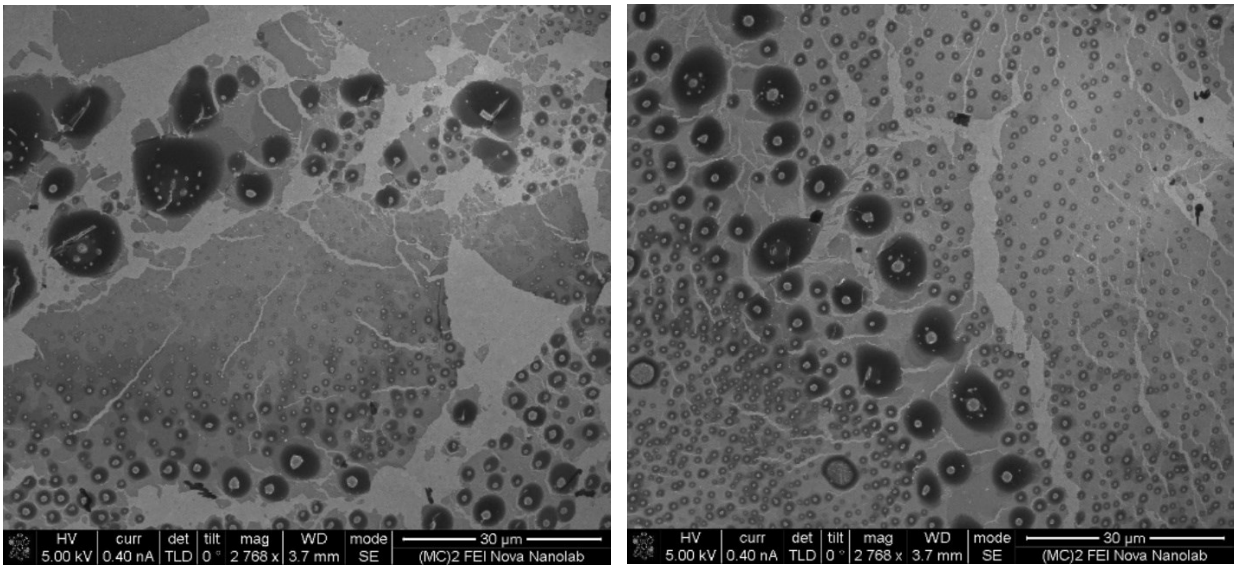

Fig. 3.68 | SEM images showing samples of broken up superlattices along with a solvent/EG combination which has yet to fully evaporate from sample prior to image collection. Aliquots throughout the sample provide great reason to need to wait for full evaporation prior to moving forward for device fabrication.

3.6.1.3 Interatomic Bonding

Oriented attachment in the presence of EG also resulted in the creation of nanowire-like networks, some possessing far more distortion/deformation than the closely-packed hexagonal and square ordered structured with only slight distortion/deformation. This separate deformation action of EG has significant impact on the superlattice formation processes and structural perfection. With high NC concentration, similar square superlattices can be obtained in EG through a topological pathway of symmetric growth from small to larger squares. The resultant superlattices are more uniform and less flawed because NCs in pure EG retain their initial shape during self-assembly (e.g., fewer missing connections).[261-262]

We consider two possibilities in order to explain the fundamental cause of distortion within superlattices and how it is related to the symmetry of the interaction potential: (1) electrostatic interactions arising from dipole-dipole coupling of proximate NCs, or (2) forces dependent on anisotropic interactions between surface-bound ligands.[261] Analogies to similar effects in atomic crystals has led to the theory that dipole-dipole interactions are the driving force behind the coherent NC superlattice distortion. Electronic interactions that contribute to lattice structure transformation in atomic systems include the Jahn-Teller effect and martensitic phase transitions.[49, 262-265] Since NC superlattices can be thought of as artificial crystals, we hypothesized that dipole-dipole interactions between neighboring NCs could cause similar symmetry distortions. Specific NCs with cuboctahedron shapes or charged surface states are thought to have an uneven distribution of Pb- and Se-terminated {111} facets, resulting in dipole interactions.

In the presence of toluene vapor, ligand–ligand interactions take precedence over ligand–solvent interactions, resulting in an anisotropic interaction potential that represents the NC core's structure, resulting in the development of a *bcc* NC superlattice with a high degree of orientational and translational order. This can be seen in Fig. 3.69 while another form of it was also witnessed earlier in Fig. 3.66. Solvent uptake in the NC superlattice can also swell the assembly in the presence of saturated octane vapor, eventually resulting in totally disordered thin films of saturated NC suspension. Unlike the traditional view, which assumes that the NCs have a rigid form during superlattice self-assembly before connecting to each other, we discovered that that NCs can dramatically change shape before touching each other.[257] This demonstrates how after the surface ligands are separated, NCs are not always rigid. It may also demonstrate how ligands may not cause a "long" -range interaction.

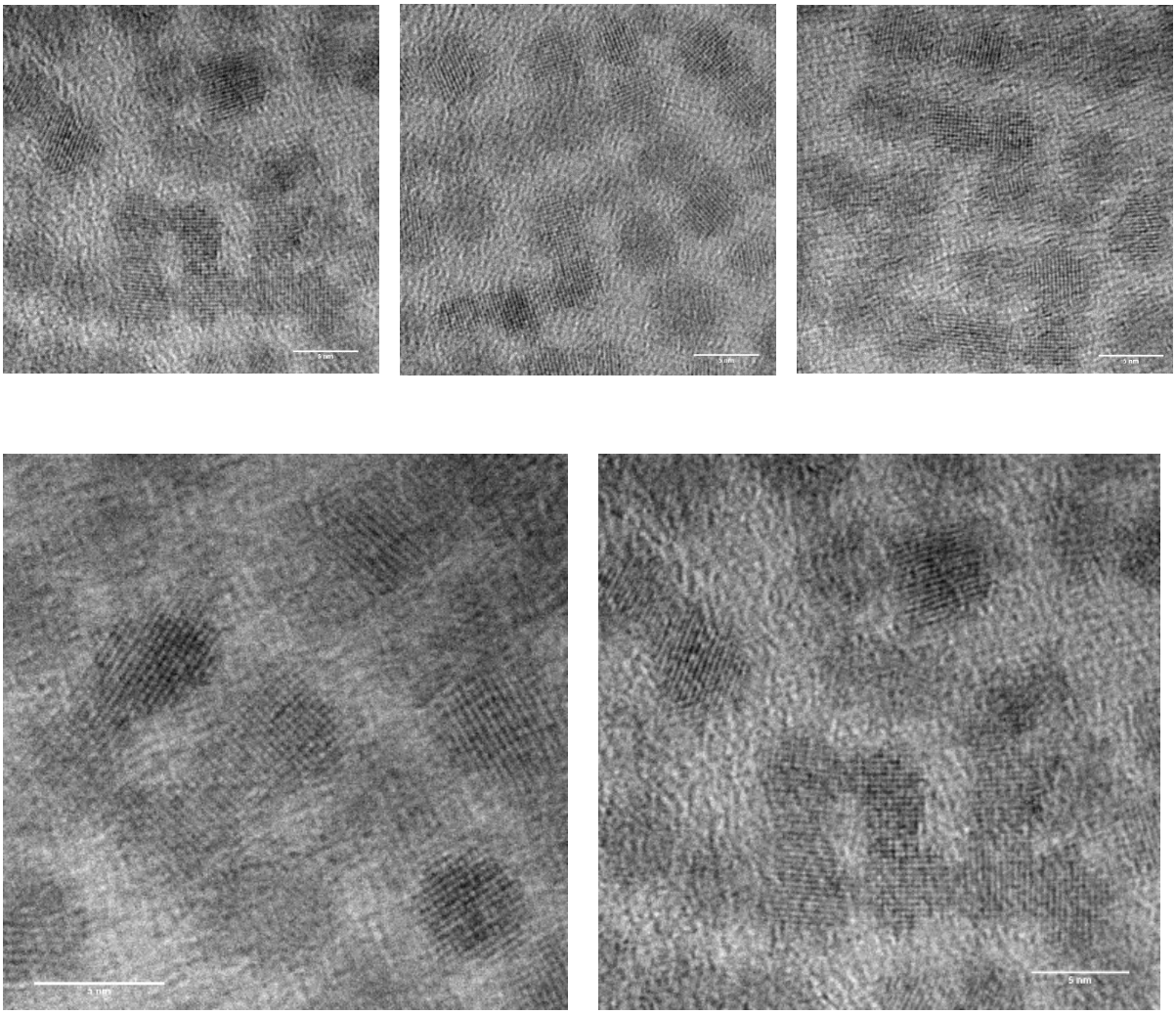

Fig. 3.69 | TEM image displaying PbSe NCs after capping ligands having been completely detaching from their NC surface and toluene/EG comdination has completely evaporated from sample. All images show NCs sharing atomic lattice throughout as well as NCs rotated in various directions based on the atomic lattice which is seen. Free from capping ligands, the PbSe NCs either join or fuse together as a way to show oriented attachment was indeed successful.

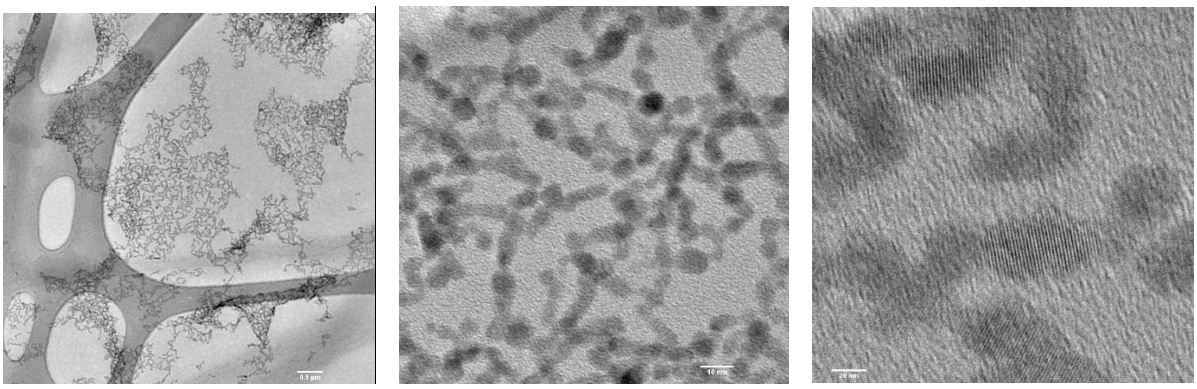

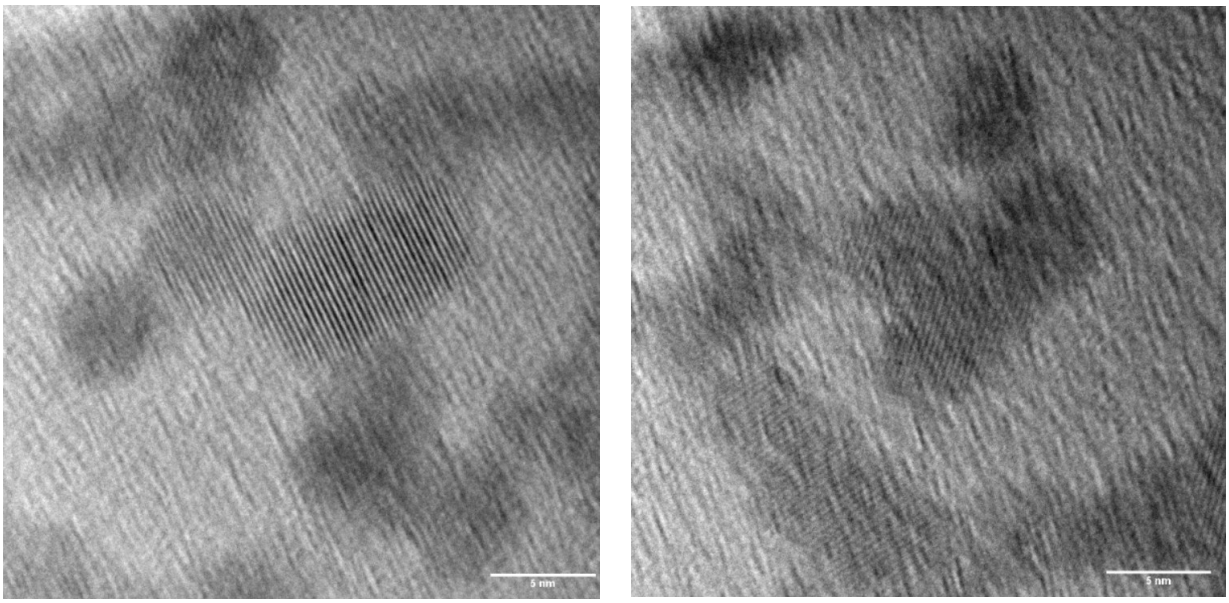

Fig. 3.70 | Free from capping ligands, the PbSe experience a change in shape due to octane/octanol solvent combination. It is implied the NCs surface is not as rigid, as an interconnected network of NCs form in a disordered nanostructure.

3.7 Device Fabrication

3.7.1 Photolithography: Silicon Wafer Substrate Design

The chemical recipes used to form colloidal dispersions can be found in the synthesis Section 3.1.2. In the fabrication of the NC assembly detector, one forms a mold in a substrate which acts as a basin into which the colloidal dispersion is poured. Furthermore, a metal contact must be accessible in order to connect each face of the detector to the readout electronics. Typically, a silicon (Si) substrate was used for our thin-film (10's of μm to 100's of μm) detector devices. Fig. 3.71 shows the typical processing carried out for the use a Si substrate in the research. This process makes use of photolithography processes.

Initially, 4-in. silicon (Si) wafers (p-type) are cleansed with piranha then thoroughly rinsed with DIW and put through a spinner. Next, a plasma enhanced chemical vapor deposition is taken place to apply ~1.5 μm of silicon dioxide (SiO_2) to the clean Si wafer surfaces. Prior to moving forward with this process, the SiO_2 thickness is measured for assurance purposes. Lift-off resist (LOR), a chemical which provides better structural definition while carrying out a lift-off procedure, was applied and baked to the SiO_2 surface of the Si wafer. This was followed by the application of the photo-resist (PR), which was also baked atop. An AutoCAD design of 32 12.7-mm x 14.6-mm rectangular pieces within a 4" circle (Si wafer diameter) was pre-prepared and etched into a 5-in. mask plate. Within the center of each rectangle, a large square (for NC colloidal solution deposition) and small square (for electrical readout) was created. Using a mask aligner, the Si-LOR-PR wafer was then exposed to UV light with the mask plate in between to apply the designed pattern to the Si-LOR-PR wafer surface. After exposure, the PR was developed and a thin layer (100 Å) of gold (Au) was evaporated onto the entire surface of the wafer. The wafer was then placed into a chemical bath with remover PG, where it was left to soak anyway for ≥ 12 hrs. (usually left overnight). Once the desired time expires, the areas not exposed to the UV light was lifted-off the Si wafer to only reveal the Au and PR on the entire wafer. The lines stretching horizontally and vertically in Figs. 3.72 (a, b) are due the dicing of the substrate going into 32 rectangular pieces.

3.7.2 Drop-Casting Deposition

NC colloidal solution is then applied to the gold areas of each Si substrate rectangular piece. After NC deposition is carried out, a final metal contact was applied to the small Si substrate. Fig. 3.72c, shows an additional option created where several locations can be electrically tested without

the interference of possibly non-uniform areas within the NC colloidal solution using a shadow mask.

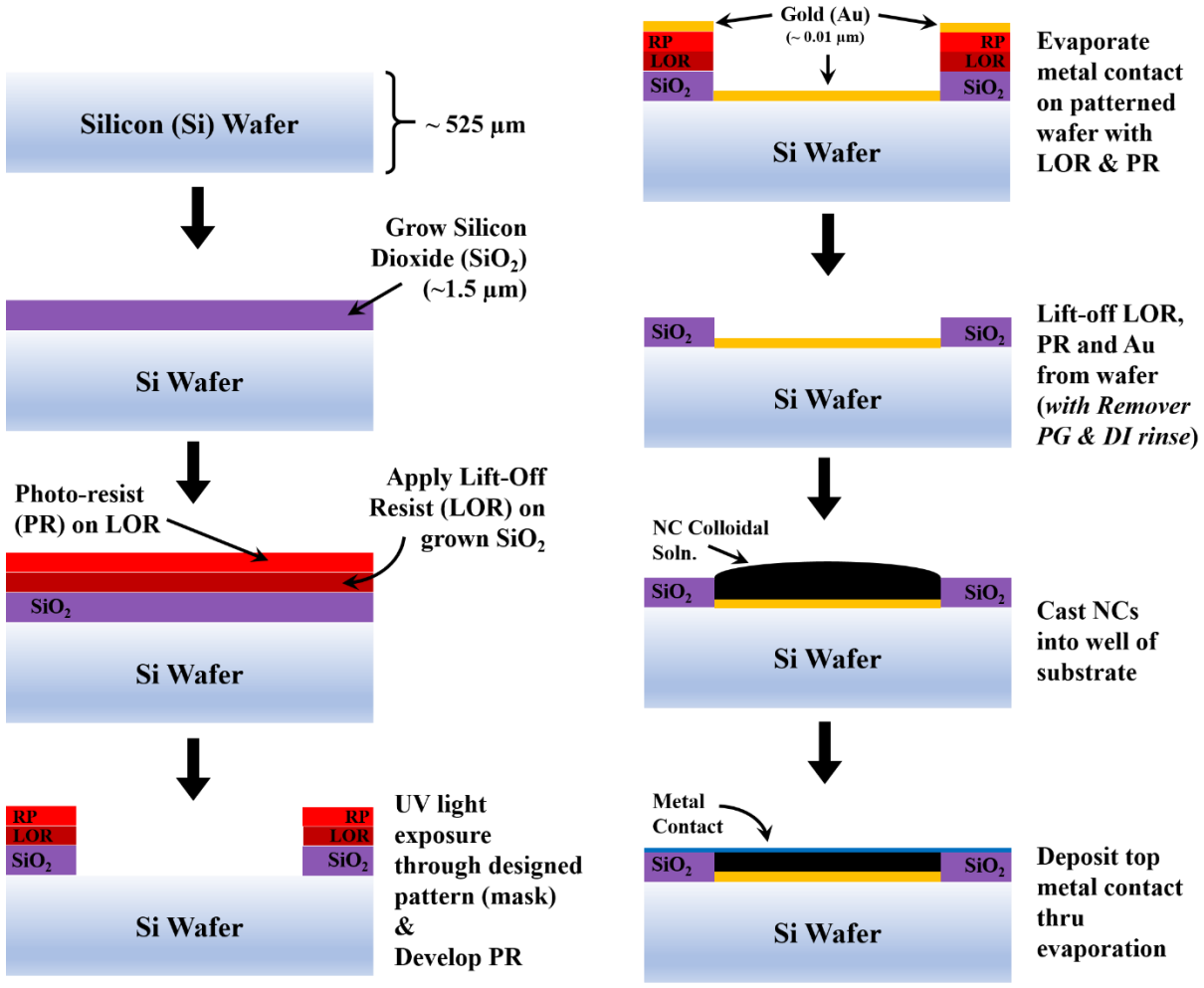

Fig. 3.71 | Schematic of silicon wafer-based NC assembly substrate fabrication procedure.

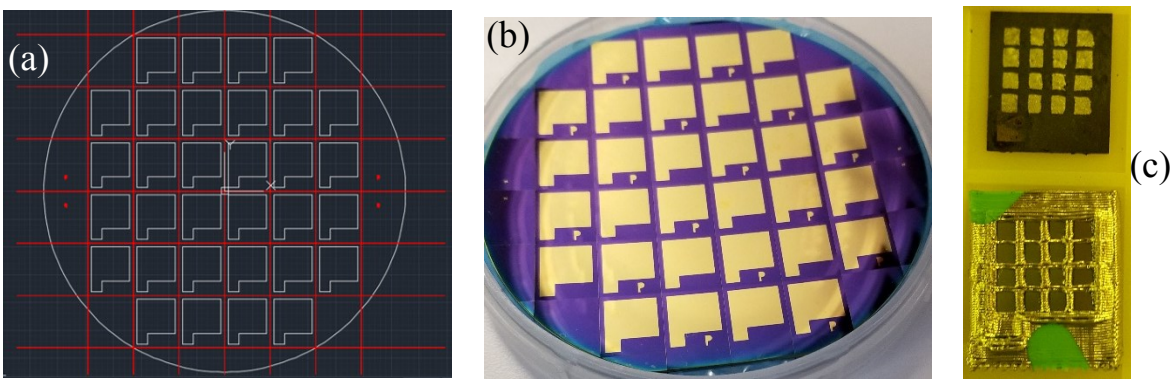

Fig. 3.72 | (a) Blueprint of 32 rectangular substrate pieces altogether within the dimensions of a circle representing a 4-in. diameter silicon wafer. A large and small square are attached and placed within each piece. (b) Final product from device fabrication procedure to produce Si wafer substrates. Blue colored tape was attached to the backside of the Si wafer prior to dicing. (c) (*top*) Fabricated Si wafer with NC colloidal solution deposited to the surface. (*bottom*) A shadow mask created and used during evaporation of top metal contact as a way to create several sections capable of being electrically tested.

3.7.3 Oriented Attachment

Following the characterization of the sample involving PbSe with EG, solvent within the NC suspensions were evaporated under either open or in an inert atmosphere at a room termperature. After a given evaporation time frame, the sample was heated to only 30 °C. Though three parameters can be varied, only (i) the initial NC concentration in the suspension ((ii) temperature at which the solvent was evaporated, (iii) temperature at which the thin film was heated), was varied. Over time, a thin film of PbSe NCs reveals itself, as seen in Fig. 3.73a. Si wafers were then used to gently retract the NC film from atop the immiscible liquid, Fig. 3.73c.

In efforts to fabricate a detector with multiple monolayers of PbSe NCs, the back of a Si substrate was attached to double-sided tape which was also attached to a manual pipet for the

freedom to extend into the container possessing EG and NCs. This overall setup can be seen throughout Fig. 3.73 (a & b).

Fig. 3.73 | Fabricated detector samples possessed multiple layers of PbSe NCs which formed into superlattices. The lift-off procedure took place several times with multiple monolayers prepared prior. The result of this procedure can be seen in the inset of Fig. 4.6.

(a)

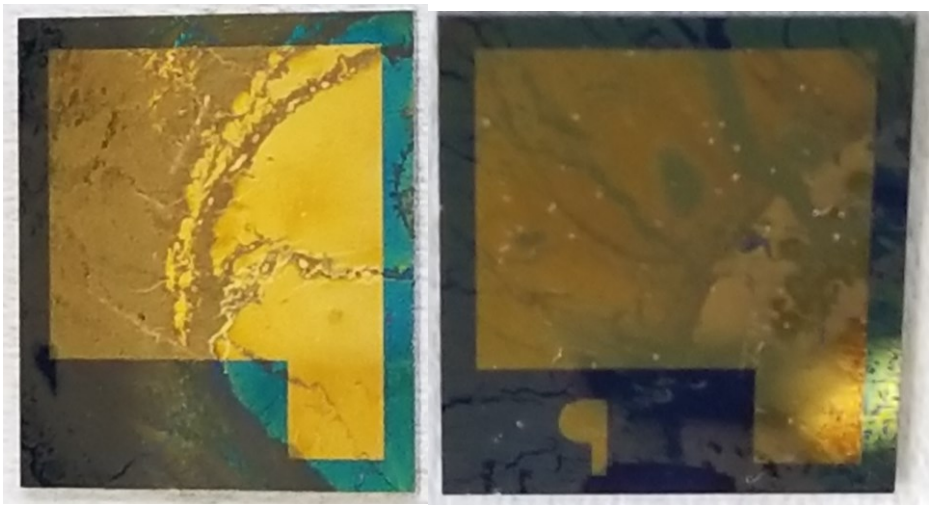

(b)

(c)

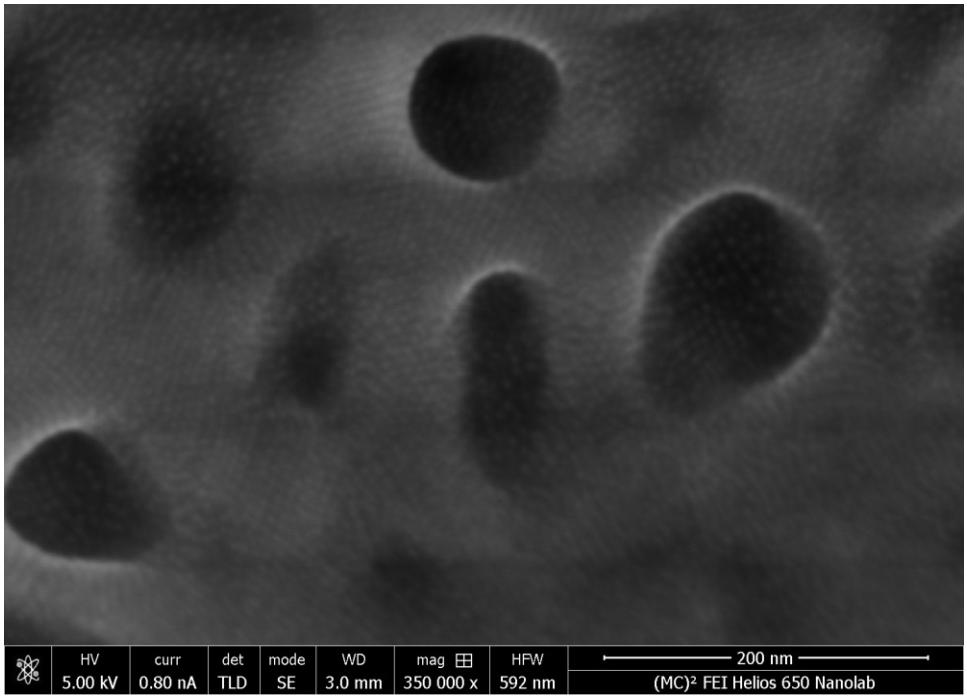

(d)

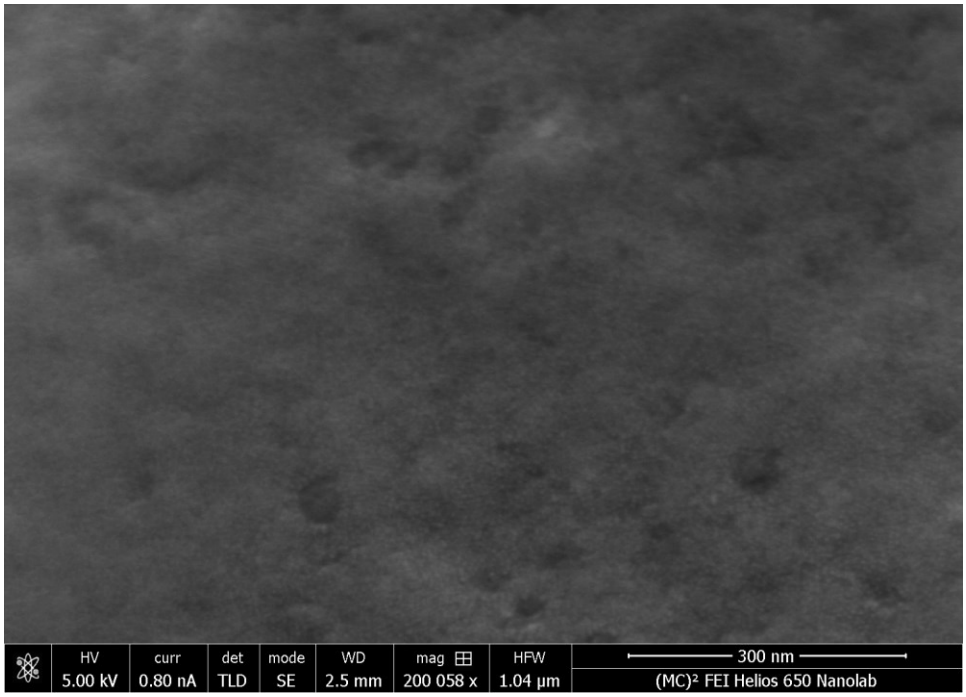

Fig. 3.74 | PbSe NCs deposited onto Si wafers. (a) and (b) reveal an optical image of how the surface of Si wafers can look after NC deposition. (c) High resolution SEM image of PbSe NCs on a Si wafer with valleys and/or indentions throughout the selected area along with views of NC ordering. (d) High resolution SEM image of a somewhat smooth PbSe NC surface on top of a Si wafer.

3.7.4 Tube-Casting Deposition

With a fabricated Si metal substrate laying on a flat surface, a small tube is placed on top with the hole of the tube over the majority of the large Au square instead of the electrode designed for readout purposes. In our setup, ~ 1.25 mL of PbSe colloidal solution is placed inside an open glass tubing, using the tube to hold the colloidal solution until the solvent completely evaporates. Additionally, this process also took place with a small vial (no lid) which simply needed to be flipped over (with the Si substrate) and placed onto a flat surface. It was hoped that this process results in QD film that atop the Si substrate, calling this method tube casting. Tube casting is carried out in open-air since at this point it has been discovered our fabricated TDP-PbSe NCs possess air-enhanced stability.

A long glass tube, with 10-15 mm wall thickness, was cut in 1-inch lengths and smoothed on the cut ends to eliminate the possibilities of scraping away any Au or SiO_2 on top the Si substrate. However, due the possible human error in either the smoothing process for the glass tube ends, the rough edges along the end rims of the tube brought on by smoothing, or the final cutting angle on the glass tubes not being an actual 90° perpendicular to the tube, this method occasionally experiences colloidal solution leakage between the tube and Si substrate. To remedy this issue more pressure was applied to possibly secure the glass-substrate connection. Increasing pressure was carried out with either weights atop the glass tube or having the deposition carried out between a laboratory scissors jack and extension clamp holding the glass tube in place. With additional concerns regarding the solvent evaporation time for the colloidal solution, changing to a solvent which allows more time for natural self-assembly to occur and a heating the Si substrate occasionally took place to speed up the process.

With the diameter of the glass-tube being so small along with exposure to air, the tube casting encountered adhesion and capillary effects along the walls of the tubing.[266] The electronegative difference between the QDs and the glass wall was greater than the electronegative difference between the QDs and the solvent used. Therefore, the QDs had the tendency to adhere to the glass tube wall. At times, adhesion would occur more intensively between QDs and tube wall as seen in Fig. 3.75.

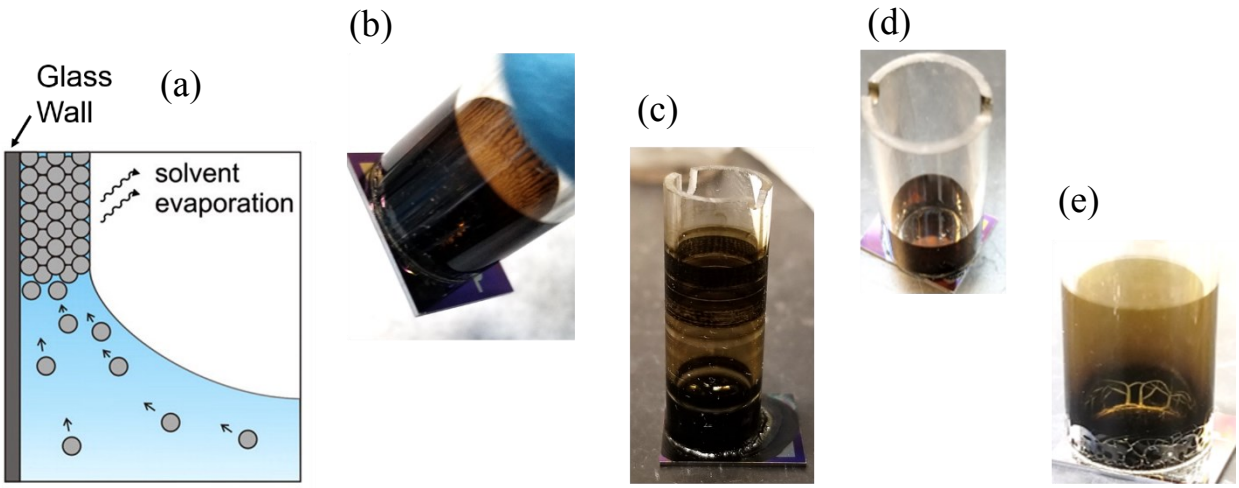

Fig. 3.75 | (a) Schematic of QDs adhering to the glass-tube wall as solvent evaporate occurs over time during glass-tube casting process. Figure adapted from reference.[266] (b, c, d, e) Visual evidence of glass-tube casting experiencing capillary and adhesion effects.

The time consumed in tube casting varied based on whether vials or open glass-tubes were used during deposition. Evaporating solvent from ~1.25 mL of colloidal solution could take up to 6 days since the system relies on vapor pressure at room temperature. However, the glass-tube method is associated with air flow while it has the open end on top which can speed the evaporation process occasionally. This could lead to deposition times of ~ 4 hrs., though the potential for cracks can still be strong.

The remaining NC solute and/or QDs that traveled to the bottom of the glass-tube and atop the Si substrate does manage to cover the surface over time; however, glass-tube casting occasionally brings about a mixed results, including cracked films and coffee ring effects once the solvent evaporated. In Fig. 3.76 one can observe results of colloidal solutions acting as glue with the rough edges along the exterior of circular QD films where the rim of the glass-tube resided during the deposition process. Cracked films and peeling atop the Si substrate can also be seen here. Outside of those two defects, glass-tube casting also brings about smooth, shiny QD films atop the Si wafer, as seen in Fig. 3.76, though visually they come across as non-uniform and wet.

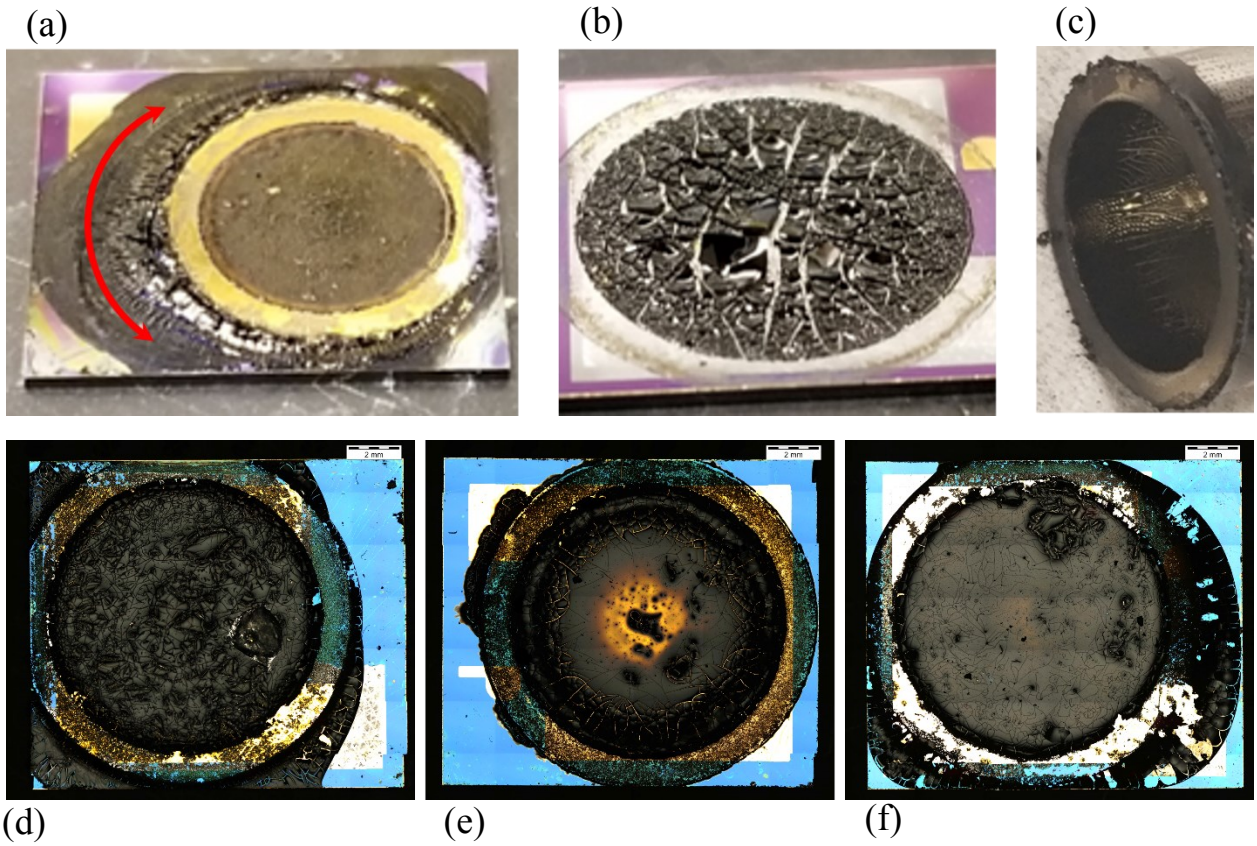

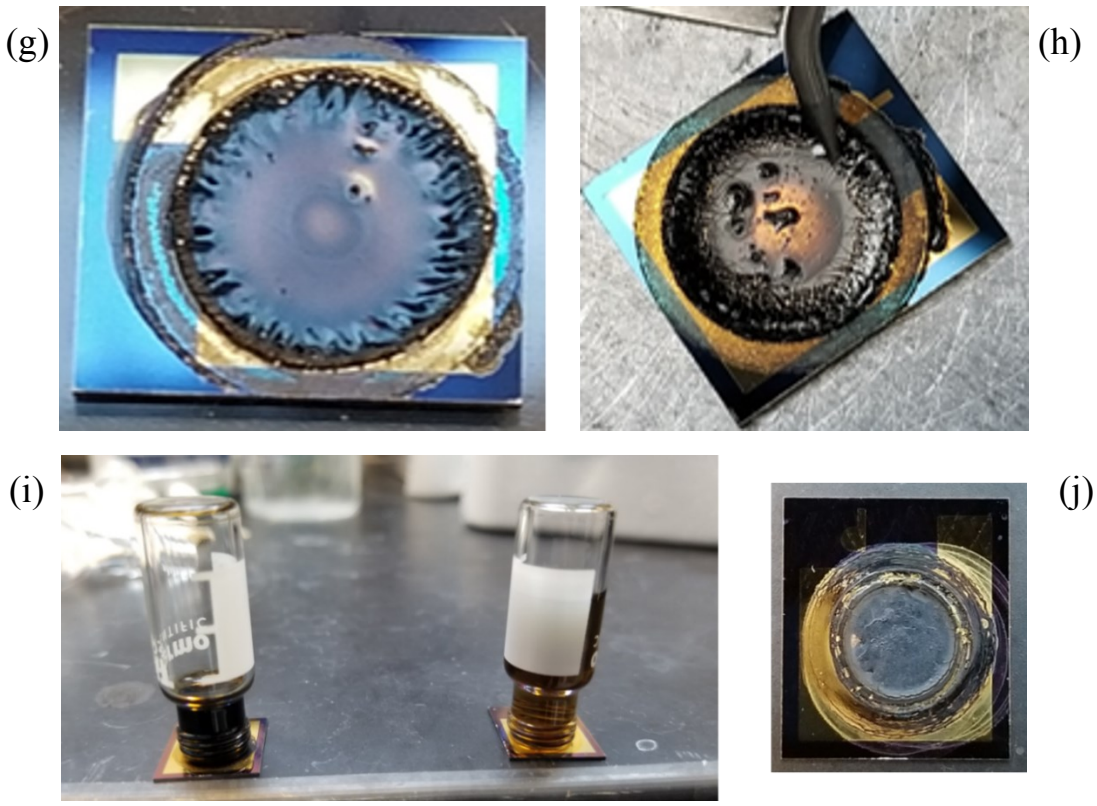

Fig. 3.76 | Results from glass-tube casting once solvent in TDP-PbSe colloidal solution evaporates inside open glass tube. (a) Dried colloidal solution after leakage (red arrow) from insecure connection between bottom rim of glass tube edge and Si substrate. (b) TDP-PbSe QD film with cracked pieces peeling, pointing upwards along the corners. (c) Result of bottom edge rim of glass-tube once removed from Si substrate tube-casting was completed. High-resolution imaging of Si substrates with QD films (device samples) on top. (d) Rough QD film with cracks throughout and colloidal solution leakage along the edges of Si substrate. (e) Non-uniform QD film on atop Si substrate. (f) Very thin QD film atop Si substrate. (g, h) Smooth and shiny QD film atop Si substrate. (d) Minor smooth and shiny areas at inner circle of the device sample along with cracks along outer thick circle of device sample. (i) Two tube-casting depositions with closed vials resulting in (j) a QD film with multiple rings surrounding.

Due to the severity colloidal solution leakage brought within this version of deposition and having QD thicknesses of roughly 50 µm, we began using automatic pipette tips (cut off tips) in the place of glass tubes. The tips benefit this process since the bottom of the tip is truly flat, allowing the tip to seal to the Si substrate, while the material itself, polypropylene (PP), can resist

the severe cases of capillary and adhesion tendencies which usually plagued the deposition. As a result, to this switch, the diameter of the QD film was smaller causing the QD film to be thicker (~ 300 µm). Coffee ring and colloidal solution leakage effects still exist with the modification, however, the desire for thicker QDs films outweighed those defects.

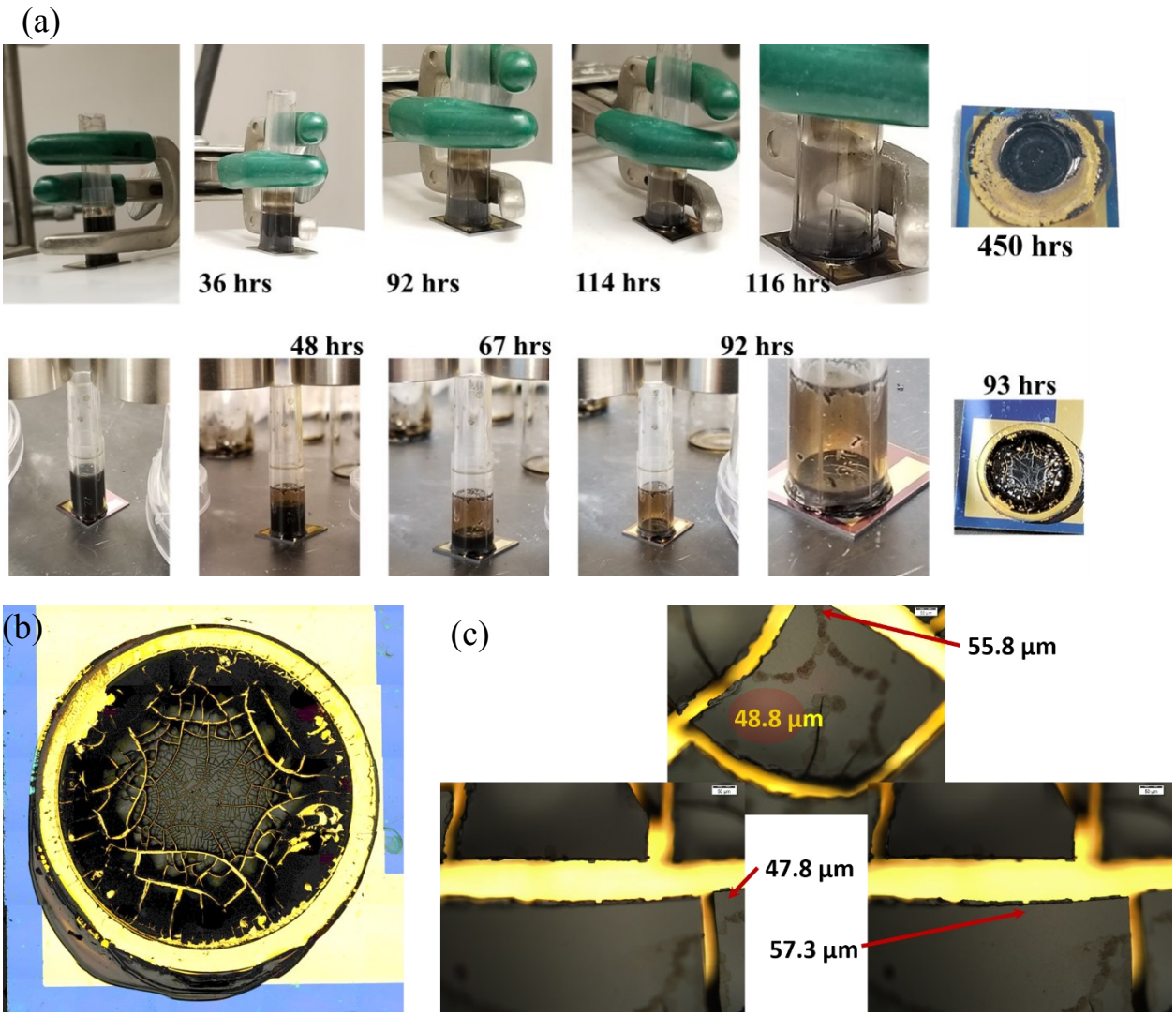

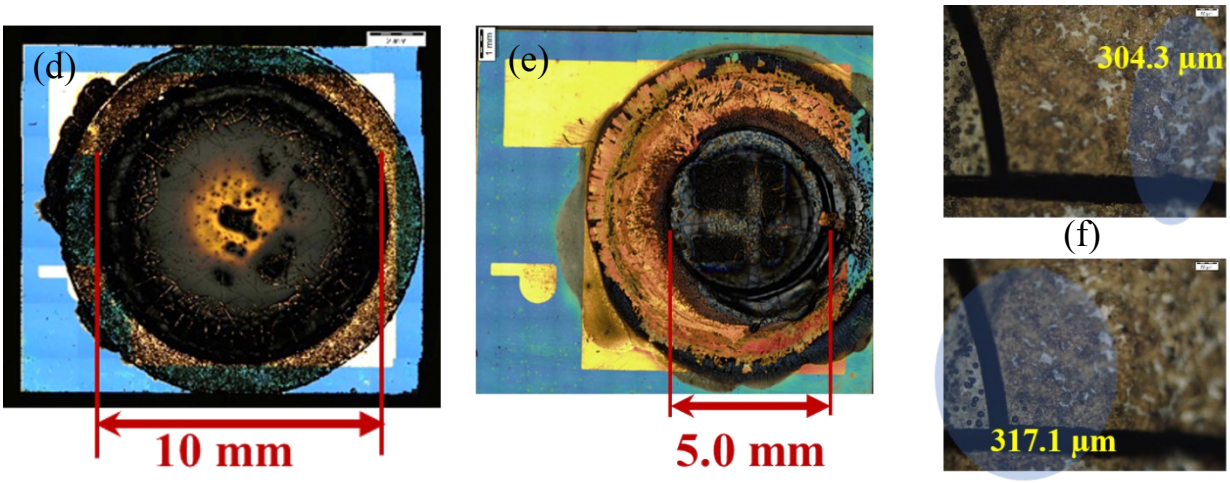

Fig. 3.77 | (a) Tube casting deposition from beginning to end with PP pipette tip being (top row) held by extension arm to secure the setup and (bottom row) weighed down by weights. (b) High-resolution image of QD film displaying cracks and (c) pieces peeling away from Si substrate. (d, e) Visual differences between glass-tube- and pipette-tube-casting. (f) High-resolution imaging of QD film thickness in various areas across the pipette-tube-casting device sample.

CHAPTER IV

Electrical Results & Evaluation

4.1 TOP-PbSe Devices

The main challenge for transforming a nanostructural concept into a high-performance macroscopic sensor is to realize good electronic coupling between neighboring NCs throughout the volume. For composite materials in general, the realization of a transformative performance is usually hampered by charge-trapping at the innumerable interfaces that the charge encounters during its drift through the solid.

During our experimentations, we successfully coordinated the colloidal ensemble using various chemical synthesis approaches that facilitate dot-to-dot charge transport, including short-chained ligands and ligand-exchange techniques with which we not only realized good charge transport, but low-Z coordinating molecules didn't substantially participate in the energy-to-charge conversions, as the high-energy recoil electrons traversed the assembly.

As a result, we measured an energy resolution of 0.16 % at a gamma-ray energy of 356 keV (from ^{133}Ba) for 7 nm diameter PbSe NCs. For 4 nm diameter PbSe NCs, an energy resolution of 0.42 % (1.5 keV) at 356 keV was realized, compared to a resolution of 0.96 % (3.4 keV) for CZT and 0.39 % (1.4 keV) for HPGe, as shown in Fig. 4.1.[6] Furthermore, this result was achieved at room temperature, with a chemical solution fabrication methodology that allows one to deposit the active material across large areas at atmospheric pressure using wet-chemistry techniques.

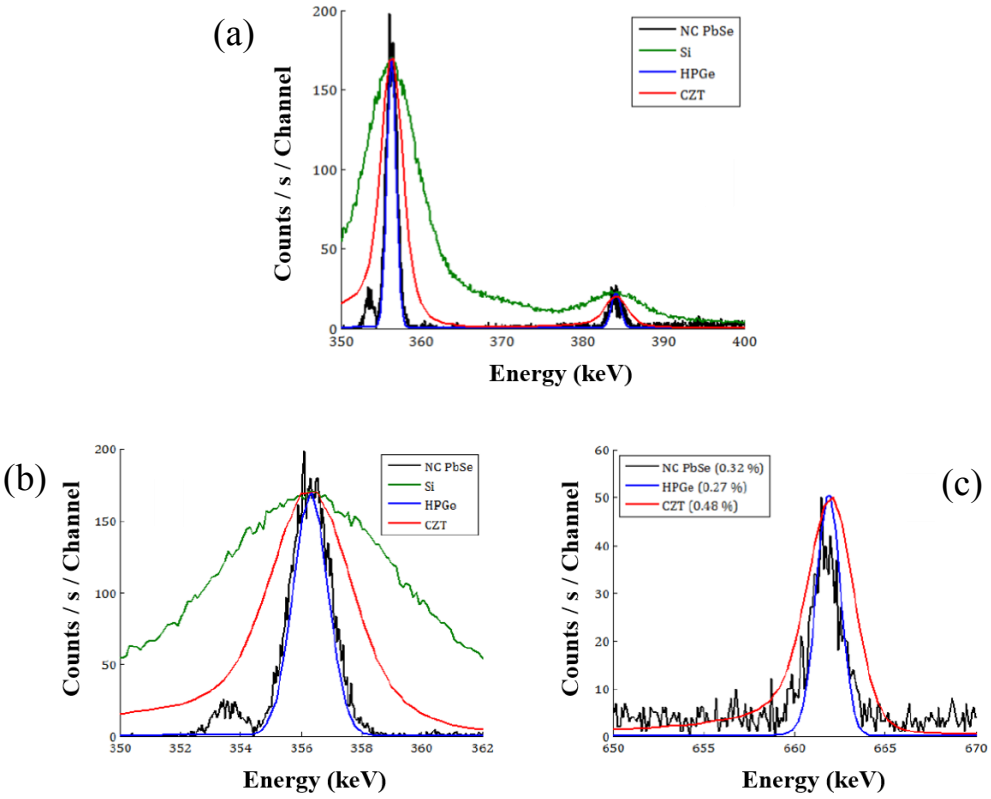

Fig. 4.1 | (a) Spectral comparison between high-sensitivity silicon (green), CZT (red), HPGe (blue), and PbSe nanocomposite (black), when exposed to gamma-ray emitted from ^{133}Ba. The different measurement periods (e.g. 21.2 min. for PbSe NC, 2 hrs. for HPGe) account for the differences in curve smoothness, and the curves were normalized to the number of counts in the PbSe peak. Note that the HPGe and PbSe NC traces largely overlap except for the x-ray escape peak from the PbSe NC detector. (b) Close-up of the 356.02 keV peak. (c) Spectral comparison when impinged upon by gamma-ray emitted from ^{137}Cs.[6]

Due to the phonon-electron coupling being substantially weakened in strongly-confined systems when compared to thermally-driven scattering in the bulk state, the leakage current is far less than that of a bulk material with equivalent band-gap. As a consequence, the detection element draws very low power. Specifically, a typical 2.0 mm thick 1.0 cm^2 PbSe nanosemiconductor detector draws less than one tenth the power of a silicon element of equivalent volume. Thus, one

can make a multifunctional device that presents a large-capture area to the radiation field and good intrinsic efficiency while delivering this capability at low-power.

4.2 PbS Devices

The PbS-based snowflake NCs possess a face centered cubic (*fcc*) structure. The main advantage with this type of NC would be that their nanostructure growth is functionalized by short-chained ligands (TAA precursor; length < 1 nm), therefore, each NC-NC linkage should be conductive. However, although the NC-NC (6 – 8 nm scale) interconnection can be strong *within* a particular snowflake or dendritic structure (micrometer-scale), the interconnection between PbS snowflakes themselves can be quite limited with their long trunks and branches extending in out in various directions. That is, since the individual PbS snowflakes do not possess (functionally) identical sizes and shape, interdigitation and close-packing is difficult to achieve.

Instead of attempting to rely on self-assembly for the alignment of an enumerable amount of 4 – 7 nm sized PbSe NCs throughout the depth of a ~1 mm thick colloidal film, we examined, through PbS, the utilization of star-shaped and cubic microstructures for the sake of controlling the size-dependent band-gap and quenching thermal noise. The introduction of these new shapes and forms of PbS NCs, though they are roughly 200 times larger than the PbSe NCs, still possess nanostructural features.

From Section 3.4.1, several figures of PbS NCs demonstrate several single-crystalline microstructures in which we utilized shorter ligands during the NC growth, resulting in star-shaped and cubic microstructures (~1 μm dia.) with underlying nanostructural order (Figs. 3.6c and 3.10).

The advantage of such a configuration is that the problem of conductivity involving particle interconnectivity is reduced by roughly 200x as long as the charge flows freely within each NC. Though the E_{bg} in bulk for PbS sits at 0.41 eV, E_{bg} of a PbS star-shaped NC would be ~1.98 eV for one with a wingspan of 625 nm (as seen in absorption spectra from Fig. 4.2a).[267] This confirms that charges are confined along the platelets that comprise the NC.

In observing figures from Section 3.4.1, closely-packed arrays of microcubes with less open volume than an assembly of star-shaped NCs were visible, therefore, one would rather expect truncated microcubes to produce the best starting material for a detector. Although XRD studies of these star-shaped NCs indicate they are single-crystalline, absorption studies of the microcubes indicate charges are strongly confined, implying lamination can exist within the NCs.[267] During this task, we characterized the NCs to determine the geometric nature of the charge confinement and determine the relationship between the synthesis recipe and the size dispersion of the solid. To determine the charge conversion efficiency and transport characteristics of the star-shaped NCs, we formed drop-cast solids bound between Au and aluminum contacts. Shown in the current-voltage (I-V) characteristic of Fig. 4.2b, the resulting solid can form a Schottky junction with low noise in reverse bias (10's of fA). The offset in the zero-crossing point in Fig. 4.2b could indicate space-charge trapping, most likely at the NC interfaces. Nevertheless, an applied voltage can drift radiation-induced charges and allow us to characterize the material as a radiation-detection medium.

Fig. 4.2c corresponds to the charge pulse following a gamma-ray interaction. The charges move rapidly (< 1 μs drift) while possessing good charge conversion, which is indicated by the fact that the size of the pulses are comparable to those produced in a Si-based detector. The pulse-height distribution, for alpha particles and gamma-rays in Fig. 4.2d shows that 5.49 MeV alpha

particles transmit through the active medium and deposit energy consistent with that of ~100 keV electrons (secondary electrons from gamma-ray). The physical depth of the solid can rapidly (~1 day) be made millimeters thick since the underlying structural layer is relatively large.

The lack of spectroscopic definition in Fig. 4.2d is a reflection of the fact that the active volume is too small to capture either the high energy alpha particle or the lower energy but lower deposition-density electrons that result from the gamma-ray and x-ray interactions. As noted in Chapter 3, the extent of the active volume depends on the degree to which one can achieve long-range ordering. If the drop-cast PbS nanostars are annealed near 70 °C during drying, then the NCs possess enough thermally sourced motive energy to reorient and interdigitate as shown in Chapter 3.

The sensing consequence of this NC ordering is shown in Fig. 4.2e, in which the spectral step at the 81 keV photopeak and he lower-energy escape features are well-resolved. In general, the energy resolution is much poorer than that of PbSe because the sensor's leakage current was much higher. Specifically, for the spectrum in Fig. 4.2e, the applied voltage was a low 25.7 V (compared with typical ~300 V applied bias for the PbSe solids) and the leakage current at bias was 4.6 nA compared with sub-nanoamp values for the PbSe solids. In general, the PbS solids exhibited higher leakage than the PbSe equivalent, preventing the observation of extremely high-resolution devices. This is due to the lower band-gap that can exist throughout the sample (cf. the broad absorbance spectrum of Fig. 4.2a), which increases the thermal noise.

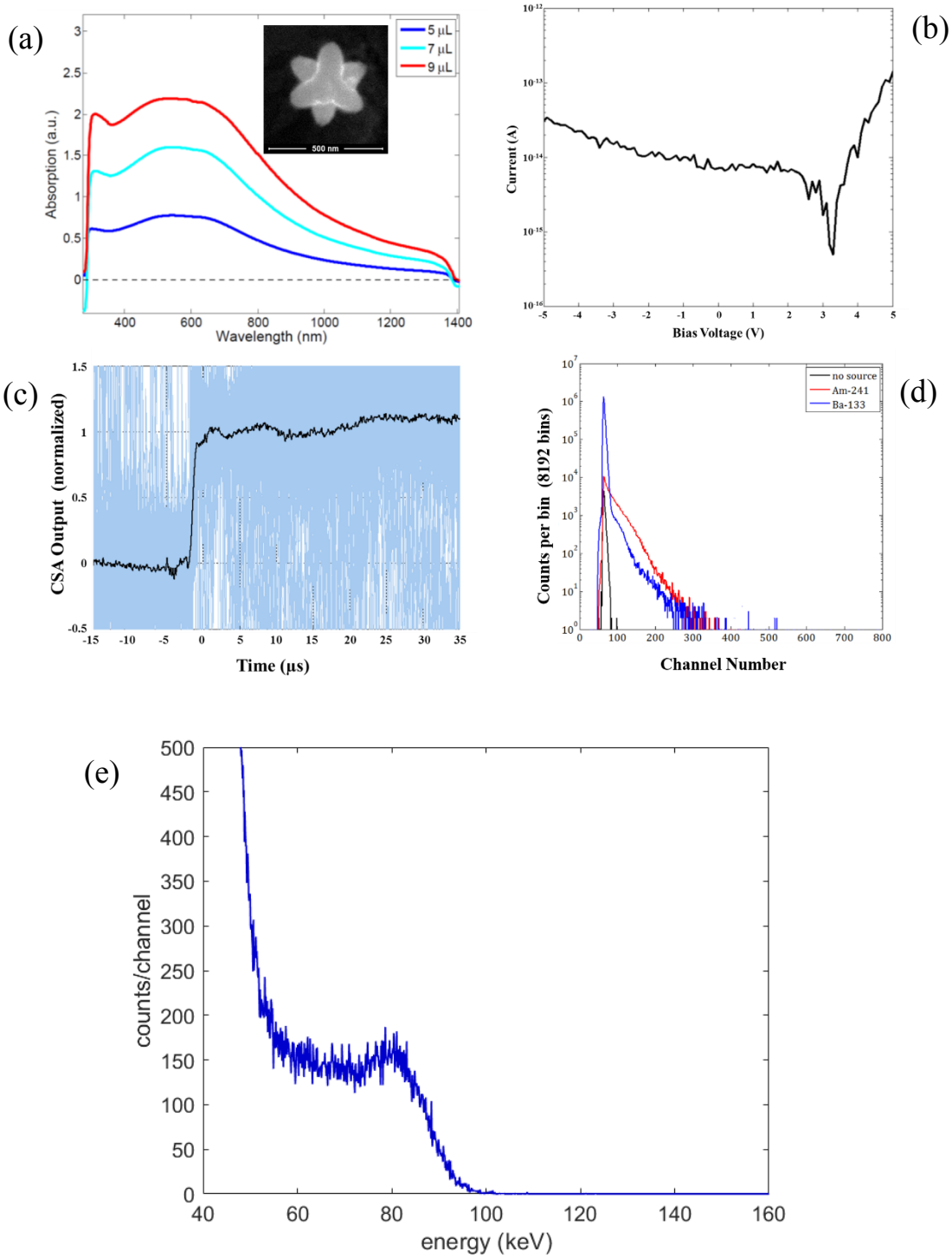

Fig. 4.2 | (a) Absorbance spectra for PbS-based microstructures (inset), which exhibit quantum confinement. (b) I-V curve of PbS NCs formed into a metal-semiconductor junction. (c) Normalized and averaged (black) preamp pulse shape. (d) Pulse-height distribution showing alpha and gamma-ray sensitivity from ^{241}Am and ^{133}Ba. (e) ^{133}Ba energy spectrum derived from PbS nanostars annealed to 70 °C upon the Au-covered silicon substrate.

In applying a shadow mask to the PbS device surface, the IV-curve in Fig. 4.3a shows resistance solid across the entire solid, which is what was expected given the weak star-to-star coupling. The PbS snowflakes were also fused together with heating to see if this improves the performance. However, despite the low and careful heating, it held no effect on the results.

Alpha spectra from ^{241}Am was collected at 80 V in Fig. 4.3b. A broad well-separated peak exists away from the noise/background of the spectra, but again the active region is too small to collect the entirety of the 5.49 MeV deposition. The high channel peaks represent regions of the device sample for which charge carriers are being created most efficiently and maximally transferable to the electrode. Responses from ionizing radiation with ^{241}Am reveal the device was responsive but not sharply spectroscopic. The sample itself was physically 10 times thicker than what was needed to stop alpha particles, and the partial energy deposition therefore reveals imperfect percolation throughout the solid. The gamma-ray response using a ^{133}Ba source is shown in Fig. 4.3c, where the PbS snowflake detector appeared to show very good charge conversion efficiency (comparable or better than single-crystal semiconductors).

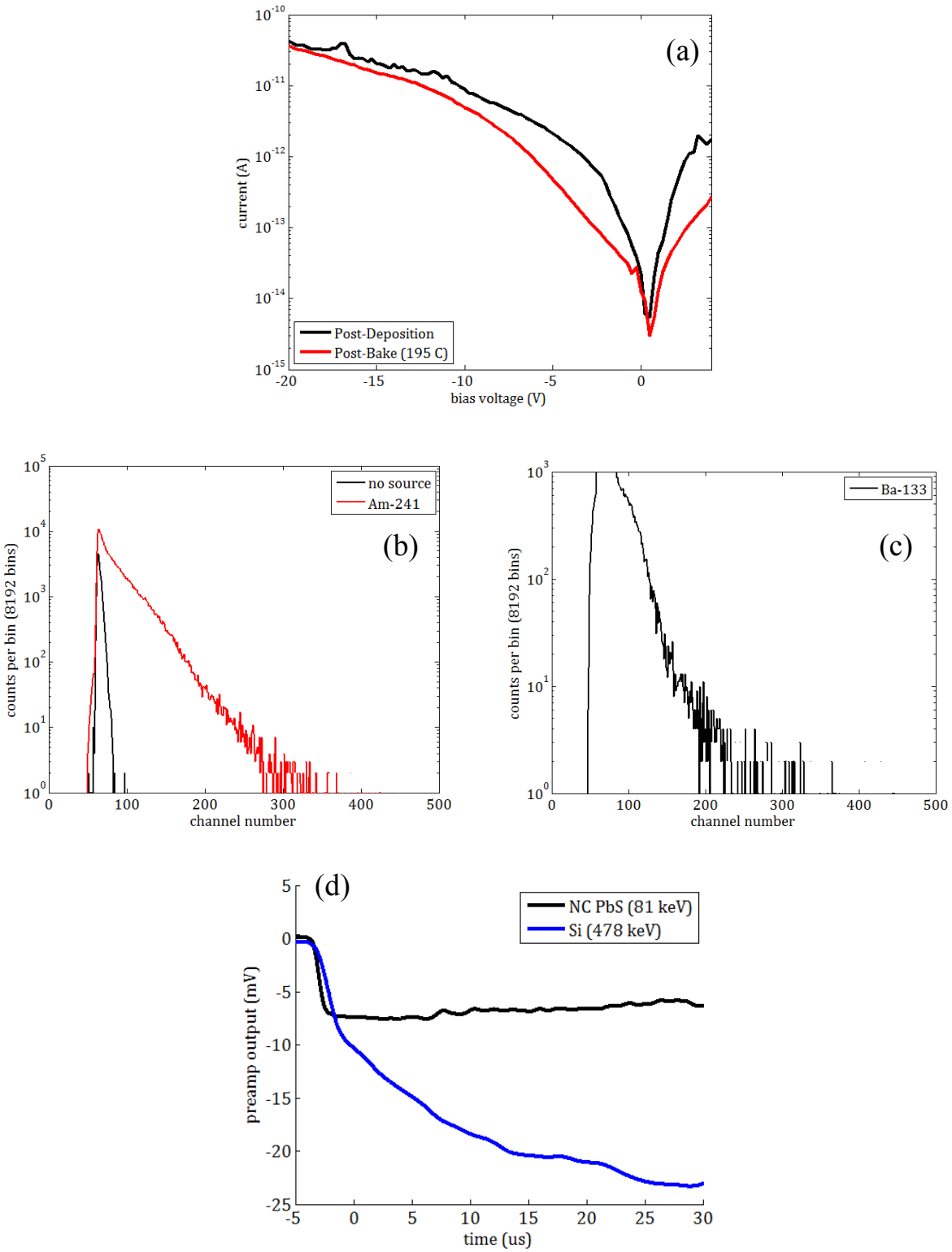

Fig. 4.3 | (a) I-V curve of PbS NCs formed into a metal-semiconductor junction after experiencing rapid thermal processing at 195 °C for ~10 min. Spectra collected for a PbS device sample possessing snowflake-shaped QDs, using (b) ^{241}Am for alpha response and (c) ^{133}Ba for gamma-

ray response. (d) Pulse shape derived from charge sensitive preamplifier (ORTEC 142) when gamma-rays from ^{133}Ba are incident upon a PbS detector, operated at 80 V applied bias. PbS detector possesses snowflake-shaped QDs fused together by heat.

Fig. 4.3d shows acceptable mobility in the relatively rapid pulse rise of the PbS snowflake-shaped QDs. More importantly, there appears to be negligible charge trapping effects. Typically, charge trapping can reveal itself by either (a) showing slope variations within the induced-charge pulse shape or (b) a very low energy tailing of the gamma-ray peaks due to diminished charge collection at increasing interaction depths. If trapping did exist here, the pulse shape for the PbS QDs would carry two components on the dropping edge: a prompt time component, and slow component due to thermal emission of trapped charge. The existence of these components in the pulse spectra are minimal. Along with there being no lack of peaks in the tail end of the gamma-ray response spectra (Fig. 4.3c), neither the pulse shape nor the gamma-ray spectra reveal real cases for charge trapping. Thus, the medium is excellent for converting gamma-ray energy into charge, but the uniformity and extent of the active region remains to be improved.

In conclusion, the PbS QDs were fabricated using a reproducible aqueous-based synthesis. The electrical evidence seen here from a snowflake-shaped QD device sample indicates they are capable of performing as good radiation detectors, given the QDs are interdigitated or fused together via annealing.

4.3 Devices formed via Oriented Attachment

We used a hypothesis in which nanostructured detectors that exhibit good detector properties were realized by selectively removing capping ligands. This occurred either chemically for the long-chained oleic acids or thermally for the short-chained thioglycolic acid. This hypothesis was proven by systematically reducing the number of capping ligands in order to alter the energy-preferred hexagonal ordering (Fig. 4.4a) of the spherical NCs into a square packing which results in close-proximity bridging, which can be seen in Fig. 4.4b.

After achieving close-packed long-range arrays and heating samples to 200 °C, the resulting ^{137}Cs gamma-ray spectra, in Fig. 4.5, yields a resolution (at 662 keV) of 3.2 %. The relatively poor resolution is due to the high capacitance of the thin sample, noting that the electronic noise floor in Fig. 4.5 is near that of the spectral features. Specifically, a high detector capacitance reduces the amplitude of the step pulse extracted from the sensor because of current-sharing between the detector and the feedback capacitance in the charge-sensitive preamp.

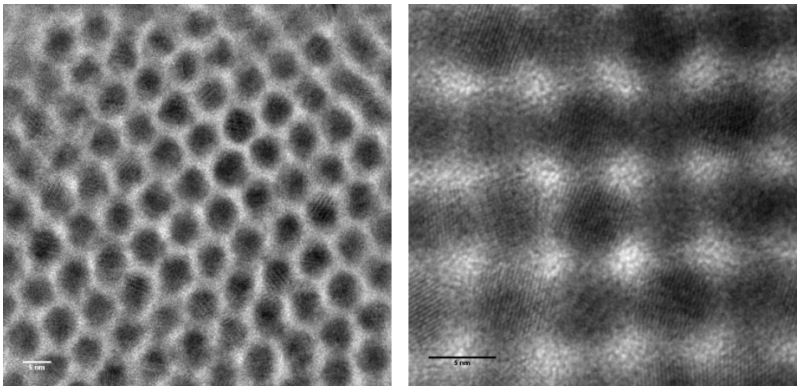

Fig. 4.4 | TEM micrograph of spherical PbSe NCs (a) hexagonally close-packed and (b) NCs transitioned from hexagonal ordering into square ordering, with close proximity bridging and neck growth.

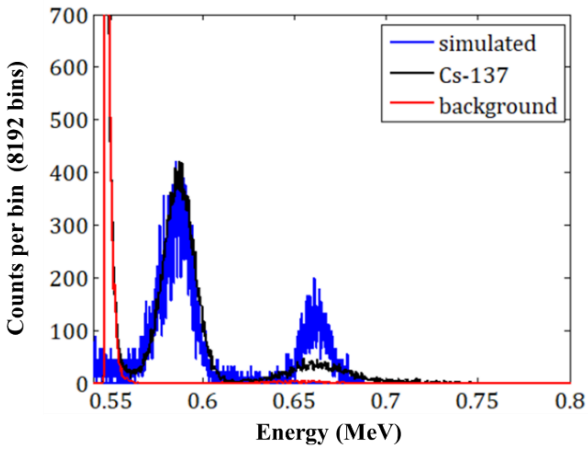

Fig. 4.5 | ^{137}Cs gamma-ray pulse height distribution from 500.03 mg of PbSe colloidal solution drop-casted atop a uniquely designed silicon substrate (12.7 x 14.6 mm) (details in Section 3.7). Measurement time was 400 s for both source and background. Simulated data is derived from MCNP-simulated for a 75 μm PbSe solid impinged by 662 keV gamma-ray.

Despite the small signals, the sensor works quite well. In particular, notice how the blue MCNP-simulated distribution captures the escape peak (large feature near 590 keV) in both location and lower-energy tailing (also due to x-ray escape).

There are a variety of chemical methodologies to for achieving oriented attachment, including experiments including liquid substrates to weaken and/or diminish/remove capping ligands, resulting in a reduction in interparticle spacing. This reduction reduces the possibility of charge traps within the semiconducting material and allows for a stronger charge transport throughout the system. Though the developmental process for oriented attachment based devices did not produce uniform NC films (on the liquid substrate), the data shows this process could work with the 81 and 356 keV peaks revealing themselves from gamma-ray exposure. In Fig. 4.6 (a & b) we see broad full-energy gamma-ray peaks of pulse amplitudes. The 50-drop device sample reveals peaks at 61.62, 76.22, and 100 keV while the 15-drop device sample shows peaks at 354.98 and 357.8 keV.

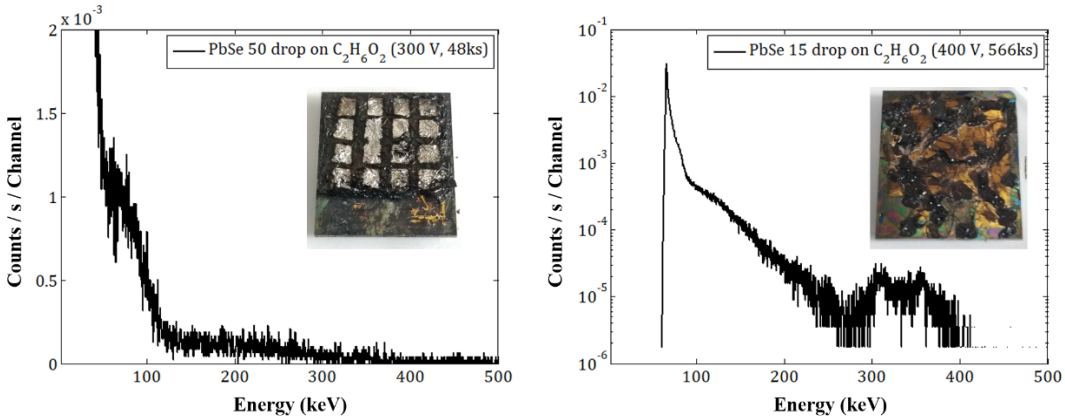

Fig. 4.6 | Energy spectrum derived from ^{133}Ba gamma-rays on a PbS device sample showing broad Pb and Se x-ray escape peaks, developed through the layer-by-layer with oriented attachment, going through (a) 50 layers at bias setting of 300 V and (b) 15 layers at a bias setting of 400 V.

4.4 Devices formed via Glass-Tubing

When testing devices with air-enhanced PbSe NCs, the 81 keV peak was most prominent, showing that we can collect from this type of sample, with the energy resolution proving to be 1.41 %. We also conducted a MCNP simulation in efforts to replicate the results. As shown in Fig. 4.7, the relatively thin detector exhibits x-ray escape peaks at 69, 62, and 53 keV from the 81 keV peak because of (principally) Se K_α and Pb L_α escape features. There are large features in both measurements (Fig. 4.7a) and MCNP simulations (Fig. 4.7 (b, d)) due to x-ray production from the ^{133}Ba source at 35 keV and 31 keV energies (grow beyond the ordinate scales shown).

One can use pulse shape analysis (PSA), such as that suggested in Fig. 4.7c, in which only those pulses below a particular rise-time are included in the histograms. The idea in this approach is that are different regions that can drift the charges over different periods depending on the local electric field. Ideally, one would make the electric field uniform via effective contacting, but for this point-contacted solids, one can have a distribution of rise times. As shown in the plot of Fig

4.7c, the 81 keV peak and neighboring features are captured if the pulse rise time is greater than microseconds, but no additional resolution is revealed.

Instead of point contacting, as shown in the insets of Fig. 4.7 (c, d), one can attempt to make the field more uniform via evaporated contacts, as shown in the inset images of Fig. 4.7e. The indium (In) square contacts are intended to increase the interactions rate and spectral precision, but as shown in the legend of Fig. 4.7f, which denotes the real time of the measurement, several days are sometimes required to accumulate spectral features, reflecting the thinness of these tube-casted samples. In general, the tube-casted samples could produce uniform, thick solids, but refilling the tube is needed to reach the millimeter-scale desired thickness.

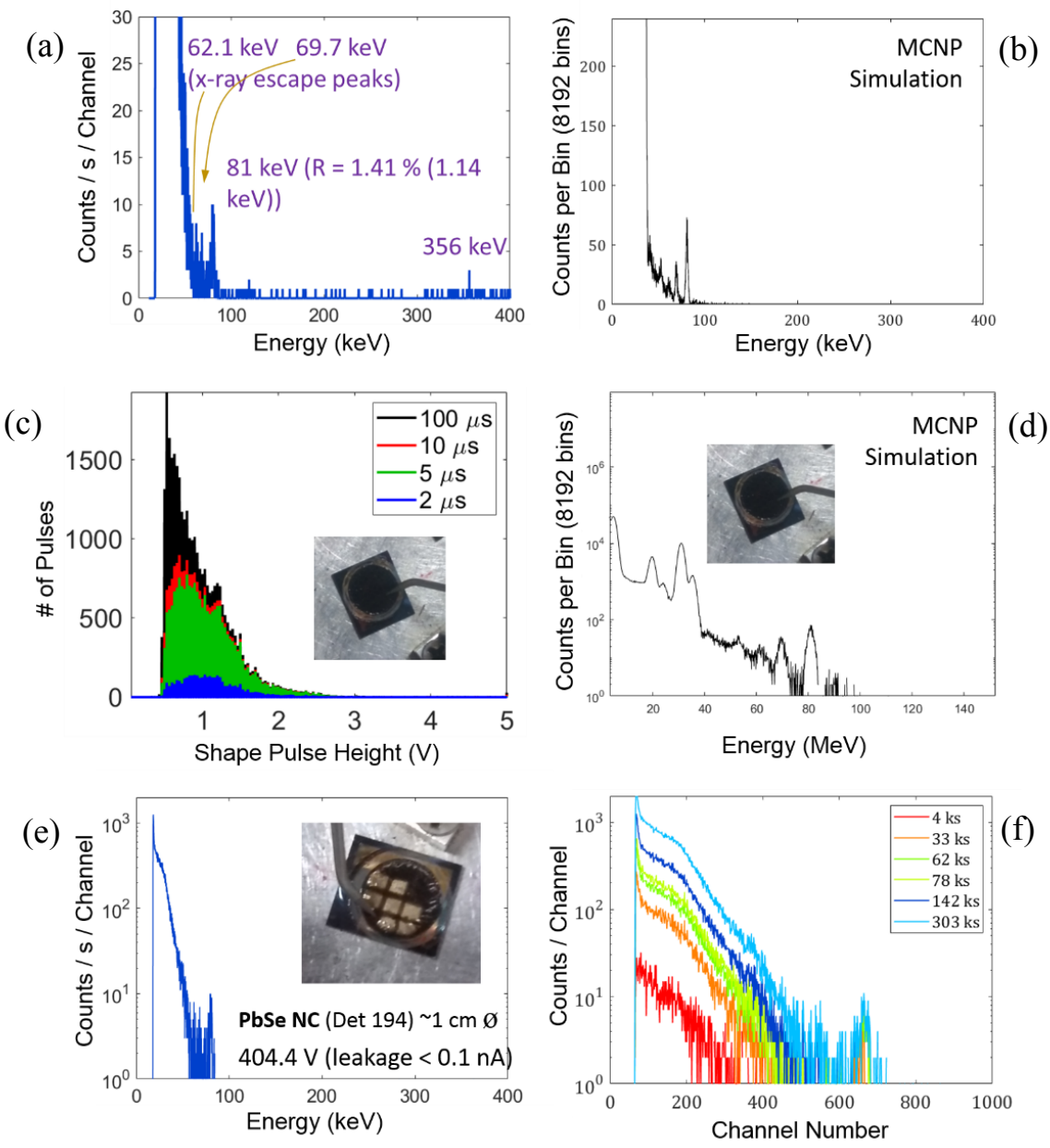

Fig. 4.7 | (a) ^{133}Ba spectrum derived from TOP-PbSe tube casted sample, and (b) the corresponding MCNP-generated simulation. (c) Pulse height distribution from ^{133}Ba gamma-rays impinged upon the sample shown in the inset, in which the legend shows the rise time below which the pulses were allowed to contribute to the distribution. (d) Semilog plot of the MCNP-simulated response showing the 81 keV features as well as the large 35, 31, and 20 keV x-ray features. (e, f) ^{133}Ba spectra for Indium-evaporated PbSe tube-casted samples.

4.5 PbSe Colloidal Solids as High-Resolution X-ray and Gamma-ray Sensors

The sensing properties of the PbSe colloidal solid can be measured by impinging both x-rays and gamma-rays upon the solid from a barium-133 (^{133}Ba) isotropic radioactive source. We previously showed that *drop-cast* PbSe colloidal solids derived from different NC geometries and different ligand chemistries could yield room-temperature energy resolution comparable to that of state-of-the-art, liquid nitrogen-cooled HPGe detectors.[6] The enhanced resolution of the nanostructured media can arise from mitigating energy, and therefore information loss to thermal mechanisms by shifting the phonon density of states away from those modes that preferentially scatter with electrons.[231-232, 268] As mentioned in the introduction, quantum dots have been previously shown to be able to achieve internal quantum efficiencies exceeding 100% in solar cells from multiple exciton generation.[251-252, 261] This enhancement in efficiency is a consequence of the reduction in the information loss due to the phonon bottleneck effect.[6, 231-232, 268-269] The interaction between electrons and longitudinal optical phonons can be suppressed to a larger degree in quantum dots than in bulk semiconductor materials, leading to a larger fraction of information carriers participating in the signal formation.[11] The result is the potential for sharper spectral features due to reduced statistical counting noise because the photon energy is converted into a greater number of charge-carriers.

As shown in Fig.4.9a, the tested devices consisted solely of the self-assembled PbSe colloidal solids, contacted mechanically on the backside with an aluminum plane on the topside with a blunt aluminum probe. That is, electron- and hole-transport layers and associated electrical contacts deposited via vacuum-deposition or spin-casting were not utilized, nor were they needed in order to establish excellent and uniform charge collection as revealed via the gamma-ray spectra, as

follows. When the spectrum is collected with a standard experimental setup (Fig. 4.9a), Fig. 4.8b shows that mm-scale PbSe solids can achieve fine energy resolution. Specifically, for the 1.11 x 1.11 x 0.68 mm^3 PbSe solid, the energy resolution, shown in the purple fit of Fig. 4.9d, is measured as 0.8 % (0.65 keV) at 81 keV, which is superior to that of a commercial cadmium telluride (CdTe) detector (red line) and only slightly worse than that of HPGe, as shown in the similar widths between the green HPGe line and the purple fit line. The distribution of radiation-induced energy depositions within the solid is simulated with the Monte Carlo N-Particle Transport Code (MCNP)[270] and shown in the blue trace. Note that the MCNP simulation nicely capture the x-ray escape features that contribute to the various spectral features such as those escape features that contribute to the 81 keV peak. Furthermore, in both the simulated and measured distributions, the absence of a gamma-ray peak at 53 keV and a highly muted escape feature at ~69 keV (confluence of Se K_α, Pb L_α, and Pb L_β x-ray escape from 81 keV photopeak) indicated that the entire solid is active.

One challenge of integrating lead chalcogenides into *pulse-mode* photon sensors is the high permittivity[224, 271-272] and thus significant detector capacitance of the device. As Kwon *et al*.[222-223] has shown, the detector capacitance can attenuate the photo-induced pulse amplitude and temporarily expand the charge integration across the charge sensitive amplifier (CSA) used to collect the energy information. A conventional CSA, when employed as a preamplifier, is generally connected to one side of the photon detector in order to collect the induced charge generated by a radiation impact event and convert it to a voltage signal through a feedback capacitor, C_F, providing gain as: $V_{out} = -AQ/(C_D + (A+1)C_F)$, where Q is the induced charge, A is the CSA internal gain, and C_D is the detector capacitance. If a conventional CSA is employed, then the consequence of a non-negligible detector capacitance is therefore an attenuated voltage output

that can potentially be impacted by the front-end electronic noise, as can be seen from example pulses (Fig. 4.8 (a, b)).

The diminishment in the measured energy resolution for higher capacitance PbSe NC sensors is shown in Fig. 4.9d. Specifically, a thinner sample will result in a greater prominence of the x-ray escape feature at 69 keV, the backscatter peak at 62 keV (81 keV gamma-ray backscattering from the underlying aluminum and returning to be detected in the sensor's active volume) as well as the 53 keV gamma-ray peak. More importantly, the higher detector capacitance attenuates the output of the CSA such that the electronic noise is nearly as large as the amplitude from the 53 keV gamma-ray peak, as shown in the large noise curve near 50 keV. As a consequence, the resolution degrades from 0.8% to 2.3% (1.90 keV) at 81 keV. For the sensing of low-energy x-rays with a NC device, one must either employ a thick (~nm scale) solid or employ a capacitance-insensitive CSA.[222-223]

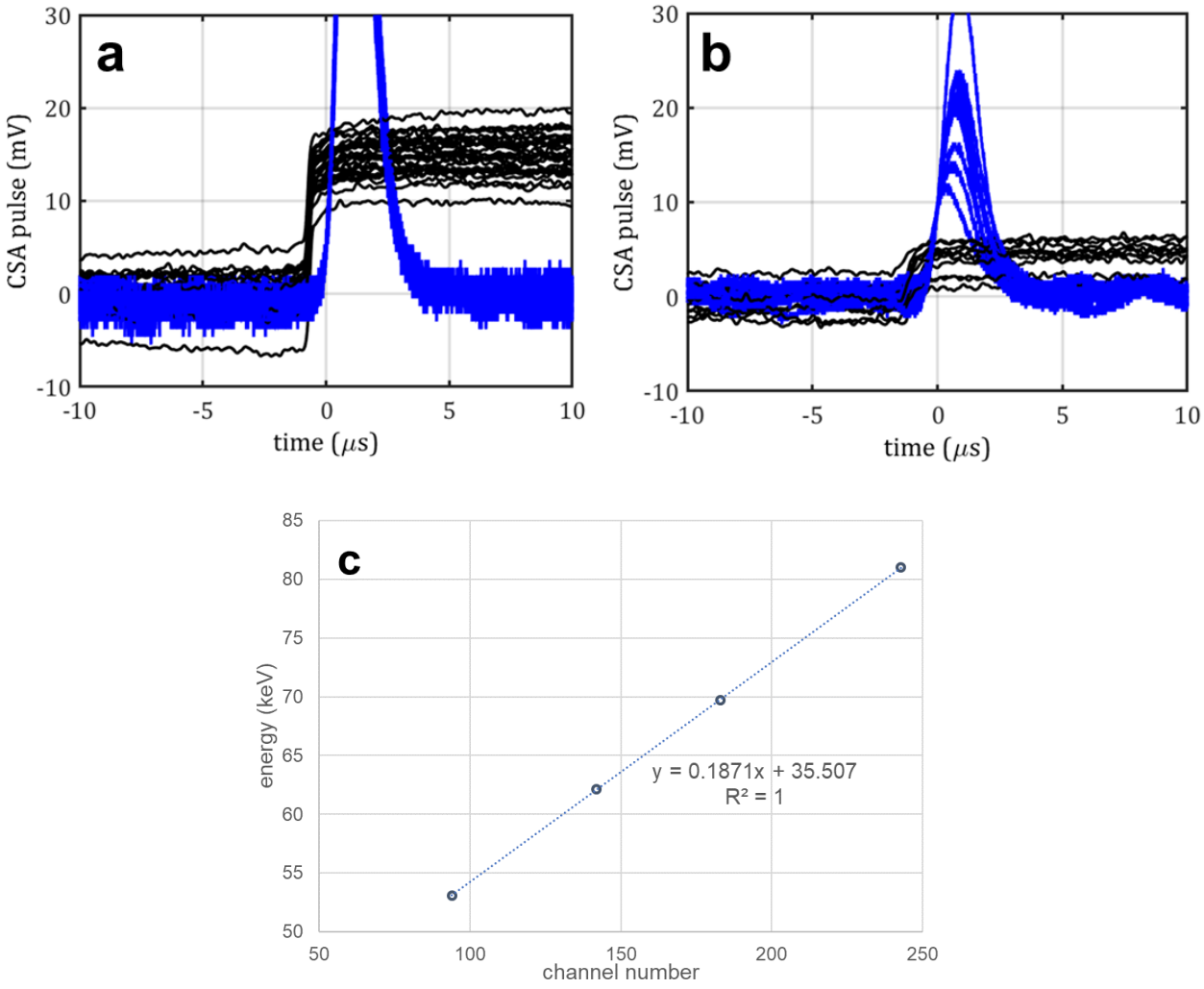

Fig. 4.8 | (a) Typical CSA pulses in black and pulse-shaped pulses in blue derived from a ^{133}Ba gamma-ray source for a PbSe solid for which the detector capacitance (measured at 0.57 pF) has minimal impact on the SNR (~2 x 2 x 1 mm^3). (b) Attenuation of the pulse amplitude and elongation of the rise time for thinner samples (10's of micrometers) due to higher detector capacitance. (c) Example energy calibration (for Fig. 5d) from channel number to energy, in which the raw channel number is derived from the amplitude of the shaped pulses (blue in (a) and (b)).

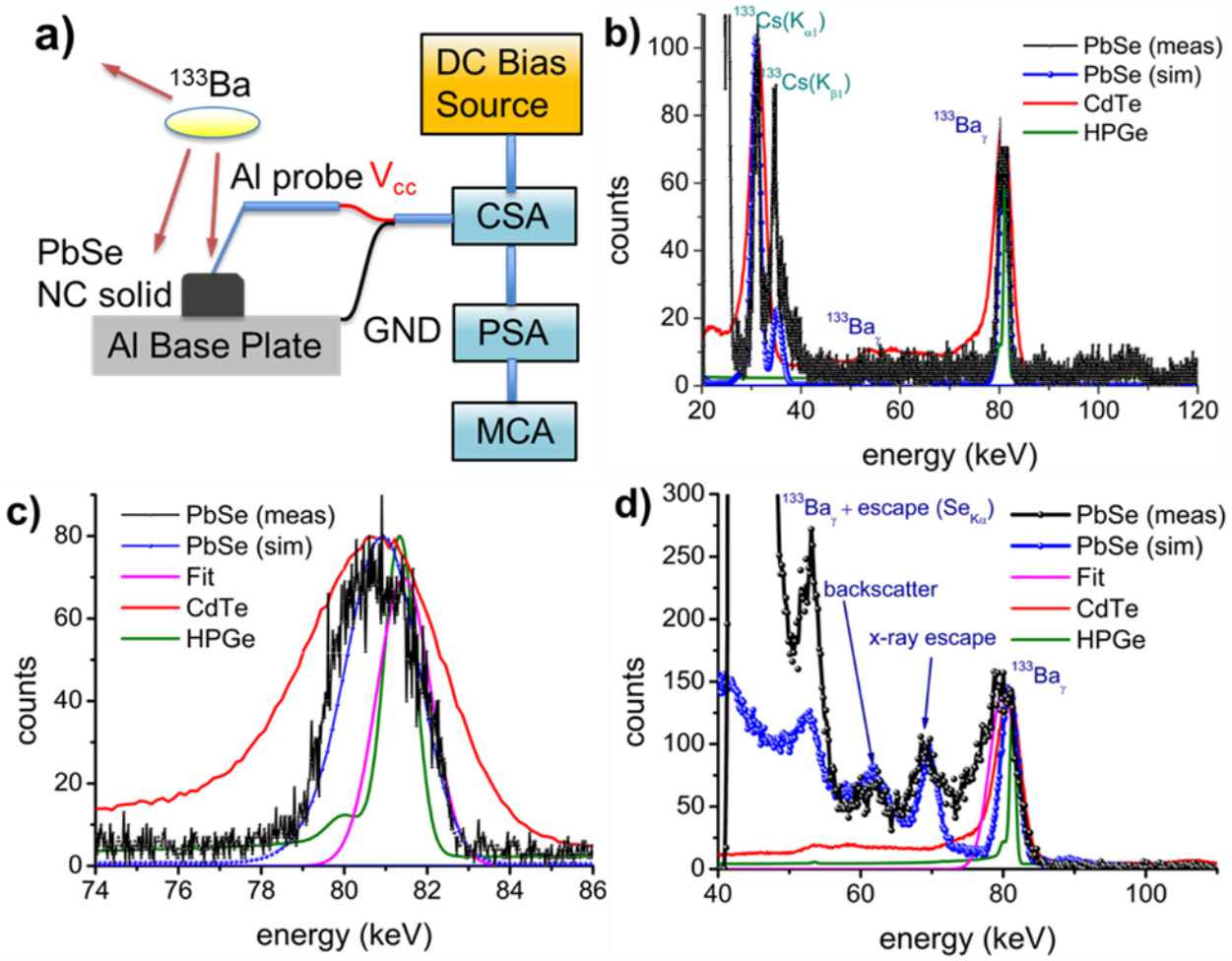

Fig. 4.9 | Photon Spectra from TDP-PbSe NC solids. (a) Schematic diagram of experimental setup. The induced current pulse from the detector is integrated and amplified by the charge-sensitive amplifier (CSA). The output is band-pass filtered through the pulse-shape amplifier (PSA) to improve the signal-to-noise ratio and eliminate the long-integrated tail of the CSA pulse. The multi-channel analyzer linearly bins the pulse heights across 0 – 10 V. (b) Spectral comparison between commercial (1 mm thick from Acrorad) CdTe single-crystalline (SC) detector (red), a commercial HPGe (3" x 3" liquid-nitrogen cooled HPGe from Ortec with optimized operating conditions), and a nanostructured PbSe colloidal solid, when exposed to x-rays and gamma-rays emitted from ^{133}Ba. The PbSe NC solid is biased to 300 V (leakage current: 1.0 nA). (c) Expanded view of (b) with MCNP simulation results included in blue, HPGe-derived peak shown in green, and Gaussian-fit to the full-energy peak in purple. (d) Spectral comparison between CdTe single-crystalline (SC) detector (red), HPGe detector (green) and nanostructured PbSe colloidal solid, when exposed to x-rays and gamma-rays emitted from ^{133}Ba. The PbSe detector is biased to 100 V (leakage current = 1.1 nA).

CHAPTER IV

Conclusions

In this research, nanostructured PbS and PbSe NCs QDs have been extensively studied as advanced media for ionizing radiation detectors. For PbS-based devices, assembling superlattices of interdigitated QDs was the key to developing good charge transport. Seeing that heating improves the NC-to-NC connectivity of the self-assembled nanostructure, there lies potential to perfect a device with PbS QDs of particular shapes.

The move from TOP-based PbSe QDs to TDP-based PbSe QDs resulted not only in long-term stability against oxidation, but more importantly, self-assembly of NCs within solution, resulting in the formation of percolation paths throughout the solid. In making the chemical transition, we developed a new solution-process method to dramatically enhance the stability of PbSe NCs by way of both TDPSe and a refined Pb oleate. Together, the process changes to strongly enhanced, air-stable PbSe QDs. In contrast to (a) recent reports involving a less refined Pb source for PbSe syntheses, (b) passivating PbSe NC surfaces with inorganic shells, or (c) etching out surface Se atoms, our results demonstrate that PbSe NCs maintain air-stability for at least 1.6 years. Those same NCs can also be solution grown into colloidal solids with sufficiently dense NC-to-NC coupling and be more than capable of facilitating charge transport through that solid. The high efficiency with which the initial photon's energy information is transformed into countable electron-hole pairs, and the effectiveness with which those charges induce a current in the solid, are reflected in the fine energy resolution. The results indicate that TDP-PbSe NCs can be

effectively employed for the sensing of high-energy quanta. At times, the self-assembly process can lead to complex geometries where assemblies are governed by the balance between attraction and repulsion. Using this knowledge can realize controlled self-assembly in a format suitable for various applications. For example, absorption of colloidal NCs at a particular liquid surface can in time reveal an ensuing structural transformation of a NC monolayer. Oriented attachment contributes to further understanding the mechanisms of interfacial self-assembly processes and the many differences within self-assembly. The use of nanoparticles as building blocks for the fabrication of superstructures is a powerful way to obtain nanomaterials with collective properties. Among the various processes to self-assemble colloids into larger structures, oriented attachment is a particularly versatile approach mainly due to the fact that it allows the preparation of anisotropic nanostructures. But more importantly, tailoring precursor reactivity greatly advanced our ability to design high performance materials and to relate atomic structure to nanocrystal function. The results from TDP-PbSe NCs highlight the value of controlling the NC synthesis mechanism to obtain a desired NC product.

We have hypothesized that those nanostructured detectors that exhibit good detector properties were realized by selectively removing the long-chained oleic acids capping ligands, either chemically or thermally. In the end, tailoring precursor reactivity can greatly advance our ability to rationally design high performance materials and then relate atomic structure to NC function. If done property, this surface chemistry can advance the systemic development of solution-processed NC photovoltaics.

The main principles of future work revolve around (a) manufacturing scale-up and (b) physics education. Regarding the former, one would prefer the 2 x 2 x 2 mm^3 – 3 x 3 x 3 mm^3 TDP-PbSe solids be grown on the centimeter-scale for the sake of increased detection efficiency. This will

require a detailed characterization of the (NC) solubility curve so one can either (a) epitaxially grow additional PbSe nanomaterial upon the pre-existing seed crystal, or (b) suppress large-volume homogeneous nucleation so a smaller number of nucleates are grown into larger crystals in a single step. Another part of this scale-up approach is to reduce the time required to form the colloidal crystal, via either higher NC concentrations or reduced temperatures, both of which increase the NC-to-NC interaction rate. We have reduced the growth time from 3 months to 2 weeks using cooled solutions but mapping the full solubility profile has not yet been completed.

With respect to the layer-by-layer processes such as the ethylene glycol facilitated oriented attachment PbSe layers, one can envision robotic systems that build up monolayers to sufficient thickness so gamma-ray detection can be efficiently achieved, as we have done some work with robot arms in repeated dip-cast recipes in the past. However, optimizing that process so re-dissolution of the PbSe solid doesn't occur upon each dip is required. Regardless of the underlying Pb chalcogenide solid, the electrode design has not been optimized, in terms of the deposition of efficient electron and hole transport layers that can serve as blocking and non-blocking contacts.

This dissertation work was focused on building the chemical synthesis tools needed to make a variety of PbSe and PbS nanostructured solids. The next steps are to use these newly found tools to build solids with which one can study the underlying physics of nanoparticle systems. Particularly, the phonon bottleneck effect for energy depositions well above the band-gap has not yet been explored theoretically nor experimentally. We can quantify the degree of charge multiplication via measurements of the W-value (energy required to create an electron-hole pair), information that can be used to inform predictive models. Furthermore, we observe unusual degrees of stopping high energy quanta compared with homogeneously equivalent material, which we expect is due to enhanced interfacial scattering in these nanostructured media, particularly for

the charged particles that result from interactions. The exact nature of those interactions are not yet fully understood experimentally nor theoretically, but since it can be scientifically novel and the underlying process can be technologically exploited in both sensors and protective materials, the first priority of follow-up work should be to detail the physics of these interactions.

APPENDICES

APPENDIX A

A.1 Gamma-ray Interaction Simulations for TDP Samples

The thickness of the solid was measured via SEM cross-sectional analysis (677 ± 10 μm), the latter quantity used in the simulations. The lateral area of the PbSe solids (1.114 x 1.114 mm^2) was measured via SEM cross-sectional analysis and the density (3.84 g/cm^3) was derived from the measured volumes and the measured mass. The relative weight fraction of the inorganic (Pb, Se) and organic (C, H, O, P) constituents were derived from energy dispersive spectroscopy (EDS). The MCNP simulation included the target, an assumed point ^{133}Ba source 1 cm distant from the source and the aluminum block upon which the sensor was placed to simulate the effects of aluminum backscatter. The ^{133}Ba energy distribution consisted of the following peaks (in MeV): 0.00467, 0.03063, 0.03097, 0.03492, 0.03499, 0.03525, 0.035822, 0.035907, 0.035972, 0.053, 0.0796, 0.0809 ,0.1606, 0.2232, 0.2763, 0.3028, 0.3560, 0.3838, with the following relative intensities: 0.03725, 0.07934, 0.1464, 0.01427, 0.01427, 0.01427, 0.00347, 0.00347, 0.00347, 0.00502, 0.0263, 0.3331, 0.00638, 0.0045, 0.0713, 0.1831, 0.6205, 0.0894.[262] In general, a total number of 10^{10} photons were simulated per run and the F8 (energy deposition) tally used to capture the spectrum. The subsequent charge electron-hole transport within the sensor wasn't included as we did in Joglekar *et al.*[273] because of negligible charge trapping within the sensor, as evidenced via the sharp rise (< 1 μs) time and symmetric energy peaks.

A.2 Gamma-ray Interaction Measurements for TDP Samples

A 31.55 MBq ^{133}Ba x-ray and gamma-ray disk source (radius 5 mm) was placed upon a polypropylene stand and separated from the sensor by 2 cm. Both the source and detector were placed within a vacuum chamber test box that was evacuated during measurements. The sensor sat upon an aluminum test stand and was contacted on its top surface via an aluminum probe tip. The gamma-ray spectra were collected with an eV-550 charge sensitive preamp, an Ortec 572A shaping amplifier (shaping time: 500 ns), and an Ortec Maestro multi-channel analyzer (MCA). The raw pulse height data collected by the MCA are channel numbers between 1 and 8192 that are derived from shaped pulses with voltage amplitudes between 0 and 10 V. The energy spectra shown in Fig. 4.13 are linear conversions of the pulse-height spectra derived from channel number-to-energy calibrations (e.g. Fig. 4.12c) that come from the measured peaks. The energetic positions of are identified with assistance from the MCNP simulations.

APPENDIX B

Electrophoretic Deposition

A promising technique performed at one point during this research was electrophoretic coating/deposition (EPD), a method of colloidal deposition to our own designed substrates via an electric field. This method was initially proposed for two main reasons. As the NCs are believed to be charged particles, the application of an electric field across a substrate may deem useful in the alignment process for NCs. The other reason is to address the problem of large variances in detector thickness when using drop-casting and/or spin-coating techniques.

This method was performed using two 12.7 x 14.6 mm substrates which were designed and diced as mentioned in Section 3.7. An end of a thin rubber coated wire was exposed and clamped to the female end of a small alligator clip. The male end of an alligator clip clamped onto the small square of each substrate (Fig. B.1c). Attaching the exposed wire to the small square of the substrate was also occasionally done by way of silver conductive epoxy (SCE), as seen in Fig. B.1d. The substrates with alligator clip, or SCE, wires are then placed in a custom-made, substrate holder capable of holding two substrates vertically, made via 3D printing. The substrates were placed in the holder with their attached wires pointing up. The substrate-holder assembly is then placed in a vial capable of holding 20 – 50 mL while both wires run through a septum cap. The substrates are designed with an exposed square in the middle surrounded by an Au plated border. To embrace the process of EPD, PbSe colloidal solution fills the vial up to the height of the top Au plated

border of the Si substrates and not to the alligator clips, or SCE, above. This way the exposed surface of our Si substrates has the potential to be fully covered in NCs. This amount was equivalent to ~ 4.0 mL. Fig. B.1b displays this experimental setup and pieces for performing this experiment. Varying levels of voltage was applied across the wires and the plating could occur over multiple days.

Fig. B.1 | Electrophoretic deposition (EPD) experiment. (a) Custom 3D-printed two-way Si substrate holder with 20 mL vial with septum screw cap. Two-way Si holder possessing two custom designed substrates, with each either (b) clamped with alligator clips on the ends or (c) directly attached wires via silver conductive epoxy to have positive and negative voltage to pass through substrates while submerged PbSe colloidal solution. (d) Si substrate connected to exposed end of wire via silver conductive epoxy. (e) Both Si substrates after EPD for roughly 65 hrs.

With an applied voltage of 1 V, NCs were not visually deposited onto either substrate even after 26 hrs. Two tests were then performed at 45 V. These experiments revealed thin layers of NC

film along both the exposed and Au plated areas of the substrate after 60 – 70 hrs., seen in Fig. B.1d.

Alpha responses were seen at high voltages while current-voltage (I-V) measurements were taken from an Alessi probe station with a 2-point probe setup. The I-V curves appeared to be very sensitive to the amount of pressure applied to the detector and showed no diode-like response.

To examine the upper limit or our ability to deposit using the EPD method, the voltage source was set 2000 V for over 4 days. This resulted in NC film along the positive and negative (anode and cathode) substrates with the negative side possessing a thicker NC layer. Despite the layer being thicker in this scenario, all results layers throughout this technique come out to be soft and capable of easily being scratched away. With a high voltage power supply utilized for this technique, a measurement of the current flowing between the electrodes could be taken which is present in Fig. B.2.

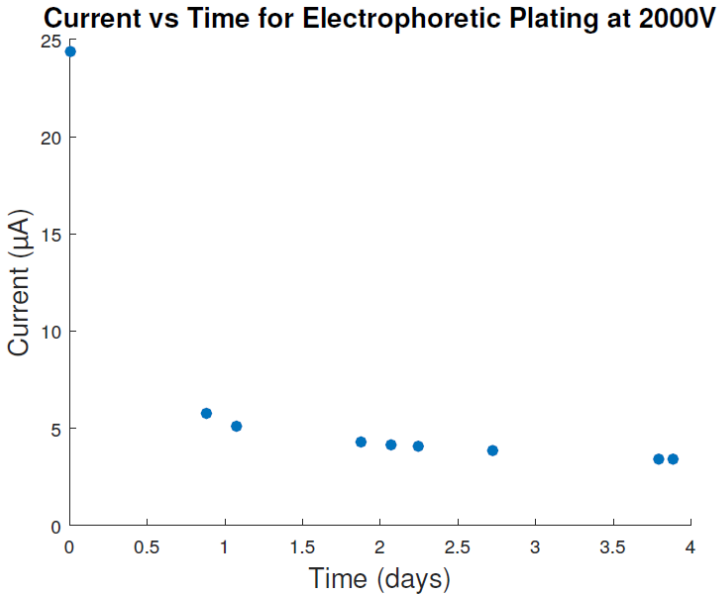

Fig. B.2 | Current present between two plated at 2000 V during electrophoretic deposition.

With not receiving desired alpha and gamma responses after initial testing, it was apparent with the as-deposited detectors using this EPD method may need post-deposition modifications to achieve the desired responses.

The previous detectors that have performed as sensors have shown gamma responses in only very small regions of the detector, therefore, it was reasonable to believe that modifying the electrical characteristics so charge can move from point to point within the detectors with less difficulty. This would allow small functional sections to output the desired pulses more frequently. While it is expected to increase the dark current which is normally a very negative attribute for signal detection, any increase in signal response was desired, at that point, and noise could be dealt with in a variety of ways later on.

Removal and/or shortening of the oleic acid groups connecting to NCs as a method for increasing the electrical conduction in PbSe NCs has been achieved in other publications.[92, 106] Their three methods were examined and applied to our experiments as a starting point for post-deposition response modifications. Low-temperature annealing, high-temperature annealing, and detector soaking within hydrazine-acetonitrile solution all showed change in detector response.

B.1 Hydrazine Treatment

A set of detectors, each possessing twenty 10 mL drops of PbSe colloidal solution atop a copper substrate, were fabricated to carry-out the hydrazine experiment. Each detector individually experienced a hydrazine-acetonitrile solution at various times ranging in 10 – 240 min. Results, shown in Figs. B.3a and B.3b, reveal even a short soak time provides a drastic difference in electrical conductivity for these samples. The set of detectors representing the data seen in Figs.

B.3a and B.3b possess alpha responses (Fig. B.6a) seen at lower voltages (<100 V) while the requisite voltage for large breakdown pulses was substantially reduced. For soak sessions longer than 2 hrs., the PbSe solid atop the copper substrate becomes discolored and whitening significantly.

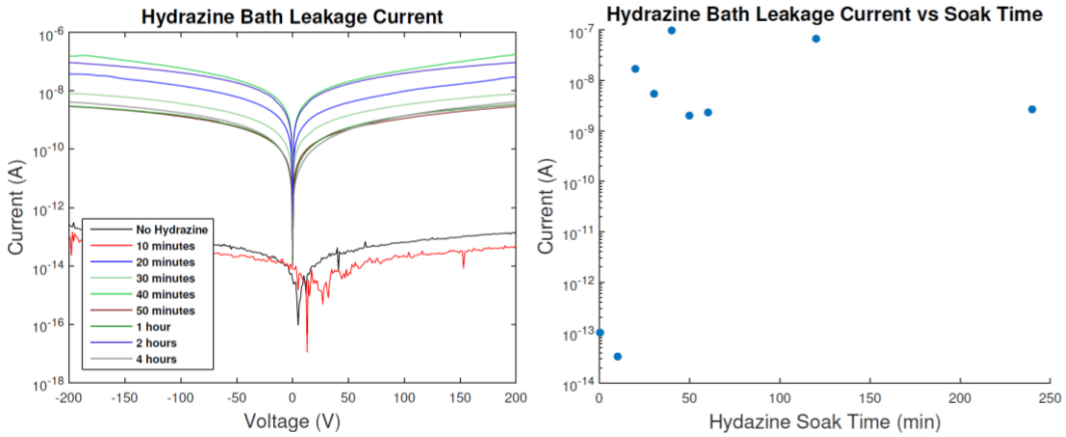

Fig. B.3 | (a) Current-Voltage curves and (b) current at 150 V for detectors after experiencing hydrazine-acetonitrile soaks at various times.

B.2 Annealing

In examining high-temperature annealing of the samples prior to low-temperature examination, a 4.64 mg PbSe sample was heated up to 600 °C. The resulting weight percentage throughout this experiment can be seen in Fig. B.4a. With the boiling point of oleic acid being listed as 360 °C, it can be seen that oleic acid groups begin to evaporate around ~300 °C and completely evaporated at ~500 °C. In observing the sample converting from a solid shavings of PbSe NCs to nearly transparent layer within the petri dish (Fig. B.4 (a, b)) for thermogravimetric analysis (TGA), there was no need to observe samples experience temperatures close to 500 °C.

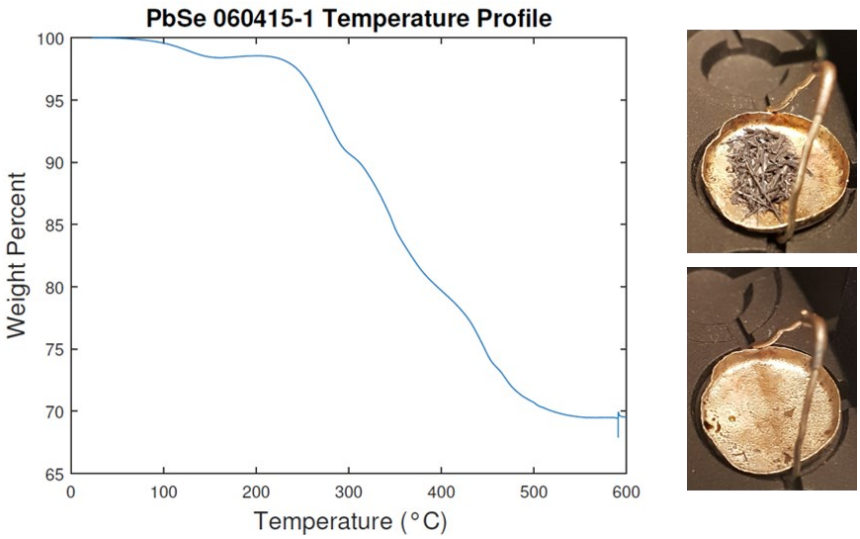

Fig. B.4 | (a) Thermogravimetric analysis (TGA) from PbSe solid after experiencing heating up to 600 °C. (b) Before and (c) experiencing TGA.

Low-temperature annealing is suggested as a method that causes sintering in the oleic acid groups, shortening the length between the NCs in order to allow easier electrical conduction between the NCs.[92] Devices composed of Si substrates, SiO_2, Au plating and twenty 5 mL drops each experienced rapid thermal processing (RTP) at 200 °C for times ranging from 1 to 3 hrs. Ridges form during the annealing process with the hopes of this experiment minimizing space within the NC film, pulling NCs closer together. This result potentially creates problems when attempting to metalize the surface of the detectors, as thinner areas may short through the device.

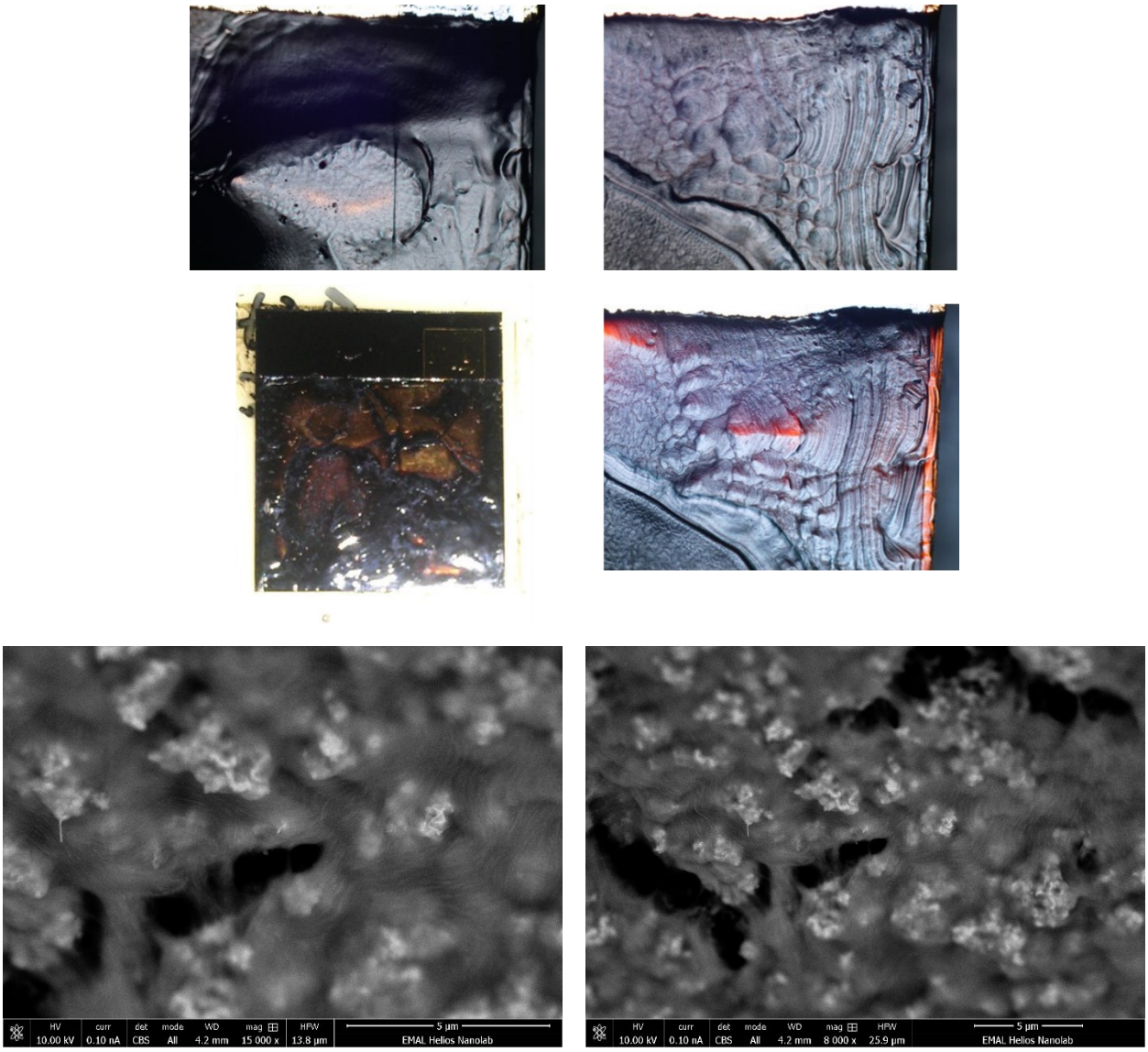

Fig. B.5 | Two PbSe detectors before experiencing rapid thermal processing (RTP); composed to 20-drops of PbSe colloidal solution atop SiO_2 and Au plating. (a, c) Before annealing. (b, d) After annealing with RTP for 2 hrs. at 150 °C. (e, f) SEM images of RTP results.

In looking at alpha and gamma with a device which hasn't experienced a hydrazine-acetonitrile soak, we already see solid responses with strong peaks for both an ^{241}Am and ^{133}Ba source. This proves EPD is a labor friendly technique which can result in uniform films of usable thickness deposited in ~2 or more hours.

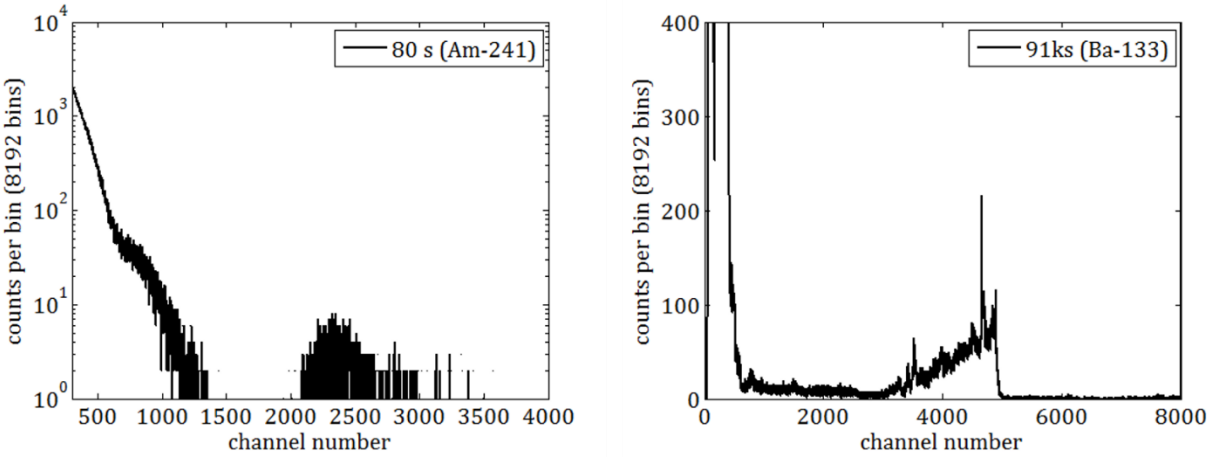

Fig. B.6 | (a) Alpha response from ^{241}Am and (b) Gamma response from ^{133}Ba from a device which has not experienced a hydrazine-acetonitrile soak.

BIBLIOGRAPHY

BIBLIOGRAPHY

1. Alivisatos, A. P., Semiconductor Clusters, Nanocrystals, and Quantum Dots. **1996,** *271* (5251), 933-937.

2. and, C. B. M.; Kagan, C. R.; Bawendi, M. G., Synthesis and Characterization of Monodisperse Nanocrystals and Close-Packed Nanocrystal Assemblies. **2000,** *30* (1), 545-610.

3. Burda, C.; Chen, X.; Narayanan, R.; El-Sayed, M. A., Chemistry and Properties of Nanocrystals of Different Shapes. *Chemical Reviews* **2005,** *105* (4), 1025-1102.

4. Chen, X.; Lou, Y.; Dayal, S.; Qiu, X.; Krolicki, R.; Burda, C.; Zhao, C.; Becker, J., Doped semiconductor nanomaterials. *Journal of nanoscience and nanotechnology* **2005,** *5* (9), 1408-20.

5. H, S.; Künzli, N.; Seethaler, R.; Chanel, O.; M, H.; Vergnaud, J.-C.; P, F.; Kaiser, R.; Horak, F.; Medina, S.; V, P.-T.; Quénel, P.; J, S.; Studnicka, M., Economic evaluation of health impacts due to road traffic-related air pollution: an impact assessment project of Austria, France and Switzerland. 2000; pp 451-479.

6. Hammig, M. D. In *Nanoscale Methods to Enhance the Detection of Ionizing Radiation. In Nenoi M., ed. Current Topics in Ionizing Radiation Research. London: IntechOpen*, 2012; pp 557-578.

7. Kim, G.; Hammig, M. D. In *Development of lead chalcogenide nanocrystalline (NC) semiconductor ionizing radiation detectors*, 2009 IEEE Nuclear Science Symposium Conference Record (NSS/MIC), 24 Oct.-1 Nov. 2009; 2009; pp 1317-1320.

8. Kim, G.; Huang, J.; Hammig, M. D., An Investigation of Nanocrystalline Semiconductor Assemblies as a Material Basis for Ionizing-Radiation Detectors. *IEEE Transactions on Nuclear Science* **2009,** *56* (3), 841-848.

9. Abel, K. A.; Shan, J.; Boyer, J.-C.; Harris, F.; van Veggel, F. C. J. M., Highly Photoluminescent PbS Nanocrystals: The Beneficial Effect of Trioctylphosphine. *Chemistry of Materials* **2008,** *20* (12), 3794-3796.

10. Kang, I.; Wise, F. W., Electronic structure and optical properties of PbS and PbSe quantum dots. *J. Opt. Soc. Am. B* **1997,** *14* (7), 1632-1646.

11. Wise, F. W., Lead Salt Quantum Dots: the Limit of Strong Quantum Confinement. *Accounts of Chemical Research* **2000,** *33* (11), 773-780.

12. Efros, A.; Efros, A., Interband Light Absorption in Semiconductor Spheres. *Soviet physics. Semiconductors* **1982,** *16*, 772-775.

13. Ekimov, A. I.; Efros, A. L.; Onushchenko, A. A., Quantum size effect in semiconductor microcrystals. *Solid State Communications* **1985,** *56* (11), 921-924.

14. Ekimov, A.; Onushchenko, A. J. S. P. S.-U., Quantum size effect in the optical-spectra of semiconductor micro-crystals. **1982,** *16* (7), 775-778.

15. Brus, L. E., Electron–electron and electron-hole interactions in small semiconductor crystallites: The size dependence of the lowest excited electronic state. **1984,** *80* (9), 4403-4409.

16. Brus, L., Electronic wave functions in semiconductor clusters: experiment and theory. *The Journal of Physical Chemistry* **1986,** *90* (12), 2555-2560.

17. Rossetti, R.; Nakahara, S.; Brus, L. E., Quantum size effects in the redox potentials, resonance Raman spectra, and electronic spectra of CdS crystallites in aqueous solution. **1983,** *79* (2), 1086-1088.

18. Weller, H.; Koch, U.; Gutiérrez, M.; Henglein, A., Photochemistry of Colloidal Metal Sulfides. 7. Absorption and Fluorescence of Extremely Small ZnS Particles (The World of the Neglected Dimensions). **1984,** *88* (7), 649-656.

19. Schornbaum, J. Lead Chalcogenide Quantum Dots and Quantum Dot Hybrids for Optoelectronic Devices

Bleichalkogenidquantenpunkte und Quantenpunkthybridverbindungen für optoelektronische Bauteile. 2015.

20. Wheeler, D. A.; Zhang, J. Z., Exciton Dynamics in Semiconductor Nanocrystals. **2013,** *25* (21), 2878-2896.

21. Alivisatos, A. P., Perspectives on the Physical Chemistry of Semiconductor Nanocrystals. *The Journal of Physical Chemistry* **1996,** *100* (31), 13226-13239.

22. *Colloidal Quantum Dot Optoelectronics and Photovoltaics*. Cambridge University Press: Cambridge, 2013.

23. Cossairt, B. M.; Juhas, P.; Billinge, S. J. L.; Owen, J. S., Tuning the Surface Structure and Optical Properties of CdSe Clusters Using Coordination Chemistry. *The Journal of Physical Chemistry Letters* **2011,** *2* (24), 3075-3080.

24. Spanhel, L.; Haase, M.; Weller, H.; Henglein, A., Photochemistry of colloidal semiconductors. 20. Surface modification and stability of strong luminescing CdS particles. *Journal of the American Chemical Society* **1987,** *109* (19), 5649-5655.

25. Weller, H.; Schmidt, H. M.; Koch, U.; Fojtik, A.; Baral, S.; Henglein, A.; Kunath, W.; Weiss, K.; Dieman, E., Photochemistry of colloidal semiconductors. Onset of light absorption as

a function of size of extremely small CdS particles. *Chemical Physics Letters* **1986,** *124* (6), 557-560.

26. Steigerwald, M. L.; Brus, L. E., Semiconductor crystallites: a class of large molecules. *Accounts of Chemical Research* **1990,** *23* (6), 183-188.

27. Henglein, A., Small-particle research: physicochemical properties of extremely small colloidal metal and semiconductor particles. *Chemical Reviews* **1989,** *89* (8), 1861-1873.

28. Eychmüller, A., Structure and Photophysics of Semiconductor Nanocrystals. *The Journal of Physical Chemistry B* **2000,** *104* (28), 6514-6528.

29. Murray, C. B.; Norris, D. J.; Bawendi, M. G., Synthesis and characterization of nearly monodisperse CdE (E = sulfur, selenium, tellurium) semiconductor nanocrystallites. *Journal of the American Chemical Society* **1993,** *115* (19), 8706-8715.

30. Yu, W. W.; Peng, X., Formation of High-Quality CdS and Other II–VI Semiconductor Nanocrystals in Noncoordinating Solvents: Tunable Reactivity of Monomers. **2002,** *41* (13), 2368-2371.

31. Yin, Y.; Alivisatos, A. P., Colloidal nanocrystal synthesis and the organic–inorganic interface. *Nature* **2005,** *437* (7059), 664-670.

32. de Mello Donegá, C.; Liljeroth, P.; Vanmaekelbergh, D., Physicochemical evaluation of the hot-injection method, a synthesis route for monodisperse nanocrystals. *Small (Weinheim an der Bergstrasse, Germany)* **2005,** *1* (12), 1152-62.

33. LaMer, V. K.; Dinegar, R. H., Theory, Production and Mechanism of Formation of Monodispersed Hydrosols. *Journal of the American Chemical Society* **1950,** *72* (11), 4847-4854.

34. Qu, L.; Yu, W. W.; Peng, X., In Situ Observation of the Nucleation and Growth of CdSe Nanocrystals. *Nano Letters* **2004,** *4* (3), 465-469.

35. Rempel, J. Y.; Bawendi, M. G.; Jensen, K. F., Insights into the Kinetics of Semiconductor Nanocrystal Nucleation and Growth. *Journal of the American Chemical Society* **2009,** *131* (12), 4479-4489.

36. Reiss, H., The Growth of Uniform Colloidal Dispersions. **1951,** *19* (4), 482-487.

37. Peng, X.; Wickham, J.; Alivisatos, A. P., Kinetics of II-VI and III-V Colloidal Semiconductor Nanocrystal Growth: "Focusing" of Size Distributions. *Journal of the American Chemical Society* **1998,** *120* (21), 5343-5344.

38. Kirakosyan, A.; Kim, J.; Lee, S. W.; Swathi, I.; Yoon, S.-G.; Choi, J., Optical Properties of Colloidal CH3NH3PbBr3 Nanocrystals by Controlled Growth of Lateral Dimension. *Crystal Growth & Design* **2017,** *17* (2), 794-799.

39. Bodnarchuk, M. I.; Kovalenko, M. V., Engineering colloidal quantum dots: Synthesis, surface chemistry, and self-assembly. In *Colloidal Quantum Dot Optoelectronics and Photovoltaics*, Sargent, E. H.; Konstantatos, G., Eds. Cambridge University Press: Cambridge, 2013; pp 1-29.

40. Hetsch, F.; Zhao, N.; Kershaw, S. V.; Rogach, A. L., Quantum dot field effect transistors. *Materials Today* **2013,** *16* (9), 312-325.

41. Hassinen, A.; Moreels, I.; De Nolf, K.; Smet, P. F.; Martins, J. C.; Hens, Z., Short-Chain Alcohols Strip X-Type Ligands and Quench the Luminescence of PbSe and CdSe Quantum Dots, Acetonitrile Does Not. *Journal of the American Chemical Society* **2012,** *134* (51), 20705-20712.

42. Goodwin, E. D.; Diroll, B. T.; Oh, S. J.; Paik, T.; Murray, C. B.; Kagan, C. R., Effects of Post-Synthesis Processing on CdSe Nanocrystals and Their Solids: Correlation between Surface Chemistry and Optoelectronic Properties. *The Journal of Physical Chemistry C* **2014,** *118* (46), 27097-27105.

43. Hu, J.; Li, L.-s.; Yang, W.; Manna, L.; Wang, L.-w.; Alivisatos, A. P., Linearly Polarized Emission from Colloidal Semiconductor Quantum Rods. **2001,** *292* (5524), 2060-2063.

44. Jun, Y.-w.; Choi, J.-s.; Cheon, J., Shape Control of Semiconductor and Metal Oxide Nanocrystals through Nonhydrolytic Colloidal Routes. **2006,** *45* (21), 3414-3439.

45. Peng, X.; Manna, L.; Yang, W.; Wickham, J.; Scher, E.; Kadavanich, A.; Alivisatos, A. P., Shape control of CdSe nanocrystals. *Nature* **2000,** *404* (6773), 59-61.

46. Milliron, D. J.; Hughes, S. M.; Cui, Y.; Manna, L.; Li, J.; Wang, L.-W.; Paul Alivisatos, A., Colloidal nanocrystal heterostructures with linear and branched topology. *Nature* **2004,** *430* (6996), 190-195.

47. Li, H.; Kanaras, A. G.; Manna, L., Colloidal Branched Semiconductor Nanocrystals: State of the Art and Perspectives. *Accounts of Chemical Research* **2013,** *46* (7), 1387-1396.

48. Jawaid, A. M.; Asunskis, D. J.; Snee, P. T., Shape-Controlled Colloidal Synthesis of Rock-Salt Lead Selenide Nanocrystals. *ACS Nano* **2011,** *5* (8), 6465-6471.

49. Cho, K.-S.; Talapin, D. V.; Gaschler, W.; Murray, C. B., Designing PbSe Nanowires and Nanorings through Oriented Attachment of Nanoparticles. *Journal of the American Chemical Society* **2005,** *127* (19), 7140-7147.

50. Penn, R. L.; Banfield, J. F., Imperfect Oriented Attachment: Dislocation Generation in Defect-Free Nanocrystals. **1998,** *281* (5379), 969-971.

51. Manna, L.; Milliron, D. J.; Meisel, A.; Scher, E. C.; Alivisatos, A. P., Controlled growth of tetrapod-branched inorganic nanocrystals. *Nat Mater* **2003,** *2* (6), 382-5.

52. Kim, M.-S.; Sung, Y.-M., Successive Solution–Liquid–Solid (SLS) Growth of Heterogeneous Nanowires. *Chemistry of Materials* **2013,** *25* (21), 4156-4164.

53. Yong, K.-T.; Sahoo, Y.; Choudhury, K. R.; Swihart, M. T.; Minter, J. R.; Prasad, P. N., Shape Control of PbSe Nanocrystals Using Noble Metal Seed Particles. *Nano Letters* **2006,** *6* (4), 709-714.

54. Na, Y. J.; Kim, H. S.; Park, J., Morphology-controlled Lead Selenide Nanocrystals and Their In Situ Growth on Carbon Nanotubes. *The Journal of Physical Chemistry C* **2008,** *112* (30), 11218-11226.

55. Penn, R. L.; Banfield, J. F., Oriented attachment and growth, twinning, polytypism, and formation of metastable phases: Insights from nanocrystalline TiO2 %J American Mineralogist. **1998,** *83* (9-10), 1077-1082.

56. Penn, R. L.; Banfield, J. F., Morphology development and crystal growth in nanocrystalline aggregates under hydrothermal conditions: insights from titania. *Geochimica et Cosmochimica Acta* **1999,** *63* (10), 1549-1557.

57. Li, D.; Nielsen, M. H.; Lee, J. R.; Frandsen, C.; Banfield, J. F.; De Yoreo, J. J., Direction-specific interactions control crystal growth by oriented attachment. *Science* **2012,** *336* (6084), 1014-8.

58. van Huis, M. A.; Kunneman, L. T.; Overgaag, K.; Xu, Q.; Pandraud, G.; Zandbergen, H. W.; Vanmaekelbergh, D., Low-temperature nanocrystal unification through rotations and relaxations probed by in situ transmission electron microscopy. *Nano Lett* **2008,** *8* (11), 3959-63.

59. Tang, Z.; Kotov, N. A.; Giersig, M., Spontaneous Organization of Single CdTe Nanoparticles into Luminescent Nanowires. **2002,** *297* (5579), 237-240.

60. Pacholski, C.; Kornowski, A.; Weller, H., Self-assembly of ZnO: from nanodots to nanorods. *Angewandte Chemie (International ed. in English)* **2002,** *41* (7), 1188-91.

61. Boneschanscher, M. P.; Evers, W. H.; Geuchies, J. J.; Altantzis, T.; Goris, B.; Rabouw, F. T.; van Rossum, S. A. P.; van der Zant, H. S. J.; Siebbeles, L. D. A.; Van Tendeloo, G.; Swart, I.; Hilhorst, J.; Petukhov, A. V.; Bals, S.; Vanmaekelbergh, D., Long-range orientation and atomic attachment of nanocrystals in 2D honeycomb superlattices. **2014,** *344* (6190), 1377-1380.

62. Peng, X., Mechanisms for the Shape-Control and Shape-Evolution of Colloidal Semiconductor Nanocrystals. **2003,** *15* (5), 459-463.

63. Peng, Z. A.; Peng, X., Nearly Monodisperse and Shape-Controlled CdSe Nanocrystals via Alternative Routes: Nucleation and Growth. *Journal of the American Chemical Society* **2002,** *124* (13), 3343-3353.

64. Nann, T.; Skinner, W. M., Quantum Dots for Electro-Optic Devices. *ACS Nano* **2011,** *5* (7), 5291-5295.

65. Shirasaki, Y.; Supran, G. J.; Bawendi, M. G.; Bulović, V., Emergence of colloidal quantum-dot light-emitting technologies. *Nature Photonics* **2013,** *7* (1), 13-23.

66. Konstantatos, G.; Sargent, E. H., Nanostructured materials for photon detection. *Nature Nanotechnology* **2010,** *5* (6), 391-400.

67. Chen, O.; Zhao, J.; Chauhan, V. P.; Cui, J.; Wong, C.; Harris, D. K.; Wei, H.; Han, H. S.; Fukumura, D.; Jain, R. K.; Bawendi, M. G., Compact high-quality CdSe-CdS core-shell nanocrystals with narrow emission linewidths and suppressed blinking. *Nat Mater* **2013,** *12* (5), 445-51.

68. Talapin, D. V.; Rogach, A. L.; Kornowski, A.; Haase, M.; Weller, H., Highly Luminescent Monodisperse CdSe and CdSe/ZnS Nanocrystals Synthesized in a Hexadecylamine-Trioctylphosphine Oxide-Trioctylphospine Mixture. *Nano Letters* **2001,** *1* (4), 207-211.

69. Gao, J.; Johnson, J. C., Charge Trapping in Bright and Dark States of Coupled PbS Quantum Dot Films. *ACS Nano* **2012,** *6* (4), 3292-3303.

70. Schaller, R. D.; Klimov, V. I., High efficiency carrier multiplication in PbSe nanocrystals: implications for solar energy conversion. *Phys Rev Lett* **2004,** *92* (18), 186601.

71. Maiti, S.; Laan, M. v. d.; Poonia, D.; Schall, P.; Kinge, S.; Siebbeles, L. D. A., Emergence of new materials for exploiting highly efficient carrier multiplication in photovoltaics. **2020,** *1* (1), 011302.

72. Ellingson, R. J.; Beard, M. C.; Johnson, J. C.; Yu, P.; Micic, O. I.; Nozik, A. J.; Shabaev, A.; Efros, A. L., Highly Efficient Multiple Exciton Generation in Colloidal PbSe and PbS Quantum Dots. *Nano Letters* **2005,** *5* (5), 865-871.

73. Allan, G.; Delerue, C., Role of impact ionization in multiple exciton generation in PbSe nanocrystals. *Physical Review B* **2006,** *73* (20), 205423.

74. Klimov, V. I., Optical Nonlinearities and Ultrafast Carrier Dynamics in Semiconductor Nanocrystals. *The Journal of Physical Chemistry B* **2000,** *104* (26), 6112-6123.

75. Klimov, V. I., Mechanisms for Photogeneration and Recombination of Multiexcitons in Semiconductor Nanocrystals: Implications for Lasing and Solar Energy Conversion. *The Journal of Physical Chemistry B* **2006,** *110* (34), 16827-16845.

76. Roy, D.; Das, A.; De, C. K.; Mandal, S.; Bangal, P. R.; Mandal, P. K., Why Does the Photoluminescence Efficiency Depend on Excitation Energy in Case of a Quantum Dot? A Case Study of CdSe-Based Core/Alloy Shell/Shell Quantum Dots Employing Ultrafast Pump–Probe Spectroscopy and Single Particle Spectroscopy. *The Journal of Physical Chemistry C* **2019,** *123* (11), 6922-6933.

77. Schaller, R. D.; Pietryga, J. M.; Klimov, V. I., Carrier Multiplication in InAs Nanocrystal Quantum Dots with an Onset Defined by the Energy Conservation Limit. *Nano Letters* **2007,** *7* (11), 3469-3476.

78. Beard, M. C.; Midgett, A. G.; Hanna, M. C.; Luther, J. M.; Hughes, B. K.; Nozik, A. J., Comparing Multiple Exciton Generation in Quantum Dots To Impact Ionization in Bulk Semiconductors: Implications for Enhancement of Solar Energy Conversion. *Nano Letters* **2010,** *10* (8), 3019-3027.

79. Beard, M. C.; Ellingson, R. J., Multiple exciton generation in semiconductor nanocrystals: Toward efficient solar energy conversion. **2008,** *2* (5), 377-399.

80. Nozik, A. J., Spectroscopy and hot electron relaxation dynamics in semiconductor quantum wells and quantum dots. *Annu Rev Phys Chem* **2001,** *52*, 193-231.

81. Nozik, A. J., SPECTROSCOPY AND HOT ELECTRON RELAXATION DYNAMICS IN SEMICONDUCTOR QUANTUM WELLS AND QUANTUM DOTS. **2001,** *52* (1), 193-231.

82. Schaller, R. D.; Pietryga, J. M.; Goupalov, S. V.; Petruska, M. A.; Ivanov, S. A.; Klimov, V. I., Breaking the Phonon Bottleneck in Semiconductor Nanocrystals via Multiphonon Emission Induced by Intrinsic Nonadiabatic Interactions. *Physical Review Letters* **2005,** *95* (19), 196401.

83. Schaller, R. D.; Sykora, M.; Pietryga, J. M.; Klimov, V. I., Seven Excitons at a Cost of One: Redefining the Limits for Conversion Efficiency of Photons into Charge Carriers. *Nano Letters* **2006,** *6* (3), 424-429.

84. Beard, M. C.; Knutsen, K. P.; Yu, P.; Luther, J. M.; Song, Q.; Metzger, W. K.; Ellingson, R. J.; Nozik, A. J., Multiple Exciton Generation in Colloidal Silicon Nanocrystals. *Nano Letters* **2007,** *7* (8), 2506-2512.

85. Shabaev, A.; Efros, A. L.; Nozik, A. J., Multiexciton Generation by a Single Photon in Nanocrystals. *Nano Letters* **2006,** *6* (12), 2856-2863.

86. Nair, G.; Bawendi, M. G., Carrier multiplication yields of CdSe and CdTe nanocrystals by transient photoluminescence spectroscopy. *Physical Review B* **2007,** *76* (8), 081304.

87. Nair, G.; Geyer, S. M.; Chang, L.-Y.; Bawendi, M. G., Carrier multiplication yields in PbS and PbSe nanocrystals measured by transient photoluminescence. *Physical Review B* **2008,** *78* (12), 125325.

88. McGuire, J. A.; Joo, J.; Pietryga, J. M.; Schaller, R. D.; Klimov, V. I., New Aspects of Carrier Multiplication in Semiconductor Nanocrystals. *Accounts of Chemical Research* **2008,** *41* (12), 1810-1819.

89. McGuire, J. A.; Sykora, M.; Joo, J.; Pietryga, J. M.; Klimov, V. I., Apparent versus true carrier multiplication yields in semiconductor nanocrystals. *Nano Lett* **2010,** *10* (6), 2049-57.

90. Nozik, A. J., Quantum dot solar cells. *Physica E: Low-dimensional Systems and Nanostructures* **2002,** *14* (1), 115-120.

91. Stewart, J. T.; Padilha, L. A.; Qazilbash, M. M.; Pietryga, J. M.; Midgett, A. G.; Luther, J. M.; Beard, M. C.; Nozik, A. J.; Klimov, V. I., Comparison of Carrier Multiplication Yields in PbS and PbSe Nanocrystals: The Role of Competing Energy-Loss Processes. *Nano Letters* **2012,** *12* (2), 622-628.

92. Law, M.; Luther, J. M.; Song, Q.; Hughes, B. K.; Perkins, C. L.; Nozik, A. J., Structural, optical, and electrical properties of PbSe nanocrystal solids treated thermally or with simple amines. *J Am Chem Soc* **2008,** *130* (18), 5974-85.

93. Oh, S. J.; Berry, N. E.; Choi, J.-H.; Gaulding, E. A.; Lin, H.; Paik, T.; Diroll, B. T.; Muramoto, S.; Murray, C. B.; Kagan, C. R., Designing High-Performance PbS and PbSe Nanocrystal Electronic Devices through Stepwise, Post-Synthesis, Colloidal Atomic Layer Deposition. *Nano Letters* **2014,** *14* (3), 1559-1566.

94. Coe-Sullivan, S.; Steckel, J. S.; Woo, W.-K.; Bawendi, M. G.; Bulović, V., Large-Area Ordered Quantum-Dot Monolayers via Phase Separation During Spin-Casting. **2005,** *15* (7), 1117-1124.

95. Liu, Y.; Gibbs, M.; Puthussery, J.; Gaik, S.; Ihly, R.; Hillhouse, H. W.; Law, M., Dependence of Carrier Mobility on Nanocrystal Size and Ligand Length in PbSe Nanocrystal Solids. *Nano Letters* **2010,** *10* (5), 1960-1969.

96. Tang, J.; Konstantatos, G.; Hinds, S.; Myrskog, S.; Pattantyus-Abraham, A. G.; Clifford, J.; Sargent, E. H., Heavy-Metal-Free Solution-Processed Nanoparticle-Based Photodetectors: Doping of Intrinsic Vacancies Enables Engineering of Sensitivity and Speed. *ACS Nano* **2009,** *3* (2), 331-338.

97. Haverinen, H. M.; Myllylä, R. A.; Jabbour, G. E., Inkjet printing of light emitting quantum dots. **2009,** *94* (7), 073108.

98. Kramer, I. J.; Minor, J. C.; Moreno-Bautista, G.; Rollny, L.; Kanjanaboos, P.; Kopilovic, D.; Thon, S. M.; Carey, G. H.; Chou, K. W.; Zhitomirsky, D.; Amassian, A.; Sargent, E. H., Efficient Spray-Coated Colloidal Quantum Dot Solar Cells. **2015,** *27* (1), 116-121.

99. Choi, J.-H.; Fafarman, A. T.; Oh, S. J.; Ko, D.-K.; Kim, D. K.; Diroll, B. T.; Muramoto, S.; Gillen, J. G.; Murray, C. B.; Kagan, C. R., Bandlike Transport in Strongly Coupled and Doped Quantum Dot Solids: A Route to High-Performance Thin-Film Electronics. *Nano Letters* **2012,** *12* (5), 2631-2638.

100. Talgorn, E.; Gao, Y.; Aerts, M.; Kunneman, L. T.; Schins, J. M.; Savenije, T. J.; van Huis, M. A.; van der Zant, H. S. J.; Houtepen, A. J.; Siebbeles, L. D. A., Unity quantum yield of photogenerated charges and band-like transport in quantum-dot solids. *Nature Nanotechnology* **2011,** *6* (11), 733-739.

101. Jarosz, M. V.; Porter, V. J.; Fisher, B. R.; Kastner, M. A.; Bawendi, M. G., Photoconductivity studies of treated CdSe quantum dot films exhibiting increased exciton ionization efficiency. *Physical Review B* **2004,** *70* (19), 195327.

102. Jeong, K. S.; Tang, J.; Liu, H.; Kim, J.; Schaefer, A. W.; Kemp, K.; Levina, L.; Wang, X.; Hoogland, S.; Debnath, R.; Brzozowski, L.; Sargent, E. H.; Asbury, J. B., Enhanced Mobility-Lifetime Products in PbS Colloidal Quantum Dot Photovoltaics. *ACS Nano* **2012,** *6* (1), 89-99.

103. Luther, J. M.; Law, M.; Song, Q.; Perkins, C. L.; Beard, M. C.; Nozik, A. J., Structural, Optical, and Electrical Properties of Self-Assembled Films of PbSe Nanocrystals Treated with 1,2-Ethanedithiol. *ACS Nano* **2008,** *2* (2), 271-280.

104. Tang, J.; Kemp, K. W.; Hoogland, S.; Jeong, K. S.; Liu, H.; Levina, L.; Furukawa, M.; Wang, X.; Debnath, R.; Cha, D.; Chou, K. W.; Fischer, A.; Amassian, A.; Asbury, J. B.; Sargent, E. H., Colloidal-quantum-dot photovoltaics using atomic-ligand passivation. *Nature Materials* **2011,** *10* (10), 765-771.

105. Kang, M. S.; Sahu, A.; Norris, D. J.; Frisbie, C. D., Size- and temperature-dependent charge transport in PbSe nanocrystal thin films. *Nano Lett* **2011,** *11* (9), 3887-92.

106. Talapin, D. V.; Murray, C. B., PbSe Nanocrystal Solids for n- and p-Channel Thin Film Field-Effect Transistors. **2005,** *310* (5745), 86-89.

107. Konstantatos, G.; Howard, I.; Fischer, A.; Hoogland, S.; Clifford, J.; Klem, E.; Levina, L.; Sargent, E. H., Ultrasensitive solution-cast quantum dot photodetectors. *Nature* **2006,** *442* (7099), 180-183.

108. Sun, B.; Findikoglu, A. T.; Sykora, M.; Werder, D. J.; Klimov, V. I., Hybrid photovoltaics based on semiconductor nanocrystals and amorphous silicon. *Nano Lett* **2009,** *9* (3), 1235-41.

109. Poznyak, S. K.; Osipovich, N. P.; Shavel, A.; Talapin, D. V.; Gao, M.; Eychmüller, A.; Gaponik, N., Size-dependent electrochemical behavior of thiol-capped CdTe nanocrystals in aqueous solution. *The journal of physical chemistry. B* **2005,** *109* (3), 1094-100.

110. Kovalenko, M. V.; Scheele, M.; Talapin, D. V., Colloidal Nanocrystals with Molecular Metal Chalcogenide Surface Ligands. **2009,** *324* (5933), 1417-1420.

111. Kovalenko, M. V.; Bodnarchuk, M. I.; Zaumseil, J.; Lee, J. S.; Talapin, D. V., Expanding the chemical versatility of colloidal nanocrystals capped with molecular metal chalcogenide ligands. *J Am Chem Soc* **2010,** *132* (29), 10085-92.

112. Zhang, H.; Jang, J.; Liu, W.; Talapin, D. V., Colloidal Nanocrystals with Inorganic Halide, Pseudohalide, and Halometallate Ligands. *ACS Nano* **2014,** *8* (7), 7359-7369.

113. Luther, J. M.; Law, M.; Beard, M. C.; Song, Q.; Reese, M. O.; Ellingson, R. J.; Nozik, A. J., Schottky Solar Cells Based on Colloidal Nanocrystal Films. *Nano Letters* **2008,** *8* (10), 3488-3492.

114. Bae, W. K.; Joo, J.; Padilha, L. A.; Won, J.; Lee, D. C.; Lin, Q.; Koh, W.-k.; Luo, H.; Klimov, V. I.; Pietryga, J. M., Highly Effective Surface Passivation of PbSe Quantum Dots through Reaction with Molecular Chlorine. *Journal of the American Chemical Society* **2012,** *134* (49), 20160-20168.

115. Drndić, M.; Jarosz, M. V.; Morgan, N. Y.; Kastner, M. A.; Bawendi, M. G., Transport properties of annealed CdSe colloidal nanocrystal solids. **2002,** *92* (12), 7498-7503.

116. Turyanska, L.; Elfurawi, U.; Li, M.; Fay, M. W.; Thomas, N. R.; Mann, S.; Blokland, J. H.; Christianen, P. C. M.; Patanè, A., Tailoring the physical properties of thiol-capped PbS quantum dots by thermal annealing. *Nanotechnology* **2009,** *20* (31), 315604.

117. Baik, S. J.; Kim, K.; Lim, K. S.; Jung, S.; Park, Y.-C.; Han, D. G.; Lim, S.; Yoo, S.; Jeong, S., Low-Temperature Annealing for Highly Conductive Lead Chalcogenide Quantum Dot Solids. *The Journal of Physical Chemistry C* **2011,** *115* (3), 607-612.

118. Kang, M. S.; Sahu, A.; Frisbie, C. D.; Norris, D. J., Influence of Silver Doping on Electron Transport in Thin Films of PbSe Nanocrystals. **2013,** *25* (5), 725-731.

119. Baumgardner, W. J.; Whitham, K.; Hanrath, T., Confined-but-Connected Quantum Solids via Controlled Ligand Displacement. *Nano Letters* **2013,** *13* (7), 3225-3231.

120. Sandeep, C. S. S.; Azpiroz, J. M.; Evers, W. H.; Boehme, S. C.; Moreels, I.; Kinge, S.; Siebbeles, L. D. A.; Infante, I.; Houtepen, A. J., Epitaxially Connected PbSe Quantum-Dot Films: Controlled Neck Formation and Optoelectronic Properties. *ACS Nano* **2014,** *8* (11), 11499-11511.

121. Yu, W. W.; Falkner, J. C.; Shih, B. S.; Colvin, V. L., Preparation and Characterization of Monodisperse PbSe Semiconductor Nanocrystals in a Noncoordinating Solvent. *Chemistry of Materials* **2004,** *16* (17), 3318-3322.

122. Mentzel, T. S.; Porter, V. J.; Geyer, S.; MacLean, K.; Bawendi, M. G.; Kastner, M. A., Charge transport in PbSe nanocrystal arrays. *Physical Review B* **2008,** *77* (7), 075316.

123. Oh, S. J.; Wang, Z.; Berry, N. E.; Choi, J. H.; Zhao, T.; Gaulding, E. A.; Paik, T.; Lai, Y.; Murray, C. B.; Kagan, C. R., Engineering charge injection and charge transport for high performance PbSe nanocrystal thin film devices and circuits. *Nano Lett* **2014,** *14* (11), 6210-6.

124. Ihly, R.; Tolentino, J.; Liu, Y.; Gibbs, M.; Law, M., The Photothermal Stability of PbS Quantum Dot Solids. *ACS Nano* **2011,** *5* (10), 8175-8186.

125. Mott, N. F., Conduction in non-crystalline materials. *The Philosophical Magazine: A Journal of Theoretical Experimental and Applied Physics* **1969,** *19* (160), 835-852.

126. Chung, D. S.; Lee, J. S.; Huang, J.; Nag, A.; Ithurria, S.; Talapin, D. V., Low voltage, hysteresis free, and high mobility transistors from all-inorganic colloidal nanocrystals. *Nano Lett* **2012,** *12* (4), 1813-20.

127. Murray, C. B.; Sun, S.; Gaschler, W.; Doyle, H.; Betley, T. A.; Kagan, C. R., Colloidal synthesis of nanocrystals and nanocrystal superlattices. *IBM Journal of Research and Development* **2001,** *45* (1), 47-56.

128. Hines, M. A.; Scholes, G. D., Colloidal PbS Nanocrystals with Size-Tunable Near-Infrared Emission: Observation of Post-Synthesis Self-Narrowing of the Particle Size Distribution. **2003,** *15* (21), 1844-1849.

129. Du, H.; Chen, C.; Krishnan, R.; Krauss, T. D.; Harbold, J. M.; Wise, F. W.; Thomas, M. G.; Silcox, J., Optical Properties of Colloidal PbSe Nanocrystals. *Nano Letters* **2002,** *2* (11), 1321-1324.

130. Murphy, J. E.; Beard, M. C.; Norman, A. G.; Ahrenkiel, S. P.; Johnson, J. C.; Yu, P.; Mićić, O. I.; Ellingson, R. J.; Nozik, A. J., PbTe Colloidal Nanocrystals: Synthesis, Characterization, and Multiple Exciton Generation. *Journal of the American Chemical Society* **2006,** *128* (10), 3241-3247.

131. Urban, J. J.; Talapin, D. V.; Shevchenko, E. V.; Murray, C. B., Self-Assembly of PbTe Quantum Dots into Nanocrystal Superlattices and Glassy Films. *Journal of the American Chemical Society* **2006,** *128* (10), 3248-3255.

132. Lu, W.; Fang, J.; Stokes, K. L.; Lin, J., Shape Evolution and Self Assembly of Monodisperse PbTe Nanocrystals. *Journal of the American Chemical Society* **2004,** *126* (38), 11798-11799.

133. Machol, J. L.; Wise, F. W.; Patel, R. C.; Tanner, D. B., Vibronic quantum beats in PbS microcrystallites. *Physical Review B* **1993,** *48* (4), 2819-2822.

134. Moreels, I.; Lambert, K.; Smeets, D.; De Muynck, D.; Nollet, T.; Martins, J. C.; Vanhaecke, F.; Vantomme, A.; Delerue, C.; Allan, G.; Hens, Z., Size-Dependent Optical Properties of Colloidal PbS Quantum Dots. *ACS Nano* **2009,** *3* (10), 3023-3030.

135. Moreels, I.; Fritzinger, B.; Martins, J. C.; Hens, Z., Surface Chemistry of Colloidal PbSe Nanocrystals. *Journal of the American Chemical Society* **2008,** *130* (45), 15081-15086.

136. Semonin, O. E.; Johnson, J. C.; Luther, J. M.; Midgett, A. G.; Nozik, A. J.; Beard, M. C., Absolute Photoluminescence Quantum Yields of IR-26 Dye, PbS, and PbSe Quantum Dots. *The Journal of Physical Chemistry Letters* **2010,** *1* (16), 2445-2450.

137. Moreels, I.; Justo, Y.; De Geyter, B.; Haustraete, K.; Martins, J. C.; Hens, Z., Size-Tunable, Bright, and Stable PbS Quantum Dots: A Surface Chemistry Study. *ACS Nano* **2011,** *5* (3), 2004-2012.

138. Fang, C.; van Huis, M. A.; Vanmaekelbergh, D.; Zandbergen, H. W., Energetics of Polar and Nonpolar Facets of PbSe Nanocrystals from Theory and Experiment. *ACS Nano* **2010,** *4* (1), 211-218.

139. Boles, M. A.; Talapin, D. V., Connecting the dots. **2014,** *344* (6190), 1340-1341.

140. Moreels, I.; Lambert, K.; De Muynck, D.; Vanhaecke, F.; Poelman, D.; Martins, J. C.; Allan, G.; Hens, Z., Composition and Size-Dependent Extinction Coefficient of Colloidal PbSe Quantum Dots. *Chemistry of Materials* **2007,** *19* (25), 6101-6106.

141. Dai, Q.; Wang, Y.; Li, X.; Zhang, Y.; Pellegrino, D. J.; Zhao, M.; Zou, B.; Seo, J.; Wang, Y.; Yu, W. W., Size-Dependent Composition and Molar Extinction Coefficient of PbSe Semiconductor Nanocrystals. *ACS Nano* **2009,** *3* (6), 1518-1524.

142. Garcia-Gutierrez, D. I.; Garcia-Gutierrez, D. F.; De Leon-Covian, L. M.; Treviño-Gonzalez, M. T.; Garza-Navarro, M. A.; Moreno-Cortez, I. E.; Cienfuegos-Pelaes, R. F., Aberration Corrected STEM Study of the Surface of Lead Chalcogenide Nanoparticles. *The Journal of Physical Chemistry C* **2014,** *118* (38), 22291-22298.

143. Kim, D.; Kim, D.-H.; Lee, J.-H.; Grossman, J. C., Impact of Stoichiometry on the Electronic Structure of PbS Quantum Dots. *Physical Review Letters* **2013,** *110* (19), 196802.

144. Hendricks, M. P.; Campos, M. P.; Cleveland, G. T.; Jen-La Plante, I.; Owen, J. S., A tunable library of substituted thiourea precursors to metal sulfide nanocrystals. *Science* **2015,** *348* (6240), 1226-1230.

145. Koh, W.-k.; Bartnik, A. C.; Wise, F. W.; Murray, C. B., Synthesis of Monodisperse PbSe Nanorods: A Case for Oriented Attachment. *Journal of the American Chemical Society* **2010,** *132* (11), 3909-3913.

146. Swapp, S. Scanning Electron Microscopy (SEM). https://serc.carleton.edu/research_education/geochemsheets/techniques/SEM.html.

147. L. Reimer, H. K., *Transmission Electron Microscopy*. Springer Science+Business Media, Inc.: 2008; Vol. 5. Aufl.

148. J. F. Watts, J. W., *An Introduction to Surface Analysis by XPS and AES*. John Wiley & Sons Ltd: 2003.

149. Xia, Y.; Yang, P.; Sun, Y.; Wu, Y.; Mayers, B.; Gates, B.; Yin, Y.; Kim, F.; Yan, H., One-Dimensional Nanostructures: Synthesis, Characterization, and Applications. *Advanced Materials* **2003,** *15* (5), 353-389.

150. Xiao, Z.-L.; Han, C. Y.; Kwok, W.-K.; Wang, H.-H.; Welp, U.; Wang, J.; Crabtree, G. W., Tuning the Architecture of Mesostructures by Electrodeposition. *Journal of the American Chemical Society* **2004,** *126* (8), 2316-2317.

151. Gao, F.; Lu, Q.; Xie, S.; Zhao, D., A Simple Route for the Synthesis of Multi-Armed CdS Nanorod-Based Materials. *Advanced Materials* **2002,** *14* (21), 1537-1540.

152. Sone, E. D.; Zubarev, E. R.; Stupp, S. I., Semiconductor Nanohelices Templated by Supramolecular Ribbons. *Angewandte Chemie International Edition* **2002,** *41* (10), 1705-1709.

153. Jun, Y.-w.; Lee, S.-M.; Kang, N.-J.; Cheon, J., Controlled Synthesis of Multi-armed CdS Nanorod Architectures Using Monosurfactant System. *Journal of the American Chemical Society* **2001,** *123* (21), 5150-5151.

154. Yu, S.-H.; Yoshimura, M., Shape and Phase Control of ZnS Nanocrystals: Template Fabrication of Wurtzite ZnS Single-Crystal Nanosheets and ZnO Flake-like Dendrites from a Lamellar Molecular Precursor ZnS·(NH2CH2CH2NH2)0.5. *Advanced Materials* **2002,** *14* (4), 296-300.

155. Ma, C.; Moore, D.; Li, J.; Wang, Z. L., Nanobelts, Nanocombs, and Nanowindmills of Wurtzite ZnS. *Advanced Materials* **2003,** *15* (3), 228-231.

156. Lu, Q.; Gao, F.; Zhao, D., Creation of a Unique Self-Supported Pattern of Radially Aligned Semiconductor Ag2S Nanorods. *Angewandte Chemie International Edition* **2002,** *41* (11), 1932-1934.

157. Lu, Q.; Gao, F.; Zhao, D., One-Step Synthesis and Assembly of Copper Sulfide Nanoparticles to Nanowires, Nanotubes, and Nanovesicles by a Simple Organic Amine-Assisted Hydrothermal Process. *Nano Letters* **2002,** *2* (7), 725-728.

158. Warner, J. H.; Thomsen, E.; Watt, A. R.; Heckenberg, N. R.; Rubinsztein-Dunlop, H., Time-resolved photoluminescence spectroscopy of ligand-capped PbS nanocrystals. *Nanotechnology* **2004,** *16* (2), 175-179.

159. McDonald, S. A.; Konstantatos, G.; Zhang, S.; Cyr, P. W.; Klem, E. J. D.; Levina, L.; Sargent, E. H., Solution-processed PbS quantum dot infrared photodetectors and photovoltaics. *Nature Materials* **2005,** *4* (2), 138-142.

160. Roy Choudhury, K.; Sahoo, Y.; Jang, S.; Prasad, P. N., Efficient Photosensitization and High Optical Gain in a Novel Quantum-Dot-Sensitized Hybrid Photorefractive Nanocomposite at a Telecommunications Wavelength. *Advanced Functional Materials* **2005,** *15* (5), 751-756.

161. Levina, L.; Sukhovatkin, V.; Musikhin, S.; Cauchi, S.; Nisman, R.; Bazett-Jones, D. P.; Sargent, E. H., Efficient Infrared-Emitting PbS Quantum Dots Grown on DNA and Stable in Aqueous Solution and Blood Plasma. *Advanced Materials* **2005,** *17* (15), 1854-1857.

162. Bakueva, L.; Musikhin, S.; Hines, M. A.; Chang, T.-W. F.; Tzolov, M.; Scholes, G. D.; Sargent, E. H., Size-tunable infrared (1000–1600 nm) electroluminescence from PbS quantum-dot nanocrystals in a semiconducting polymer. *Applied Physics Letters* **2003,** *82* (17), 2895-2897.

163. Tamulaitis, G.; Gulbinas, V.; Kodis, G.; Dementjev, A.; Valkunas, L.; Motchalov, I.; Raaben, H., Optical nonlinearities of glass doped with PbS nanocrystals. *Journal of Applied Physics* **2000,** *88* (1), 178-182.

164. Dantas, N. O.; Qu, F.; Silva, R. S.; Morais, P. C., Anti-Stokes Photoluminescence in Nanocrystal Quantum Dots. *The Journal of Physical Chemistry B* **2002,** *106* (30), 7453-7457.

165. Plass, R.; Pelet, S.; Krueger, J.; Grätzel, M.; Bach, U., Quantum Dot Sensitization of Organic−Inorganic Hybrid Solar Cells. *The Journal of Physical Chemistry B* **2002,** *106* (31), 7578-7580.

166. Dementjev, A.; Gulbinas, V.; Valkunas, L.; Raaben, H., Nonlinear absorption of PbS nanocrystals in silicate glass. *physica status solidi (b)* **2004,** *241* (4), 945-951.

167. Wang, Y.; Dai, Q.; Yang, X.; Zou, B.; Li, D.; Liu, B.; Hu, M. Z.; Zou, G., A facile approach to PbS nanoflowers and their shape-tunable single crystal hollow nanostructures: Morphology evolution. *CrystEngComm* **2011,** *13* (1), 199-203.

168. Gao, F.; Lu, Q.; Liu, X.; Yan, Y.; Zhao, D., Controlled Synthesis of Semiconductor PbS Nanocrystals and Nanowires Inside Mesoporous Silica SBA-15 Phase. *Nano Letters* **2001,** *1* (12), 743-748.

169. Wang, N.; Cao, X.; Guo, L.; Yang, S.; Wu, Z., Facile Synthesis of PbS Truncated Octahedron Crystals with High Symmetry and Their Large-Scale Assembly into Regular Patterns by a Simple Solution Route. *ACS Nano* **2008,** *2* (2), 184-190.

170. Wang, S.; Yang, S., Preparation and Characterization of Oriented PbS Crystalline Nanorods in Polymer Films. *Langmuir* **2000,** *16* (2), 389-397.

171. Leontidis, E.; Orphanou, M.; Kyprianidou-Leodidou, T.; Krumeich, F.; Caseri, W., Composite Nanotubes Formed by Self-Assembly of PbS Nanoparticles. *Nano Letters* **2003,** *3* (4), 569-572.

172. Ni, Y.; Liu, H.; Wang, F.; Liang, Y.; Hong, J.; Ma, X.; Xu, Z., Shape Controllable Preparation of PbS Crystals by a Simple Aqueous Phase Route. *Crystal Growth & Design* **2004,** *4* (4), 759-764.

173. Wang, D.; Yu, D.; Shao, M.; Liu, X.; Yu, W.; Qian, Y., Dendritic growth of PbS crystals with different morphologies. *Journal of Crystal Growth* **2003,** *257* (3), 384-389.

174. Wang, S. F.; Gu, F.; Lü, M. K., Sonochemical Synthesis of Hollow PbS Nanospheres. *Langmuir* **2006,** *22* (1), 398-401.

175. Lee, S.-M.; Jun, Y.-w.; Cho, S.-N.; Cheon, J., Single-Crystalline Star-Shaped Nanocrystals and Their Evolution: Programming the Geometry of Nano-Building Blocks. *Journal of the American Chemical Society* **2002,** *124* (38), 11244-11245.

176. Yu, D.; Wang, D.; Meng, Z.; Lu, J.; Qian, Y., Synthesis of closed PbS nanowires with regular geometric morphologies. *Journal of Materials Chemistry* **2002,** *12* (3), 403-405.

177. Kuang, D.; Xu, A.; Fang, Y.; Liu, H.; Frommen, C.; Fenske, D., Surfactant-Assisted Growth of Novel PbS Dendritic Nanostructures via Facile Hydrothermal Process. *Advanced Materials* **2003,** *15* (20), 1747-1750.

178. Wan, J.; Chen, X.; Wang, Z.; Yu, W.; Qian, Y., Synthesis of uniform PbS nanorod bundles via a surfactant-assisted interface reaction route. *Materials Chemistry and Physics* **2004,** *88* (1), 217-220.

179. Ge, J.-P.; Wang, J.; Zhang, H.-X.; Wang, X.; Peng, Q.; Li, Y.-D., Orthogonal PbS Nanowire Arrays and Networks and Their Raman Scattering Behavior. *Chemistry – A European Journal* **2005,** *11* (6), 1889-1894.

180. Dorokhin, D.; Hsu, S.-H.; Tomczak, N.; Reinhoudt, D. N.; Huskens, J.; Velders, A. H.; Vancso, G. J., Fabrication and Luminescence of Designer Surface Patterns with β-Cyclodextrin Functionalized Quantum Dots via Multivalent Supramolecular Coupling. *ACS Nano* **2010,** *4* (1), 137-142.

181. Hou, Y.; Kondoh, H.; Shimojo, M.; Sako, E. O.; Ozaki, N.; Kogure, T.; Ohta, T., Inorganic Nanocrystal Self-Assembly via the Inclusion Interaction of β-Cyclodextrins: Toward 3D Spherical Magnetite. *The Journal of Physical Chemistry B* **2005,** *109* (11), 4845-4852.

182. Depalo, N.; Comparelli, R.; Striccoli, M.; Curri, M. L.; Fini, P.; Giotta, L.; Agostiano, A., α-Cyclodextrin Functionalized CdS Nanocrystals for Fabrication of 2/3 D Assemblies. *The Journal of Physical Chemistry B* **2006,** *110* (35), 17388-17399.

183. Vatanparast, H.; Shahabi, F.; Bahramian, A.; Javadi, A.; Miller, R., The Role of Electrostatic Repulsion on Increasing Surface Activity of Anionic Surfactants in the Presence of Hydrophilic Silica Nanoparticles. *Scientific Reports* **2018,** *8* (1), 7251.

184. Binks, B. P.; Rodrigues, J. A.; Frith, W. J., Synergistic Interaction in Emulsions Stabilized by a Mixture of Silica Nanoparticles and Cationic Surfactant. *Langmuir* **2007,** *23* (7), 3626-3636.

185. Huang, T.; Zhao, Q.; Xiao, J.; Qi, L., Controllable Self-Assembly of PbS Nanostars into Ordered Structures: Close-Packed Arrays and Patterned Arrays. *ACS Nano* **2010,** *4* (8), 4707-4716.

186. Querejeta-Fernández, A.; Hernández-Garrido, J. C.; Yang, H.; Zhou, Y.; Varela, A.; Parras, M.; Calvino-Gámez, J. J.; González-Calbet, J. M.; Green, P. F.; Kotov, N. A., Unknown Aspects of Self-Assembly of PbS Microscale Superstructures. *ACS Nano* **2012,** *6* (5), 3800-3812.

187. Jun, Y.-w.; Lee, J.-H.; Choi, J.-s.; Cheon, J., Symmetry-Controlled Colloidal Nanocrystals: Nonhydrolytic Chemical Synthesis and Shape Determining Parameters. *The Journal of Physical Chemistry B* **2005,** *109* (31), 14795-14806.

188. Zhao, Z.; Zhang, K.; Zhang, J.; Yang, K.; He, C.; Dong, F.; Yang, B., Synthesis of size and shape controlled PbS nanocrystals and their self-assembly. *Colloids and Surfaces A: Physicochemical and Engineering Aspects* **2010,** *355* (1), 114-120.

189. Wang, Z. L., Transmission Electron Microscopy of Shape-Controlled Nanocrystals and Their Assemblies. *The Journal of Physical Chemistry B* **2000,** *104* (6), 1153-1175.

190. Quan, Z.; Li, C.; Zhang, X.; Yang, J.; Yang, P.; Zhang, C.; Lin, J., Polyol-Mediated Synthesis of PbS Crystals: Shape Evolution and Growth Mechanism. *Crystal Growth & Design* **2008,** *8* (7), 2384-2392.

191. Lu, Q.; Gao, F.; Komarneni, S., Biomolecule-Assisted Synthesis of Highly Ordered Snowflakelike Structures of Bismuth Sulfide Nanorods. *Journal of the American Chemical Society* **2004,** *126* (1), 54-55.

192. Shanbhag, S.; Kotov, N. A., On the Origin of a Permanent Dipole Moment in Nanocrystals with a Cubic Crystal Lattice: Effects of Truncation, Stabilizers, and Medium for CdS Tetrahedral Homologues. *The Journal of Physical Chemistry B* **2006,** *110* (25), 12211-12217.

193. Shim, M.; Guyot-Sionnest, P., Permanent dipole moment and charges in colloidal semiconductor quantum dots. **1999,** *111* (15), 6955-6964.

194. Look, D. C.; Reynolds, D. C.; Sizelove, J. R.; Jones, R. L.; Litton, C. W.; Cantwell, G.; Harsch, W. C., Electrical properties of bulk ZnO. *Solid State Communications* **1998,** *105* (6), 399-401.

195. Xu, X.; Kweon, K. E.; Keuleyan, S.; Sawvel, A.; Cho, E. J.; Orme, C., Rapid In Situ Ligand-Exchange Process Used to Prepare 3D PbSe Nanocrystal Superlattice Infrared Photodetectors. **2021,** *17* (25), 2101166.

196. Joo, J.; Pietryga, J. M.; McGuire, J. A.; Jeon, S.-H.; Williams, D. J.; Wang, H.-L.; Klimov, V. I., A Reduction Pathway in the Synthesis of PbSe Nanocrystal Quantum Dots. *Journal of the American Chemical Society* **2009,** *131* (30), 10620-10628.

197. Strehlow, W. H.; Cook, E. L., Compilation of Energy Band Gaps in Elemental and Binary Compound Semiconductors and Insulators. **1973,** *2* (1), 163-200.

198. Cockins, L.; Miyahara, Y.; Bennett, S. D.; Clerk, A. A.; Studenikin, S.; Poole, P.; Sachrajda, A.; Grutter, P., Energy levels of few-electron quantum dots imaged and characterized by atomic force microscopy. **2010,** *107* (21), 9496-9501.

199. Geuchies, J. J.; van Overbeek, C.; Evers, W. H.; Goris, B.; de Backer, A.; Gantapara, A. P.; Rabouw, F. T.; Hilhorst, J.; Peters, J. L.; Konovalov, O.; Petukhov, A. V.; Dijkstra, M.; Siebbeles, L. D. A.; van Aert, S.; Bals, S.; Vanmaekelbergh, D., In situ study of the formation mechanism of two-dimensional superlattices from PbSe nanocrystals. *Nature Materials* **2016,** *15* (12), 1248-1254.

200. Whitham, K.; Hanrath, T., Formation of Epitaxially Connected Quantum Dot Solids: Nucleation and Coherent Phase Transition. *The Journal of Physical Chemistry Letters* **2017,** *8* (12), 2623-2628.

201. Weidman, M. C.; Nguyen, Q.; Smilgies, D.-M.; Tisdale, W. A., Impact of Size Dispersity, Ligand Coverage, and Ligand Length on the Structure of PbS Nanocrystal Superlattices. *Chemistry of Materials* **2018,** *30* (3), 807-816.

202. Weidman, M. C.; Smilgies, D.-M.; Tisdale, W. A., Kinetics of the self-assembly of nanocrystal superlattices measured by real-time in situ X-ray scattering. *Nature Materials* **2016,** *15* (7), 775-781.

203. Maiti, S.; André, A.; Banerjee, R.; Hagenlocher, J.; Konovalov, O.; Schreiber, F.; Scheele, M., Monitoring Self-Assembly and Ligand Exchange of PbS Nanocrystal Superlattices at the Liquid/Air Interface in Real Time. *The Journal of Physical Chemistry Letters* **2018,** *9* (4), 739-744.

204. Zaluzhnyy, I. A.; Kurta, R. P.; André, A.; Gorobtsov, O. Y.; Rose, M.; Skopintsev, P.; Besedin, I.; Zozulya, A. V.; Sprung, M.; Schreiber, F.; Vartanyants, I. A.; Scheele, M., Quantifying Angular Correlations between the Atomic Lattice and the Superlattice of Nanocrystals Assembled with Directional Linking. *Nano Letters* **2017,** *17* (6), 3511-3517.

205. Choi, J. J.; Lim, Y.-F.; Santiago-Berrios, M. E. B.; Oh, M.; Hyun, B.-R.; Sun, L.; Bartnik, A. C.; Goedhart, A.; Malliaras, G. G.; Abruña, H. D.; Wise, F. W.; Hanrath, T., PbSe Nanocrystal Excitonic Solar Cells. *Nano Letters* **2009,** *9* (11), 3749-3755.

206. Luther, J. M.; Beard, M. C.; Song, Q.; Law, M.; Ellingson, R. J.; Nozik, A. J., Multiple Exciton Generation in Films of Electronically Coupled PbSe Quantum Dots. *Nano Letters* **2007,** *7* (6), 1779-1784.

207. Nozik, A. J.; Beard, M. C.; Luther, J. M.; Law, M.; Ellingson, R. J.; Johnson, J. C., Semiconductor Quantum Dots and Quantum Dot Arrays and Applications of Multiple Exciton Generation to Third-Generation Photovoltaic Solar Cells. *Chemical Reviews* **2010,** *110* (11), 6873-6890.

208. Qi, D.; Fischbein, M.; Drndić, M.; Šelmić, S., Efficient polymer-nanocrystal quantum-dot photodetectors. *Applied Physics Letters* **2005,** *86* (9), 093103.

209. Schaller, R. D.; Klimov, V. I., High Efficiency Carrier Multiplication in PbSe Nanocrystals: Implications for Solar Energy Conversion. *Physical Review Letters* **2004,** *92* (18), 186601.

210. Semonin, O. E.; Luther, J. M.; Choi, S.; Chen, H.-Y.; Gao, J.; Nozik, A. J.; Beard, M. C., Peak External Photocurrent Quantum Efficiency Exceeding 100% via MEG in a Quantum Dot Solar Cell. *Science* **2011,** *334* (6062), 1530-1533.

211. Midgett, A. G.; Hillhouse, H. W.; Hughes, B. K.; Nozik, A. J.; Beard, M. C., Flowing versus Static Conditions for Measuring Multiple Exciton Generation in PbSe Quantum Dots. *The Journal of Physical Chemistry C* **2010,** *114* (41), 17486-17500.

212. Geiregat, P.; Delerue, C.; Justo, Y.; Aerts, M.; Spoor, F.; Van Thourhout, D.; Siebbeles, L. D. A.; Allan, G.; Houtepen, A. J.; Hens, Z., A Phonon Scattering Bottleneck for Carrier Cooling in Lead Chalcogenide Nanocrystals. *ACS Nano* **2015,** *9* (1), 778-788.

213. Pietryga, J. M.; Werder, D. J.; Williams, D. J.; Casson, J. L.; Schaller, R. D.; Klimov, V. I.; Hollingsworth, J. A., Utilizing the Lability of Lead Selenide to Produce Heterostructured Nanocrystals with Bright, Stable Infrared Emission. *Journal of the American Chemical Society* **2008,** *130* (14), 4879-4885.

214. Böhm, M. L.; Jellicoe, T. C.; Tabachnyk, M.; Davis, N. J. L. K.; Wisnivesky-Rocca-Rivarola, F.; Ducati, C.; Ehrler, B.; Bakulin, A. A.; Greenham, N. C., Lead Telluride Quantum Dot Solar Cells Displaying External Quantum Efficiencies Exceeding 120%. *Nano Letters* **2015,** *15* (12), 7987-7993.

215. Goodwin, H.; Jellicoe, T. C.; Davis, N. J. L. K.; Böhm, M. L., Multiple exciton generation in quantum dot-based solar cells %J Nanophotonics. **2018,** *7* (1), 111-126.

216. Zhang, Y.; Sun, R.; Ou, X.; Fu, K.; Chen, Q.; Ding, Y.; Xu, L.-J.; Liu, L.; Han, Y.; Malko, A. V.; Liu, X.; Yang, H.; Bakr, O. M.; Liu, H.; Mohammed, O. F., Metal Halide Perovskite Nanosheet for X-ray High-Resolution Scintillation Imaging Screens. *ACS Nano* **2019,** *13* (2), 2520-2525.

217. McCall, K. M.; Sakhatskyi, K.; Lehmann, E.; Walfort, B.; Losko, A. S.; Montanarella, F.; Bodnarchuk, M. I.; Krieg, F.; Kelestemur, Y.; Mannes, D.; Shynkarenko, Y.; Yakunin, S.; Kovalenko, M. V., Fast Neutron Imaging with Semiconductor Nanocrystal Scintillators. *ACS Nano* **2020,** *14* (11), 14686-14697.

218. Lyu, J.; Wang, X.; Liu, L.; Kim, Y.; Tanyi, E. K.; Chi, H.; Feng, W.; Xu, L.; Li, T.; Noginov, M. A.; Uher, C.; Hammig, M. D.; Kotov, N. A., High Strength Conductive Composites with Plasmonic Nanoparticles Aligned on Aramid Nanofibers. **2016,** *26* (46), 8435-8445.

219. Lyu, J.; Hammig, M. D.; Liu, L.; Xu, L.; Chi, H.; Uher, C.; Li, T.; Kotov, N. A., Stretchable conductors by kirigami patterning of aramid-silver nanocomposites with zero conductance gradient. **2017,** *111* (16), 161901.

220. Sykora, M.; Koposov, A. Y.; McGuire, J. A.; Schulze, R. K.; Tretiak, O.; Pietryga, J. M.; Klimov, V. I., Effect of Air Exposure on Surface Properties, Electronic Structure, and Carrier Relaxation in PbSe Nanocrystals. *ACS Nano* **2010,** *4* (4), 2021-2034.

221. Woo, J. Y.; Ko, J.-H.; Song, J. H.; Kim, K.; Choi, H.; Kim, Y.-H.; Lee, D. C.; Jeong, S., Ultrastable PbSe Nanocrystal Quantum Dots via in Situ Formation of Atomically Thin Halide Adlayers on PbSe(100). *Journal of the American Chemical Society* **2014,** *136* (25), 8883-8886.

222. Kwon, I.; Kang, T.; Wells, B. T.; D'Aries, L. J.; Hammig, M. D., Compensation of the detector capacitance presented to charge-sensitive preamplifiers using the Miller effect. *Nuclear Instruments and Methods in Physics Research Section A: Accelerators, Spectrometers, Detectors and Associated Equipment* **2015,** *784*, 220-225.

223. Kwon, I.; Kang, T.; Hammig, M. D., Experimental Validation of Charge-Sensitive Amplifier Configuration that Compensates for Detector Capacitance. *IEEE Transactions on Nuclear Science* **2016,** *63* (2), 1202-1208.

224. Madelung, O.; Rössler, U.; Schulz, M. *Lead selenide (PbSe) optical properties, dielectric constant: Datasheet from Landolt-Börnstein - Group III Condensed Matter · Volume 41C: "Non-Tetrahedrally Bonded Elements and Binary Compounds I" in SpringerMaterials (https://doi.org/10.1007/10681727_895)*, Springer-Verlag Berlin Heidelberg.

225. Woo, J. Y.; Lee, S.; Lee, S.; Kim, W. D.; Lee, K.; Kim, K.; An, H. J.; Lee, D. C.; Jeong, S., Air-Stable PbSe Nanocrystals Passivated by Phosphonic Acids. *Journal of the American Chemical Society* **2016,** *138* (3), 876-883.

226. Koh, S.; Lee, D. C., Molecular valves for colloidal growth of nanocrystal quantum dots: effect of precursor decomposition and intermediate species. *MRS Communications* **2018,** *8* (3), 742-753.

227. Brown, A. A. M.; Hooper, T. J. N.; Veldhuis, S. A.; Chin, X. Y.; Bruno, A.; Vashishtha, P.; Tey, J. N.; Jiang, L.; Damodaran, B.; Pu, S. H.; Mhaisalkar, S. G.; Mathews, N., Self-assembly of a robust hydrogen-bonded octylphosphonate network on cesium lead bromide perovskite nanocrystals for light-emitting diodes. *Nanoscale* **2019,** *11* (25), 12370-12380.

228. Lee, D.; Koh, S.; Yoon, D.-E.; Lee, S.; Kim, W. D.; Kim, D.; Bae, W. K.; Lim, J.; Lee, D. C., Synthesis of InP nanocrystals using triphenyl phosphite as phosphorus source. *Korean Journal of Chemical Engineering* **2019,** *36* (9), 1518-1526.

229. Sekhar, M. C.; Paul, S.; De, A.; Samanta, A., An Ultrafast Transient Absorption Study of Charge Separation and Recombination Dynamics in CdSe QDs and Methyl Viologen: Dependence on Surface Stoichiometry. *ChemistrySelect* **2018,** *3* (9), 2675-2682.

230. Lifshitz, E.; Brumer, M.; Kigel, A.; Sashchiuk, A.; Bashouti, M.; Sirota, M.; Galun, E.; Burshtein, Z.; Le Quang, A. Q.; Ledoux-Rak, I.; Zyss, J., Air-Stable PbSe/PbS and PbSe/PbSexS1-x Core−Shell Nanocrystal Quantum Dots and Their Applications. *The Journal of Physical Chemistry B* **2006,** *110* (50), 25356-25365.

231. Bockelmann, U.; Bastard, G., Phonon scattering and energy relaxation in two-, one-, and zero-dimensional electron gases. *Physical Review B* **1990,** *42* (14), 8947-8951.

232. Inoshita, T.; Sakaki, H., Electron-phonon interaction and the so-called phonon bottleneck effect in semiconductor quantum dots. *Physica B: Condensed Matter* **1996,** *227* (1), 373-377.

233. Leschkies, K. S.; Kang, M. S.; Aydil, E. S.; Norris, D. J., Influence of Atmospheric Gases on the Electrical Properties of PbSe Quantum-Dot Films. *The Journal of Physical Chemistry C* **2010,** *114* (21), 9988-9996.

234. Boercker, J. E.; Foos, E. E.; Placencia, D.; Tischler, J. G., Control of PbSe Nanorod Aspect Ratio by Limiting Phosphine Hydrolysis. *Journal of the American Chemical Society* **2013,** *135* (40), 15071-15076.

235. Koh, W.-k.; Yoon, Y.; Murray, C. B., Investigating the Phosphine Chemistry of Se Precursors for the Synthesis of PbSe Nanorods. *Chemistry of Materials* **2011,** *23* (7), 1825-1829.

236. Sannigrahi, P.; Ingall, E., Polyphosphates as a source of enhanced P fluxes in marine sediments overlain by anoxic waters: Evidence from 31P NMR. *Geochemical Transactions* **2005,** *6* (3), 52-59.

237. Owen, J. S.; Park, J.; Trudeau, P.-E.; Alivisatos, A. P., Reaction Chemistry and Ligand Exchange at Cadmium−Selenide Nanocrystal Surfaces. *Journal of the American Chemical Society* **2008,** *130* (37), 12279-12281.

238. Gomes, R.; Hassinen, A.; Szczygiel, A.; Zhao, Q.; Vantomme, A.; Martins, J. C.; Hens, Z., Binding of Phosphonic Acids to CdSe Quantum Dots: A Solution NMR Study. *The Journal of Physical Chemistry Letters* **2011,** *2* (3), 145-152.

239. Fan, Q.; Liu, K.; Liu, Z.; Liu, H.; Zhang, L.; Zhong, P.; Gao, C., A Ligand-Exchange Route to Nobel Metal Nanocrystals with a Clean Surface for Enhanced Optical and Catalytic Properties. **2017,** *34* (8), 1700075.

240. Gao , C.; Lu , Z.; Liu , Y.; Zhang, Q.; Chi, M.; Cheng, Q.; Yin, Y., Highly Stable Silver Nanoplates for Surface Plasmon Resonance Biosensing. **2012,** *51* (23), 5629-5633.

241. Habicher, W. D.; Pawelke, B.; Bauer, I.; Yamaguchi, K.; Kósa, C.; Chmela, Š.; Pospíšil, J., Synthesis and antioxidative properties of novel multifunctional stabilizers. **2001,** *7* (1), 4-18.

242. Gautier, C.; Cambon-Muller, M.; Averous, M., Study of PbSe layer oxidation and oxide dissolution. *Applied Surface Science* **1999,** *141* (1), 157-163.

243. Wanger, C. D. R., W. M.; Davis, L. E.; Moulder, J. F.; Muilenberg, G. E., *Handbook of X-ray Photoelectron Spectroscopy*. Perkin Elmer, Corporation: Eden Prairie, Minnesota, 1979; Vol. 3.

244. Švrček, V.; Mariotti, D.; Mitra, S.; Kaneko, T.; Li, L.; Cvelbar, U.; Matsubara, K.; Kondo, M., Built-In Charges and Photoluminescence Stability of 3D Surface-Engineered Silicon Nanocrystals by a Nanosecond Laser and a Direct Current Microplasma. *The Journal of Physical Chemistry C* **2013,** *117* (21), 10939-10948.

245. Hanson, C. J.; Hartmann, N. F.; Singh, A.; Ma, X.; DeBenedetti, W. J. I.; Casson, J. L.; Grey, J. K.; Chabal, Y. J.; Malko, A. V.; Sykora, M.; Piryatinski, A.; Htoon, H.; Hollingsworth, J. A., Giant PbSe/CdSe/CdSe Quantum Dots: Crystal-Structure-Defined Ultrastable Near-

Infrared Photoluminescence from Single Nanocrystals. *Journal of the American Chemical Society* **2017,** *139* (32), 11081-11088.

246. Choi, H.; Ko, J.-H.; Kim, Y.-H.; Jeong, S., Steric-Hindrance-Driven Shape Transition in PbS Quantum Dots: Understanding Size-Dependent Stability. *Journal of the American Chemical Society* **2013,** *135* (14), 5278-5281.

247. Saari, J. I.; Dias, E. A.; Reifsnyder, D.; Krause, M. M.; Walsh, B. R.; Murray, C. B.; Kambhampati, P., Ultrafast Electron Trapping at the Surface of Semiconductor Nanocrystals: Excitonic and Biexcitonic Processes. *The Journal of Physical Chemistry B* **2013,** *117* (16), 4412-4421.

248. Ying, W. B.; Mizokawa, Y.; Kamiura, Y.; Kawamoto, K.; Yang, W. Y., The chemical composition changes of silicon and phosphorus in the process of native oxide formation of heavily phosphorus doped silicon. *Applied Surface Science* **2001,** *181* (1), 1-14.

249. Alexander V. Naumkin, A. K.-V., Stephen W. Gaarenstroom, Cedric J. Powell, NIST Standard Reference Database 20. **2003,** (Version 3.4 (web version)).

250. Dong, A.; Chen, J.; Vora, P. M.; Kikkawa, J. M.; Murray, C. B., Binary nanocrystal superlattice membranes self-assembled at the liquid–air interface. *Nature* **2010,** *466* (7305), 474-477.

251. LaCour, R. A.; Adorf, C. S.; Dshemuchadse, J.; Glotzer, S. C., Influence of Softness on the Stability of Binary Colloidal Crystals. *ACS Nano* **2019,** *13* (12), 13829-13842.

252. Boles, M. A.; Talapin, D. V., Many-Body Effects in Nanocrystal Superlattices: Departure from Sphere Packing Explains Stability of Binary Phases. *Journal of the American Chemical Society* **2015,** *137* (13), 4494-4502.

253. Gebauer, D.; Cölfen, H., Prenucleation clusters and non-classical nucleation. *Nano Today* **2011,** *6* (6), 564-584.

254. Gebauer, D.; Völkel, A.; Cölfen, H., Stable Prenucleation Calcium Carbonate Clusters. **2008,** *322* (5909), 1819-1822.

255. D. Vecchio, M. D. H., N. A. Kotov, High band-gap aqeous synthesized lead telluride nanoparticles that assemble via prenucleation cluster pathway. *ACS Nano* **2021 (in preparation)**.

256. Geuchies, J. J.; Soligno, G.; Geraffy, E.; Hendrikx, C. P.; Overbeek, C. v.; Montanarella, F.; Slot, M. R.; Konovalov, O. V.; Petukhov, A. V.; Vanmaekelbergh, D., Unravelling three-dimensional adsorption geometries of PbSe nanocrystal monolayers at a liquid-air interface. *Communications Chemistry* **2020,** *3* (1), 28.

257. Wang, Y.; Peng, X.; Abelson, A.; Xiao, P.; Qian, C.; Yu, L.; Ophus, C.; Ercius, P.; Wang, L.-W.; Law, M.; Zheng, H., Dynamic deformability of individual PbSe nanocrystals during superlattice phase transitions. **2019,** *5* (6), eaaw5623.

258. Dalmaschio, C. J.; Ribeiro, C.; Leite, E. R., Impact of the colloidal state on the oriented attachment growth mechanism. *Nanoscale* **2010,** *2* (11), 2336-2345.

259. Lee, E. J. H.; Ribeiro, C.; Longo, E.; Leite, E. R., Oriented Attachment: An Effective Mechanism in the Formation of Anisotropic Nanocrystals. *The Journal of Physical Chemistry B* **2005,** *109* (44), 20842-20846.

260. Leite, E. R.; Giraldi, T. R.; Pontes, F. M.; Longo, E.; Beltrán, A.; Andrés, J., Crystal growth in colloidal tin oxide nanocrystals induced by coalescence at room temperature. **2003,** *83* (8), 1566-1568.

261. Whitham, K.; Yang, J.; Savitzky, B. H.; Kourkoutis, L. F.; Wise, F.; Hanrath, T., Charge transport and localization in atomically coherent quantum dot solids. *Nature Materials* **2016,** *15* (5), 557-563.

262. Evers, W. H.; Schins, J. M.; Aerts, M.; Kulkarni, A.; Capiod, P.; Berthe, M.; Grandidier, B.; Delerue, C.; van der Zant, H. S. J.; van Overbeek, C.; Peters, J. L.; Vanmaekelbergh, D.; Siebbeles, L. D. A., High charge mobility in two-dimensional percolative networks of PbSe quantum dots connected by atomic bonds. *Nature Communications* **2015,** *6* (1), 8195.

263. Banerjee, A.; Bernoulli, D.; Zhang, H.; Yuen, M.-F.; Liu, J.; Dong, J.; Ding, F.; Lu, J.; Dao, M.; Zhang, W.; Lu, Y.; Suresh, S., Ultralarge elastic deformation of nanoscale diamond. **2018,** *360* (6386), 300-302.

264. Schliehe, C.; Juarez, B. H.; Pelletier, M.; Jander, S.; Greshnykh, D.; Nagel, M.; Meyer, A.; Foerster, S.; Kornowski, A.; Klinke, C.; Weller, H., Ultrathin PbS Sheets by Two-Dimensional Oriented Attachment. **2010,** *329* (5991), 550-553.

265. Sutter, E.; Sutter, P.; Tkachenko, A. V.; Krahne, R.; de Graaf, J.; Arciniegas, M.; Manna, L., In situ microscopy of the self-assembly of branched nanocrystals in solution. *Nature Communications* **2016,** *7* (1), 11213.

266. Hatton, B.; Mishchenko, L.; Davis, S.; Sandhage, K. H.; Aizenberg, J., Assembly of large-area, highly ordered, crack-free inverse opal films. **2010,** *107* (23), 10354-10359.

267. Zhou, G.; Lü, M.; Xiu, Z.; Wang, S.; Zhang, H.; Zhou, Y.; Wang, S., Controlled Synthesis of High-Quality PbS Star-Shaped Dendrites, Multipods, Truncated Nanocubes, and Nanocubes and Their Shape Evolution Process. *The Journal of Physical Chemistry B* **2006,** *110* (13), 6543-6548.

268. Hammig, M. D.; Kang, T.; Jeong, M.; Jarrett, M. In *Suppression of interface-induced noise by the control of electron-phonon interactions*, 2012 IEEE Nuclear Science Symposium and Medical Imaging Conference Record (NSS/MIC), 27 Oct.-3 Nov. 2012; 2012; pp 4188-4195.

269. Beugeling, W.; Kalesaki, E.; Delerue, C.; Niquet, Y. M.; Vanmaekelbergh, D.; Smith, C. M., Topological states in multi-orbital HgTe honeycomb lattices. *Nature Communications* **2015,** *6* (1), 6316.

270. Werner, C. J., MCNP Users Manual-Code Version 6.2. *Los Alamos National Laoratory* **2017,** *report LA-17-29981*.

271. Burstein, E.; Perkowitz, S.; Brodsky, M., THE DIELECTRIC PROPERTIES OF THE CUBIC IV-VI COMPOUND SEMICONDUCTORS. **1968,** *29* (C4), C4-78-C4-83.

272. Jacob, J. M.; Raj Mohan, B.; Akshay Gowda, K. M., Insights into the optical and anti-bacterial properties of biogenic PbSe quantum rods. *Journal of Saudi Chemical Society* **2016,** *20* (4), 480-485.

273. Joglekar, S. G.; Hammig, M. D.; Guo, L. J., High-Energy Photon Spectroscopy Using All Solution-Processed Heterojunctioned Surface-Modified Perovskite Single Crystals. *ACS Applied Materials & Interfaces* **2019,** *11* (36), 33399-33408.